UNIVERSITY OF CAPE TOWN

FACULTY OF ENGINEERING AND BUILT ENVIRONMENT

Department of Civil Engineering

Investigation of Hydro-Mechanical Particle Flow through Horizontal Orifices

---

Geotechnical Engineering Group

AUTHOR:	**ZHENGHUI QIU**
SUPERVISOR:	**DR DENIS KALUMBA**
CO-SUPERVISOR:	**JOHNNY LAI SANG**

A thesis submitted in partial fulfilment of the requirements for a Master of Science in Engineering, specialising in Geotechnical Engineering at the University of Cape Town
[October 2017]

Preface

This dissertation was prepared for Dr Denis Kalumba in partial fulfilment of the requirements for the degree of Master of Science in Engineering specialising in Geotechnical Engineering.

The research described in this dissertation was conducted as part of the Research and Development Department of De Beers Marine Pty (Ltd) – henceforth referred to as DBM. The research objectives were developed to align with the interests of DBM, and the investigation was facilitated by DBM software and equipment.

I, Zhenghui Qiu, declare that I know the meaning of plagiarism and that all the work in this dissertation, save for that which is properly acknowledged, is my own. This thesis has been submitted to the Turnitin module and I confirm that my supervisor has seen my report and any concerns revealed by such have been resolved with my supervisor I have used the Harvard method for citation and referencing.

Mr Zhenghui Qiu
MSc Candidate
Author

Signed by candidate

Signed

31/10/2017

Date

Dr Denis Kalumba
Senior Lecturer - University of Cape Town
Supervisor

Signed

Date

Mr Johnny Lai Sang
Engineer - De Beers Marine Pty(Ltd)
Co-Supervisor

Signed

Date

Dedicated to my parents-

Qiu Liangquan and Wang Guoqiu

（邱 亮权) *and* (王 国秋)

Acknowledgements

I would like to dedicate my first vote of thanks to my supervisor, Dr Denis Kalumba, whose guidance and knowledge was truly instrumental in the completion of this dissertation. The thorough review of my work and your enthusiasm for geotechnical engineering was highly appreciated.

My sincere thanks and gratitude goes to De Beers Marine (Pty) Ltd for funding my postgraduate studies and allowing me access to their resources, equipment, modelling software, laboratory facilities and offices. Special recognitions must go to my co-supervisor, Mr Johnny Lai Sang. His expertise, feedback and willingness to help were invaluable contributions. I would like to extend these acknowledgements to the following De Beers Marine personnel who assisted me in both the practical and design aspects of my work:

- Mrs Delmarie Fisch (Physical laboratory testing)
- Mrs Hendriena van der Walt (Administration of my involvement with De Beers Marine)
- Mr Imraan Parker (Running of DEM simulations)
- Mr Gerhard de Vries (Physical laboratory testing)
- The staff of the De Beers Marine Laboratory: Siza Mashicolo, Zandiba Seti, Emecca Tsala and Siphiwo Mgedle.

I wish to further express my gratitude to the following people:

- To the CG Clarkson Educational Trust and particularly Mr Charles Clarkson himself for the financial support and career advice given during my postgraduate studies.
- To the UCT postgraduate funding office for their funding throughout the duration of my postgraduate studies.
- Mr. Charles Nicholas, for his assistance towards the construction of my model.
- To the UCT Geotechnical Engineering Research Group, for allowing me to share and discuss my research. The standard of work in this department continues to inspire me.
- To the Pepler Family, for their positive influence throughout my life.
- To Jared Thom, the best flat mate and arguably human ever, for his willingness to proof read my dissertation.
- To my friends and family for their endless love and support throughout this entire process.

Abstract

In the modern world, as the global population continues to rise, the need for and recovery of natural resources is becoming ever more relevant. Identifying optimisation solutions for the recovery of granular resources has progressed into one of the most dominant development areas in the mining and processing industries. Two relevant examples from these sectors include the offshore extraction of materials from the ocean floor via hydraulic transport and the processing of mineral particulates through chutes, and hoppers. A common feature of recovery employed in such areas is the rate at which these materials pass through an orifice. The orifice is the interface between the implemented collection or transport system and the targeted material source.

Extensive research has been done on the gravitational passing of particles through an orifice, where in contrast, limited knowledge exists on alternative driving factors of flow. The movement of particles induced both mechanically and hydraulically formed the basis of this dissertation in which selected granular materials were experimentally characterised. Specifically, the following were studied: the effect of orifice and particle size, changes in system velocity and the effects of suction. The system encompassed a scaled down model of a real-life application. An experimental and numerical analysis approach was undertaken, where the calibration of the simulated model was dependent on the former. A total of 327 experimental tests were conducted on the flow ability of high sphericity (±95% roundness) glass beads. A numerical model based on the physical parameters was calibrated to further assist in the overall analysis of the system. The model was of a discrete element method (DEM) type.

Empirically, it was found that the Beverloo law, an expression used to describe the discharge of particles through a hopper, had many aspects that were dimensionally suited for the study. Through certain boundary assumptions made in the study, the law was in agreement with the stated outputs. The ratio (R) between the orifice (D_o) and particle diameter (d_p) had a significant influence on the entrainment rate, where there existed a region ($R > 4$) of limiting flow. Changes in the system velocity, were found to have a negligible effect on the overall recovery but a direct relationship with the rate at which the material was collected. The introduction of suction improved the recovery of materials greatly, increasing the mass flow rate by more than 300%.

The in-depth analysis on a multitude of orifice configurations, considerably extended the understanding of the behaviour of particles passing through an opening, particularly spherical particles under fluid or mechanical driven flow. Results indicated that there was a lot of potential for improving the optimisation of granular flow. Optimisation in this sense was defined as maximising the recovery (%) or collection rate (kg/s) of the system. Boundary conditions and design guidelines were offered to address this issue. Areas where further research could advance this understanding were highlighted.

Table of Contents

List of Appendices

List of Figures

List of Tables

Notation

The metric units (SI) and prefixes used in this dissertation were in accordance with standard nomenclature recommended by the International Society of Soil Mechanics and Geotechnical Engineering (ISSMGE). However, due to the broad scope of the project, other symbols were selected to conform to other engineering disciplines evident in this dissertation. The distinctions are made clear in the text.

For ease of analysis, symbols and abbreviations will be described when they first appear. Acronyms and symbols that are repeated later on in the text, are listed below. Appropriate units were used when representing quantities of known dimensions. To avoid inconsistency, the SI unit convention was utilised. If no dimension is indicated, the symbol represents a dimensionless number.

Acronyms

2D	Two-dimensional
3D	Three-dimensional
CI	Confidence interval
CM	Collection machine
DBM	De Beers Marine
DBMN	De Beers Marine Namibia
DEM	Discrete Element Method
FEM	Finite Element Method
GB	Glass beads
GB16	16mm diameter beads
GB6	6mm diameter beads
HAR	Horizontal aspect ratio
ILS	Inductive limit switches
MMS	Mechnical movement system
MSS	Mechanical movement and suction system
PSD	Particle size distribution
UCT	University of Cape Town
VAR	Vertical aspect ratio
VSD	Variable speed drive

Granular Flow Symbols

C_D	Drag coefficient
μ_d	Dynamic friction
μ_p	Particle friction
μ_r	Rolling resistance
μ_s	Static friction
A_e (mm^2)	Effective area
A_0 (mm^2)	Area of orifice
C	Discharge coefficient
C_D	Drag coefficient
C_m	Mass concentration
C_v (kg/l)	Volumetric concentration
C_{vb}	Maximum volume fraction
C_{vd}	Delivery concentration
D_B (mm)	Barrel diameter
D_e (mm)	Effective hydraulic diameter
D_h (mm)	Hydraulic diameter
D_o (mm)	Orifice diameter
d_p (mm)	Particle diameter
d (mm)	Effective bed depth

F (kN)	Force vector
F_b (kN)	Buoyancy force
F_D (kN)	Drag force
F_D (kN)	Gravity/Weight force
F_L (kN)	Lift force
F_N (kN)	Normal force
g (m/s^2)	Gravitational acceleration
G_s	Specific gravity of material
H (mm)	Height of bed
H (cm)	Head of sample
k	Particle shape factor
k_n	Normal stiffness
k_s	Tangential stiffness
m (g)	Mass of particles
n	Porosity
p (kPa)	Pressure
Q (l/s)	Flow rate
R	Ratio between D_o/d_p
Re	Reynold's number
Re_p	Particle Reynold's number
t (s)	Time /Simulation time
t_s (s)	Modelled simulation time
v (m/s)	Velocity vector
v_f (m/s)	Fluid velocity
v_p (m/s)	Particle velocity
V (m^3)	Volume
W (kg/s)	Discharge rate/ Mass flow rate
w_t (mm)	Wall thickness
w (mm)	Width
x (mm)	Displacement
α (°)	Angle of wall with opening
β	Entree loss coefficient
γ (kN/m^3)	Unit weight of material

Δ	Change in variable
λ	Darcy-Weisbach coefficient
μ (N.s/m^2)	Absolute viscosity
ρ_b (kg/m^3)	Buk Density
ρ_s (kg/m3)	Particle density
ρ_{sm} (kg/m3)	Modelled particle density
υ (N.s/m^2)	Kinematic viscosity
ϕ (°)	Angle of repose
ϕ_w	Wall friction
τ (kPa)	Shear stress
σ_n (kPa)	Normal stress

Units

cm	centimetres
g	Gram
hr	Hour
kg	Kilogram
kN	Kilonewton
kPa	Kilopascals
MPa	Megapascals
m	Metres
µm	Micron-metres
mm	Millimetres
min	Minute
N	Newton
s	Seconds
Hz	Hertz
l	Litre

Scaling Law Symbols

μ (N.s/m2)	Dynamic viscosity
a (m/s^2)	Acceleration
c	Material constant
E (N/m^2)	Modulus of elasticity
Ɛ (mm)	Strain
Fr	Froude number
i	Electric current factor
kn	Scaling exponents
l	Length factor
m	Mass factor
p (kPa)	Pressure
R_i	Radii of spheres
r_i	Position of spheres
S	Dynamics of system
t	Time factor
t (s)	Time
U	Energy dissipation
α (°)	Angle of wall with opening
θ	Temperature factor
λ_n	Scale factor
ν	Poisson ratio
π	Principal Pi-number
σ (MPa)	Stress / Surface tension
σ_m (MPa)	Maximum stress

1. Introduction

1.1 Background to Study

The passing of granular particles through an orifice under different flow mechanisms, presents many engineering challenges. A sound understanding of the behaviour of granular flow is relevant to the analysis and design of many extraction and transport systems in the processing and material handling industries. For example, in offshore mining and dredging practices, the primary interface between the collection system and raw material is a region of critical importance to optimise the flow of materials. Apart from the historical extraction of resource orientated ores in the marine mining industry, current 21st century examples of extraction, include the gathering of granular materials through suction based nozzle dredgers used for land reclamation projects in Dubai - "The Palm Islands" (Jackson & della Dora, 2009).

The general background to the project analysed the behaviour of particles passing through an orifice, highlighting the effect of certain variables and parameters within a closed domain. The analysis was supported in the context of common granular flow and hydraulic transport practices. The assembled system utilised spherical glass beads, chosen to provide a well-defined granular assembly, such that interactions were limited to glass-glass and glass-boundary contacts (Kasangaki, 2012).

Figure 1-1: Artificial Palm Islands created through complex dredging work
Source: (Jackson & della Dora, 2009)

The collection of granular materials was driven by hydraulic transport or mechanical inertial systems, or a combination of the two. Newton's law regarding the conservation of mass and energy, was one of the principle laws governing the motion of particles through an orifice. The pressure difference between two points, as conceptualised below, is a common example prevalent to Newton's law of energy (Finnemore & Franzini, 2002). In many cases, the movement of particles is assisted by the presence of fluid as a transport medium.

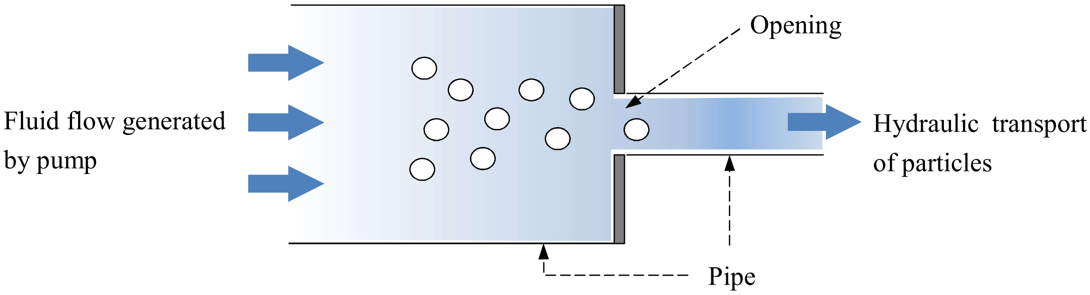

Figure 1-2: Hydraulic transport of particles through an opening

Theories surrounding the movement of particles through an orifice have been studied extensively. However, many have made references to the poor understanding of the variables and parameters considered in the predictability and behaviour of such an effect (Nedderman et al., 1982; Bao et al., 2003; Mankoc et al., 2007; Aguirre et al., 2010; Kasangaki, 2012). To gain a theoretical understanding on the recovery phenomenon, topics such as common offshore particle extraction techniques and constitutive flow laws were investigated. This allowed a detailed analysis on parameters governing the flow of particles through an orifice to be completed. Both physical and numerical models were used to aid in this investigation.

1.1.1 Common Particle Entrainment Practices

A wide variety of operations exist that deal with particle entrainment, specifically in the geotechnical engineering field. In keeping with the relevance of geotechnical engineering, such operations include the physical core sampling of materials both offshore and onshore, the extraction of granular materials for offshore mining and the discharge of materials through hoppers or pipes in the dredging industry. Reasons for investigating these practices were based on the following statements:

a) Operations in these industries display a form of tool-to-particle interaction;

b) The type of systems utilised were dependent on the material encountered;

c) Coring and mining have targeted specifications over the materials involved. Mining tools may need to be modified according to the type of materials found within a certain particle size distribution. Coring tools have different shaped cutter heads corresponding to the type and strength of the materials to be recovered.

d) Efficiency is based entirely on the amount of resources collected, recovered or produced.

1.2 Significance of the Study

Theories and principles behind the entrainment of particles through an orifice, have a major role in the extraction of granular resources around the world (Lafond et al., 2013). More specifically, as the need for ocean resources increases, the significance of particle entrainment continues to grow and become ever more relevant (Chung, 1991; Hein et al., 2013). This is most notably evident in the suction of granular particles from the implemented tools in offshore mining and dredging practices, where certain production targets must be met to allow for such ventures to be economically viable (Richardson, 2007; Heydon, 2012). Highlighting the importance of investigating and characterising the flow phenomena.

Minor modifications of the opening have led to massive fluctuations in efficiency, both positive and negative as evident in studies conducted by Garcimartín et al. (2009) and Beverloo et al. (1961) . A common negative effect includes systems becoming prone to clogging or jamming caused by the interlocking of larger particles. Over time, researchers have identified that the granular flow of particles were dependent on the variables near the orifice of the system used (Seville, Tüzün & Clift, 2012). This included the shape and size of the orifice along with the properties of the particles to be entrained. Therefore, it was common practice for extraction industries to gain an understanding of the geology of the site before commencing with operations. This was to allow them to make the necessary modifications to entrain the material. Some of the theories involved in the modification of interface parameters included laws derived by Janssen (1895) and Beverloo et al. (1961).

Empirical relations used to characterise the behaviour of gravity driven flow through an opening has been extensively covered (Franklin & Johanson, 1955; Le Pennec et al., 1995; Harris, 2001; Seville, Tüzün & Clift, 2012; Lafond et al., 2013). Whereas studies in mechanical or fluid driven flow has tended to be limited (Bao et al., 2003; Roussel, Nguyen & Coussot, 2007; Aguirre et al., 2010; Lafond et al., 2013). In the field of fluid mechanics and geotechnical engineering, a governing granular flow law known as "The Beverloo Law", looks at the discharge rate of granular particles through a hopper (Figure 1-3). Common constitutive laws such as this were reviewed as it dealt with variables near the aperture interface which were of comparable relevance.

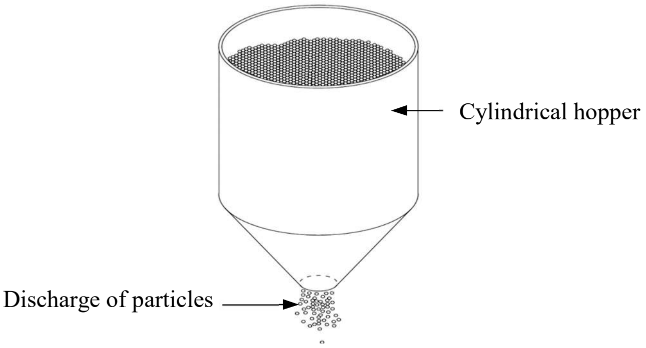

Figure 1-3: Discharge of particles through hopper

The study of particles passing through an orifice under fluid or mechanically driven flow, will improve the understanding of its behaviour amongst communities that deal with particulate materials. Such communities include agronomists, geotechnical consultants, researchers and those involved in the handling and storage of granular materials.

In addition to the physical tests, focus was given to DEM, a method based on the use of an explicit numerical scheme. The method developed by Cundall and Strack in 1979, monitors the interaction and motion of particles through interparticle contact and singular elements respectively. The DEM method was applied to model the interaction between the passing granular materials and the orifice. In this setting, the material behaviour was observed and evaluated in terms of its influence on the final output.

1.3 Research Objectives and Methodology

The main objective was to analyse the hydro-mechanical behaviour of granular materials passing through an orifice. Specifically, the investigation focussed on the effects of particle size, orifice diameter, suction, and mechanical entrainment. Using the results obtained from both experimental and numerical tests, the robustness of popular constitutive models found in literature was assessed, whilst simultaneously analysing the data from first principles and conducting a sensitivity analysis amongst the variables interplayed. It was anticipated that the project would enhance ones understanding of the physical parameters influencing the level of flow through an orifice. Recognising the gap of knowledge, the methodology used to achieve these objectives were as follows:

- Design and construct an appropriate model to experimentally evaluate the parameters of interest regarding orifice flow;
- Using the physical outputs, calibrate a three-dimensional (3D) DEM model to further investigate the behaviour of granular materials;
- Assess the physical and numerical results, offering insight into the modelled behaviour of the granular particles and orifice system;
- Establish design rules and boundary conditions in the handling of particulate materials as a guide for researchers, consultants and interested communities.

Methods of optimising flow and addressing common flow problems were the main products of this study.

1.4 Scope and Limitations of Investigation

The scope was limited to the interface between the orifice and granular particles under various testing conditions and system operations. Therefore, only certain aspects and variables were considered during the testing and analysis phase. In addition to the set out scope, the following limitations were encountered:

- All physical tests were carried out at the De Beers Marine (DBM) Research and Development Test Faciliy in Paarden Eiland, Cape Town. The facility consisted of various model-scale equipment and devices for the analysis of recovery operations utilised in the mining industry.
- All numerical testing was conducted with Rocky DEM Software-henceforth referred to as Rocky. Rocky, a 3D Discrete Element Modelling (DEM) programme, was capable of simulating complex inter-particle behaviour. The modelling of complex granular shapes (low sphericity) was deemed impractical due to the high computational demand. To simplify the problem, granular materials were modelled as spherical glass beads (GB) of limited size.
- Due to the complex nature surrounding granular flow, the majority of the constitutive laws reviewed were derived empirically.

1.5 Structure of Thesis

The research document begins with an introduction to the topic, highlighting the main objectives and limitations. The body of the thesis was divided into four main parts where each part contained several chapters. Summarised as follows:

Part I consisted of five chapters, encompassing the literature review, wherein previously related research on the optimisation of granular flow, offshore extraction techniques, granular flow theories, and numerical modelling methods was reviewed.

Part II detailed the physical testing methodology, experimental setup and the apparatus used. All encompassed in two chapters.

Part III aimed to provide a complete overview on the assembly of the Rocky DEM numerical model and the simulation methodology carried out. The chapter looked at the various input parameters, geometries and dynamic properties considered to calibrate the model.

Part IV looked at the overall assessment and conclusions of the results obtained both experimentally and numerically. The part consisted of two chapters with recommendations for future research provided in the last.

PART I

Literature Review

Contents

Chapter 2 - Offshore Extraction Techniques
A brief review of the different types of offshore extraction methods used in the mining and dredging industries and their applicability within the dissertation.

Chapter 3 - Granular Flow Immersed in Fluid
The principles of fluid and granular flow were reviewed.

Chapter 4 - The Beverloo Law
The main governing law of the project was reviewed; describing the key parameters and limitations associated with it. The law looks at the discharge rate of granular materials through a hopper.

Chapter 5 – Theory and Application of DEM
The numerical modelling methods were summarised with a focus on the discrete element method, its applications and limitations.

Chapter 6 – Case Studies
Case studies revolving around the granular flow phenomenon were used to assist in the flow analysis of this research.

2. Offshore Particle Extraction Techniques

2.1 Introduction

Offshore extraction techniques are particularly relevant as their functionality was based on concepts surrounding the movement of materials through an orifice in a fluid medium. Several modern extraction operations exist, currently used in the 21st century, include: a) Offshore mining, b) Sampling and c) Ocean floor dredging. This chapter investigates the design and function of the tools used in such operations before reviewing the constitutive flow laws in the following chapter.

2.2 Offshore Mining Tools

Marine mining on the ocean floor has occurred over many years, with most commercial ventures focussing on granular resources such as diamonds, sulphur, magnesium, gold and other heavy minerals (Baker et al., 2016). The increasing depletion of finite land resources has led to the demand for minerals found in offshore deposits (Liu et al., 2016). The extraction of these deposits is essential in satisfying resource demands and facilitating future human development. Granular orifice flow is best portrayed by suction based mining techniques. The techniques are commonly applied to loose granular deposits or seabeds with poor cohesive properties. The reason for this being that suction based tools require a significant amount of force to lift large material fragments or agitate densely packed (consolidated) beds (Vlasblom, 2003).

A combination of suction and mechanical movement entrainment is an added option often practiced in unfavourable conditions. This can include moving suction nozzles or cutter-suction hybrid tools. In some cases, these tools may be produced as separate entities. Nautilus Minerals, a commercial offshore mining company, specialise in such tools (Heydon, 2012). The company uses one of their two large robotic machines to excavate the ocean floor via a cutting process. Both machines leave behind material to be collected by a collection machine (CM). The CM is a large robotic machine that extracts the loosened material by drawing it in as a seawater slurry via an internal pump and passing it through to the lifter and riser system (Heydon, 2012). The utilisation of the aforementioned tools and pure suction based techniques, is most evident along the coasts of Namibia, Mexico, Chile, Indonesia, Australia and New Zealand. (Charlier, 1992; Osterkamp & Morton, 2005; Baker et al., 2016)

2.2.1 Overview of Offshore Mining Techniques

The tools of interest included pure suction or suction based composite tools. Table 2-1 below looks at commercially used tools that are operated by large offshore mining industries (Heydon, 2012; De Beers Group, 2016). The systems available include: a) seabed crawler, b) cutter-suction tool, c) vertical-suction drill and d) collection machine.

Table 2-1: Different offshore suction mining techniques
Source: Heydon (2012); Richardson (2007)

Mining Technique	Sampling Depiction	Description
Seabed Crawler **(De Beers Marine)**		Offshore mining tool capable of sucking/entraining materials off the ocean floor at a rate of 1000m^2/hour. Collection is done via a nozzle connected to a manually operated swinging arm. It is powered by 700mm diameter centrifugal pump.
Cutter Suction Tool **(Royal IHC, 2017)**		The cutter suction system serves as both a dredging and mining tool. It is a combination of suction and cutting, with mining rates ranging between 1900-2200 kg/m3. The cutter loosens the materials and the suction pump extracts the material. The dredge pump is powered through continuous engine power: 1350kW @ 1600rpm.
Vertical Suction Drill: **Scaled Model** (Richardson, 2014)		The system can transport approximately 3500m^3 of granular solids in a 24-hour operational period. It is designed to have a diameter of approximately seven metres and a flanged pipe with an inner diameter of 600mm. The system operates a rotating drill bit powered by a power swivel via the drill pipe. (Kuehnlein, 2010)
Collection Machine **(Nautilus Minerals, 2012)**	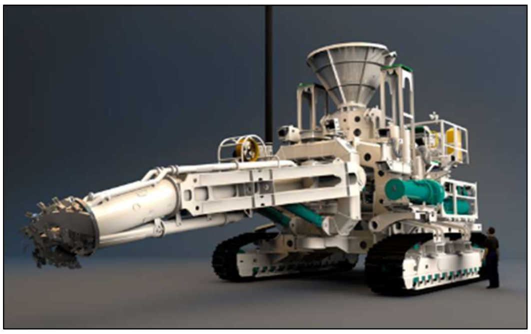	The tool works in unison with an auxiliary cutter tool designed by Nautilus (Heydon, 2012). The collection machine collects disaggregated material left behind by the cutter. The material is mixed with seawater and drawn into a flexible pipe via internal pumps as slurry

2.2.2 Optimisation of Mining Tools

With respect to granular fluid flow through an orifice, the optimisation of mining tools can be achieved through the modification of geometries around the face of the interacting segment. In some cases, modifications are made following the limitations of a motorised suction pump (Kirby, 2017). The maximum flow rate of a suction pipe is important, but in extraction practices, more so the volumetric (C_v) or mass concentration (C_m) between the number of particles collected and transported fluid. These terms which describe the rate of recovery within the suction pipe, are presented using the following equations (Vlasblom, 2003):

$$C_v = \frac{V_s}{V_s + V_w} \tag{2-1}$$

Where,

V_s = Volume of solid particles in m^3
V_w = Volume of water in m^3

$$C_m = \frac{M_s}{M_s + M_w} \tag{2-2}$$

Where,

M_s = Mass of solid particles in kg
M_w = Mass of water in kg

The two terms differ, where the former looks at the space occupied within the pipe and the latter the density ratio between the constituents within the pipe and the total mixture. Although both relevant, in dredging and mining practices, one would prefer to evaluate the delivery concentration defined as:

$$C_{vd} = \frac{Q_s}{Q_m} = C_v \frac{v_s}{v_m} \tag{2-3}$$

Where,

Q_s = Flow rate of solids in l/s
Q_m = Flow rate of mixture in l/s
v_m = Velocity of mixture in m/s

This indicates the rate of flow of solid particles with respect to the overall flow of the mixture. Theoretically, the higher the delivery concentration is, the higher the production output will be.

2.3 Soil Sampling Techniques

Soil sampling is a subsurface exploration method used to retrieve representative samples of an investigated site (Al-Khafaji & Andersland, 2007; Das, 2011). The soil samples recovered provide useful geological information such as its structure, consistency, origin and engineering parameters. They are obtained during boring or excavation processes and may often require the use of specialised tools when ground conditions are unfavourable such as soils beneath the water table or problem soils such as expansive clay. Since relevance was given to movement of particles in fluid, sampling techniques that cater for operations beneath the water table were evaluated. A sample that truly represents an in-situ sedimentary structure is one that is undisturbed. Specialised sampling systems which can include drive sampling (coring) or rotary sampling are capable of such an act provided that when forced into the ground, minimal displacement, remoulding and disturbance is incurred (Das, 2011).

2.3.1 Overview of Offshore Drive Sampling Techniques

Various coring techniques exist, each with their own set of advantages and disadvantages. In this section, focus was given to primary drive sampling techniques- that is, common geotechnical coring systems lowered from a vessel onto the seabed via an umbilical cable (Danson, 2005). Rotary sampling tools were not considered since the rotational component was not applicable. Examples of drive samplers included gravity corers, vibrocorers and piston corers. The contact made between the cutting edge of a corer and the soil is an aspect of interest. Table 2-2 depicts the different coring tools and a summary of their properties.

Table 2-2: Different drive sampling techniques

Source: (Smith, 1992; Danson, 2005; Lunne & Long, 2006; Wegener, 2015)

Coring Technique	Sampling Depiction	Description
Gravity coring	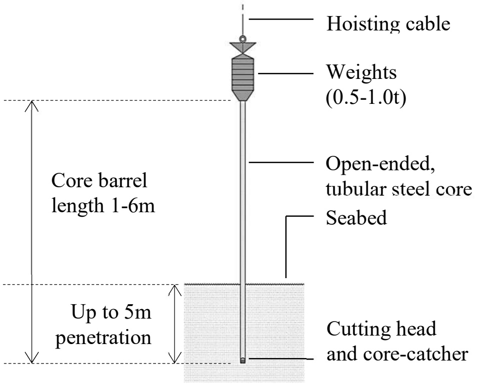	• Consists of an open ended, tubular steel core barrel, with a plastic liner inserted in it to hold the soil sample. • Device driven into seabed through a weighted core barrel (±1t). Assisted by gravity. • Sample retained through core-catcher and a cutting head fitted at the penetration end of the barrel. • Dropped from ±10m above seabed • Barrels range between 60-100mm diameter; <5m penetration depth

Coring Technique	Sampling Depiction	Description
Piston coring	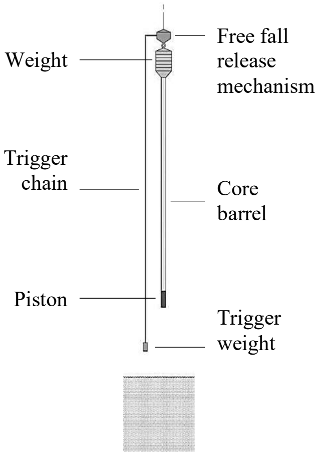	• Penetrates seabed under the act of gravity. Dropped in free-fall from a limited height. Triggered by a weight at the end of the chain touching the seabed. • Like gravity corer, but core-barrel contains an added piston mechanism • Lower end of barrel enclosed by piston until soil penetration • During penetration, piston should remain stationary. Thus, maintaining low relative pressure above soil sample.
Vibrocoring	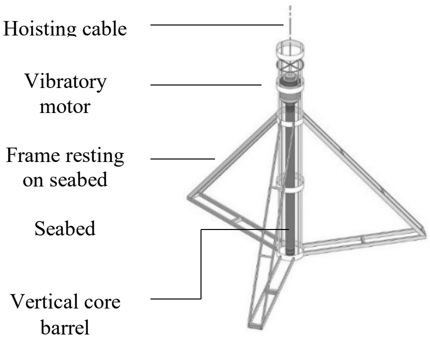	• Sampling system similar to both gravity and piston corers, but barrel driven into ground through vibratory means • Barrel driven by a vibratory motor with a high-frequency (100-200Hz) and low-amplitude (0.1-1.0mm) • A 1-2mm thick sediment layer surrounds the sample tube to reduce friction between the core barrel and soil via liquefaction • When greater penetration is necessary or when gravity/piston corers are not suitable, Vibrocoring is used

2.3.2 Soil Sampling Disturbance

The efficiency of a sampling tool, such as those described above, is commonly graded according the level of soil recovery. This is defined as the ratio between the penetrating barrel length and the length of the retrieved sample (Lunne & Long, 2006). Unity (ratio=1) is theoretically impossible to achieve and is often caused by factors such as skin friction within the pipe, soil plugging and other soil disturbance factors (Clayton, Siddique & Hopper, 1998; Lunne & Long, 2006). Soil disturbance, in many ways, may be considered as a separate field from soil recovery. However, certain aspects of soil disturbance are closely related to the practicalities of soil recovery and therefore warrant consideration.

Sampling disturbance has an impact on the effective stress state of a soil sample. The impacts are in the form of mechanical disturbances during barrel penetration. Disturbance in this instance refers to the distortion of the soil stratigraphy, where the soil is sheared and displaced by a penetrating tube. This effect can be quite significant as seen in Figure 2-1, where the compaction, remoulding and displacement of the soil beneath the tube opening is clearly shown.

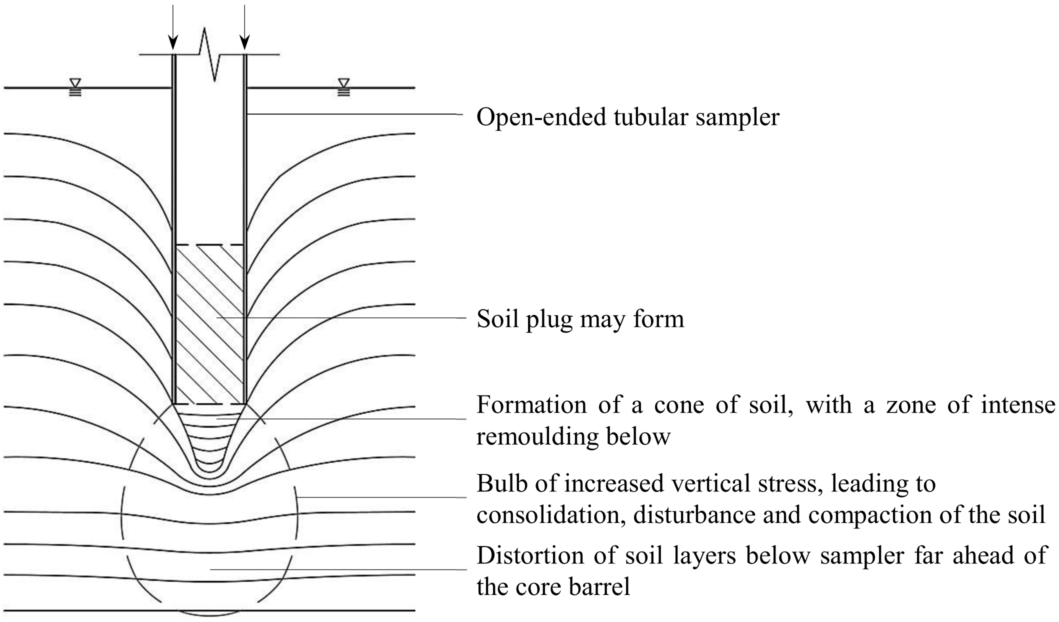

Figure 2-1: Displacement of soil beneath a sampler tube
Source: (Wegener, 2015) from (Hvorslev, 1949)

Physical characteristics with an influence on the sample quality, include the geometry of the core barrel cutting head, barrel thickness and the friction induced between the pipe and soil both inside and outside. The internal diameter of the pipe, a focal element in this research, has been investigated extensively, where it has been confirmed that an increase in diameter would lead to decreases in soil disturbance during sampling. (Hvorslev, 1949).

2.4 Ocean Floor Dredging

The interaction of dredgers with seabed sediment can be closely related to the soil interaction of offshore mining equipment. The main difference between dredging and offshore mining systems was the targeted range of particles. The main function of dredgers was to excavate material off the seabed to create channels or gather material for land reclamation (Bray, Bates & Land, 1979). Hence, a targeted particle range is not as significant of a parameter for dredgers as opposed to diamond mining systems. This ultimately leads to the design of simple entrainment devices. It is of interest to note that dredgers can achieve slurry concentrations C_v, as high as 30% compared to mining systems with concentrations as low as 5% (Vlasblom, 2003; Lai Sang, 2017).

The type of ground being dredged has a major influence on the choice of dredging technique. Rocks and soils have complex behaviours making them hard to predict. Complications may arise where excessive wear of dredging equipment can lead to serious financial consequences. A common dredging difficulty is the presence of problematic ground conditions that can lead to abrasive wear of dredging teeth. This is usually related to the presence of abrasive minerals such as quartz in soil or rock.(Verhoef, 1997)

As described by Verhoef (1997) and Bray (1997), the dredging process can be classified according to their methods of extraction, transportation and deposition. Similar to mining, the choice of dredger usually depends on the amount of rock to be excavated and the nature of the rock. Presently the systems are categorised as either hydraulic or mechanical. Mechanical dredgers rely on vessels that scoop up the soil (e.g. backhoe, dipper, bucket and grab dredgers) whereas hydraulic dredgers (e.g. suction hopper and cutter suction dredger) suck up the soil. The different types of dredgers and their application are highlighted in Table 2-3 below.

Table 2-3: Types of dredgers
Source: Verhoef (1997) & Vlasblom (2003)

Dredging Technique	Dredging Depiction	Direct Rock Dredging	Remarks
Grab Dredger	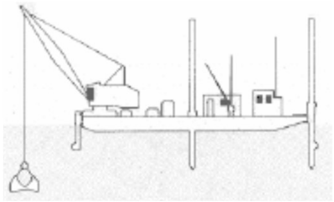	Weak rocks, up to 20 MPa, using heavy bucket, but difficult	Used in very weak rock. More efficient than a backhoe.
Bucket Dredger	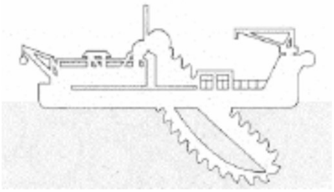	Weak to moderately strong rock, but difficult	Rock dredging only possible if buckets have cutting teeth adapted.

Dredging Technique	Dredging Depiction	Direct Rock Dredging	Remarks
Dipper Dredger	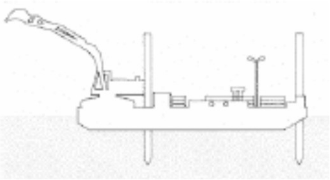	Weak rock, but difficult	Dippers can pick up fragments larger than 800mm, determined by its size and lifting power
Backhoe	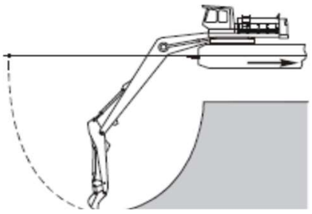	Weak to moderately strong rock, but difficult	Can pick up larger fragments
Trailing Suction Hopper Dredger	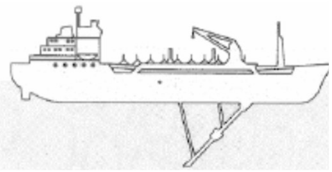	Weak rocks may be dredged	Drag head may be equipped with ripper teeth
Cutter Suction Dredger	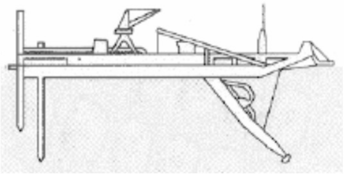	Weak to moderately strong rock with increasing difficulty	Fragments need to pass cutter blades. Small fragments favourable

From the different dredging systems mentioned above, only suction based techniques were considered. This included a) Trailing suction hopper dredgers, b) Cutter suction dredgers and c) Plain suction dredgers. Their application closely resembles the interaction of systems used in the offshore mining industry. As such, the mechanics and practicality of these systems were further analysed.

2.4.1 Trailing Suction Hopper Dredger

The trailing suction hopper dredger is a self-propelled waterway vessel equipped with a hopper and a dredge installation to load and unload itself as pictured in Figure 2-2 below. A standard trailing suction hopper is equipped with one or more suction pipes connected to a drag head running across the ocean floor. Gantries are used to hoist the suction pipes on board after the extraction of particles off the seabed into the containment hopper.

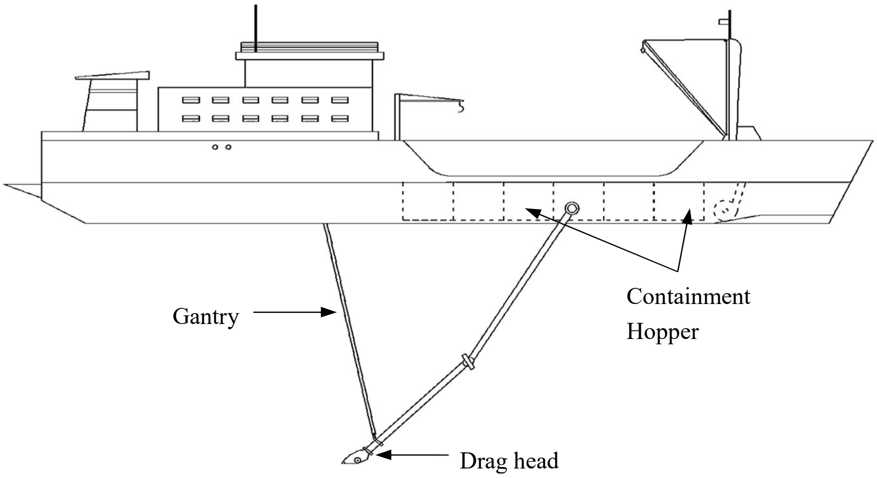

Figure 2-2: Trailing suction hopper
Adapted from Vlasblom (2003)

The dredging components of interest include:

1. Suction and discharge pipe diameters (m)
2. Type and size of the draghead(s)

2.4.1.1 Suction and Discharge Pipe Diameter

In the past, the diameters of the pipes were based on minimising the pressure loss in the suction pipe to avoid cavitation caused in the dredge pump (Vlasblom, 2003). However, this assumed that the concentration distribution was homogenous over the entire diameter, which was not always the case. Assuming homogenous flow, it can be shown that the suction production is maximised at a certain suction velocity. This can be computed using a suction formula based on the force balance over the suction pipe.

Referring to Figure 2-3, for a pump that is positioned *k* meters below the water surface, the pressure at the suction mouth can be calculated using Equation (2-4).

$$P = \rho_m g H \tag{2-4}$$

Where,

ρ_m = Density of the mixture in kg/m^3
g = Acceleration due to gravity in m/s^2
H= Depth of suction mouth below water surface in m

The pressure in front of the pipe, P_p, is equal to the allowable under pressure (vacuum) as given in Equation (2-5).

$$P_P = VAC \tag{2-5}$$

Where,

V = Suction velocity in m/s
A = Cross-sectional area of pipe in mm^2
C = Discharge coefficient

The pressure difference over the suction pipe equals the weight of the mixture and the losses in the pipe. Based on the conservation of energy, the Bernoulli equation is applied. By further substituting Equation (2-4) and (2-5) into Bernoulli's equation, the relationship depicting the pressure difference over the two points is given in the balanced equation below, also known as the suction formula.

$$\rho_w gH + VAC = \rho_w gh_z + \varphi \frac{1}{2} \rho_m v^2 \tag{2-6}$$

A resistance factor, φ, is included in Equation (2-6), to account for entrée losses and pipe characteristics. The factor can be written as:

$$\varphi = \beta + \lambda \frac{L}{D} \tag{2-7}$$

Where,

β = Entrée loss coefficient
λ = Darcy-Weisbach resistance coefficient
L = Length of suction pipe in m
D = Diameter of suction pipe in m

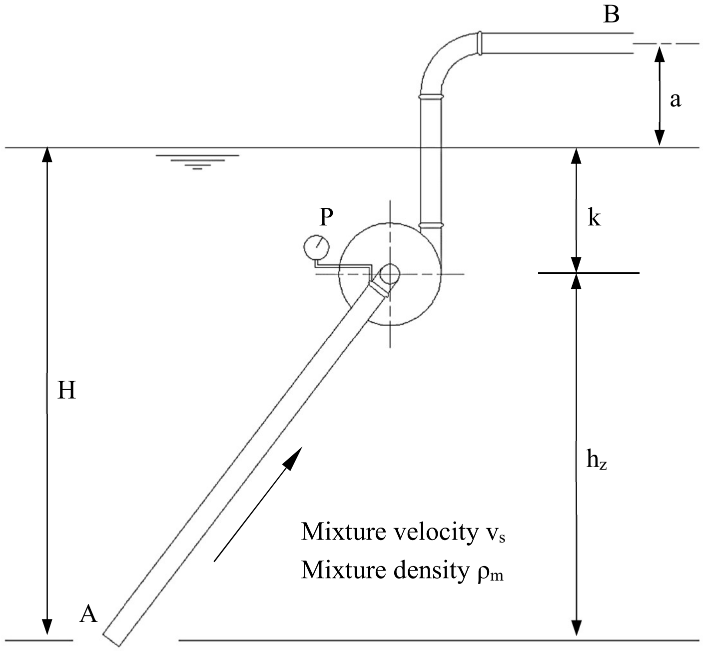

Figure 2-3: Dimensions of trailing suction hopper pipes
Adapted from Vlasblom (2001)

The specified diameter of the pipe is determined based on the vacuum of the pump and when the suction production is maximised for a certain suction velocity. However, the application of the suction formula has several disadvantages:

1. The parameters for mixture density ρ_m, resistance factor φ and the suction velocity V_s, are not independent of each other but are rather dependent on the pump characteristics and the erosion process.
2. For sand types with a $d_{50} > 0.15$mm, the flow is no longer homogenous.

2.4.1.2 Type and Size of Dragheads

To achieve optimum performance, the type of draghead selected is dependent on the type of material to be dredged, and the dredger used (Bray, Bates & Land, 1979). However the main function of the draghead is to allow the material to flow into the suction pipe as efficiently as possible (Yell & Riddell, 1995).

Dragheads are designed to excavate soil and combine it with water to form a mixture that is suitable for hydraulic transport. The soil can be excavated either physically or hydraulically or a combination of both. Hydraulic excavation can be done by either the erosion of the dredge pump flow or by pressurised water jets. For cohesive soils, such as clay or very soft rock, mechanical excavation is generally chosen, where teeth or blades are fitted to the underside of the draghead (Figure 2-4).(Vlasblom, 2003)

Modern dragheads adopt the use of water jets assisted with teeth or blades. The combination of the hydraulic and mechanical system allows for improved suction capacity of the dredged system, enhanced sizing of material and reduction on potential blockages. (Wyatt & Miller, 2013)

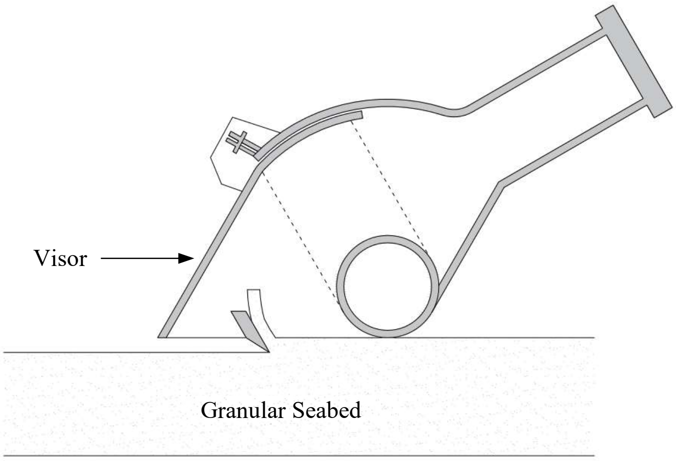

Figure 2-4: Draghead used to excavate soft rock
Adapted by Vlasblom (2003)

The dredger has a wide application area and can operate without an anchorage system. During its initial application, it was used to deepen and maintain waterways. Nowadays the systems are regularly utilised for land reclamation as evident by the structural work carried out in the United Arab Emirates, particularly in the city of Dubai (Jackson & della Dora, 2009).

Per Vlasblom (2003), the concerning parameters of the suction dredger were determined per the required payload, draught and speed of the vessel. Therefore, they were built according to certain ship ratios, such as L/B, B/H and B/T (L=length, B=width, H=depth and T=draught).

2.4.2 Cutter Suction Dredger

A cutter suction dredger utilizes a stationary system with an attached cutterhead (Figure 2-5). The cutterhead swings from side to side to make a cut in the dredged surface before being sucked up by the flow of the dredge pump. The cutter head is incorporated as a form of mechanical loosening where in-situ material is too compact to be removed by suction action alone (Yell & Riddell, 1995). The dredger is commonly used for land reclamation and hydraulic filling, but it can be employed for a wider range of applications (Bray, Bates & Land, 1979).

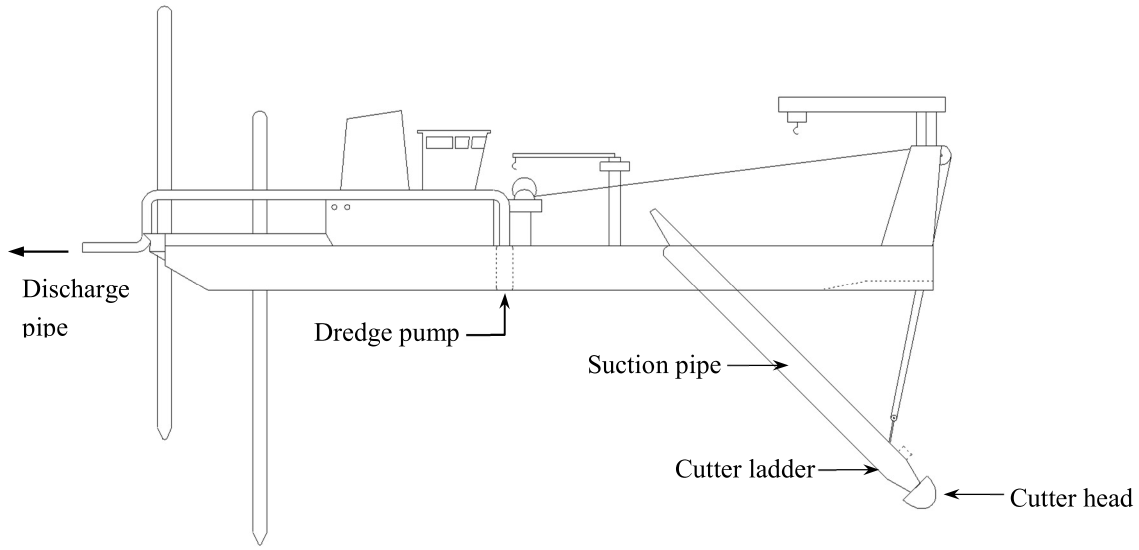

Figure 2-5: Layout of cutter suction dredger
Adapted from Vlasblom (2003)

The main advantages of this system are its ability to dredge a wide range of materials in shallow waters and its ability to dredge a pre-defined profile. However, its disadvantages include its sensitivity to sea conditions, limited dredging depth and high mobilisation costs (Bray, Bates & Land, 1979; British Standards Institution, 2000). The proficiency of a cutter suction dredger is determined by either the power driving the cutter head, which may range from 50kW to 5000kW or the diameter of the discharge pipe, which may range from 150mm to 1100mm (Vlasblom, 2003). Modern automated cutter suction dredgers are capable of achieving high outputs over a sustained period, reaching production rates of around 500 000m^3/week under favourable conditions (Yell & Riddell, 1995).

In keeping with the scope, the components of interest will include:

1. Dredging depth of the dredger
2. The cutter head

2.4.2.1 Dredging Depth

The applicability of a cutter suction dredger is influenced by both maximum and minimum dredging depths. Often when designing a dredger for use at greater depths; a pontoon with a deeper draught is required. The use of a deeper draught inadvertently reduces the minimum dredging depth meaning that the usability of the dredger with increased dredging depth converges with a minimum dredging depth. Furthermore, the market demand is an added attribute to the selection of the best choice dredger. (Vlasblom, 2003)

Therefore, the limits on where a dredger can operate will vary depending on the size and characteristics of a particular dredger. The extreme depth limits applied to the smallest and largest cutter suction dredgers in common use for economic operations are given below. (Bray, Bates & Land, 1979)

Table 2-4: Limiting depth factor for cutter suction hopper

Limiting depth factor	Depth (m)
Minimum water depth to operate	0.75
Maximum water depth to dredge	35

2.4.2.2 The Cutterhead

The cutterhead is the main component of this type of dredger. It most significantly influences the production capacity of the system and it is important for the mixture forming process. The most common cutterheads are of the "crown" type, where the main body is formed in a cast steel alloy. Alternatively, a wheel based cutterhead can be used, leading to a design of a dredger known as the bucket wheel dredger. A cutter of the "crown" type was as follows:

Figure 2-6: Rock bladed cutter
Source: Vlasblom (2003)

2.4.3 Plain Suction Dredger

The plain suction dredger shares many characteristics with the trailing suction hopper dredger. The dredger utilizes a stationary system, consisting of a pontoon moored by one or more wires with at least one sand pump connected to the suction pipe (Vlasblom, 2003). However unlike the trailer, the stationary suction dredger does not dredge whilst moving, but first anchors and then loads the hopper when moored. The usual role of the plain suction dredger is the suction of granular materials for reclamation or construction aggregate purposes. Most stationary dredgers are not equipped with hoppers but rather load the material onto barges or pump it to a delivery point through a pipeline (Bray, Bates & Land, 1979).

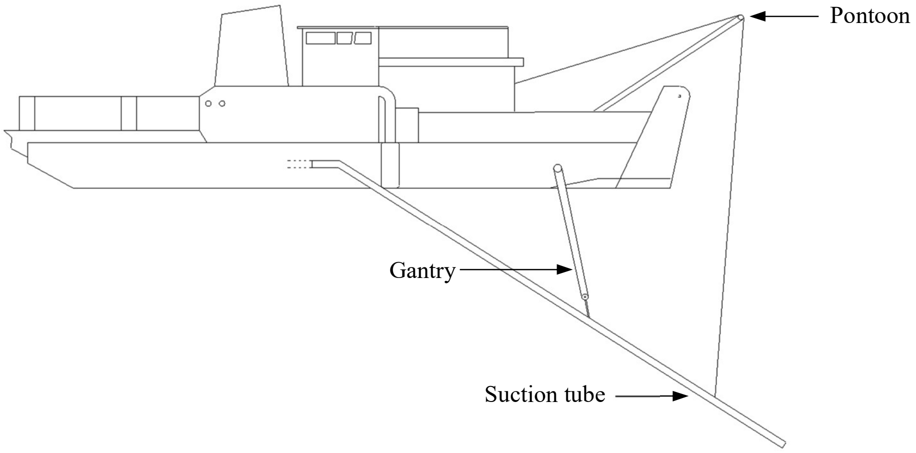

Figure 2-7: Stationary suction dredger

Adapted from Vlasblom (2003)

Stationary suction dredgers are only used to extract non-cohesive soils such as sand. The system, is however less suitable for more accurate work where precise seabed profiles are created. In general, these dredgers are designed as relatively light vessels and although they are anchored on wires, they are usually unsuitable for dredging in open waters. (Vlasblom, 2003) When designing suction dredgers, a number of fundamental components must be addressed but for the purpose of this research, the parameters of interest will include:

1. Production capacity
2. Suction mouth

2.4.3.1 Production Capacity

The plain suction dredger is used for the extraction of granular materials for reclamation and construction. The production capacity of the system per week/ per hour is important and must be known to monitor the efficiency of the dredger and concentration of the mixture. Once the production capacity is known, it is used to determine the sand flow rate and sand concentration. Using Equation (2-8), the production capacity of the dredger can be computed. (Vlasblom, 2003)

$$Q = Q_{\text{mixture}} \frac{C_{\text{vd}}}{1 - n} \tag{2-8}$$

Where,

Q = Production capacity in m^3/s

Q_{mixture} = Flow rate in m^3/s

C_{vd} = Delivered concentration

n = Porosity

The average concentration delivered, C_{vd}, depends on the behaviour of the granular material on the seabed. The maximum C_{vd} that can be transported by a pipeline was dependent on the ratio between the maximum grain diameter or pipe diameter and the length of the pipeline. In long pipelines, the concentration could increase due to density variations during dredging (Matousek, 1995). In practice, a maximum average density of 1500kg/m^3 (C_{vd} = 30%) is generally used for sand. Based on this value, the flow rate was assumed to be fixed since the production capacity was used as a prescribed value.

2.4.3.2 Suction Mouth

Plain suction dredgers generally adapt simple suction mouth designs. Figure 2-8 depicts two of the most common mouths used for dredging which involve the use of a screen to cover the end of a pipe. Such a design is used to avoid blockages caused by boulders and debris.

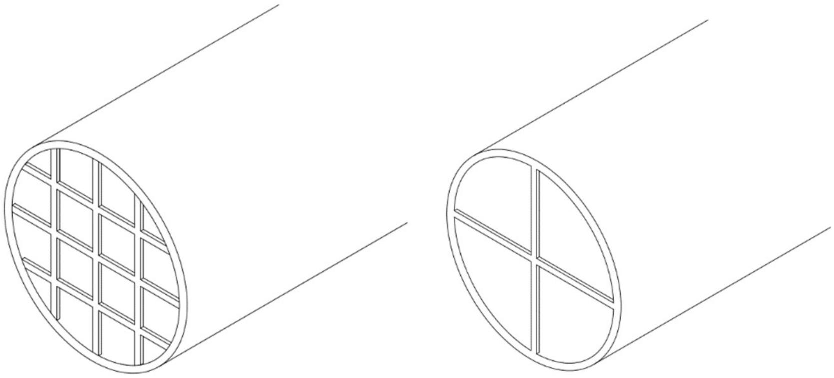

Figure 2-8: Plain suction mouths used in dredging Industry

In the past, various methods were employed to improve the performance of suction dredgers at great operating depths. Apart from mounting the dredge pump underwater, jet pumps were incorporated near the region of the suction intake. This allowed for the design to improve the breaching process and mixture forming when the suction pipe penetrated the sand.

2.4.4 Comparisons between Suction Dredgers

Suction based dredgers had their own unique set of advantages and disadvantages when compared to bucket based dredgers. They can be modified per their proposed purpose. If the dredger is to function in a tough terrain with the presence of dense materials, a combination of systems can be used such as that of the cutter suction dredger. However, modifications of these dredgers can lead to certain limitations with regards to dredging depth, water consumption, soil strength and particle size. Table 2-5 summarises the limitations encountered by suction based dredgers.

Table 2-5: Limitations for suction based dredgers
Source: (British Standards Institution, 2000)

Limitation	Units	Trailing suction hopper dredger	Cutter suction dredger	Plain suction dredger
Min. dredging depth	m	4	1	3
Max. dredging depth	m	35	35	35
Min. water consumption	m^3/h	-	300	-
Max. particle size	mm	500	500	200
Max. soil shear strength	kN/m^2	75	500	-
Max. rock crushing strength	kN/m^2	100	30 000	-

BS 6349-5 (1991) states that each type of dredger may be affected differently depending on the environment to which it is exposed.

There are very few dredgers that can operate at depths greater than 30m and even fewer at depths as great as 80m. Dredgers employed at these depths are only used for specialised applications, as the costs and risks involved increase significantly. In conclusion, the dredgers adapt optimisation techniques that are relevant to the optimisation of granular flow through a system.

3. Constitutive Laws and Associated Flow Theories

3.1 Introduction

The principles of fluid and granular flow are fundamental concepts in gaining a theoretical understanding of the behaviour of particles passing through an orifice. The chapter highlights these laws, drawing on fundamental aspects and discussing their relevance within the study. Fluid flow and granular flow were investigated individually before being analysed as a composite system.

3.2 General Characteristics of Fluid Flow

In understanding the behaviour of granular materials when transported through a system. The viscous flow of water through a conduit was addressed first, followed by Bernoulli's equation which addressed flow using the conservation of energy. Lastly, Manning's equation was introduced to provide a comparative study for flows in different scenarios, i.e. open channel versus closed channel flow. A completely filled pipe was the basic assumption used for closed channel water flow (conduit).

3.2.1 Viscous Flow in Pipes

According to British scientist and mathematician, Osborne Reynolds (1883), the fluid in a pipe can be categorised as either laminar or turbulent flow. Reynolds (1883) distinguished between the two classifications of flow using a simple apparatus as illustrated in Figure 3-1. For low flow rates, the coloured dye which was added into the fluid stream, formed a well-defined line within the flow, with only slight fluctuations due to molecular diffusion of the dye into the surrounding water. It was further determined that for intermediate flow rates, the dye streak fluctuates in time and space with minor irregular bursts along the streak. For large enough flow rates, the dye streak almost immediately becomes blurred and spreads across the entire pipe. Figure 3-1 shows the three different flow scenarios, denoted as laminar, transitional and turbulent flow respectively (Janna, 2010; Young et al., 2011).

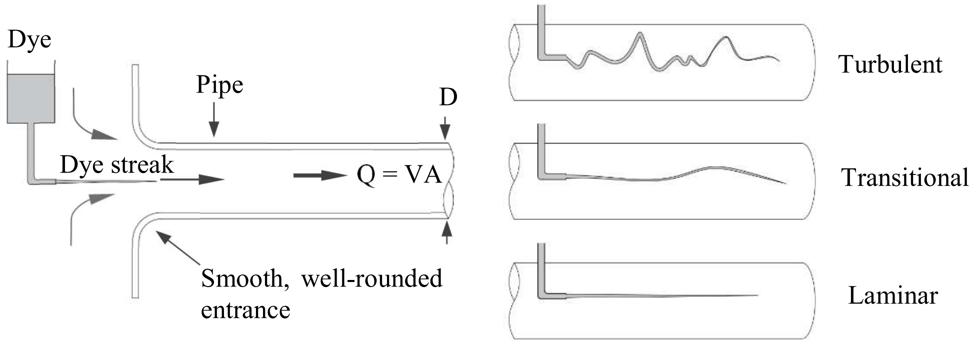

Figure 3-1: Experiment used to illustrate type of flow, along with typical dye streaks.
Adapted From Young et al. (2011)

Reynolds (1883) was further able to characterize flow regimes using a dimensionless number, giving the ratio between the viscous and inertial forces. The dimensionless parameter was known as Reynold's number and was measured using Equation (3-1). The Equation was derived from the process of dimensional analysis (Concept detailed in Appendix G: pg217).

$$\text{Reynold's number (Re)} = \frac{\rho v L}{\mu} = \frac{vL}{\upsilon} \tag{3-1}$$

Where,

ρ = Density in kg/m^3
μ = Absolute viscosity in N.s/m^2
υ = Kinematic viscosity in N.s/m^2
v = Velocity in m^2/s
L = Characteristic length in m

In theory, if the Reynolds number is small, then the flow is determined to be laminar and, if the number is large, then the flow is said to be turbulent. The type of flow is grouped according to the constrained values of (Shaughnessy, Katz & Schaffer, 2005; Janna, 2010; Young et al., 2011):

$0 < Re < 2100$ → Laminar flow
$2100 < Re < 4000$ → Transition flow
$Re > 4000$ → Turbulent flow

3.2.2 Bernoulli's Equation

For steady state flow, a fluid particle along a streamline is said to have a velocity tangent to the streamline at all points (Finnemore & Franzini, 2002). Furthermore, the fluid particle may experience acceleration or deceleration due to the forces acting on the particle (Hewakandamby, 2012). Assuming flow to be steady and incompressible, Newton's second law of motion can be applied. Newton's Law, guided by the principle for the conservation of energy was given by the equation below.

$$\frac{p}{\gamma} + \frac{V^2}{2g} + z = \text{constant along streamline} \tag{3-2}$$

Where,

p = Pressure measured in kPa
γ = Unit weight of water measured in N/m3
V = Velocity of fluid in m/s
g = Acceleration due to gravity in m/s2
z = Change in height from datum to point of interest in m

Equation (3-2), also known as the Bernoulli equation, is a widely-used tool in fluid mechanics. The equation states that the sum of mechanical energy, kinetic energy and potential energy is constant along a streamline, whereby it only considers the pressure and gravitational forces acting on the fluid particles. Therefore since there is no change in height along a streamline, Bernoulli's equation is addressed as a balance between the static pressure and velocity. (Finnemore & Franzini, 2002)

For other fluid applications, the Bernoulli equation is used to determine the pressure drop between two points, A and B. Assuming the fluid to be inviscid, one can determine the change in pressure between the two points. The change can be determined using Equation (3-3), a derivation of Equation (3-2).

$$\frac{p_A}{\gamma}+\frac{{V_A}^2}{2g}+Z_A=\frac{p_B}{\gamma}+\frac{{V_B}^2}{2g}+Z_B \qquad (3\text{-}3)$$

Suction mechanisms are governed by the change in pressure between two points. When one point has greater pressure, a vacuum is generated causing fluid or air to travel to a point of low pressure. The behaviour of the pressure drop can be characterised by Bernoulli's equation, where the conservation of energy between two points is evident. There are many common household appliances that utilize the principles of vacuum mechanics. Such appliances include pool cleaners and vacuum machines.

3.2.3 Manning's Equation

Open channel flow involves a free water surface capable of deforming from its usual undisturbed; and relatively flat configuration to form waves (Young et al., 2011). One of the most commonly used governing equations for open channel flow is Manning's equation. It is an empirical relation applicable to uniform flow where the depth of flow does not vary along the channel. Manning's equation as defined below, is a function of channel velocity, flow area and channel slope (Bloodgood & Bell, 1961; Fischenich, 2000; Anderson, 2002; Finnemore & Franzini, 2002).

$$Q=\frac{k_n}{n}AR_h^{\frac{2}{3}}S^{\frac{1}{2}} \qquad (3\text{-}4)$$

Where,

Q = Cross-sectional flow rate in m^3/s

k_n = 1 for SI units

n = Manning's roughness coefficient

A = Flow area in m^2

R_h = Hydraulic radius in m

S = Channel slope

The hydraulic radius is defined as the cross-sectional area A, of the channel divided by the wetted perimeter P, in contact with fluid (Anderson, 2002). The property is used to characterise open channel flow for various shapes which can include rectangular, circular, square or trapezium channels. However, for closed conduit flows, a hydraulic diameter D_h is used instead. This is defined as 4 times the cross-sectional area A, over the wetted perimeter P of the conduit. The aspect plays a vital role in the discharge of materials through an orifice, later discussed in Chapter 4.

$$\mathrm{D_h} = \frac{4\mathrm{A}}{\mathrm{P}} \tag{3-5}$$

Table 3-1 below, contains a list of relevant shapes with their associated hydraulic diameters.

Table 3-1: Hydraulic diameter $\mathbf{D_h}$ for different orifice shapes
Source: (Perry & Green, 1997)

Shape	Dimensions	Formula	Hydraulic diameter
Square	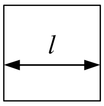	$D_h = \frac{4l^2}{4l}$	$D_h = l$
Circle	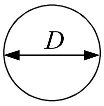	$D_h = \frac{4\frac{\pi D^2}{4}}{\pi D}$	$D_h = D$
Rectangle	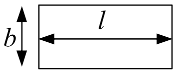	$D_h = \frac{4bl}{2(b+l)}$	$D_h = \frac{2bl}{(b+l)}$

3.3 Dry Granular Flow

Granular flow entails the fluid like movement of particles under specific conditions, which occur naturally or by the influence of physical human initiated processes. Granular flow is evident in a wide variety of applications such as sand through the hourglass, a naturally occurring avalanche or the flow of sand down dunes. Research in this area has been motivated in recent times through the interest of applications in industrial processes and the behaviour of natural hazards such as landslides or rock avalanches. (Forterre & Pouliquen, 2011)

Granular media can exhibit different states of matter. Dependent on external stimuli, a granular material is able to behave like a solid, a liquid or a gas (Andreotti, Forterre & Pouliquen, 2013). As a solid, they are equipped to support large structures under great stresses, as a liquid they can flow like sand through an hourglass and as a gas, they can be dispersed into air when strongly agitated. The different states of granular media are pictured in Figure 3-2.

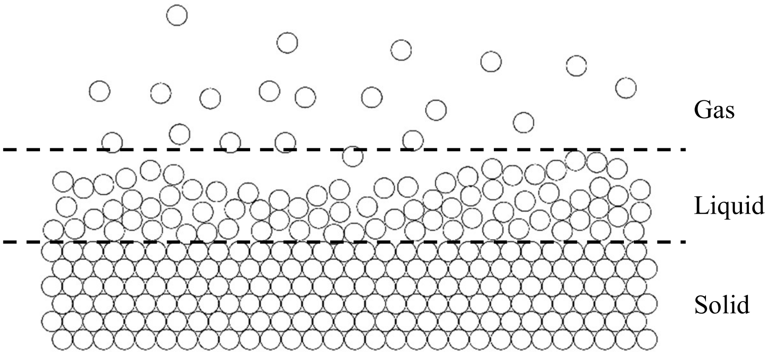

Figure 3-2: Different states of granular media
Adapted from Andreotti et al. (2013)

In most practical situations regarding granular flow, such as rock avalanches or silo flows, flow is determined to be dense, where the volume fraction, C_{vb}, is high and close to its maximum value. The volume fraction is defined as the ratio of volume occupied by grains to the total volume occupied by the packing. The fraction cannot exceed unity, as it corresponds to grains occupying the entire space.

Granular flow is often associated with grains of order or larger than 10μm, visible to the naked eye (Mitarai & Nakanishi, 2012). The size limitation is induced by the type of interactions encountered between particles. For small particles, interactions caused by Van der Waals forces or humidity come into effect. For large macroscopic particles, interactions are based on physical contact, leading to dissipative interactions. For example, consider a natural pile of particles placed on a plate, to induce granular flow, energy must be added constantly to avoid kinetic energy being fully dissipated. This is addressed by inclining the plate at some angle (α) where the grains will begin to flow (Figure 3-3). The effect comes from the frictional behaviour of granular materials, where the flow threshold proportional to the normal stress is surpassed (Andreotti, Forterre & Pouliquen, 2013).

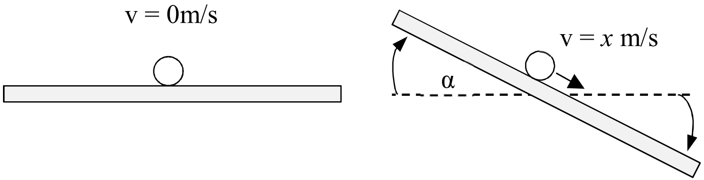

Figure 3-3: Granular flow down an inclined plane

3.4 Immersed Granular Media

The dynamics of fluid particle systems have been extensively investigated in recent times due to their relevance in many engineering problems. Such problems can include the transport of sediment in open channels, the behaviour of fluidised beds or dust flow in geophysical problems (Pai, 1977). Compared to dry granular flow, the behaviour of immersed granular media, where interstitial fluid plays a non-negligible role, is a complicated system.

3.4.1 Phases of Immersed Granular Flow

The behaviour of the immersed media can change drastically depending on how saturated the grains are (Mitarai & Nakanishi, 2012). When grains are partially wet, cohesive forces between particles play a significant role. In contrast, when the voids between the grains are further saturated, the system will reach a point where it becomes dense slurry. At this stage, both grain-liquid and grain-grain interactions play an important role (Mitarai & Nakanishi, 2012). Additionally, if more liquid is added, the direct interaction amongst grains becomes less significant. In this research project, focus was given to the latter scenario of grains being completely immersed in fluid. Thus, to further understand the phenomena, a fluidized bed and its different stages of fluid-solid flow were investigated. The different phases were detailed according to literature by Pai (1977) and Andreotti et al. (2013).

a) Fixed Bed Phase (Dense Limit)

Consider a liquid such as water flowing through a well packed volume of solid particles. If the flow rate of the liquid is too small, the well packed particles will not be disturbed and the fluid velocity will be constant through the porous medium. Therefore, the volume of particles is best described as being fixed in space. The fixed bed phase was relevant to the intermediate stages of the experimental work.

b) Sedimentation Stage

When the flow rate increases, some of the smaller particles are subjected to movements caused by the fluid. Proportionally, an increase in flow rate leads to an increase in displaced particles. At first, the volume of well packed particles would not be considered as a quasi-fluid as only some of the particles are transported by the fluid. The properties of the individual particles play a significant role in the magnitude and rheology of the fluid flow.

c) Fluidisation Stage

When the flow of the fluid reaches a critical rate, also known as the incipient fluidisation flow, the character of the granular particles changes shortly into a pseudo-fluid. The slurry combination of fluid and solids behaves similarly to ordinary fluids where it is able to form a level surface. At this stage, the overall density of the mixture decreases by a percentage of 10-50% as compared to the fixed bed phase.

d) Two-Phase Flow (Dilute Phase)

If the flow rate is increased even further, the solid particles will occupy less than 5% of the total volume of the fluidised bed. This implies that the particles have mixed well with the fluid in the flow field. This stage is referred to as the dilute phase of the two-phase flow of a mixture. In this stage, the particles and fluid are described as two continuous flows of different velocities. The velocity of the mixture is defined as the average velocity of each phase in the volume. Two-phase flow is generally analysed as whole entities governed by the conservation of mass and momentum. From first principles, the particles are analysed as single elements to recognise the contributing forces. The contributing forces originate from either particle-fluid interactions or particle-particle interactions.

It is worth covering, that the hydraulic transport of particles is different for horizontal and vertical pipes. For instance, the concentration of particle increases towards the bottom of the pipe, decreases as the flow rate velocity decreases. However, in vertical transport, axial symmetry is maintained with the solid being evenly distributed over the pipe cross-section. (Coulson et al., 1999)

3.4.2 Solid Particles in a Carrying Liquid

The forces acting on a single particle in a dilute suspension are the body forces. For particle-fluid interactions, these forces include buoyancy, lift and drag forces. In contrast, body forces due to particle-particle interaction are transmitted as inter-particle stresses. Depending on the phase of contact between the particles, Coulomb stresses may also play a role. Additionally, of valid interest, is a particle's settling velocity within a fluid, dependent on the body forces acting on it, such as gravity, lift and drag. It is worth noting, the drag force, defined by the drag coefficient C_D, as a function of a particle's Reynolds number (Re_p), is derived as follows:

$$\text{Particle reynold's number } (\mathrm{Re}_p) = \frac{\rho v d_p}{\mu} = \frac{v d_p}{\upsilon} \qquad (3\text{-}6)$$

Where,

v = Relative velocity in carrying liquid in m^2/s
d_p = Particle diameter in mm

This number, similar to that of a fluid, describes the flow around the particle. (Andreotti, Forterre & Pouliquen, 2013)

a) Gravitational and Buoyancy Force

The gravitational force acting on a particle is dependent on its volume and density. Considering a solid particle with a diameter, d_p, the gravitational force can be calculated using Equation (3-7).

$$F_{Gp} = \rho_s g \frac{\pi {d_p}^3}{6} \tag{3-7}$$

Where,

F_{Gp} = Gravitational force on a spherical particle in kN
ρ_s = Density of solid in kg/m^3

When a solid is immersed in a liquid, the effects of buoyancy become relevant. The solid particle reduces in weight due to the carrying medium. The submerged unit weight of a spherical particle can be determined by the expression:

$$F_{Wp} = (\rho_s - \rho_f) g \frac{\pi {d_p}^3}{6} \tag{3-8}$$

Where,

F_{Wp} = Submerged weight of a spherical particle in kN
ρ_f = Density of liquid in kg/m^3

b) Drag Force

An additional force is exerted onto the submerged particle when the surrounding fluid moves at a velocity relative to that of the solid. The drag force, F_D, acts in the direction of the relative velocity, v_r, calculated as the difference in velocities between the fluid and solid. The magnitude of the drag force is expressed in terms of the drag coefficient C_D which is given by the dimensionless parameter in Equation (3-9) (Shook, Roco & Brenner, 1991; Young et al., 2011; Hewakandamby, 2012). The drag coefficient is dependent on the shape of the particles. For smooth spheres at high Re_p (>500), the experimental value of C_D is approximately 0.44. For natural grains, measurements give C_D around 1.

$$C_D = \frac{8F_D}{\pi d^2 {v_r}^2 \rho_f} \tag{3-9}$$

$$F_D = \frac{C_D \pi d^2 {v_r}^2 \rho_f}{8}$$

The equation above is a product of Stokes law which derived an expression for the frictional force exerted on spherical objects with very small Reynolds numbers ($Re_p < 1$) in viscous fluids (Finnemore & Franzini, 2002; Young et al., 2011; Andreotti, Forterre & Pouliquen, 2013). The drag force for a low Re_p, was expressed as follows, where viscous forces play a significant role:

$$F_D = -3\pi\mu d v_s \tag{3-10}$$

Where,

μ = Absolute viscosity in N.s/m^2
v_s = Settling velocity of solid particle in m/s
d = Diameter of sphere in mm

Noting the similarities between Re_p and Re, the type of flow regime around a particle was governed by the shape and roughness of the particle (Finnemore & Franzini, 2002; Young et al., 2011). The discharge coefficient C_D which is a function of Re_p has a direct impact on the settling velocity. Different coefficients exist for different flow regimes as depicted in the plot for smooth spherical beads below.

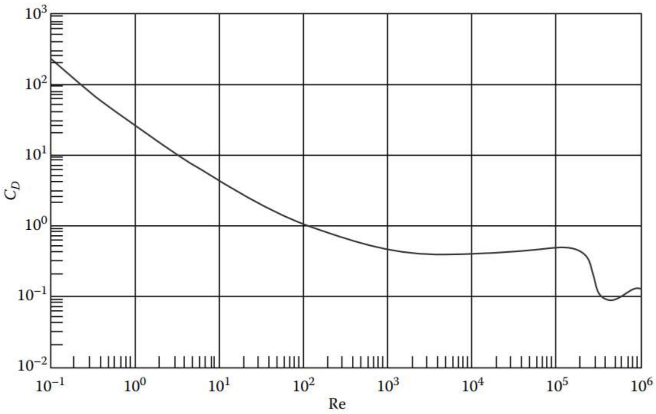

Figure 3-4: Drag coefficient as a function of Reynolds number for Spheres
Source: (Janna, 2010)

The drag force, also known as Stokes law, is derived from the distribution of viscous stresses which can be determined dimensionally. At $Re_p < 1$ the exchanges of momentum between the grain and fluid are mostly influenced by viscous diffusion. Therefore the derivation of Stokes law was formulated through the stress applied by the fluid onto the surface of the sphere and the resultant hydrodynamic force (Andreotti, Forterre & Pouliquen, 2013). By combining Equation (3-9) and (3-10), an expression relating Re_p to the drag coefficient was given as:

$$C_D = \frac{8(3\pi\mu d v_r)}{\pi d^2 {v_r}^2 \rho_f} \tag{3-11}$$

$$C_D = \frac{24}{\frac{v_r d}{\upsilon}} = \frac{24}{Re_p} \tag{3-12}$$

However, the formula stated is only applicable for low Reynolds numbers < 1 where viscous forces dominate. For $Re_p > 1$ the drag coefficient is given by the following formula:

$$C_D = \frac{24}{Re_p}\left(1 + \frac{3Re_p}{16}\right) \tag{3-13}$$

As Re_p increases, inertial forces begin to have a major influence on the drag forces. For large Reynolds number ($Re_p > 500$), the flow pattern around a single sphere becomes complicated as viscous forces no longer become the dominant mechanism of transfer for momentum but rather external body forces (Finnemore & Franzini, 2002). By balancing the drag, buoyancy and gravitational forces on a solid particle, the settling velocity can be determined, conceptualised in Figure 3-5 (Bagnold, 1956).

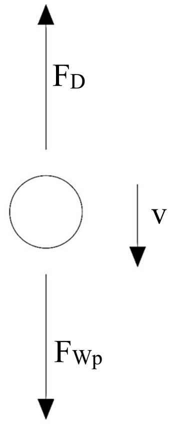

Figure 3-5: Settling Velocity of Particle

With reference to Figure 3-5, the terminal velocity of a particle in suspension can be determined by balancing the forces over a submerged particle (Equation (3-8) and (3-9)), such that:

$$F_D = F_{W_P} \tag{3-14}$$

$$\frac{C_D \pi d^2 {v_s}^2 \rho_f}{8} = (\rho_s - \rho_f) g \frac{\pi d^3}{6}$$

$$v_s = \sqrt{\frac{4}{3} \frac{(\rho_s - \rho_f)}{\rho_f} \frac{gd}{C_D}}$$

Since the drag coefficient is a function of the Reynolds number and terminal velocity, which is not known, an iterative process must be carried out by assuming a value for C_D based on Figure 3-4 and then reiterating until v_s converges to a particular C_D.(Janna, 2010)

c) *Lift Force*

The lift force acting on a single solid particle is a product of particle rotation and simultaneous slip, given by the relative velocity v_r, which is defined as the difference between the velocity of the fluid and solid particle. The lift force acts in a direction normal to both the relative velocity and particle rotation factor. The combination of particle rotation and slip leads to a lower hydrodynamic pressure in flow above the particle compared to flow below. The lift force is best described by the pressure gradient shown below. (Bagnold, 1954)

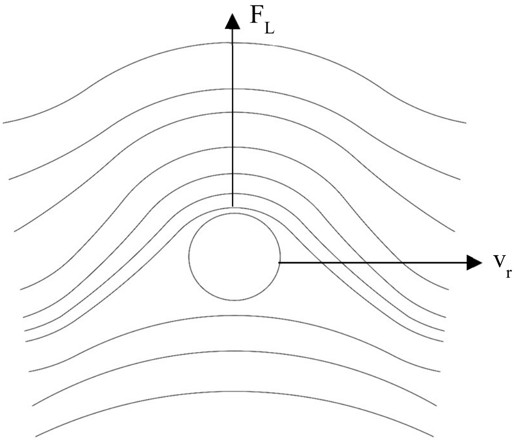

Figure 3-6: Relative velocity of particle based on lift force
Adapted from Garcimartín et al. (2009)

d) Coulombic Contact Force

The stress distribution on a granular body where non-cohesive particles are in continuous contact (dense limit), is a product of the weight occupying the total granular volume (TUDelft, 2017). Moreover, the inter-granular stress derived from the weight is transmitted within the granular body through inter-particle contact. The stress transmitted is composed of two components: inter-granular normal stress, σ_s and inter-granular shear stress, τ_s. As per Coulomb's law, the two stresses were related to the coefficient of friction. Thus Du Boys (1879) applied Coulomb's law to sheared granular sea beds and was able to deduce a relationship between the stresses at the bottom of a flowing bed by a coefficient.

$$\tan \phi = \frac{\tau_s}{\sigma_s} = \frac{\tau_s}{\rho_f g (G_s - 1) C_{vb} H_s} \tag{3-15}$$

Where,

ϕ = Angle of repose of the grains
G_s = Specific gravity of solids
C_{vb} = Maximum volume fraction of solids in the granular bed
ρ_f = Density of liquid in kg/m^3

The angle of repose, ϕ, is defined as the angle of internal failure of a static granular body (Craig & Knappett, 2012).The magnitude of the angle is dependent on the friction coefficient of the surface over which the grains start to move. In principle, the higher the coefficient of friction is, the greater the angle of repose will be.

4. The Beverloo Law

4.1 Introduction

In 1961, the Beverloo law, developed by Beverloo, Leniger and van de Velde, was used to determine the discharge rate of various granular materials through orifices of different shapes and sizes. Most studies related to the discharge rate of granular particles through apertures are linked to agricultural, chemical, manufacturing and pharmaceutical industries, where the use of hoppers is applicable. The consistent delivery of granular materials through the aperture of a hopper can be compared to many applications in the engineering industry, such as tools used in the dredging, mining and processing industries.

Beverloo, Leniger and van de Velde (1961) compared their investigations with results published by others in similar fields. Their theory of granular flow was found to be accurate by many subsequent researchers. However, over the years, a number of variables such as particle shape, particle diameter, material density and friction, were considered to further improve the mathematical model. The model was based on dimensional analysis and empirical lab experiments, hence the potential to modify the law to accommodate various scenarios. This chapter reviews the origin and formulation of the law, along with its major advantages and limitations.

4.2 Origin and Formulation

It was identified that the formulation of Beverloo's expression began in 1852, where Hagen et al. managed to correlate the behaviour between the discharge rate of granular particles and the orifice diameter of a hopper as depicted in Figure 4-1. Although more well known for his work in laminar flow (Poiseuille Law), he is still considered as one of the founding members of the expression which is interchangeably referred to as the Hagen-Beverloo Law.

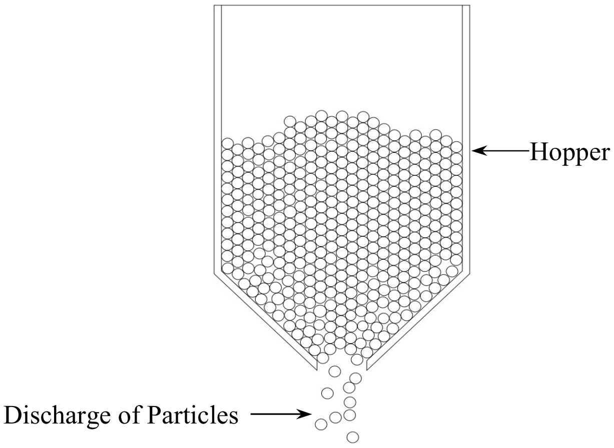

Figure 4-1: Discharge of grain through hopper

After a number of years, many researchers like Beverloo et al (1961), formulated their own theories for the prediction of discharge rates through an aperture. In 1945, Newton examined the discharge rate of catalyst pellets from a flat-bottomed hopper with a circular orifice. It was found that the limiting flow rate could be predicted using Equation (4-1).

$$W = 213D^{2.96}H^{0.04} \tag{4-1}$$

Where,

W = Discharge rate in g/min
D = Orifice diameter in mm
H = Head in cm

Equation (4-1) was found to hold true when the orifice diameter did not exceed six times the size of the particle diameter. This was because flow tended to be irregular for orifices smaller than this ratio (Newton & Dunham, 1945). It was evident from the above equation that the discharge rate was dependent on the diameter of the orifice and the head of the granular material. However, for smaller orifice sizes, the ratio of the granular particle with the orifice diameter should have been addressed (Janssen, 1895).

Franklin and Johanson (1955) studied the flow of a number of different shaped materials such as glass beads, lead shots, cracking catalysts and coal from a cylindrical hopper. From their investigation, it was established that the discharge rate of the granular material could be predicted using Equation (4-2).

$$W = \frac{1847\rho_s D^{2.93}}{(6.228\mu + 23.16)(0.394d_p + 1.889) - 44.90} \tag{4-2}$$

Where,

W = Discharge rate in g/min
D = Orifice diameter in mm
d_p = Particle diameter in mm
ρ_s = Particle density in g/cm^3

Equation (4-1) and (4-2) shows the different parameters which were accounted for, such as the particle diameter and particle density. The modification of earlier expressions of the discharge rate was conducted due to the discovery that the discharge rate was dependent on the factors in the vicinity of the orifice as addressed by Nedderman et al. (1982).

Fowler and Glastonbury (1959) investigated the flow of granular materials such as sand, wheat and rice, from flat-bottomed hoppers with either circular or non-circular orifices. In the case of non-circular orifices, the hydraulic diameter *D_h*, was used, and defined as four times the area of the aperture divided by its perimeter. They suggested that the maximum flow rate for spherical and non-spherical orifices could be determined using Equation (4-3).

$$W = 14.16\rho_b A_0 \sqrt{2gD_h}\left(\frac{D_h}{d_p}\right)^{0.185} \tag{4-3}$$

Where,

W = Discharge rate in g/min
g = Acceleration due to gravity in m/s^2
D_h = Hydraulic diameter in mm
A_0=Area of orifice in mm^2

The researchers mentioned above were the some of the main contributors to the formulation of granular flow theory prior to the development of the Beverloo law. Beverloo et al. (1961) were the first to apply dimensional analysis (see Appendix G) to the granular flow problem. They assumed that the flow rate was a function of the orifice diameter, *D_o*, the bulk density, *ρ_b*, and acceleration due to gravity, *g*. The function was written in the form:

$$\pi = W \propto {D_o}^{k_1}\rho_b^{k_2}g^{k_3} \tag{4-4}$$

Then, by rearranging the terms into their primary quantities or dimensions, the following was given:

$$\frac{[M]}{[T]} = [L]^{k_1}\left[\frac{M}{L^3}\right]^{k_2}\left[\frac{L}{T^2}\right]^{k_3} \tag{4-5}$$

From which $k_1 = 2.5$, $k_2 = 1$ and $k_3 = 0.5$, thus giving the idealised expression:

$$W \propto {D_o}^{2.5}\rho_B^1 g^{0.5}$$

$$W \propto \rho_b\sqrt{g}{D_o}^{\frac{5}{2}} \tag{4-6}$$

To bring the expression into accord with the observed relationship in the studies conducted by Beverloo et al (1961), a dimensionless constant known as the particle shape factor *k*, was multiplied with the diameter of the particles. Furthermore, the term *(D_o - kd_p)* was introduced, as it explained that the discharge of a particle through an aperture would be hindered if it were in close proximity to the edge of the hole and that it might not occur at all if it were closer than its radius (Brown & Richards, 1959; Mills, Day & Parkes, 1996). The theory was referred to as the “Empty Annulus” by Brown and Richards (1959), which ultimately assisted in giving the formula:

$$W = C\rho_b\sqrt{g}\left(D - kd_p\right)^{\frac{5}{2}} \tag{4-7}$$

Where,

C = Discharge coefficient
k = Particle shape factor

The discharge coefficient, *C,* along with the particle shape coefficient, *k,* can be determined from the physical experiments carried out using a linear regression analysis. Equation (4-7) has become one of the most widely used correlations to predict discharge rates of granular materials through circular orifices. After the development of the correlation between W and $D_o^{5/2}$ as previously discussed by Hagen et al (1852), a number of similar ideas were proposed by researchers such as Janssen (1895) and Beverloo et al (1961). The difference in the study executed by Beverloo et al (1961) was that they used spinach, kale, turnip and granular sand as their main testing materials and obtained a linear relationship in their research (Nedderman et al., 1982). The size of the particles, d_p, ranged between 0.45 and 0.30 cm in diameter. More recent studies conducted by Mankoc et al. (2007) suggested that the flow rate of grains through an orifice likewise followed the Beverloo law, but only when the orifice diameter, D_o, was greater than the particle diameter, d_p. This was governed by a ratio, R, between the orifice diameter and particle diameter, whereby it was established that the Beverloo expression was not adequate for small ratios, $R < 6$.

To cater for different shaped orifices, the Beverloo Law was modified using the terms derived in Fowler & Glastonbury (1959):

$$W = \frac{4C}{\pi}\rho_b A_e (gD_e)^{\frac{1}{2}} \tag{4-8}$$

Where,

A_e = Effective area calculated from D_e
D_e = Effective hydraulic diameter: D_h-kd_p

One of the more interesting issues with regards to Equation (4-7) was the dependence of the flow rate on the diameter of the orifice raised to a power of 5/2. The relationship, determined through dimensional analysis, can be physically explained by the behaviour of the grains near the outlet. This follows the theory that there is a free fall zone limited by an arch just above the orifice as depicted in Figure 4-2. The particles above the arch are tightly packed and their velocities are negligible. In contrast, the particles below the arch accelerate freely under the influence of gravity, also known as free-fall arch. (Seville, Tüzün & Clift, 2012)

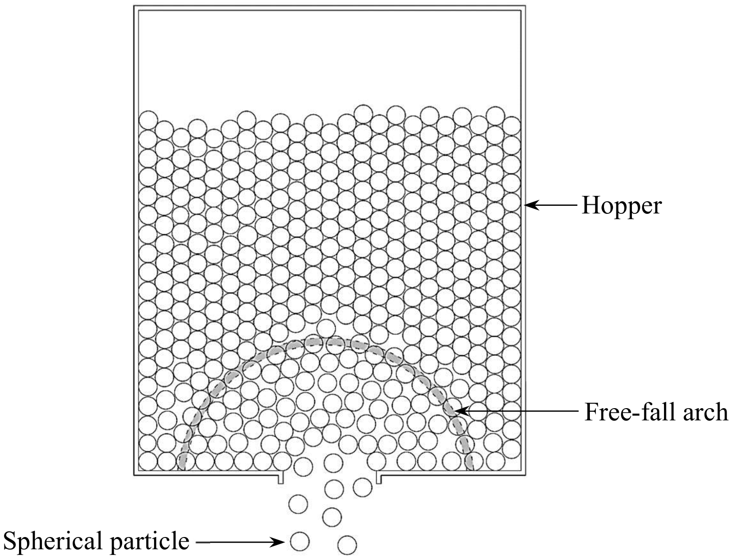

Figure 4-2: Development of free-fall arch above orifice
Adapted from Seville et al. (2012)

The majority of the earlier theoretical studies relied heavily on the concept of free-fall arch (Franklin & Johanson, 1955; Nedderman et al., 1982; Brown & Richards, 1965). .However, presently the concept has been used as a boundary condition since the normal stress on the free-fall arch must be zero (Nedderman et al., 1982). Beverloo (1961), Janssen (1895) and other preceding researchers observed that the discharge rate was independent of the height of the total granular material in the hopper, hence its close basis with the hourglass theory (Tighe & Sperl, 2007). The explanation most frequently used for its dependence is based on the Janssen effect, discussed in more detail in the next section. In light of this statement, Nedderman et al. (1982) suggested that factors in the vicinity of the orifice controlled the flow of the discharged material. Therefore, great emphasis was given to orifice vicinity parameters in past and current studies.

Although the researchers used different techniques and materials, their limitations and conclusions were closely aligned, as observed in Table 4-1 below. Many researchers of comparable studies agree with the Beverloo law to some extent, in terms of both accuracy and definition.

Table 4-1: Summary of articles synthesised

Author	Year	Material Used	Shape Parameter (k)	Discharge Coefficient (C)	Overall Remarks
Franklin et al.	1953	• Glass Beads • Lead shots	-	-	Results similar to present correlations of Beverloo.
Beverloo et al.	1961	• Sand • Linseed • Turnip • Kale	1.3 - 2.9	±0.58	Discharge rate dependent on the orifice diameter raised to a power of 2.5
Nedderman et al.	1982	-	2.5 - 7.5	0.575 - 0.595	The Beverloo expression is accurate to some extent
Mankoc	2007	• Glass Beads • Lead Shots • Delrin Beads	1.0 – 2.0	0.55 - 0.65	Beverloo law has the correct asymptotic behaviour
Tighe et al.	2007	• Sand	-	-	Hagen (1852) predicted similar correlations to Beverloo
Sheldon et al.	2010	• Glass Beads	1.2 - 3	0.5 - 0.7	In agreement with the Beverloo law

4.3 Janssen's Approach

The difference between fluid flow and granular flow, through a hopper, was the different dictating factors that controlled the output. The discharge rate of a liquid in a hopper is dependent on the height of water above the orifice whereas granular particles depend on the diameter of the orifice (Nedderman et al., 1982; Sperl, 2006). The former was defined through the modification of Equation (3-2) under Bernoulli's principle. Considering a silo completely filled with fluid of height H, the discharge velocity v, was defined as:

$$v = \sqrt{2gH} \tag{4-9}$$

In 1895, Janssen was one of the first researchers to investigate the behaviour of granular materials in a confined environment. His approach involved the analysis of the pressure distribution of a vertical cylindrical column packed with corn. By conducting a force balance over the entire domain he was able to deduce an expression for the average solid pressure at the bottom of the column. It was noted that for small column heights, the solid pressure varied linearly with depth, like a liquid. However, for large depths, the pressure became constant, reaching a saturation plateau.

This was only valid when the overall height, was larger than twice the diameter ($H > 2D_o$)of the hopper or silo. Using Janssen's approach, the discharge of granular materials could be computed using the equation below. (Di Felice & Scapinello, 2010)

$$v = \sqrt{gD_o} \tag{4-10}$$

Note that the discharge velocity is based solely on the gravity and orifice diameter. Indicating that Janssen (1895) assisted in formulating the basis of the Beverloo law. Principally, the mass flow rate of granular particles through an orifice was calculated generically using the expression below:

$$W = \rho v A \tag{4-11}$$

Where,

W = Mass flow rate in kg/s
ρ = Density of the granular material in kg/m^3
v = Velocity as calculated using Equation (4-11) in m/s
A = Area of the orifice/opening in m^2

Such that,

$$W = \rho v A$$
$$W = \rho\sqrt{gD_o}\left(\pi\frac{{D_o}^2}{4}\right)$$
$$W = C\rho\sqrt{g}{D_o}^{\frac{5}{2}} \tag{4-12}$$

4.4 Jamming Effects of Granular Flow through Apertures

It was discussed earlier that the flow rate of particles through an aperture can be hindered by the effects of jamming. The effects are induced when the formation of arches occurs near the discharge outlets of the hopper or bin. The phenomenon is often described as the transition from fluid to solid behaviour and has been recognised as a distinctive feature of granular matter. To draw valid comparisons and applications of jamming, the literature review focused on the jamming effects caused by dry granular flow driven by gravity and wet granular flow by a flowing liquid.

4.4.1 Dry Granular Flow with Gravity

For simplification purposes, the jamming of granular flow was based on the outpouring of grains, under the influence of gravity, through an orifice at the base of a hopper. This allowed research to be restricted to a single variable whilst letting other variables such as the compaction density, evolve independently. One of the key concepts involved is the fact that the jamming of particles is kept in place by external mechanical stresses instead of internal forces of attraction between them. The formation of the arch is sustained by these external forces which can include gravity, drag and lift forces. When the forces are changed or disrupted in any way, the arch structure may lose its stability. (Garcimartín et al., 2009)

Research in this area was carried out by determining the jamming probability of the granular materials where it was evident in past studies such as Garcimartin et al (2009), that above a certain orifice size, no jamming could further occur. Figure 4-3 illustrates that both wet and dry flows exhibit three different flow regimes: a) dilute state, b) dense state and c) jammed state (Guariguata et al., 2012). It was evident in various studies that jamming occurs most frequently in dense state flows (Mankoc et al., 2007; Garcimartín et al., 2009a; Lafond et al., 2013).

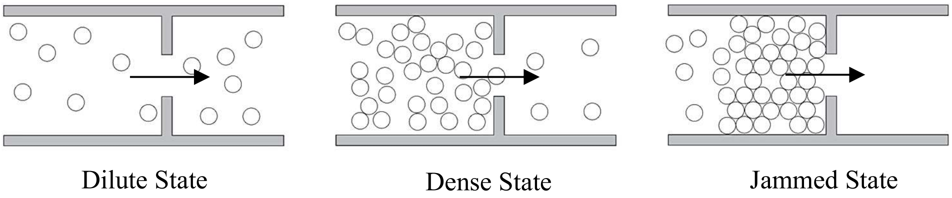

Figure 4-3: Different states of granular flow
Adapted from Guariguata et al. (2012)

4.4.2 Granular Flow Driven by Flowing Fluid

The jamming of solid particles occurs frequently in both natural and industrial processes. Natural examples include the clogging of ice or granular materials in rivers, and in industrial processes the jamming of materials through pipes. The flow of materials in a fluid medium shares many characteristics with the gravity flow of particles in hoppers, however, it differs in certain fundamental aspects with respect to principal forces and particle coefficients. Fluid-driven flows can potentially improve the jamming of immersed particles caused by the flowing fluid principals of hydrodynamics (Guariguata et al., 2012).

It can be concluded that the Beverloo law was applicable for both spherical and non-spherical particles. However, the relationship between the discharge rate and particle has still not yet been fully understood. The particle diameter d_p, was described by Hagen (1852) as the average screen size of the particles, a statement not clearly defined by boundaries and domains. Conversely, such a definition might not accurately represent the particle diameter for non-spherical materials such as rice grains.

Subsequent to the formation of the Beverloo Law, many researchers such as Mankoc (2007), Tighe (2007) and Sheldon (2010), have found their results to correlate with the expression, fluctuating within an acceptable range (±10%). Although slight modifications may have supported some of their claims, their determination of the behaviour of the flow of granular particles was in accord with the past theory.

Modifications were made to increase the accuracy of the expression or to design for a specific scenario. The reason for this was that the soil structure phenomenon was a multifaceted investigation that required complex modelling methods from first principles to accurately predict the behaviour of the interacting materials. An example of such a case would be the use of a discrete element model (DEM), a numerical tool capable of simulating the interaction of individual particles within a large sample space.

The Beverloo law was derived empirically over years of iterative testing, using several different materials under various conditions. Some of the main concerns with the law was its susceptibility to jamming effects and height independence derived from Janssen (1895). Over the years, many researchers have conducted their own granular flow experiments to address these concerns, formulating their own set of limitations or boundary conditions as summarised in Table 4-2. Please note that the limitations suggested may only be valid according to a specific set of materials or conditions.

Table 4-2: Empirical limitations encountered with the Beverloo Law

Year	Limitation	Comments	Researcher
1926	$H > 2.5D_o$	To satisfy Janssen (Height independence)	Hinchley et al.
1955	$H > D$	For consistent results	Brown & Richards
1929/1960	$D/D_o > 2.5$	To overcome boundary effects	Ketchum
1955	$D-D_o > 30d_p$	To avoid jamming	Franklin & Johanson
2006	$D_o > 6\ d_p$	To avoid jamming	Xie & Puri
2007	$H > 2D$	Pressure height independence	Mankoc et al.
2003	$D_o > 4d_p$	To avoid jamming	De-Song et al.
2011	$D_o > d_p$	To avoid jamming	Medina et. al
2015	$D_o > 4.94d_p$	Mitigates the effects of jamming	Serrano et al.

5. Theory and Application of DEM

5.1 Introduction

The theory and recent applications of discrete element methods (DEM) were reviewed in this chapter to highlight their relevance to the optimisation of granular flow and its high computational demands. There are two distinct numerical systems that exist, Finite Element Method (FEM) and Discrete Element Method (DEM). Both methods can be applied in the modelling of geotechnical mechanisms through a powerful computational interface. Numerical models are a simplification of reality, where their main objective is to find solutions to real world problems (Wood, 2004). For this dissertation, specific focus was given to the use of DEM, attributable to its relevance to the soil-structure phenomena on the ocean floor. The chapter aimed to provide an overview of the key parameters, mathematic principles and calculation processes underlying the DEM.

5.2 The Basic Calculation Cycle

DEM as described by O'Sullivan et al (2006), is a method of modelling granular materials as an assembly of rigid particles. In DEM simulations, soil is composed of individual particles relative to the size of the interacting mechanism (Li, Chen & Chen, 2016). The particle-based numerical method is a dynamic analysis that evaluates the movement of particles over a given time step where velocities and accelerations are constant.

Cundall and Strack (1979) described the calculations performed in DEM as alternating between the applications of Newton's second law and the force-displacement law. Newton's law describes the motion of the particle as a result of the forces acting on it, whereas the displacement law is used to calculate the contact forces derived from displacement.

The deformation of individual particles is relatively small in comparison with the deformation of particles in a rigid assembly. The latter deformation is caused by the movements of the particles as rigid bodies. Therefore, an adequate approximation of the mechanical behaviour of the particle deformation can be achieved without a precise modelling system. The forces and displacements of the interacting particles during the calculation cycle, are shown in Figure 5-1 below. The cycle considers two particle discs. (Cundall & Strack, 1979)

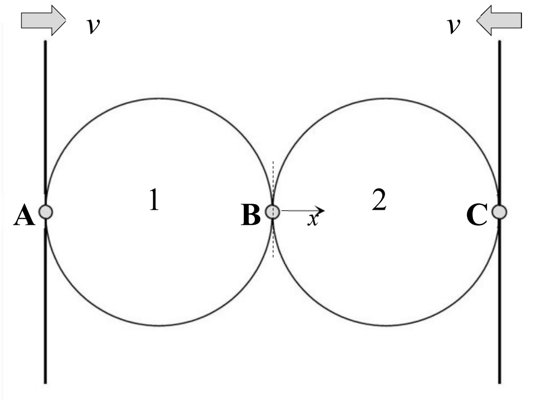

a) $t = t_0$

Two particle discs, labelled 1 and 2, are positioned between a pair of rigid walls

The walls move toward one another at a constant velocity v

At time $t = t_0$, the walls and discs are touching and no contact forces exist

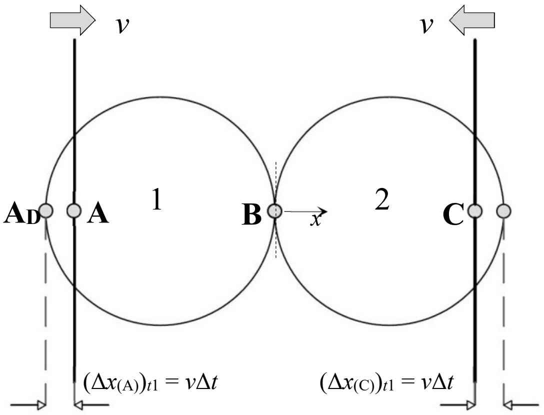

b) $t = t_0 + \Delta t = t_1$

At t_1 the rigid walls move inwards over distances $v\Delta t$

It was assumed that disturbances cannot move beyond a single disc during one time step

Thus both discs are assumed to maintain their initial positions during time interval from t_0 to t_1

Therefore overlaps exist at time t_1 at contacts A and C and are of magnitude Δx (positive for compression)

Force-displacement law is used to calculate contact forces: $\Delta F_x = k_x(\Delta x)_{t1} = k_x v \Delta t$, where k_x is the normal stiffness and ΔF_x is the increment in normal force

Therefore, at time $t_1 = t_0 + \Delta t$:

$$F_1 = k_x(\Delta x)_{t1} \; ; \; F_2 = -k_x(\Delta x)_{t1}$$

Accelerations $\ddot{x}$ for discs 1 and 2 found using Newton's second law: $\ddot{x}_1 = F_1/m_1 \; ; \; \ddot{x}_2 = F_2/m_2$

Accelerations assumed to be constant over time interval between $t_1 = t_0 + \Delta t$ and $t_2 = t_0 + 2\Delta t$

To determine velocities $\dot{x}$, accelerations are integrated: $\left[\dot{x}_1\right]_{t2} = \left[F_1/m_1\right]\Delta t \; ; \; \left[\dot{x}_2\right]_{t2} = \left[F_2/m_2\right]\Delta t$

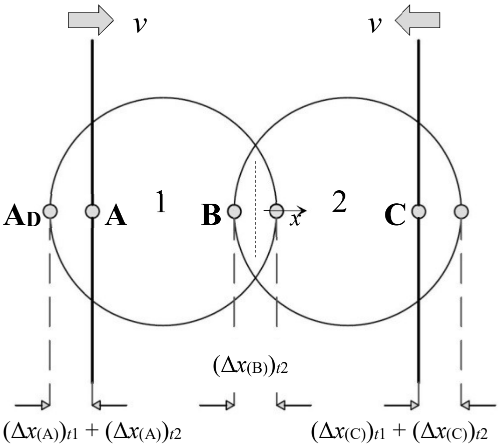

c) $t = t_0 + 2\Delta t = t_2$

The relative displacement increments at contacts A,B and C at time t_2 are calculated from

$$\left(\Delta x_{(A)}\right)_{t2} = \left(v - \left[F_1/m_1\right]\Delta t\right)\Delta t$$
$$\left(\Delta x_{(B)}\right)_{t2} = \left(\left[F_1/m_1\right]\Delta t - \left[F_2/m_2\right]\Delta t\right)\Delta t$$
$$\left(\Delta x_{(C)}\right)_{t2} = \left(\left[F_2/m_2\right]\Delta t - \left[-v\right]\right)\Delta t$$

Figure 5-1: Basic DEM calculation cycle

Source: Wegener (2015) from Cundall & Strack (1979)

In more recent studies by Coetzee & Els (2009), the calibration of discrete element parameters based on a soft particle approach were investigated. Like many other preceding DEM researchers, their research was formulated on the studies conducted by Cundall & Strack (1979). In the soft particle approach, each contact element is modelled with a linear spring in the contact normal direction (of stiffness k_n) and a linear spring in the contact tangential direction (of stiffness k_s), as illustrated in Figure 5-2. The difference with this contact model and other earlier models, was the inclusion of frictional slip in the tangential direction governed by the friction coefficient μ.

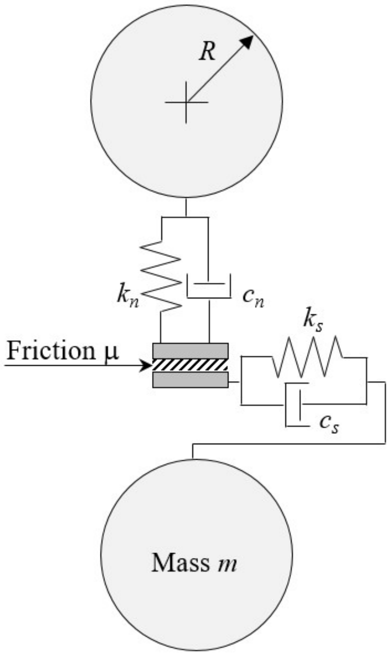

Figure 5-2: DEM contact model
Source: Adapted from Coetzee & Els (2009)

Similarly, the particles are allowed to overlap, where the amount of overlap in the normal and shear direction are given by Δx_n and Δx_s respectively. In conjunction with the spring stiffness, k_x, the relevant contact force components can be computed. The contact force in the normal direction F_n is given by:

$$F_n = k_n \Delta x_n \tag{5-1}$$

And the contact force in the shear direction, F_s is given by:

$$F_s = \begin{cases} \sum k_s \Delta x_s & \text{for } F_s < \mu F_n \\ \mu F_n & \text{for } F_s \geq \mu F_n \end{cases} \tag{5-2}$$

5.3 Application and limitations of DEM

DEM is capable of analysing particles of various shapes and sizes. The model was initially developed for the analysis of rock mechanic problems (Cundall & Strack, 1979). However, presently DEM appeals to a wide variety of disciplines such as applied physics, chemical engineering and geology.

One of the main difficulties associated with DEM is the modelling of large volumes of granular particles (O'Sullivan, Bray & Cui, 2006). The system requires high computational power to process the millions to billions of particles dependent on the sample size. One such instance may be a soil domain with final dimensions of 35mm high, 100mm wide and 120mm long. Soil particles with a fixed diameter of 2.4mm would include a total of 32,168 particles in the domain. In practice, domains can be significantly large in order to simulate mining activities of a relevant scale. A further contributing factor to the computational difficulties of DEM systems as experienced by Wegener (2015), was the shape of the particles characterised in the model. Complex shapes can drastically increase the computational time of the system. Therefore, many researchers use spherical particles as the basis of their domain (Obermayr et al., 2011; Tsuji et al., 2012; Li et al., 2016).

Despite the computing expense, the system serves as a useful tool to analyse complex shapes of different sizes and volumes. Li et al (2016) analysed the soil-tool interaction of a bear claw with a calibrated DEM model. They found that the system was a useful tool for analysing tillage effects by changing the working conditions of the different tools.

Numerical modelling is a tool that can be effectively utilised when the nature of the investigated system is clearly known and understood. For a granular particle analysis consisting of thousands to millions of interacting spheres, it was reasonable and practical to explore the benefits of utilising a DEM model. DEM models the behaviour of individual particles with regards to their interactions and movements over a given time step (t). However, the method comes with certain limitations such as its computational expense. The more complex or greater the number of particles is, the higher the computational time will be. Therefore with reference to the research project, a particle of high sphericity such as a glass bead was considered to minimise the computational expense. For a detailed description of DEM the reader is referred to Cundall & Strack (1979).

6. Case Studies

6.1 Introduction

For this chapter, three cases studies were highlighted. The first study looked at marine mining activities conducted by De Beers Marine (DBM) along the coast of Namibia. It refers to tools that show clear evidence of granular flow principles and it highlights how technological improvements of this nature can improve efficiency with respect to production rate. The next two studies focussed on the modifications of existing empirical equations based on granular orifice discharge. This provided insight into how certain dominating parameters in the experimental tests could be analysed or improved.

6.2 Offshore Diamond Mining in Africa

Author/s: De Beers Marine (Pty) Ltd

With regards to DBM mining operations off the coast of Namibia in Africa, the production of diamonds has long become a commodity of high demand. The supply of diamonds heavily depend on the discovery of new deposits as older deposits become exhausted and expensive. Presently, DBM have resorted to improving the production rate of their mining systems to match the high consumer demand of diamonds globally. Looking at Figure 6-1, the implemented production strategy was most notably depicted in the offshore production rate of the systems employed in Namibia (De Beers Group, 2016). One of the main sources of improvement included the entrainment rate of the particles through the apertures of the systems.

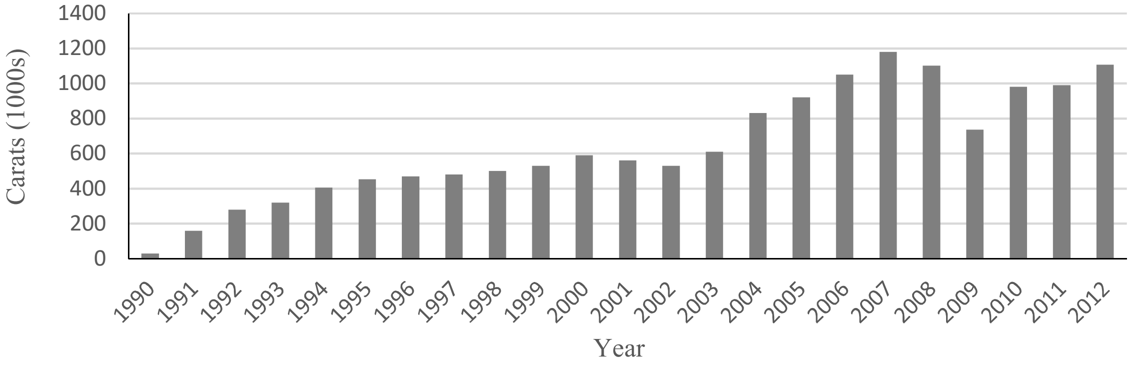

Figure 6-1: Offshore diamond production rate of Namdeb Holdings

Adapted from De Beers Group (2016)

It is known that a vast quantity of gem-quality diamonds exist off the west coast of southern Africa (Gurney, Levinson & Smith, 1991). Since diamonds are the leading commodity in the jewellery trade, the continuous supply of gem-quality diamonds is of significant importance in the industry. In the past, mining ventures of this nature were scarce due to the resources and investments required to attain a favourable return. The extracted resources are generally finite and non-renewable, thus the return on these ventures are not economical if production targets are not met or if the start-up expenses are too high, hence the limited amount of literature concerning offshore mining. The success of a venture is measured by the quantity of material entrained by the extraction system utilized, consequently introducing the need for the optimisation of these systems. The area of interest most relevant to the project was the interface between the suction nozzles used on the mining systems and the flow of materials through it.

One of the leading companies involved with offshore commercialised mining is De Beers Marine (DBM). The company specialises in the extraction of diamonds and has been exploring and mining off the continental shelf of Namibia since 1983. DBM run a sizeable mining operation that requires a high annual production rate of diamonds to achieve a profitable undertaking. Over the years, the level of production has been maintained through investments into sectors such as research and engineering. By developing advanced prototypes or optimising certain aspects of systems, the company has been able to mine at a higher efficiency and reach annual production targets. (De Beers Group, 2016)

DBM is capable of optimizing the existing systems through a number of different methods. One of the primary optimisation features include the interaction between the inlet of the nozzle and the granular materials. The two mining systems currently operational in the DBM fleet include a specialised seabed crawler and a large diameter drill bit (Figure 6-2). The systems are used rigorously and require a high level of maintenance to ensure optimum performance. (Richardson, 2014)

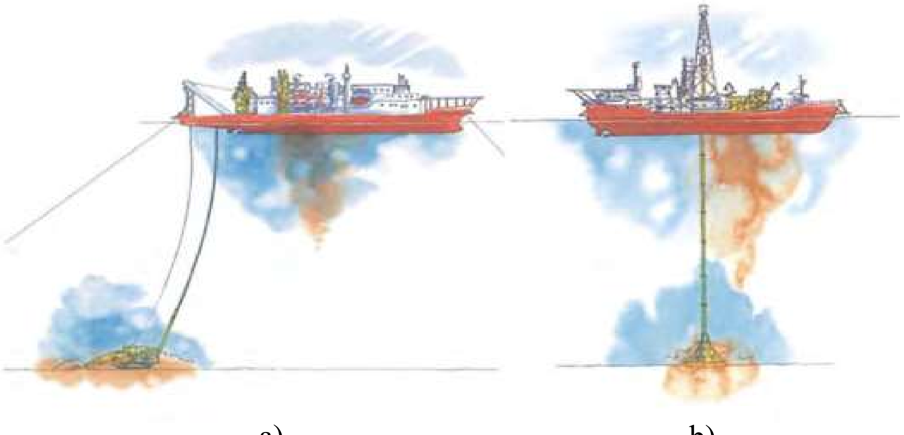
a) b)

Figure 6-2: a) Seabed crawler b) Large diameter drill
Source: (Richardson, 2014)

Over the past decade, De Beers Marine has made major technological advances in the offshore mining industry that has saved their mining business. Since the inception of the jet water drill in 1999, a number of innovative mining techniques have been introduced to improve the overall offshore diamond production rate. The technological advances in the industry in which DBM operates has shown massive growth over the years, as in Figure 6-3. The industry would have ended in the mid-2000s as it would have been a loss-making venture due to a combination of factors such as inefficient mining techniques, the global financial crisis in 2009 and China's economic slowdown in 2015 (Seccombe, 2014).

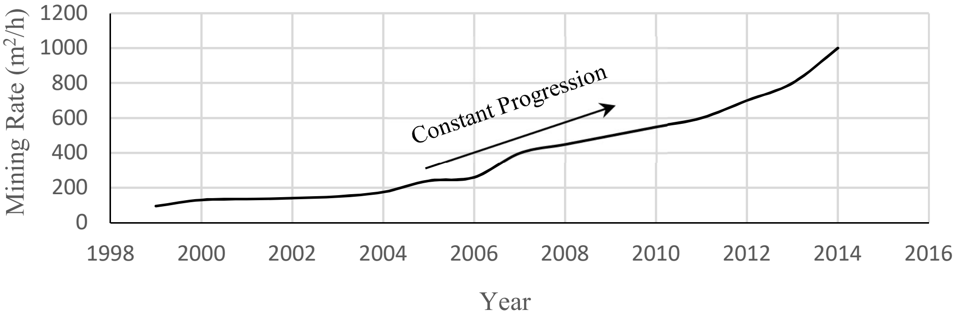

Figure 6-3: Progression of mining rate with technological advances
Source: De Beers Group (2016)

6.2.1 Specialised Seabed Crawler

Out of the two mining systems operated by DBM, the specialised seabed crawler was of greater relevance, largely due to the mechanical interaction between the system and seabed. Over a decade ago, the first generation seabed crawler was capable of mining $250m^2$ of seabed per hour and was considered to be a technological breakthrough at the time. Presently the third generation seabed crawlers can mine at a continuous rate of up to $1000m^2$ per hour. The system is made up of a suction nozzle, also known as the vacuum head, powered by a single 700mm diameter centrifugally pumped transport riser pipe. The company as of 2017, had two seabed crawler's that weighed over 260 tonnes each (Figure 6-4). To ensure that one of the systems was always operational, the crawlers were rotated every 18 months for maintenance purposes.(Seccombe, 2014)

Figure 6-4: Seabed Crawlers in for maintenance
Source: Pringle (2013)

The seabed crawler's main advantage is its increased mining rate compared to the large diameter drill bit, with rates reaching as high as 15 000m^2/day (Richardson, 2014). The rate of entrainment is dictated by a number of engineering aspects that are either dependent or independent of one another. Factors such as the hydraulic pump capacity and the diameter of the suction pipe, have a substantial effect on the allowable rate of entrainment (Kirby, 2017). The limitation has a direct influence on the number and size of openings applicable to the suction nozzle at the end of the pipe.

Diamonds are generally trapped by their surrounding ore, which is usually kimberlite. The ores were redistributed into the Namibian coast over 100 million years ago from the interior of southern Africa (Cronan, 1999). They were transported via a system of rivers, presently known as the Orange River, generally smaller in size when compared to their remaining land counterparts due to the weathering process during transport. With reference to the high concentration of diamonds near the mouths of rivers and their size, the size of the orifices on the crawler nozzle has a specific particle size target range. The nozzle was designed to take in as many diamond ore particles as possible without hindering the systems functionality. Therefore it was more economical and practical to entrain smaller particles at a higher volume than to take in larger particles that could cause jamming or effect the pumping systems (Kirby, 2017). At this stage, it is necessary to highlight the relevance of the targeted particle range. The range provides an aspect of design for the orifice and an indication of the entrainment rate. Figure 6-5 provides an illustration of ores commonly found off the coast of Namibia.

Figure 6-5: Crushing of ores containing diamonds
Source: De Beers UK Limited (2017)

The openings on the suction nozzle were found to be square shaped as they were more efficient and easy to construct. Additionally, they covered a greater surface area on the nozzle which assisted in maximising the performance and decreasing the potential of complete jamming. (Kirby, 2017)

Great detail in analysis was given to the size and shape of the orifice as it had a significant impact on the entrainment rate. Similarly, it is also worth mentioning that the proposed orifice may depend on the size and shape of the discharged material. The vacuum head itself incorporates both suction and mechanical forces. The two forces work in conjunction with one another to optimise the rate of hydraulically transported particles. Apart from the systems clear advantages, there were a number of associated disadvantages with just the interface of the nozzle and the particles. The disadvantages included its limited applicability, clogged particles within the apertures and maintenance issues caused by harsh operating environments. These issues can all affect the rate of mining when not properly accounted for in the preliminary study. As specified in the scope of the project, the research was based on the interaction of the aperture nozzle and soil particles on the seabed as conceptualised in Figure 6-6.

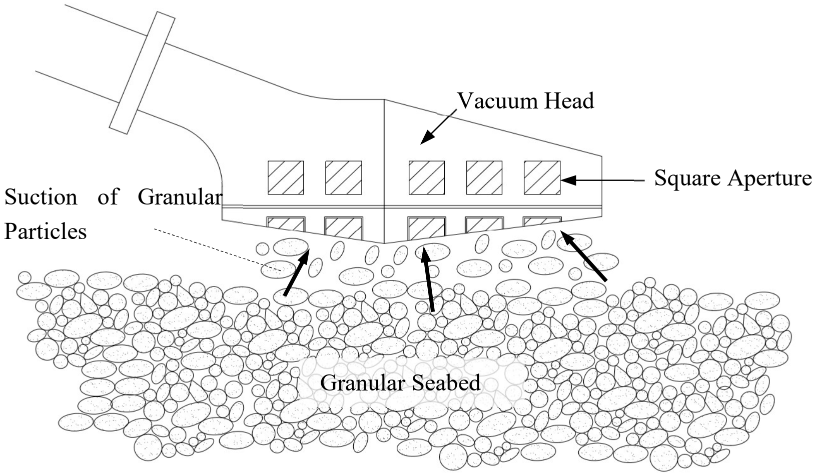

Figure 6-6: Conceptual vacuum head interaction with seabed

6.3 Pressure Independence of Granular Flow

Author/s: Aguirre et al. (2010)

Through studies conducted by Janssen (1895) and other researchers such as Hagen(1852), Beverloo et al (1961) and Mankoc et al. (2007), it was assumed for more than a century that the discharge rate was influenced by the pressure or stress near the orifice of the hopper. However, in 2010, Aguirre et al. carried out an experiment to test this theory. Their approach consisted of replacing the gravity constant in the empirical Beverloo law (Equation (4-7)) with a velocity vector. This process involved the placement of small discs on a conveyor belt, transported through a horizontal aperture at a constant rate. Their research was conducted in a two-dimensional setup (Figure 6-7).

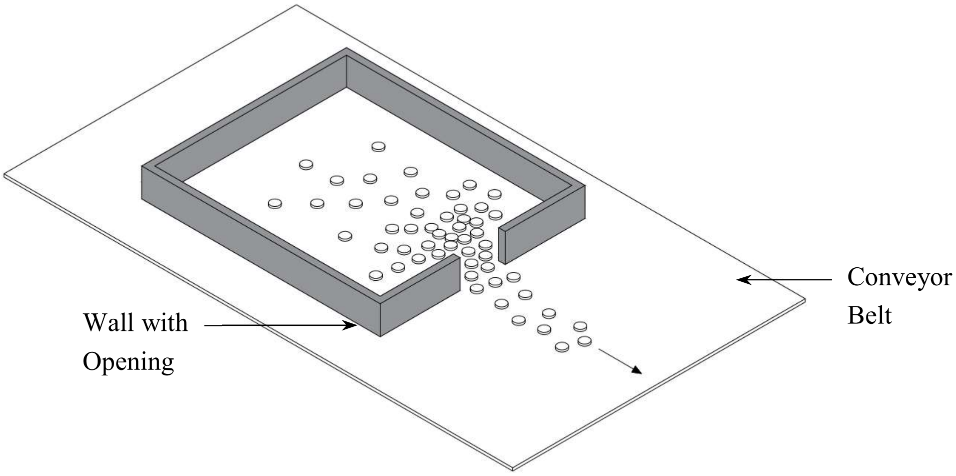

Figure 6-7: 2D Experiment highlighting pressure independence of flow
Adapted from Aguirre et al. (2010)

Prior to their testing, through dimensional analysis it was assumed that the output would agree with the results obtained via Equation (6-1) for a 2D system.

$$W_{2D} = C\rho_b\sqrt{g}\left(D_o - kd_p\right)^{\frac{3}{2}} \tag{6-1}$$

In the case of a conveyor belt moving at a constant velocity *v*, the driving force of the particles was no longer the gravitational force but the translational movement of the belt. As such the revised expression for the discharge of particles moving at a constant velocity was given as:

$$W_{2D} = \rho v d_p (\frac{D_o}{d_p} - k) \qquad (6\text{-}2)$$

Where,

W_{2D} = Flow rate of particles in 2D
v = Velocity of conveyor belt in m/s
D_o = 2D size of aperture in m

In their findings, it was discovered that for a constant pressure near the orifice, different discharge rates could be achieved by changing the velocity of the conveyor belt. In contrast, it was noted that by increasing the weight of the discs which in turn increased the effective pressure near the aperture, a constant flow rate, W, was achieved. Highlighting that the speed of the discs determined the flow rate, not the pressure induced at the bottom of the silo. This suggested that the flow of particles can be increased by increasing the velocity of the mechanism carrying the grains.

It was concluded that the dimensional analysis used to formulate the Beverloo expression, should be altered to account for pressure since it exhibited a time scale. Where in the case of a 3D silo, with pressure P at the outlet, the resulting expression is,

$$W_{3D} \propto \sqrt{\rho_{3D} P D_o^2} \qquad (6\text{-}3)$$

Thus, whether the pressure was limited by the Janssen effect or not, the discharge, W was related to D_o^2, which contradicts the earlier scaling relations of $W \propto D_o^{5/2}$.

6.4 Granular Flow through Lateral Exit Apertures

Author/s: Medina, Cabrera, López-Villa, & Pliego (2014)

The discharge of granular particles from the bottom exits of hoppers and silos, due to gravity alone, is a phenomenon that has been researched extensively. Governed by the correlation between mass flow rate and orifice diameter previously shown in Equation (4-7), the Hagen-Beverloo law is applicable for different processes. The reason for this is that the law has been modified over the years to suit different flow scenarios. Consequently, only a few studies have been conducted on the discharge of grains through horizontal apertures. In this study, conducted by Medina et al. (2014), the effect of the wall thickness and particle stresses were analysed. The researchers derived an expression for the discharge of particles through a horizontal aperture on the side of a bin. The expression was modified from Equation (4-7) in the form:

$$\mathrm{W} = \mathrm{C}\rho_{\mathrm{b}}\sqrt{\mathrm{g}}\left(\mathrm{D}_{o} - \mathrm{kd}_{p}\right)^{\frac{5}{2}}(\alpha - \emptyset) \tag{6-4}$$

Where,

α = Angle of the wall in °
$\emptyset$ = Angle of repose of the grains in °

Using Figure 6-8, the angle of the wall α, can be easily understood. Through standard trigonometry, the thickness of the wall w, and the diameter of the aperture, D_o, the expression for α was determined as α = $\tan^{-1}$ (D_o/w).

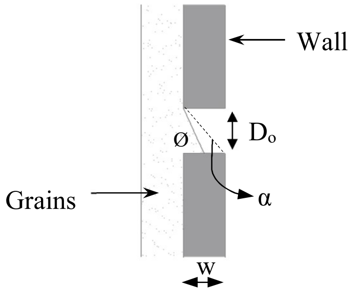

Figure 6-8: Flow of sand through lateral orifice
Adapted from Medina et al.(2014)

Their apparatus consisted of a square vertical bin with holes of different diameters on either side of the bin. Additionally, to evaluate the effect of the wall thickness, the sides of the wall each had a different thickness. It was reported from their experiment that when α > Ø gravity flow occurred but when α < Ø granular flow was not possible. From this relationship, it was possible to determine an appropriate wall thickness to achieve the optimum mass flow rate. However, in relation to the conditions mentioned about the wall thickness, another factor that can influence the discharge of particles is the formation of arches close to the hole as described by Seville et al. (2012).

Summary: Part I

Part I reviews a range of literature to provide a basis for the fundamental principles of granular flow through an orifice and the application thereof. With reference to the multiple topics covered in the part, it is clear that a number of engineering aspects must be addressed before analysing or predicting the behaviour of granular materials passing through an orifice. Literature pertaining to the basis of the objective included offshore extraction techniques utilised by the mining, sampling and dredging industries, immersed granular flow from first principles, the discharge rate of particles using constitutive laws, literature on the theory and application of discrete element modelling; and lastly relevant case studies to provide context.

In mining, dredging and sampling practices, details relating to the formation of the seabed, types of soil and soil strength parameters were fundamental in selecting or modifying tools used for extraction. Typical designs focused on the parameters near the orifice interface, giving rise to the need to construct and design a model to analyse such parameters.

Additionally, granular flow was closely related to fluid flow, where solid particles when agitated or entrained, exhibited fluid-like behaviours. It is worth noting that certain aspects in fluid flow such as hydraulic diameter, Reynolds number and change in pressure can be accustomed to granular flow. Flow governed by constitutive laws derived by Newton or Bernoulli; dimensionally and empirically formulated expressions such as the Beverloo law, provided alternative methods of predicting the flow behaviour. Beverloo predicted that the discharge of particles through an orifice would follow a relationship of $W \propto D_o^{5/2}$. In context, the discharge or collection rate was further a function of a number of other factors, which included:

1. Geometry and size of orifice including its ratio between the particle diameter,
2. Method of entrainment, whether the material was collected mechanically or hydraulically,
3. Properties of the material collected or transported, and
4. The influence of gravity.

To date, only a few studies have been found to investigate the different mechanisms of flow through an orifice. The relationship between granular flow and the governing parameters was a clear indication of the gap of knowledge in literature. The discrete element method, a powerful numerical analysis tool, was considered to be an appropriate numerical system for investigating the flow behaviour due to its capability of simulating discrete particles within a granular medium.

PART II

Physical Testing of Granular Flow through Orifice

Contents

Chapter 7 – Experimental Setup
This chapter describes the main apparatus used in the testing

Chapter 8 – Physical Test Methodology
The scaling of parameters, preparation of testing materials and the experimental testing methodology was covered.

7. Physical Testing Apparatus

7.1 Introduction

The chapter describes the apparatus used to perform the physical tests. The tests were fulfilled to validate the theories derived from literature and to analyse the granular flow phenomenon within the context of real life applications. The testing was based on common offshore particle extraction techniques, where the use of a systems or nozzles containing an opening were implemented to collect or transport granular materials. Therefore, with that in mind, the apparatus used was divided into four main sections

1. Granular seabed: The testing material to be entrained
2. Visualisation tank: Working platform of experiment
3. Nozzle attachment: Design of nozzle used for testing
4. Monitoring devices: Devices used to record the data

7.2 Granular Seabed

Properties of the tested material were assumed to have a significant influence on the discharge rate. Therefore, for a theoretical basis, the material needed to be consistent in size, shape, weight and strength. Following these factors and studies conducted by researchers such as Nedderman et al. (1982) and Serrano et al. (2015), spherical glass beads (GB) of uniform shape were selected. Sizes specifically identified were 6 (GB6) and 16mm in diameter (GB16), chosen based on the length and scaling restrictions of the visualisation tank (Figure 7-1).

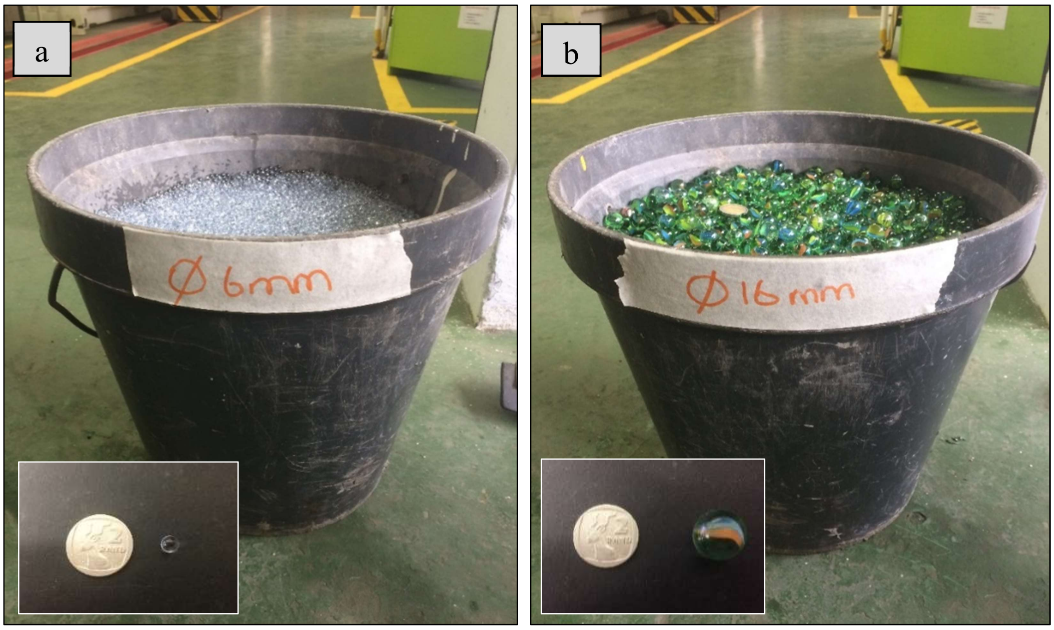

Figure 7-1: a) 6mm diameter glass beads b) 16mm diameter glass beads (R2 Coin for scale)

The beads were made from soda lime which comprised of silicon dioxide (SiO_2), sodium oxide (Na_2O), aluminium oxide (Al_2O_3) and calcium oxide (CaO) (Preciosa Ornela, 2011). Through visual inspection, the determined parameters of the GB were not only used for the physical tests but in the numerical analysis. The majority of the tests were completed using GB6, however GB16 were further introduced to investigate extended parameters of interest such as scaling effects and varying ratios between orifice and particle diameter. Additionally, they were used as a validation tool to verify the accuracies of the empirical equations formed. The average bulk density, ρ_b and specific gravity G_s were found to be similar for both beads and closely resembled the values presented in the verified data sheets (Appendix F). The other index properties and strength parameters of the GB were verified by Preciosa Ornela (2011), a certified glass supplier company. The properties as determined by their labs were summarised in Table 7-1.

Table 7-1: Verified properties of GB6 and GB16 glass beads
Source: (Preciosa Ornela, 2011)

Strength / Index Properties	Symbol	Unit	Value
Particle dry density	ρ_d	kg/m^3	2540
Submerged particle density	ρ_{sub}	kg/m^3	1540
Bulk density*	ρ_b	kg/m^3	1485
Saturated density	ρ_s	kg/m^3	1893
Specific gravity*	G_s	-	2.54
Young’s modulus of elasticity	E	MPa	78-85
Crushing strength	-	N	3600

*Verified

7.3 Visualisation Tank

The testing of the nozzle apparatus was done in a controlled environment whereby the desired inputs and outputs could be controlled and recorded. The DBM lab facility consisted of a 2.0m x 2.0m square visualisation tank with glass panels on three sides and a stainless-steel plane on the fourth side (Figure 7-3). The existing tank dimensions were suited for the proposed testing with respect to the size of the scaled down model. Additionally, the tank provided a visual space to allow for the observation and recording of the scaled models, along with a working platform (footwall) for the placement of the beads to setup a granular bed. Apart from the tank, other elements of interest included: a) the bogey unit used to translate the nozzle and b) the positive displacement pump used to provide the hydraulic transport mechanism.

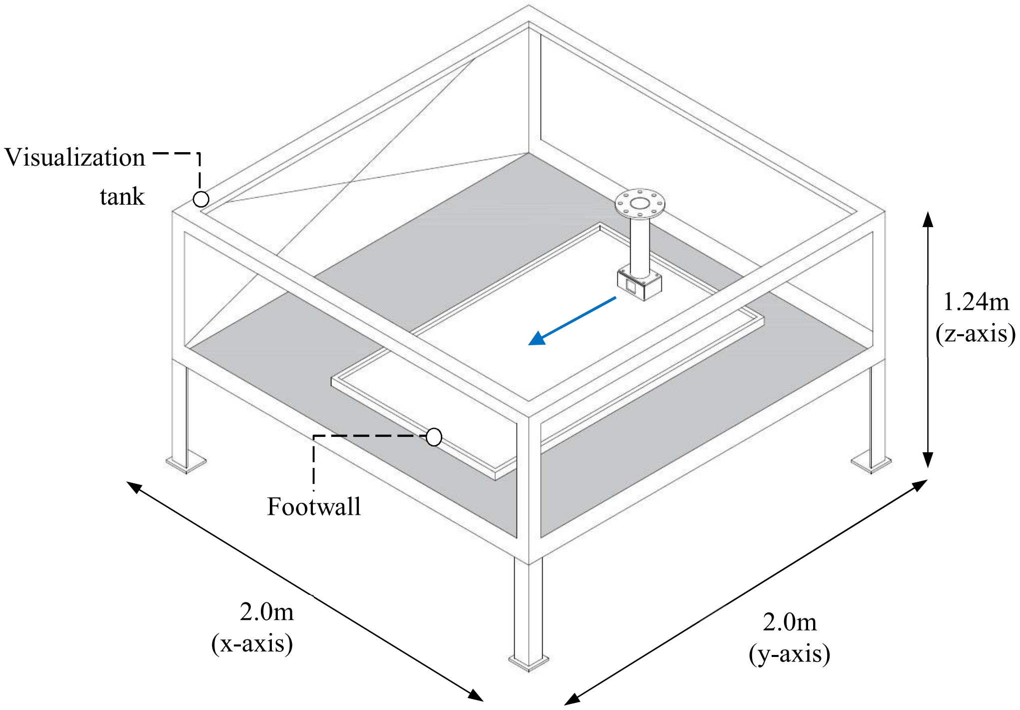

Figure 7-2: Isometric illustration of visualisation tank

7.3.1 Bogey Unit Deployment Tool

Movements of the nozzle were facilitated by a bogey unit attached to the top of the tank (Figure 7-3). The bogey unit was controllable in 3 axes, namely motion across the breadth and length of the tank, and the lifting and lowering of the tool vertically. The gantry used to transport the bogey unit was situated length wise across the tank. This provided the x-axis motion with a motor mounted on one side and a drive axle connecting the two chain pulleys.

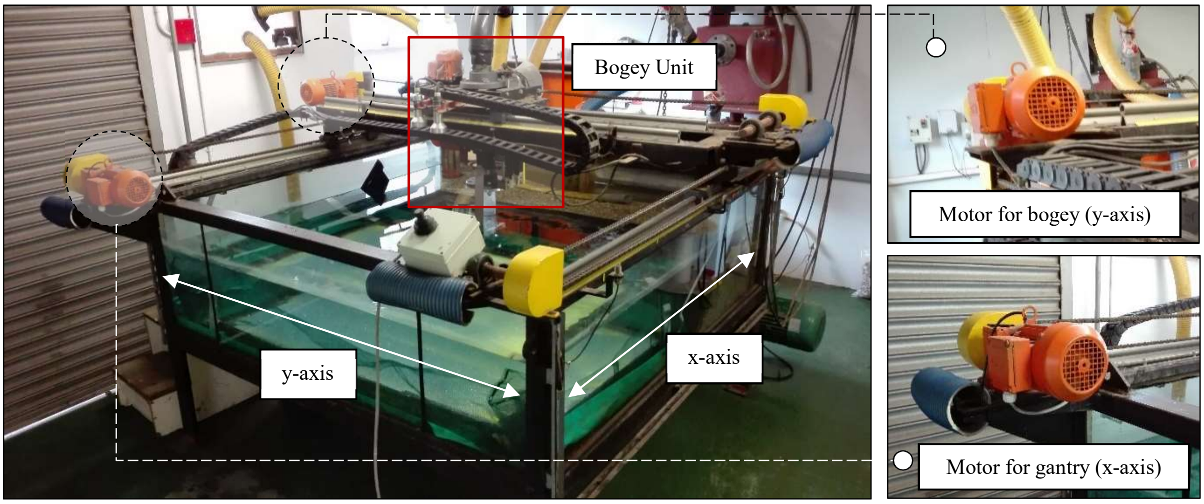

Figure 7-3: Elevated view of visualisation tank with mounted motors

The attached motor was powered by a variable speed drive (VSD) housed in an orange control box with controls mounted on the front panel. The drive was a piece of equipment used to regulate the speed and rotational force of an electric motor (ABB, 2008). The controls consisted of stop and start buttons, a direction selector, and a speed adjustment dial.

The movements of the bogey unit on the gantry were limited to the dimensions of the tank. To prevent the gantry from moving too far, inductive limit switches (ILS) were implemented. The ILS were mounted on the tank and were activated when angle iron lengths mounted to the gantry intercepted the switches. Its lengths were designed specific to the size of the tool as it prevented it from encountering the sides of the tank.

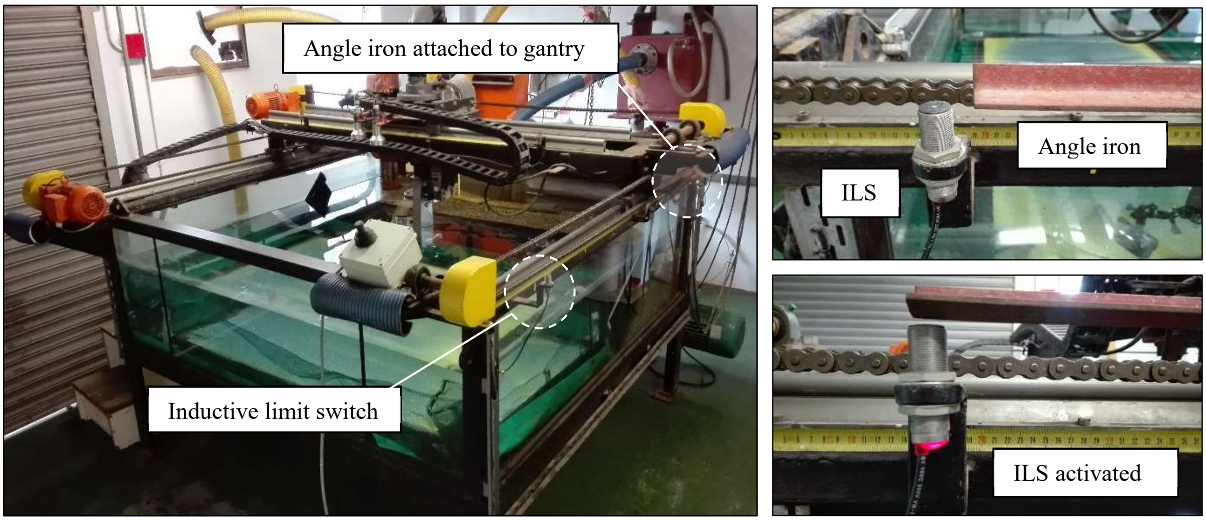

Figure 7-4: Inductive limit switch (ILS) attached along x-axis of tank

The bogey that sits on top of the gantry has a y-axis motion operated in the same fashion as the gantry. The speed of the bogey and gantry were restricted by the operating power of the VSD. The velocity increments implemented were as follows:

Table 7-2: Maximum translational velocity of bogey unit

Dial no.	Incremental speed	Translational velocity (m/s)
4	260mm/s	0.104
6		0.156
8		0.208
10		0.260

The proposed nozzle, as later discussed, was attached to a flange connection beneath the bogey unit. The length of the flange connection was designed and constructed according to the lifting and lowering constraints. The positioning of the bogey and gantry as seen in Figure 7-5a) were monitored using a measuring tape and pointer mounted onto the gantry.

a) Vertical alignment tape with pointer used to prepare the bed height or set the nozzle at a specified height

b) VSD used to control bogey unit movement in the x, y and z axis

c) Portable joystick control used to control movement of bogey unit as an alternative to VSD

Figure 7-5: Devices used to measure or control the movement of the bogey and nozzle

In addition to the controls on the orange box, there was a portable remote control that could be used to control the movement of the gantry and bogey unit. The control box, as shown above, consisted of a single 4-axis joystick and a four-meter lead which allowed it to be used around the tank. The inclusion of a portable control assisted in allowing a single operator to handle both the video monitoring and motion of the tool.

7.3.2 Positive Displacement Pump

Suction power was used as the post processing tool to analyse the influence of suction with regard to the outputs from the mechanical movement system (MMS) testing. The power was provided by a progressive cavity pump driven by a VSD mounted on a wall, as displayed in Figure 7-6, like that of the bogey. The VSD user manual was available online by Yaskawa (2002).

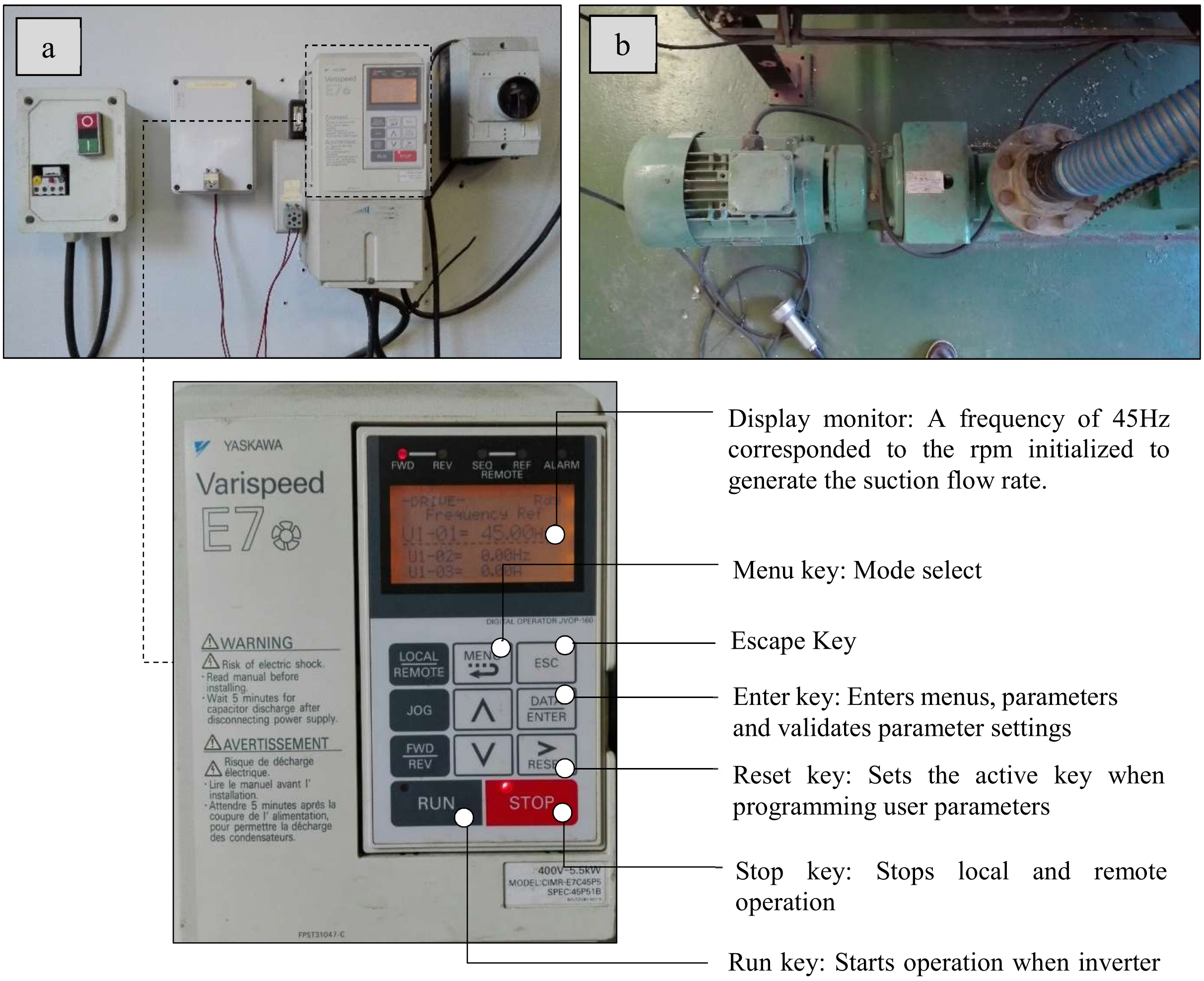

Display monitor: A frequency of 45Hz corresponded to the rpm initialized to generate the suction flow rate.

Menu key: Mode select

Escape Key

Enter key: Enters menus, parameters and validates parameter settings

Reset key: Sets the active key when programming user parameters

Stop key: Stops local and remote operation

Run key: Starts operation when inverter being controlled by digital operator

Figure 7-6: a) VSD mounted onto wall and b) Positive displacement pump

The pump allowed for the overall control of the flow rate and it prevented flow rate changes caused by fluid density. However, during the post-processing tests it was evident that the pump was sensitive to blockage caused by the accumulation of GB within the pump, similar to the jamming phenomena experienced in hoppers. A gravel box was installed on the suction line to serve as an intermediate phase for the collection of granular particles, in this case, spherical beads (Figure 7-7). The box was mounted with an inlet underneath it and an outlet on the side of it. At the end of each test, the retained material was released from the box into a suitable bin, the collection box, by opening the dump valve and draining the contents. The mass properties of the bin were first recorded before returning the material back into the tank.

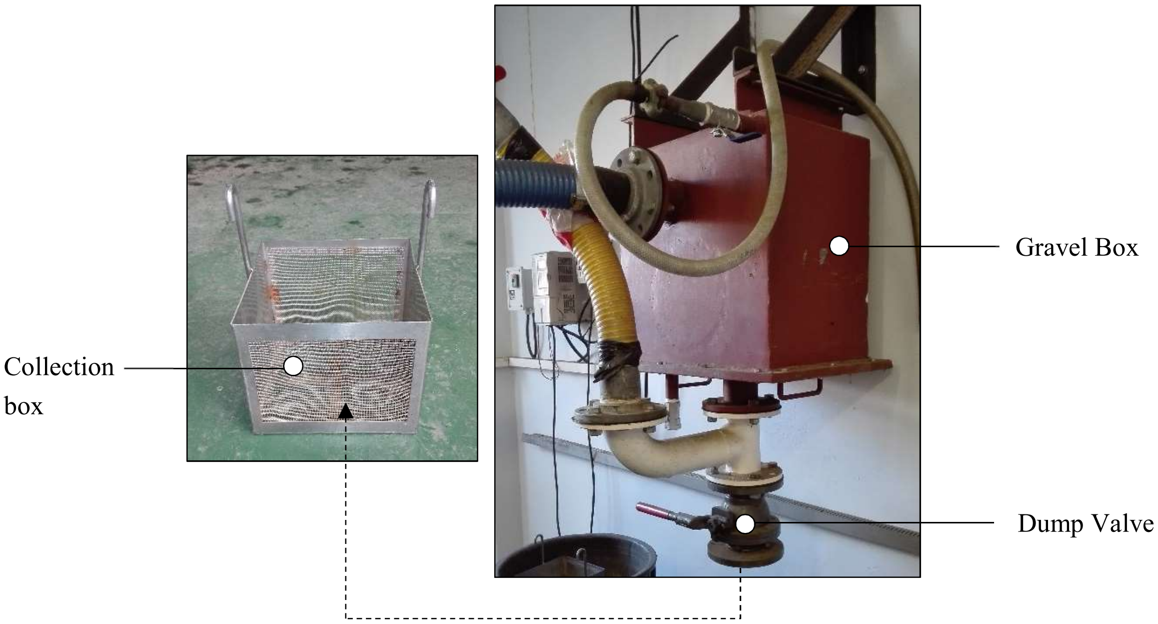

Figure 7-7: Gravel box and collection box used to capture entrained materials

Of interest regarding the pump, was its suction capabilities. To accurately predict the flow rate of the pump, a calibration process was carried out. Set intervals of flow were measured against the VSD frequency selected for the pump. The test performed was referred to as the “bucket test” as detailed in Appendix H.

7.4 Nozzle Attachment Design

The nozzle was designed to verify the entrainment effects caused by altering velocities in conjunction with different orifice shapes, sizes, and configurations. The design focussed on current granular material extraction systems and work conducted by past researchers such as Aguirre et al. (2010) and Beverloo et al. (1961). The nozzle was attached to the bogey unit via a specially designed flange of which both were constructed out of a hardened Plexiglas (Plexiglas XT-see Appendix F). This was chosen due to its transparency and strength attributes; it allowed for the visual observation of the GB entering the opening whilst having sufficient strength to withstand the passive forces induced by the prepared seabed (Appendix E: pg 177). For detailed dimensions and specifications of the nozzle, refer to Drawing A-1 in Appendix A.

7.4.1 Orifice Shape and Size

The ratio, *R,* between the orifice diameter and particle size, was a significant attribute in deriving the granular flow expressions through an orifice, partly due to the discharge rates dependence on the size of the opening. Additionally, the ratio characterised the limitations associated with granular flow such as its susceptibility to jamming or clogging. Therefore, based on the size of locally sourced spherical beads (GB6 and GB16), the range of applicable orifice sizes were selected for testing as stipulated in Table 7-3.

Table 7-3: Sizing of orifice based on GB6 and GB16

Orifice Component	Ratio Required (GB6/GB16)	Orifice Size Required	Final Size Implemented
1	10/4	60mm/64mm	60mm
2	8/3	48mm/48mm	50mm
3	6/2.5	36mm/40mm	40mm
4	4/2	24mm/32mm	30mm

*Sizes implemented, equivalent to Hydraulic Diameter, D_h, or Orifice Diameter, D_o

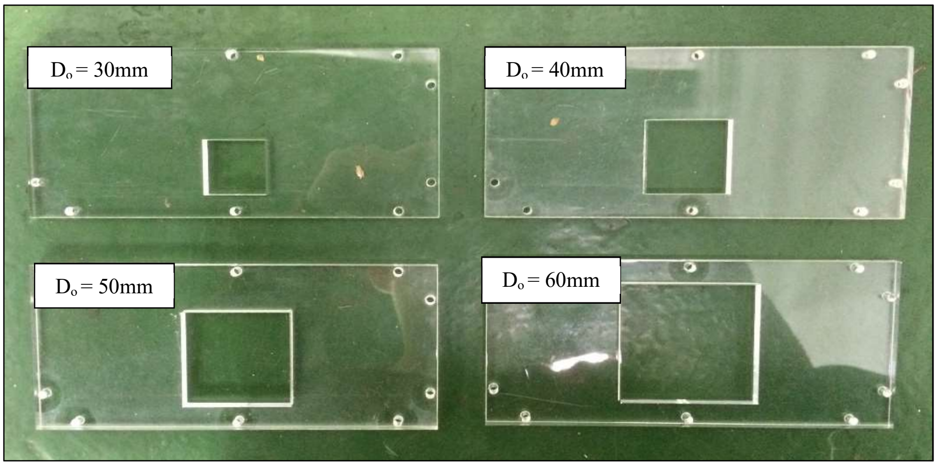

Figure 7-8: Fabricated nozzle face components (D_o=30-60mm)

Using the hydraulic diameter, D_h (Chapter 3.2.3 – Manning's Equation), the size of a square orifice equivalent to a circular orifice was determined. Coincidently, for a square orifice of length, l and a circular orifice of diameter D_o, where $D_o = l$, the hydraulic diameters, D_h for the two shapes were found to be the same.

Henceforth, any mention of the orifice diameter D_o, refers to the hydraulic diameter, D_h of a square orifice (E.g. D_o = 50mm → D_h = 50mm → square opening of length l = 50mm). The square aperture was used as the main reference of testing due to its ease of construction and context within the offshore mining industries.

7.4.2 Nozzle Face Dimensions

The dimensions of the nozzle excluding the aperture were based on the preceding physical boundary conditions and the scaling context of the experiment. In the DBM case study summarised in Chapter 6.2.1, the utilised nozzle, consisted of a fully covered face with multiple openings. Therefore, to provide a comparative basis, the height of the nozzle face was restricted to a height of 80mm to allow for a reduced face whilst accommodating the proposed orifice sizes. The spherical beads purchased, amounted to a total mass of 120kg. Using the bulk unit weight (ρ_b = 1485 kg/m^3) and the specified dimensions of the working platform (1.5m x 0.9m), a maximum depth of 60mm was calculated. Notably, higher depths could be obtained by restricting the working area (e.g. H = 80mm for 1.15m x 0.7m).

In addition to the bed depth, the position of the orifice within the face was also taken into consideration. To allow for added options of either varying the bed height or changing the orifice diameter, the opening was placed as close as reasonably possible to the base of the nozzle, precisely 10mm from the bottom.

The dimensions of the nozzle face were further configured towards a minimum ratio between the size of the orifice and the area of the face, a concept similar to the minimum thickness of a core-barrel used in sampling operations (Chapter 2.3.2). However, due to the extensive testing of various orifice sizes, the face needed to be big enough to allow for interchangeable orifices. This aided in reducing wastage of materials and speeding up testing sessions. Additionally, the general agreement in hopper flow insisted that $D_B > 2.5D_o$, with D_B equal to the silo barrel diameter or in this case the width of the nozzle face (Nedderman et al., 1982; Hirshfeld & Rapaport, 2001; Mankoc et al., 2007). The agreement assists in minimising irregular flow, such that constitutive laws like the Beverloo law are valid. Since the largest diameter to be used was a 60mm orifice it was recommended that the face have the following final dimensions:

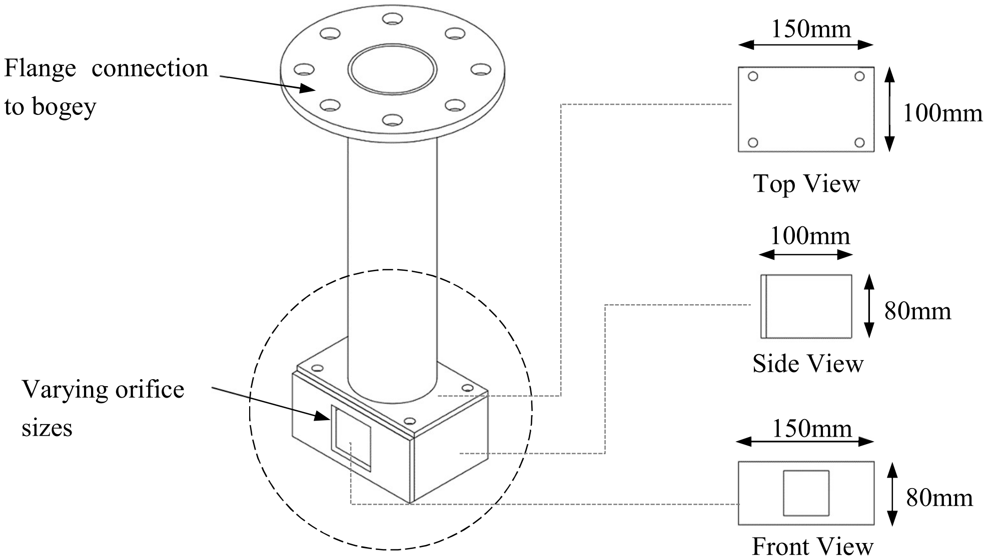

Figure 7-9: Final nozzle dimensions

7.4.3 Final Design and Construction

The primary component of the system used to investigate flow phenomenon was the nozzle face containing the opening. To further the investigation of the interface, interchangeable nozzle faces of different sizes were designed. All the components, including the flange connection, were constructed out of Plexiglas (refer to Appendix F for material data sheet) and assembled together temporarily using nuts, flat screws and bolts. Table 7-4 and Figure 7-10 highlight the components used to form the different nozzle combinations (Appendix A contains fully detailed drawings of the components).

Table 7-4: Primary and secondary components

Component	Dimension (mm)	Material	Part index
Nozzle face	80mm x 150mm	Plexiglas	A
Nozzle body	80mm x 150mm x 100mm	Plexiglas	B
Collection net	Fitted	Geotextile	C
Flange	Ø 80mm x 400mm	Plexiglas	D
Footwall	1540mm x 940mm	Plexiglas	E

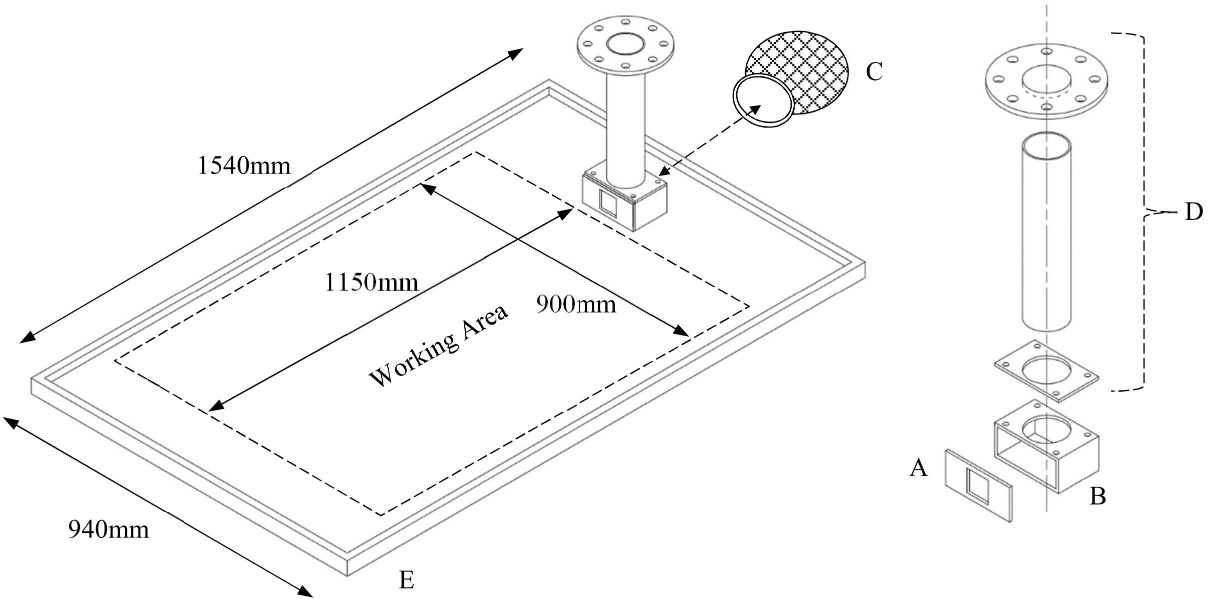

Figure 7-10: Overview of experimental components

The collection net was made from a high strength geotextile, well-suited for the particles to be collected. Its attachment to the nozzle was done using Velcro, with “hook” strips placed around the end of the nozzle box and “loop” strips fastened around the opening of the net.

The interplay of various parameters by modifying the components, allowed for the investigation of fundamental parameters such as changes in orifice size. To prevent potential uncertainties amongst the recorded results, the nozzle body components were designed to act as non-obstructive collection medium for the entering particles. A smooth transition of beads was achieved through a short nozzle body (w = 0.1m) and a durable collection net.

7.5 Monitoring Devices

Two monitoring systems were installed during experimental tests. This included a high definition visual recording device (GoPro: Model-Hero3) and a recovery measurement device. The Go-Pro was fitted with various attachment features. This allowed for a detailed visual recording of the movement of beads during the mechanical movement of the nozzle. The device was setup as shown:

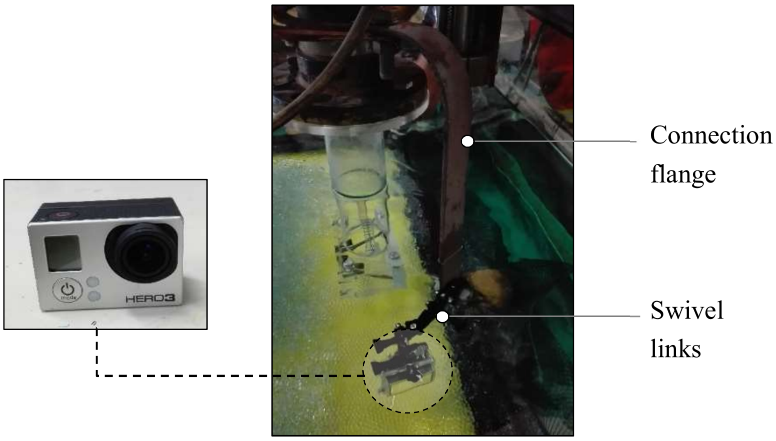

Figure 7-11: Monitoring device (Go-Pro) setup

Not only did the visual recordings record the behaviour of the interacting parts but they further allowed for the observation of the bulge height that formed in front of the aperture face during entrainment. This measurement, dependent on both the granular flow and translational rate, was used to understand the behaviour or effects on the entrainment rate for a specific velocity and orifice size.

8. Physical Test Methodology

8.1 Introduction

The overview of the various components in the previous chapter were used to carry out a specific set of tests. The tests involved investigating the interface parameters of the nozzle and determining the magnitude of their influence on the recovery efficiency and entrainment rate of particles. Two main systems were tested, this included mechanical entrainment without suction (MMS) and entrainment with suction (MSS). The scaling of the experiment, preparation of the testing material, different tests carried out and the methods used to perform them were covered in this chapter.

8.2 Scaling of Experiment

Flow of granular particulates in a fluid can be associated with hydraulic transportation systems in the mining or dredging industry. The dimensional properties of the physical model were designed based on the mining machine by DBM that was presently in use. The machine, known as the seabed crawler, transported materials hydraulically through the orifices of the nozzle. Small scale model tests were executed as the life-size tool was considerably large and would not have been practical in terms of running reiterative tests with multiple variables. A small model allowed for increased control over the working environment with the added advantage of producing consistent results. As identified from the scope and parameters of interest, the focal items to be scaled included:

- Nozzle dimensions including orifice size;
- Translational velocity (passing speed);
- Suction rate of pump.

To ensure similitude between the scaled model and life-size system, several similarities, through dimensional analysis, needed to be met. These included geometrical, kinematic and dynamic similarities. Considering the physical tests, the Froude scaling criterion derived from dimensional analysis was determined to be the most compatible scaling method (Criterion derived in Appendix G: pg 224).

8.3 Preparation of Testing Material

The GB were set up in the visualisation tank. Within the tank was a levelled (1.5m x 0.9m) Plexiglas sheet designed to act as the working platform for the experiment (Figure 8-1a). Through a systematic process, the beads were layered onto the platform. However, due to the low friction coefficient of the beads, the potential for sliding was very high. In practice, angulated granular particles have friction coefficients high enough to provide sufficient resisting forces to limit their movement during contact with another particle or boundary.

Setting up the glass bead seabed required the interlocking of the particles in contact with the Plexiglas. Thus, a wooden frame, the size of the working platform with a height of 30mm, was used to stabilise the bottom layer of the beads. Sealing tape was placed on the side of the visualisation tank (Figure 8-1d) to serve as a line of reference for the preparation of the bed and to perform consistent tests.

The tests conducted were fully submerged in water. In each case the effects of buoyancy were considered. Only in the hydraulic transport tests was the presence of water more prominent and focalised. Levelling of the seabed incorporated the use of a sweeping tool (Figure 8-1c) and a height adjusted nozzle. The desired level was first approximated using the sweeping tool together with a depth measuring device such as a tape measure (Figure 8-1b). Once approximated, the final bed height was achieved by levelling the bed using a nozzle lowered to a specified height (Figure 8-1 e).

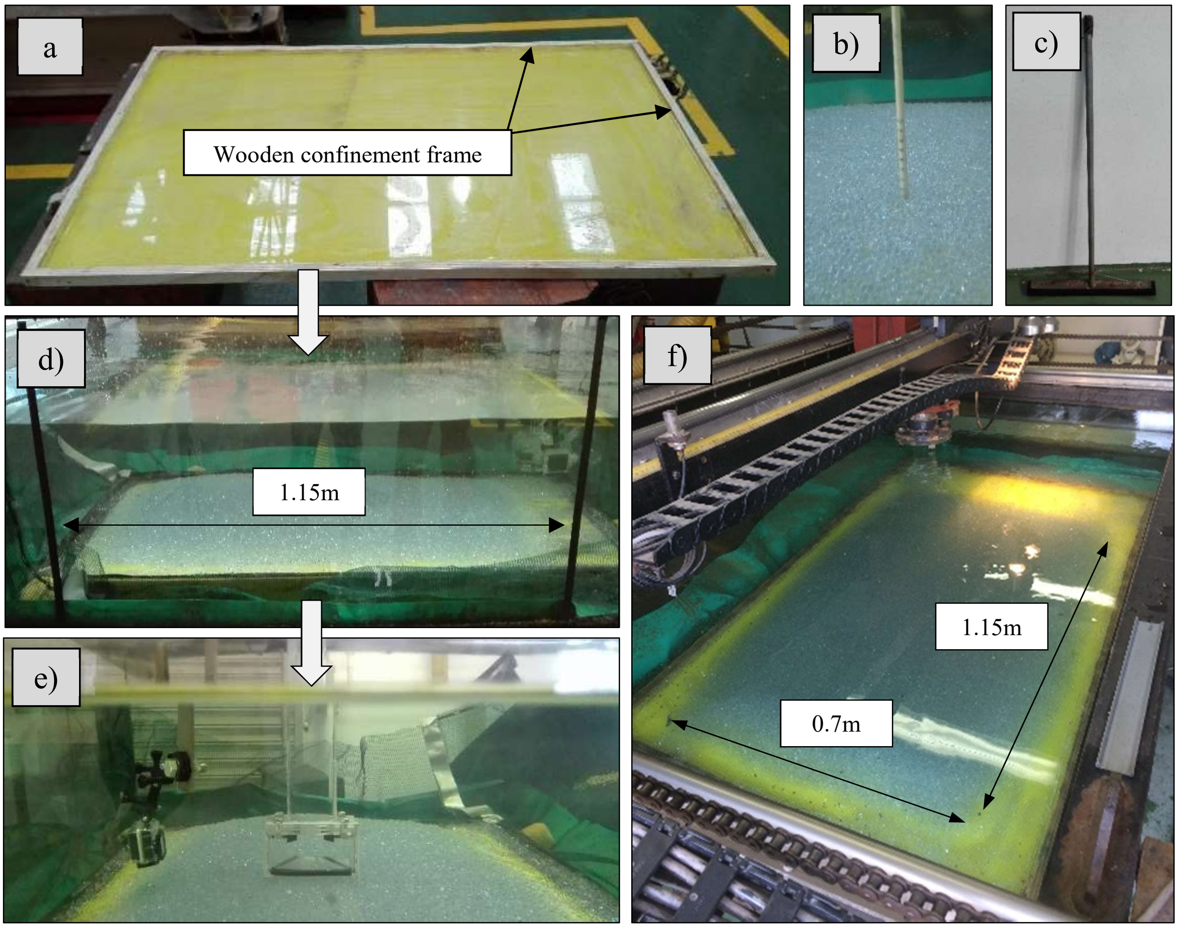

a) Confinement frame for particle stabilisation
b) Preliminary measurement of bed height
c) Rake used for initial levelling of bed
d) Initial levelling and positioning of bed
e) Final levelling using Nozzle
f) Final Setup

*Note: Other than step a), the process was repeated for each configuration

Figure 8-1: Seabed preparation procedure comprising of GB6

Interlocking of the bottom layer allowed for the packing of subsequent glass bead layers to thereon increase the overall depth of the tested seabed. It is worth mentioning that during the setup, the glass bead's natural angle of repose would form. Therefore, in the sequence of testing when a channel of material was collected, the partial absence of material around the boundary of the prepared seabed would have an influence on the measured output. By maintaining consistency, ensuring each test was carried out under identical circumstances and constraints, the side effects induced were contained or deemed negligible. It can be said that the bed was in a state of static equilibrium (Knight, 2008).

Multiple lattice arrangements exist for the packing of equal sized spheres. The greatest lattice packing density was proven to be $\pi/(18)^{1/2} = 0.74$ by Gauss as discussed in Brass, Moser, and Pach (2005). Achieving the maximum density is rarely possible, as it requires a defined lattice formation. For the loose packing of spherical particles, the packing density was approximated. Determination of the prepared bed's porosity, n, was dependent on the bulk density, ρ_b, and particle density, ρ. Much of this information was extrapolated from Appendix F. The porosity, n, for the 6mm glass beads was calculated to be:

$$n = 1 - \frac{\rho_b}{\rho} \tag{8-1}$$

$$n = 1 - \frac{1485\text{kg/m}^3}{2540\text{kg/m}^3}$$

$$n = 0.42$$

Therefore, a packing density (1-n) of 0.58 was determined for the glass beads. The value was found to be in accordance with validated packing ratios computed by Shi & Zhang (2008) for the loose packing of equal spheres. No compaction was involved in the preparation of the seabed. Thus, it was assumed that the random packing arrangement of the particles would be loose. Further assumptions were made on the consistency of the packing arrangements where it was assumed that the packing would be consistent due to the nature of the beads and the systematic approach taken.

Apart from the packing of the beads, another aspect of interest was the desired bed height of the experiment. Janssen (1895) stated in his study that granular flow within a hopper was independent of the height (H) of the retained material when $H > 2D_o$. Although different in setup, the logic of that experiment was comparable to that of the experiment conducted. The height of the prepared bed was not confined by walls or physical boundaries thus the limitation of $H > 2D_o$ did not apply for this case as it did for Garcimartín et al. (2009) and Mankoc et al. (2007). As long as the orifice was adequately submerged within the bed, the effect of bed depth, H, was negligible. Theoretically, the process was compared to horizontal coring methods used for site investigations, assuming that the total core recovery of a sample was independent of soil height (Brook, 2013; Cunningham et al., 2013).

To avoid friction effects between the nozzle and working platform (footwall), an effective depth, *d,* was used, raising the nozzle (*H-d*) above the footwall. Through preliminary experiments, an effective depth, *d,* of 45mm was selected for a 60mm diameter orifice. $d \geq$ 45mm was found to yield consistent results provided that the granular flow rate, *W,* was less than the covering rate of the nozzle. The covering rate refers to the mass of volume covered by the nozzle face with respect to time. Even though the orifice had a greater height than the bed, the effect of bulging caused the face to be fully covered. The converging of "mass collected" with respect to bed height was illustrated in Figure 8-2. The method used in this verification, followed the testing methodology covered in the next section.

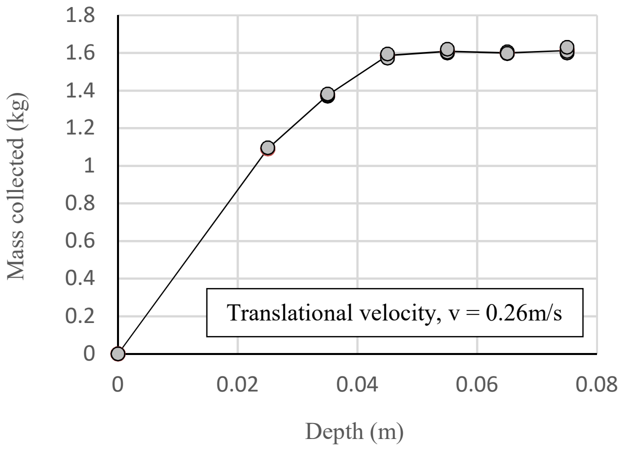

Effective depth, d (mm)	**Mass collected (kg)**
25	1.092
35	1.376
45	1.587
55	1.609
65	1.601
75	1.614

Figure 8-2: Influence of bed height for largest diameter orifice (60mm)

Granular soils exhibit certain properties which can become complex when not properly accommodated for. They are found in various shapes, sizes and compositions, making the approximation of entrainment rate of such a material through a formulated expression such as the Beverloo law a challenging task. To mimic the variability of common soils, a less complex composition consisting of two particle sizes was also tested, implementing both GB6 and GB16. A 50/50 mixture was used and was only accounted for after the primary tests. The use of GB aimed to theorise the problem to be investigated as the consistency amongst properties eliminated variability issues.

8.4 Physical Testing Procedure

This chapter entailed the general procedure undertaken for both MMS (without suction) and MSS (with suction). Each test began with the preparation of the seabed but was then followed by differences within the entrainment system used. The MSS consisted of a pump and gravel box system, whereas the MMS was facilitated by the linear movement of the nozzle and attached collection net.

8.4.1 Mechanical Movement Testing

The purpose of using mechanical entrainment was to analyse the effect of inertia and provide one of several platforms where such a scenario may be applicable. The diagram below shows the general procedure undertaken for such a case.

Step 1: Preparation of Bed

The first step began with the preparation of the seabed within the visualisation tank.

Step 2: Attachment of Nozzle

Primary nozzle system attached to bogey system along with collection-net and flange.

Step 3: Positioning and Velocity Adjustment

Movement speed of tool adjusted on orange control box followed by positioning tool at desired start point. For each setup, three iterative tests were conducted.

Step 4: Monitoring Device

Go-Pro Hero 3 attached to bogey unit through connection flange. Desired view achieved using different swivel links.

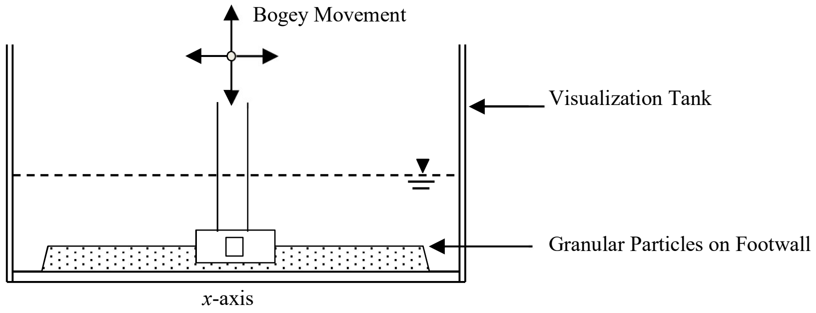

Step 5: Start Test

Testing commenced once all preparations were set. Joystick initialised testing and was stopped through Inductive Limit Switches

Step 6: Material Retrieval

Material retrieved through collection net. Mass measured and recorded

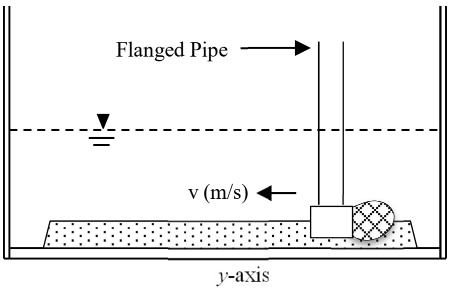

Figure 8-3: System without suction testing procedure

8.4.2 Mechanical Movement Testing with Suction

By following similar steps to the procedure above, the MSS tests gave rise to an added platform. The effects of suction could be observed and measured through the transparent bogey unit attachments and gravel box respectively. The desired suction rate was determined following the settling velocity of the beads, calculated using Equation (3-15), and an adequate amount of flow to prevent a build-up of particles within the nozzle.

Step 1: Preparation of Bed

Similarly, the first step began with the preparation of the seabed.

Step 2: Attachment of Nozzle

Same nozzle used in MMS testing was used, however, instead of a collection net the back face was closed off.

Step 3: Positioning and Velocity Adjustment

Positioning and movement of nozzle identical to MMS tests.

Step 4: Pump Setup

Required suction rate in l/s, was controlled through VSD.Collection process initialised once pump reached desired suction capacity

Step 5: Monitoring Device

GoPro reoriented to capture visual suction phenomena within pipe. Bulge height formation not as prominent, therefore not recorded.

Step 7: Start Test

When pump reached required flow rate, testing commenced along with control of joystick. Pump stopped once nozzle reached end of tank.

Step 8: Material Retrieval

Material collected in gravel box then dumped into collection box via dump valve. Total mass entrained measured and recorded.

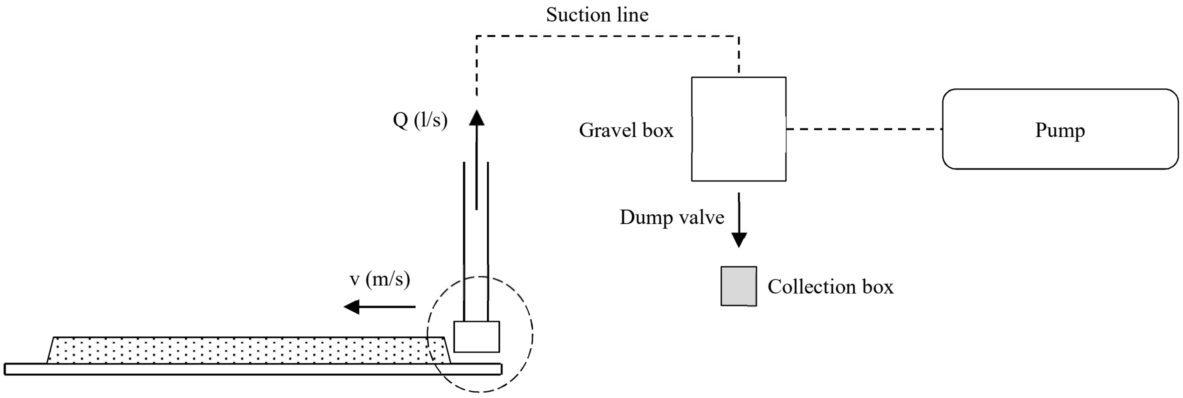

Figure 8-4: Mechanical and suction testing procedure

8.5 Laboratory Tests Conducted

The parameters of interest, as determined by Nedderman et al (1982), were aspects near the interface of the orifice. They include: a) orifice dimensions, b) entrained material properties, c) entrainment velocity and d) suction velocity. In addition to this, parameters such as the e) granular bed height and f) bulge height were also taken into consideration. This section details the total number of tests conducted with regards to the various parameter combinations.

8.5.1 Testing Breakdown

Tests were executed through two main systems: a) Mechanical Movement System without suction (MMS) and b) Mechanical Movement and Suction System (MSS). The MMS comprised the collection of particles through the use of a mechanical bogey unit which subjected the nozzle to a constant translational velocity. In addition to the MMS configuration, the effects of suction were also included, thus forming the MSS configuration. For these two categories, the set of tested variable combinations were configured to be identical. This allowed the effects of suction to be evaluated alone, with respect to its influence and behaviour. The orifice size, D_o, and dimensions of the entrained particle, d_p, were further analysed to evaluate their influence on the results. The relation between these two parameters, was best described by the ratio, $R = (D_o/d_p)$, covered in Janssen (1895), Mankoc et al. (2007) and Nedderman et al. (1982).

Four different orifice sizes, four translational velocities, two different particle diameters and two different systems were used. The combination of the different parameters, dictated the total number of tests carried out, summarised as follows (note: this excludes secondary tests):

Table 8-1: Testing matrices for primary tests

a) Each different combination consisted of three iterations

		Orifice Diameter, D_o (mm)				
		30	**40**	**50**	**60**	
Velocity (m/s)	**0.104**	3	3	3	3	12
	0.156	3	3	3	3	12
	0.208	3	3	3	3	12
	0.26	3	3	3	3	12
		12	12	12	12	**48**

b) Each test highlighted above was test conducted using either 6mm or 16mm beads

Orifice Diameter, D_o (mm)

		30	40	50	60	
Bead size (mm)	**6**	12	12	12	12	48
	16	12	12	12	12	48
		24	24	24	24	**96**

c) From a) and b), each test was conducted using suction (MSS) or without suction (MMS).

Orifice Diameter, D_o (mm)

		30	40	50	60	
System	**MMS**	24	24	24	24	96
	MSS	24	24	24	24	96
		48	48	48	48	**192**

A total of 192 tests were conducted, 96 tests per system (MMS or MSS), where a minimum of three iterative tests were carried out. Through this, an average value could be computed per combination of variables, thus increasing the overall accuracy of the readings by minimising obscurities due to practical errors (refer to Appendix I).

Apart from the primary tests, secondary tests were carried out to provide insight into other parameters of interest. The tests included a nozzle containing multiple orifices, changes in bed height and a 50/50 material mixture. Testing of these additional factors was not as rigorous as the main tests. However, it aided in identifying future studies of similar fields for recommendation. This amounted to a further 135 tests, bringing the total to 327 tests, summarized in Appendix B.

8.5.2 Testing Considerations

The practical aspect of this research comes with quantitative uncertainties that must be addressed to avoid errors in results. These aspects were found to be the following:

a) Uncertainties within technical equipment

Amongst the automated tools the positive displacement pump and mass scale were deemed to be the most vulnerable devices to uncertainties. The pump and scale although calibrated before testing yielded a negligible degree of error covered in Appendix I.

b) End effects

The movement of the nozzle was controlled by a high-powered motor. During the passing of the nozzle through the bed, the velocity remained constant. At the end of the run, the nozzle came to an abrupt stop. Due to inertia, particles that were most recently entrained through the aperture were forced back out.

c) Jamming of particles and flow limitations

The jamming phenomenon occurred when particles reached a state of equilibrium such that they were void of movement through the aperture. Similar to gravity induced particle flow, the occurrence of jamming happens as a direct result from the ratio between the orifice diameter and particle size.

d) Granular bed preparation

A clear disadvantage of the physical experiments was the inconsistency incurred during granular bed preparations. A numerical model was able to marginalise these inconsistencies thus paving the way for outputs with less associated uncertainties.

The acquired results were susceptible to errors induced by these sources. To effectively address them, the subsequent measures were taken:

Fluctuating uncertainties present in most of the aspects highlighted above (a - c), were accounted for through a normalisation method. Iterative tests were performed for each new configuration. The jamming of particles was considered to be an area of interest. Although the exact circumstances under which jamming occurred was difficult to identify, it justified further investigation.

Summary: Part II

The experimental tests conducted were extensive and covered a broad range of investigated parameters deemed relevant to the study. The following is a summary of the physical test methodology for the MMS and MSS:

- A total of 192 primary tests and 135 secondary tests were carried out on the spherical glass beads. The two different sized beads (GB6 and GB16) were prepared using an identical procedure, with the intention of achieving identical packing ratios between samples
- The MMS incorporated only the translational movement of the nozzle as the main means of collection. The MSS incorporated both the translational movement and the effect of suction with a positive displacement pump
- Materials were either collected through the collection net for the MMS or with the gravel box for the MSS. The collected samples were weighed and recorded
- The design flow rate of the pump was based on the settling velocity of the particles and their susceptibility to jamming.

The design of the nozzle focussed on the size of the orifice and particles. The face was to be large enough such that boundary effects would have a negligible effect but small enough such that the forces induced on the face would be kept to a minimum. Four orifice sizes were used D_o = [30; 40; 50; 60mm] along with two different particle sizes, d_p = [6; 16mm].

PART III

Numerical Testing

Contents

Chapter 9 – Assembly of Rocky DEM Model
Chapter 9 described the detailed process of performing a numerical analysis on the physical tests. The chapter encompassed the definition of the geometries, selection of materials and dynamic inputs.

Chapter 10 – DEM Model Calibration
The process of calibrating the model used for analysis, was discussed in this Chapter, highlighting the attuned parameters and the targeted specifications.

9. Assembly of Rocky DEM Model

9.1 Introduction

Discrete Element Method (DEM) was selected as the primary choice of numerical testing. The method itself contained advantages within its computational capabilities and was well suited towards the investigated system where hundreds of thousands of particles were present. This chapter detailed the use of Rocky DEM and the input parameters needed to assemble the moving nozzle model. Rocky DEM, henceforth referred to as "Rocky", is a numerical software package developed for the analysis of devices and systems used to transport granular materials in mining and processing industries. Such systems include conveyor belts, crushers, vibrating screens and transfer chutes amongst others. The underlying characteristic of most benefit from using Rocky was its capability of simulating the motion and interactions of every solid particle within any given system (ESSS, GDI & RDI, 2015).

The 3D numerical DEM model of the physical system shall henceforth be referred to as the "Model". The input parameters needed to fully assemble the model were detailed in this chapter. The various properties of the model were divided into three sections:

a) Definition of geometries: The selected size and shape of the orifice along with the dimensions of the nozzle body, connection flange, working platform and particles.
b) Selection of material properties: The density, friction and stiffness properties of the materials used in the model were specified.
c) Dynamic considerations: The movement of the nozzle along the working platform, as well as the input of particles into the model, were defined.

DEM parameters that were not specified in this chapter were set to default values according to the Rocky software (ESSS, GDI & RDI, 2015). The outputs obtained from the physical tests were integrated into Rocky, to form a fully calibrated model. Appendix C details the full Rocky design procedure performed.

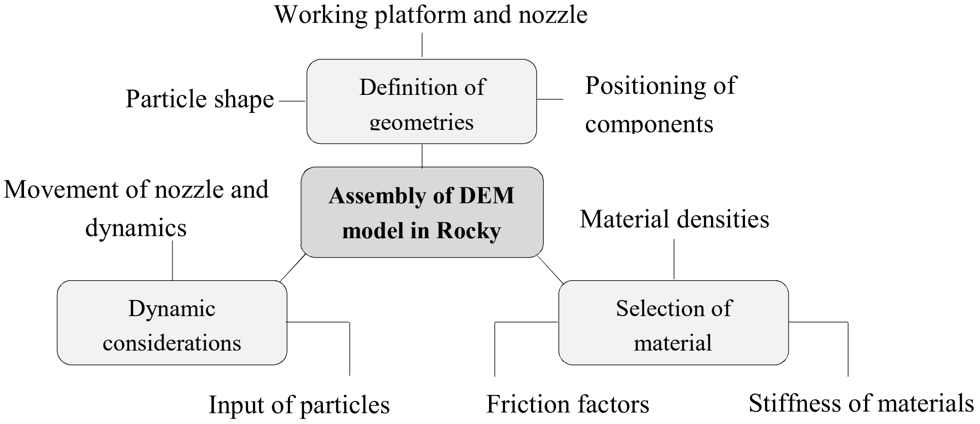

Figure 9-1: Components of the DEM model assembly
Modified from Wegener (2015)

9.2 Definition of Geometries

9.2.1 Working Platform, Nozzle and Flange Connection

The working platform, nozzle and flange connection were modelled as three separate solid 3D objects. The dimensions of these parts used in Rocky were the same as their real-life geometry. All structural components were drawn in AutoCAD 3D and then imported into Rocky in the required format. The nozzle itself was imported into Rocky several times as the different orifice sizes on the face were investigated. A 3D Cartesian coordinate system was adopted in both Rocky and CAD, where Z was the vertical axis, and X and Y the horizontal axes. This assisted in positioning and orientating the components in Rocky according to their coordinates transcribed in CAD.

If the initial position of the components involved were not correct, the coordinates could be modified manually on Rocky. The granular bed was fixed at a constant depth H = 60mm, whereas the intercepting depth or effective depth, d, of the nozzle, was set at 45mm. These depths were allocated before the start of each simulation. Other dynamics parts included the flange and collection box. The only fixed object was the working platform.

The platform was considered to represent the boundary of the model in the X, Y and Z planes. Its position in the coordinate system was arbitrary in that it was not confined or dependent on any other component. In contrast, the nozzle and flange were allocated positions based on the platform. For this exercise, the visualisation tank was not modelled for DEM as it had a negligible impact on the entities within the platform boundary. The detailed hardened Plexiglas platform with the specially designed entrainment system was illustrated as given:

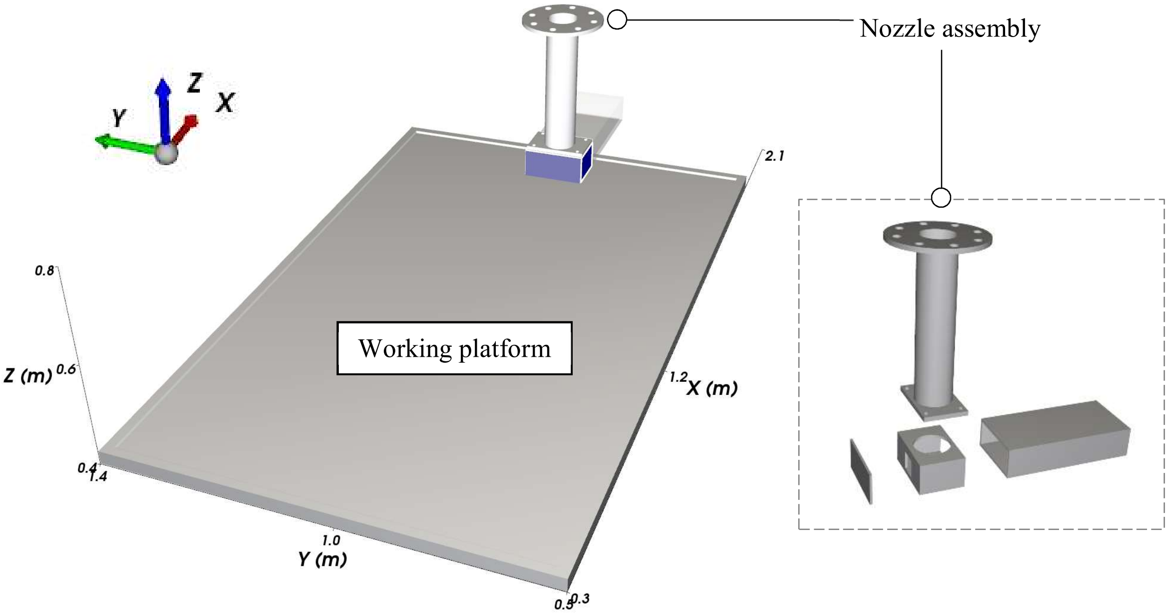

Figure 9-2: Rocky DEM 3D Setup

9.2.2 Particle Shape

The theoretical approach to the investigation brought forth the need to simulate simple particle shapes. Simples spheres of uniform size were selected as opposed to complex rounded polyhedrons (Figure 9-3). An added advantage of this choice was that it resulted in reduced simulation times.

Figure 9-3: Simulated particle shape
Source: ESSS et al. (2015)

The various parameters that defined the shape and behaviour of the particle are described in Table 9-1. The recommended ranges given were used to further calibrate the model.

Table 9-1: Input parameters used to define particle shapes in Rocky
Source: ESSS et al. (2015)

Parameter	Description	Recommended Range
Particle shape	General shape classification.	Spherical
Rolling resistance	Coefficient that described how particles roll on a surface. High values increase rolling resistance.	0.00 – 1.00
Vertical aspect ratio (VAR)	Adjusts the height (Z value) of a particle	0.70 – 2.70 (assume X and Y = 1)
Horizontal aspect ratio (HAR)	Adjusts the width and breadth (X and Y value) of a particle	0.70 – 2.70 (assume Z = 1)
Smoothness	Dictates how smooth or rough the edges of a particle are. Higher the value, smoother the edges	0.10 – 1.00

The shape of a particle has a drastic effect on the run-time of a simulation. Rocky offers five shape categories, these include (in ascending order of computational time): a) spheres, b) rounded cylinders, c) rounded polygons, d) rounded polyhedrons and e) faceted. The other parameters of VAR, HAR and rolling resistance have a significantly lessor impact on the computational requirements. The values for these parameters were chosen using the suggested values in the Rocky user manual (ESSS, GDI & RDI, 2015)

9.3 Selection of Materials

9.3.1 Material Densities

The components in the tank, apart from the platform, were constructed out of Plexiglas. The physical and chemical properties of the materials used were summarised in Appendix F along with the properties of GB6. It was assumed that GB16 would hold similar properties to its GB6 counterpart. Therefore, the Rocky material selection process was made identical to both.

Relevant data was extracted from the material data sheets (Appendix F) and served as input parameters for the Rocky model. The material density, ρ_s, for Plexiglas and soda lime GB were 1190kg/m^3 and 2540 kg/m^3 respectively. The particles in Rocky were defined individually and not as a bulk mass. Furthermore, one had to consider that the granular composition modelled in Rocky was dry as water could not be simulated in the analysis. Given that the water density, $\rho_{w,}$ was assumed to be 1000kg/m^3, an average specific gravity G_s, of 2.54 was selected. Since the main medium of testing consisted of water, buoyancy effects needed to be considered. Buoyancy in the numerical model was addressed by subtracting the density of water from the density of the solid particles. The modelled particle density, ρ_{sm}, of the glass beads was as follows:

$$\rho_{sm} = G_s(\rho_w) - \rho_w \tag{9-1}$$

$$\rho_{sm} = 2.540(1000) - 1000$$

$$\rho_{sm} = 1540 \text{ kg/m}^3$$

9.3.2 Stiffness of Materials

Stiffness properties, or Young's Modulus E, were required specifications for all modelled components. The Plexiglas components were assumed to have a stiffness of 3GPa, as stipulated in the certified data sheet. Initially the GB were assigned an E value of 78GPa. However, the modulus of elasticity (stiffness property of material) had a significant effect on the computational time. The interaction and behaviour of the particles were defined by this value, where the higher the stiffness, the greater the computational expense. By making the particles less stiff, a larger time step could be used, thus resulting in a reduction in computational time. However, it has been reported in text, that a low stiffness can significantly alter results (Lommen, Schott & Lodewijks, 2014). Therefore, values prescribed in Lommen, Schott & Lodewijks (2014), ESSS, GDI & RDI (2015) and Wegener (2015) were used (Table 9-2)

Table 9-2: Stiffness of Materials

Material Interaction	Young's Modulus, E (Pa)	
	Preliminary	Final
Glass beads	78×10^9	1×10^7
Perspex	3.3×10^9	3.3×10^9

9.3.3 Friction Factors

The interaction between two materials, amongst other factors, was governed by the friction between them (ESSS, GDI & RDI, 2015). The factors are categorised by either static friction μ_s, or dynamic friction μ_d. These terms are defined as the maximum ratio between the contact tangential force to the normal force, before and during the occurrence of sliding respectively. The factors come in the form of positive coefficients with values less than one. In most cases, $\mu_s > \mu_d$.

Preliminary friction values for the materials involved were selected per recommendations provided by ESSS et al. (2015) and material data sheets in Appendix F. The recommendations served as a guideline for the final parameters selected. Due solely to the particles' simplified shape, particles of low angularity in a bulk granular medium were more prone to inter-particle sliding than complex shapes (Donohue, 2015; Wegener, 2015). To account for the general smoothness of the spherical glass particles, the selected friction coefficients were less than the recommend values as evident in Table 9-3. Due to the nature of glass, it was assumed that the spherical beads were purely frictional with zero adhesion and cohesion.

Table 9-3: Selected friction factors for Rocky model
Source: (ESSS, GDI & RDI, 2015)

Material Interaction	Static Friction		Dynamic Friction	
	Recommended	Final	Recommended	Final
Glass - Glass	0.45	0.35	0.4	0.4
Plexiglas - Glass	0.7	0.65	0.6	0.6
Plexiglas - Plexiglas	0.6	0.6	0.65	0.65

9.4 Dynamic Considerations

The nozzle was to cover a set distance of 1.15m at different speeds for each setup. Taking this into account and the bed preparation time, simulations times, t_s, typically ran between 8 and 15 seconds. The dynamic components included the entire nozzle system and the loading of the granular bed.

9.4.1 Granular Bed Preparation

Bed preparations were facilitated by the particle input function in Rocky. Within this function, different input choices were available, either through a direct inlet opening or through a feed conveyor. The particles entered the simulations under the influence of gravity in the negative Z axis direction through an inlet of specified shape, orientation and position. The granular bed preparation was not the same in all instances. The results produced by the Rocky Software were probabilistic, where two models with identical inputs usually yielded minor variations in results. This variance was caused by the randomisation of the particle orientation and arrangement within the modelled soil mass. The inlet for the model was selected to be rectangular and horizontal with length and breadth dimensions of 1.15 and 0.7m respectively. The dimensions were chosen to match the length and breadth of the test sea bed to produce a model representative of the physical tests carried out. The inlet was situated 0.2m above the modelled platform and discharged particles at a rate of 18.3kg/s for two seconds, a total of **210 141** and **11 082** particles for GB6 and GB16 respectively (detailed calculation in Appendix C: pg 161). This flow rate was calculated based on the effective height of the desired bed, d = 0.045m and the bulk density of the bed. Differences incurred between the physical and numerical model were as follows:

a) The beads used in practice would vary slightly in strength and composition as they were bulk manufactured. In contrast, the simulated versions were consistent throughout.
b) Interactions between particles and surfaces within the simulation were not truly representative of the physical model as water could not be simulated. The effects of buoyancy were however accounted for.
c) The method of particle input was vastly different between the two systems. Rocky utilised the built-in inlet function whereas the physical tests made use of practical and systematic methods of placing and levelling the seabed (e.g. gravel broom and nozzle). Even though this may have altered the packing arrangement of the particles, it was justified through text that the shape of the beads, size of the bed and its natural lattice would produce a consistent packing ratio each time (Furukawa, Imai & Kurashige, 2000; Shi & Zhang, 2008).

9.4.2 Movement of Nozzle

Translational movements at set time intervals were assigned to the different nozzle components. Simulations of these parts had taken place after the bed had been fully prepared, t_s = 4s. An extra two seconds were allowed in addition to the two seconds already assigned to the material inlet process to allow for adequate adjustment time, such that the bed was completely fixed and all the particles were at rest. At t_s = 4s, the inlet cover in-front of the nozzle would displace vertically, exposing the specified opening to the bed. In the same interval, the nozzle would translate in the X axis at set speeds, *v*, ranging from 0.104 – 0.260m/s, simulating the speeds implemented in the practical tests. Using the dimensions of the prepared bed, the dynamic system would have to cover 1.15m. With varying speeds, the simulation time, t_s, for a particular test was as follows:

Table 9-4: Simulation times as a function of velocity

Velocity, v (m/s)	**Simulation time, t_s** (s)	**Total simulation time, t_f** t_s+4s: (s)
0.104	11.06	15.06
0.156	7.37	11.37
0.208	5.53	9.53
0.260	4.42	8.42

Rocky was not equipped to simulate the movement and properties of fluid. As a result, the MSS could not be accounted for. The analysis through Rocky was based entirely on the MMS which was broken up into three stages: a) lifting of the inlet cover, b) lateral movement of nozzle and c) simulation end time. In Figure 9-4, the different stages were visualised through a typical simulation run where the translational velocity, v = 0.260m/s.

It was highlighted in the physical tests that the materials passing through the nozzle were collected using a collection net. The net itself was determined to have a negligible effect on the materials entering the nozzle. Therefore, in the numerical system, the net was modelled as a rectangular box with low frictional properties (Figure 9-4).

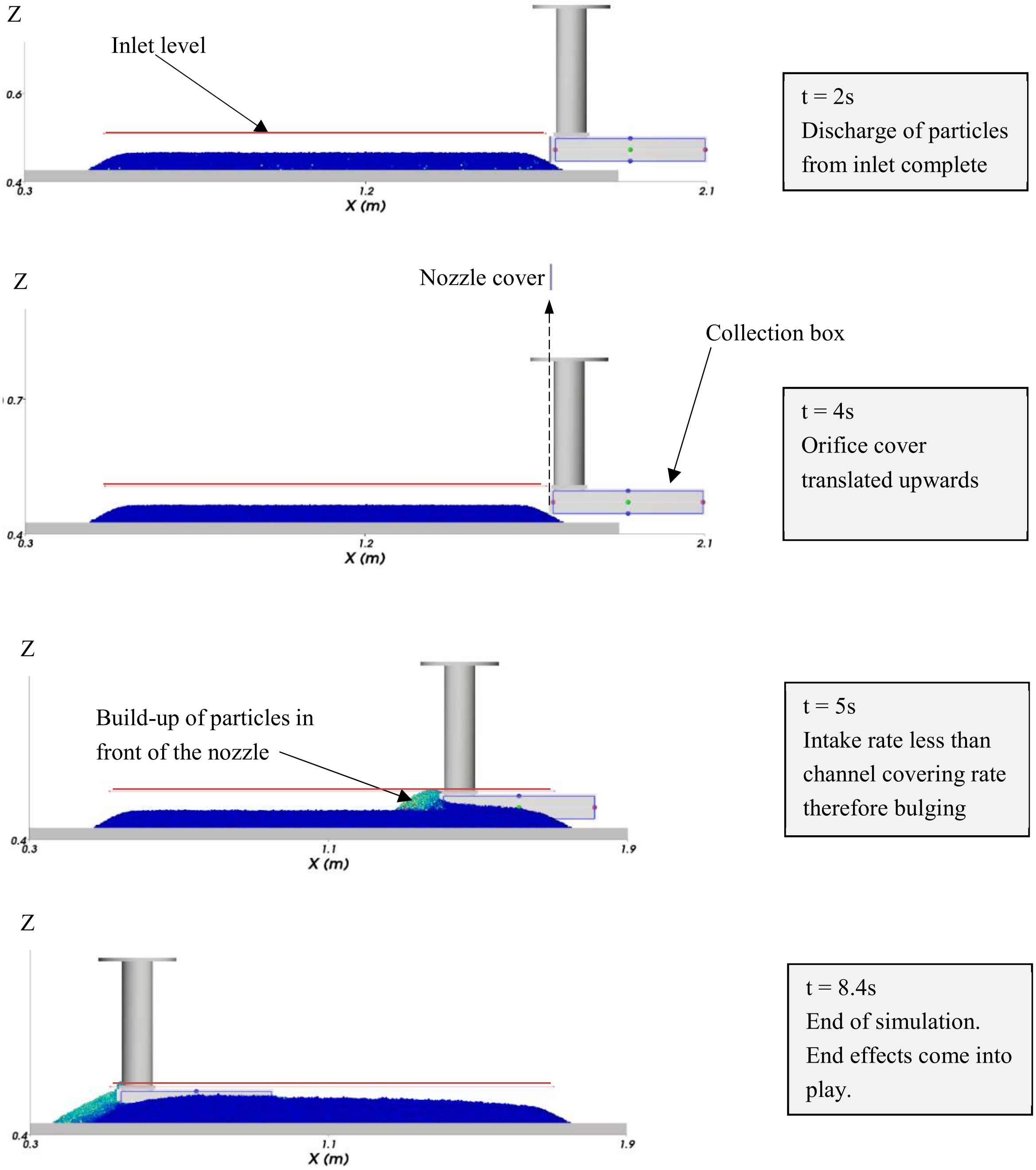

t = 2s
Discharge of particles from inlet complete

t = 4s
Orifice cover translated upwards

t = 5s
Intake rate less than channel covering rate therefore bulging

t = 8.4s
End of simulation.
End effects come into play.

Figure 9-4: Phases of Rocky simulation under default parameters

Running identical simulations to the one illustrated above with identical input parameters, would yield consistent results with minor variances. During the preliminary DEM analysis, fully detailed in Appendix C, it was expected that multiple simulations of the same model would produce results of limited variation. This was confirmed by the statistical analysis performed by Wegener (2015) on the Rocky DEM Software. The researcher performed multiple simulations of the same model, on a vibrocore sampling system, and compared the results using a two sample Kolmogorov-Smirnov method.

10. DEM Model Calibration

With reference to recent studies by Coetzee (2017), a bulk calibration process was undertaken. The approach did not necessarily assume a strong link between the physical material properties and the DEM parameters, but treated them as adjustment parameters. The approach was summarised as follows (Coetzee, 2017):

1. Laboratory experiments were performed to measure the geometric properties of the model and the bulk properties of the specific material.
2. The experiment was then replicated numerically.
3. Through an iterative process, the DEM parameter values were adjusted until the predicted bulk response matched the measured output.
4. The output could be influenced by several parameters such that no unique solution existed. More than one combination of the DEM parameters could be used to obtain identical behaviours.
5. Therefore, there was no guarantee that once the model had been calibrated for one application it would be accurate for another.

As a certain value of uncertainty was associated with the measured outputs, it was reasonable to converge the calibration towards a value within that bracket of uncertainty. The physical geometric properties of the parts involved were all measured to create a template within Rocky. Highlighting the physical boundaries, the parts involved were assigned material properties which were sourced from either certified specification sheets or computed data derived from laboratory tests.

Due to a lack of sensory equipment in the physical tests, the mass output alone was not sufficient in determining the flow behaviour of the materials. Yet, by calibrating a numerical model based on outputs at different time intervals, the granular flow behaviour within the system could be understood as shown in the overlaying curve below (Starting point at A, end point at D). The values used were found in Table 10-1, along with a plotted band of uncertainty encompassing valid values for a 95% confidence interval in Figure 10-1. The main parameters adjusted in Rocky to achieve the desired outputs included the frictional coefficients and rolling resistance.

As earlier stated, Rocky was not capable of simulating the effects of water (hydraulic transport), thus the displayed curves were limited to the MMS. This proved sufficient as the granular flow behaviour could be fully interpreted from the graphs used. Furthermore, the calibration approach was identical for both GB6 and GB16, practically this led to the presentation of only GB6.

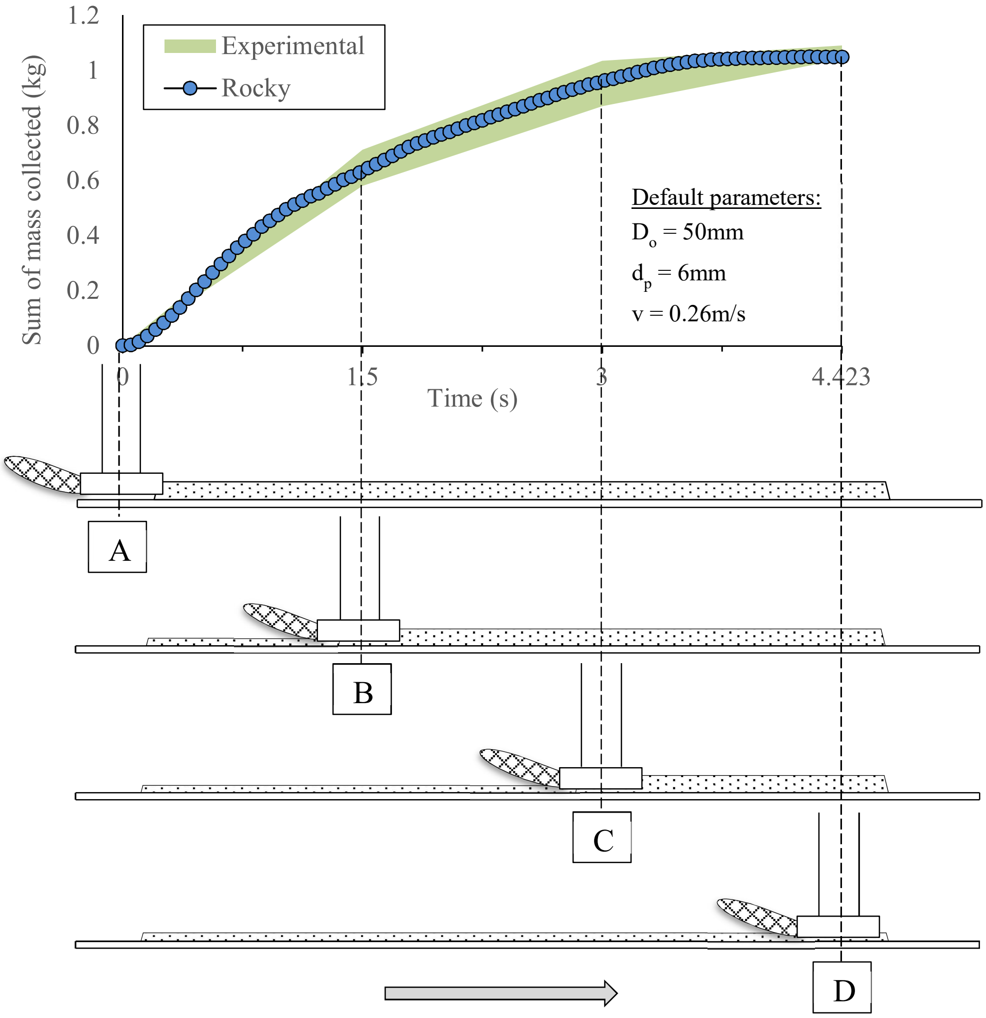

Figure 10-1: Rocky calibration for default case

Relating to Figure 10-1, the measured experimental (average) and Rocky results were compared and tabulated:

Table 10-1: Calibration of measured results with Rocky

Material Interaction	Time, t (s)	Sum of mass collected (kg)		% Δ
		Measured	Rocky	
A	0	0	0	0
B	1.5	0.646	0.645	0.155
C	3	0.952	0.970	1.856
D	4.42	1.055	1.049	0.569

The variance (% difference) between the two sets of data was found to be negligible, this was achieved through the adjustment of frictional properties. The decrease in gradient, evident in the plot, was assumed to be a product of granular material build-up within the nozzle, inhibiting the flow of materials with respect to time. Particles passing through the opening interacted with the Plexiglas nozzle surface, inducing a certain degree of frictional resistance against their movement.

The graph converged to a point or plateau where no further material could pass through. Although the default parameters were used, it was worth further validating this model against the other orifice sizes used, depicted in Figure 10-2:

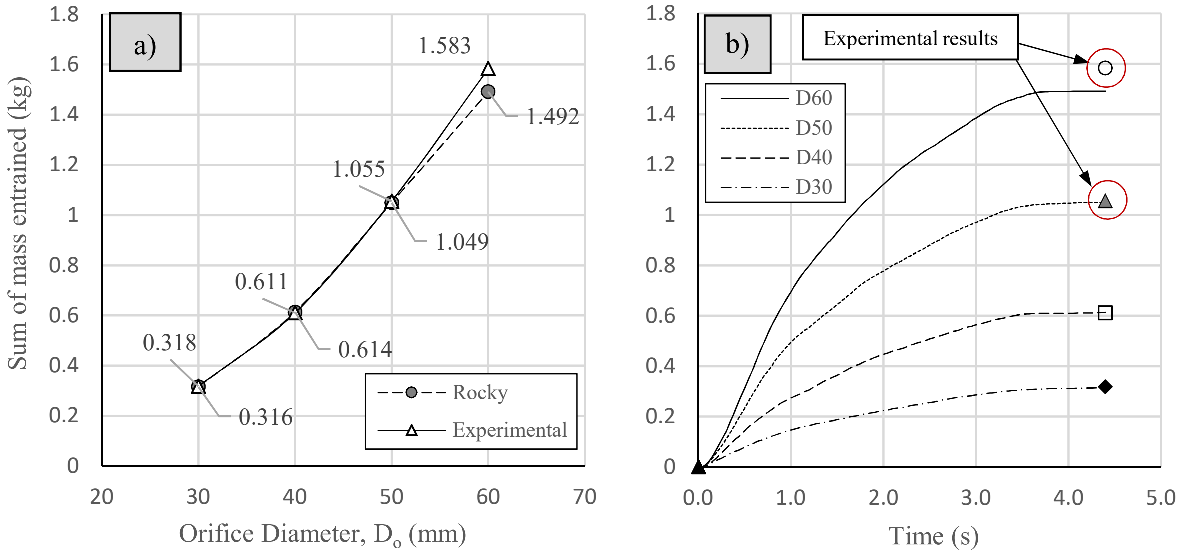

Figure 10-2: a) Calibration of Rocky model with experimental results b) Rocky output: sum of mass entrained with respect to time for other orifice sizes

Figure 10-2 b) illustrated the results corresponding to the various orifice sizes with the calibrated model from Rocky. Along with the tabulated results in Appendix D, the behaviour of the particles was interpreted. Like the default case covered earlier, a decrease in gradient occurred over a certain time interval. For the purpose of analysing the empirical relations covered in literature, the flow behaviour past this point was assumed to be irrelevant. Flow beyond this point indicates build-up of particles or resistance caused by surface friction. Thus, analysing the data in Appendix D, the approximate time at which flow was inhibited could be determined. Under default parameters for GB6 this was found to be when t = 0.75s. The assumed flow behaviour was depicted in Figure 10-3a).

Linear curves of best fit were plotted on top of the modified chart, to attain the behaviour of flow at constant velocity. In addition to this, a regression analysis was implemented. An assumption was made based on Newton’s law of inertia, that the rate of recovery or granular flow would be directly proportional to the constant velocity of the translated nozzle, under a state of dynamic equilibrium (Knight, 2008). Hence the need to justify and analyse flow at a constant velocity (no gradient change in linear plot of mass entrained versus time). One of the downfalls during the experimental tests was the initial commencement effects. Coupled with the increase in acceleration and side effects of the bed (angle of repose), the rate of recovery was not consistent within the initial stage of testing. This was evident in Figure 10-3a), where an increase in gradient is present and the linear fit curves have y-intercepts well below the origin, suggesting constant velocity was only achieved after a certain time interval (t ~ 0.1s).

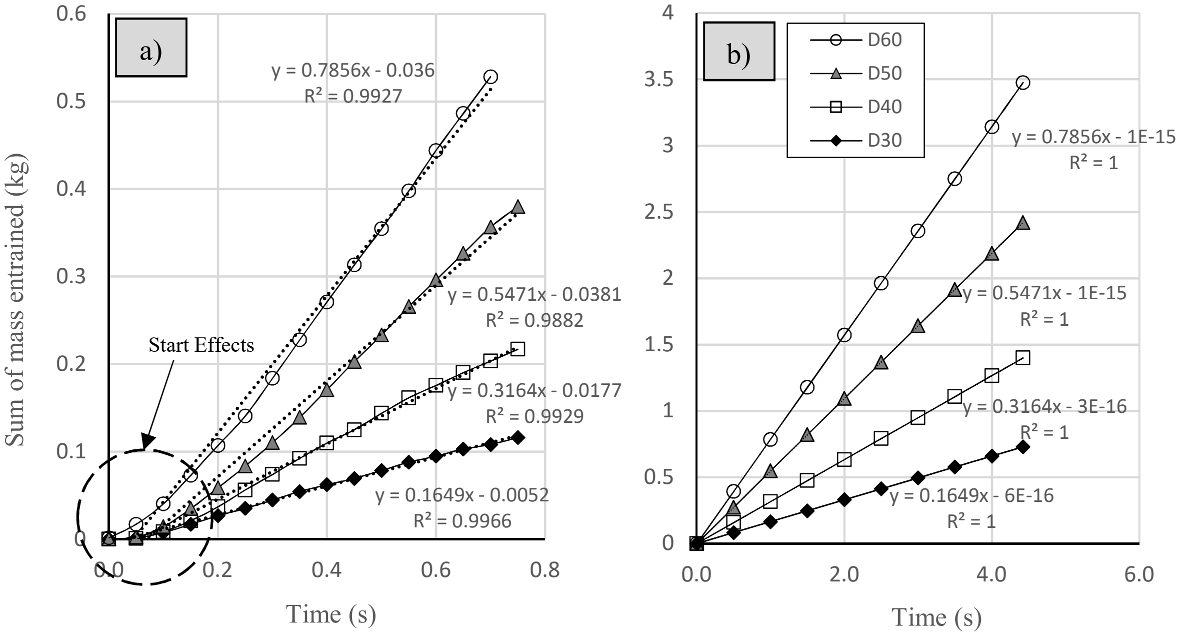

Figure 10-3: a) Rocky chart illustrating constant extraction rate b) Ideal flow rate for full simulation

The constant velocity assumption permitted the effective comparison of already developed empirical relations. Considering this assumption throughout the simulation, including the start (t = 0s) whereby the linear fit curves would intercept the origin, the analysis could be completed (Figure 10-3b). The graphs above were used to predict the intake of particles at specific times within the tests, under the assumption made with minimal initial or end effects. The same process was adopted for other MMS configurations. The modified GB6 and GB16 mass collection rates were projected in Figure 10-4. Note that, like the experimental tests, the simulated tests showed indications of irregular flow within the GB16 setup.

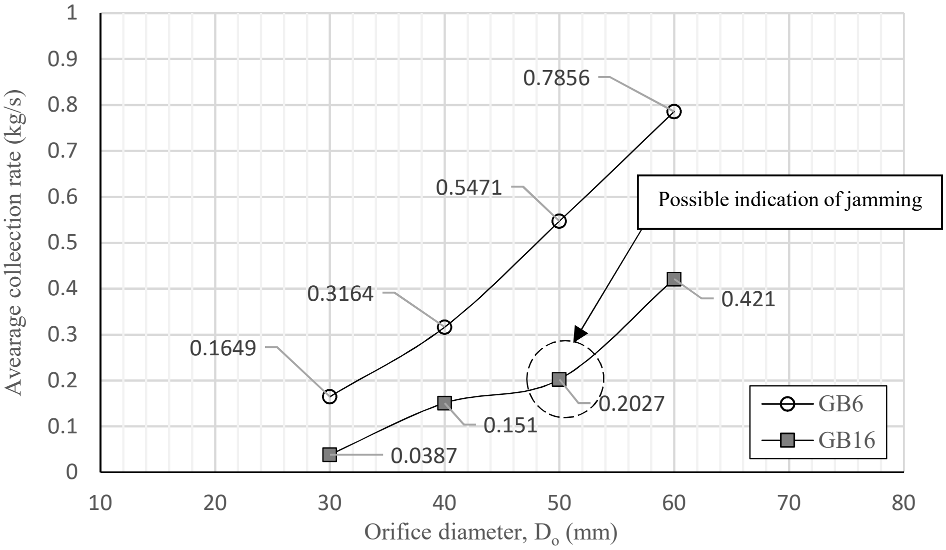

Figure 10-4: Final calibrated graph of experimental results under dynamic equilibrium

Summary: Part III

The assembly of the DEM model aimed to simulate the setup and geometries used in the physical tests. Rocky DEM was the numerical interface of choice and was used to analyse the data in greater detail. The process of setting up the model was summarised as follows:

- Geometric specifications and materials properties were inserted into Rocky. This consisted of dimensions, friction values, densities and stiffness properties.
- The nozzle, flange connection and working platform were modelled to be identical to their counterparts used during physical testing. Movements of these parts were specified in Rocky, assigning the type of movement (translational) and start/stop time within the simulation duration.
- The discharge of materials into the system was done using the inlet function over a specified domain. The packing ratio and discharge rate were further defined.
- The simulation durations ranged between t = 8.42 - 15.06s, depending on the dynamic properties of the nozzle.

The use of DEM was only a part of the overall analysis of the comprehensive tests conducted. Furthermore, the software was limited to MMS tests as the hydraulic transport of particles could not be simulated, although buoyancy effects were taken into account within the density properties of the particles.

PART IV

Analysis and Discussion of Results

Contents

Chapter 11 – Results and Assessments
Results were presented and assessments were made between the physical and numerical tests.

Chapter 12 – Conclusions and Recommendations
Final conclusions and recommendations were drawn according to the measured results, highlighting potential methods for granular flow optimisation.

References
References extending from the literature review to appendices were inserted as a full bibliography.

Appendices
All relevant appendices were attached. Refer to the Appendix table of contents, following the bibliography.

11. Results and Assessments

11.1 Introduction

Through both numerical and experimental tests, a comprehensive analysis over the recorded results was possible. Prior to analysis, a comparative assessment was conducted between the two models. Thus, validating the accuracy of the measured data. The overall assessment looked at the influence of the various parameters tested and their empirical relevance within the system. The principles defined in the Beverloo law assisted in recognising the parameters of potential influence and how they could be manipulated. Other sources of literature were utilised as a means of supporting the observations and conclusions made. To effectively assess the results, a default experimental test (default = fixed set of variables) was referred to throughout this chapter. The default allowed for context and reference to all the elements investigated. The default parameters, unless stated otherwise, were set as follows:

1. Diameter of orifice: $D_o = 50mm$
2. Diameter of particle: $d_p = 6mm$
3. Height of seabed: $d = 45m$
4. Velocity of nozzle: $v = 0.260$ m/s

11.2 Analysis of Results

Rocky served as an extension of the physical tests whereby certain intermediate aspects could not be analysed or distinguished. The two methods of testing (i.e. physical testing and numerical model) were used in unison to derive a good approximation of the behaviour of granular materials passing through an orifice. The analysis consisted of assessments of the mass collection rate, recovery efficiency and overall flow through the system. These parameters were based on the mass outputs collected from point A to point B as shown below (Note that the nozzle illustrations given were for the system without suction, the system with suction would have the nozzle body closed off at the back in place of the net).

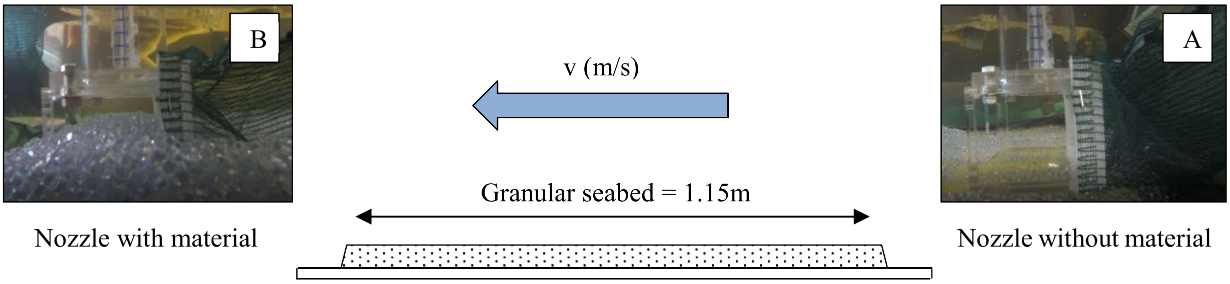

Figure 11-1: Collection of materials from A to B

11.2.1 Mass Collection Rate

Table 11-1 and Table 11-2 summarised the average measured mass and collection rates of particles during MMS tests. The collection rate was calculated by averaging the mass of collected material over the testing period (Fowler & Glastonbury, 1959). Each orifice size depicted as D_o = #(mm) was tested under four different translational velocities. The uncertainty or variability of each measurement was calculated according to the statistical methods covered in Appendix I which included the coefficient of variability and regression coefficient.

Table 11-1: Average mass collected for MMS configuration

Translational velocity (m/s)	**Average Mass Collected (kg)**							
	6mm beads, GB6				**16mm beads, GB16**			
	$D_o = 30$	$D_o = 40$	$D_o = 50$	$D_o = 60$	$D_o = 30$	$D_o = 40$	$D_o = 50$	$D_o = 60$
0.104	0.317	0.607	1.055	1.583	0.205	0.511	0.862	1.298
0.156	0.317	0.610	1.049	1.588	0.200	0.505	0.845	1.300
0.208	0.318	0.609	1.051	1.576	0.157	0.475	0.886	1.287
0.260	0.320	0.617	1.066	1.587	0.177	0.508	0.873	1.295
Average (kg)	0.318	0.611	1.055	1.58	0.180	0.500	0.867	1.300
Error (±kg)	0.010	0.009	0.009	0.010	0.022	0.014	0.021	0.008

Table 11-2: Average collection rate for MMS configuration

Translational velocity (m/s)	**Collection Rate (kg/s)**							
	6mm beads, GB6				**16mm beads, GB16**			
	$D_o = 30$	$D_o = 40$	$D_o = 50$	$D_o = 60$	$D_o = 30$	$D_o = 40$	$D_o = 50$	$D_o = 60$
0.104	0.029	0.055	0.095	0.143	0.019	0.046	0.078	0.117
0.156	0.043	0.083	0.142	0.215	0.027	0.069	0.119	0.176
0.208	0.057	0.110	0.190	0.285	0.028	0.086	0.160	0.233
0.260	0.072	0.139	0.241	0.359	0.040	0.115	0.197	0.293

Table 11-1 shows the average material entrained per setup to be consistent for varying translational velocities (readings per iteration were summarised in Appendix B). The results showed that the coefficient of variability, *C,* ranged from 1-5% and 1-18.5% for GB6 and GB16 respectively. This was defined as the ratio between the standard deviation and average of the data set. The higher variances in GB16 were worth considering. It was speculated that the cause of deviations resulted from jamming effects. This was verified through the normalisation of the results and simulated models later discussed.

The consistency in the GB6 results indicated that adjusting the translational velocity had little to no influence on the total amount of material collected for the MMS, whereby recovery was constant (Figure 11-2a). The same behaviour can be anticipated for the GB16. This further reinforced the hypothesis that although recovery was constant, the rate at which the material was collected was directly proportional to the collection speed or velocity of the passing system (Figure 11-2 c and d). However, this in the interim was only valid for MMS. The graphs of these tables with regards to adjustments in orifice diameter and translational velocity were plotted for ease of comparison.

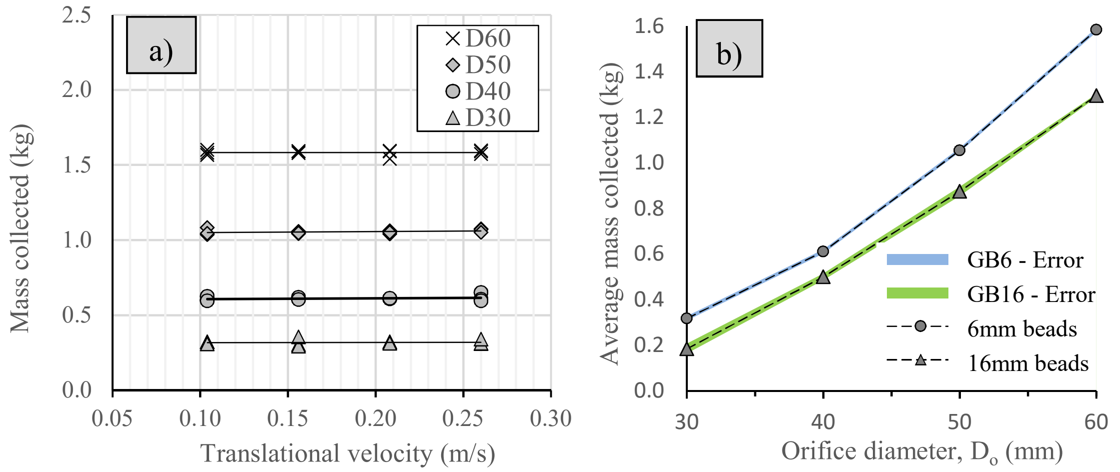

a) Mass collected versus translational velocity for GB6 **b)** Average mass collected for GB6 & GB16

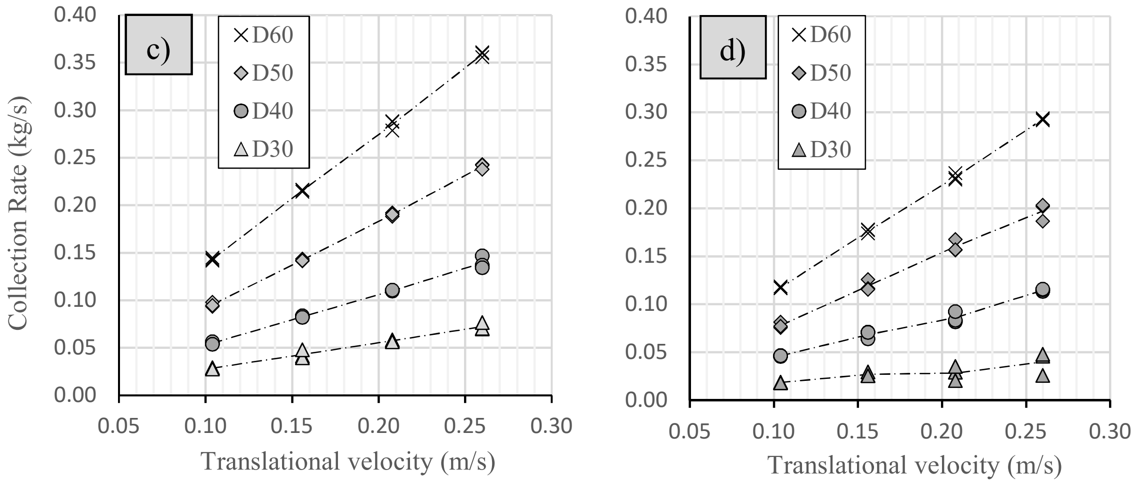

c) Collection rate of GB6 **d)** Collection rate of GB16

Figure 11-2: Graphical interpretation of results

In Figure 11-2b, the shaded bands of uncertainty (GB6-Error &GB16 Error) indicated little variance between the measured mean values in relation to the overall scale of the outputs. However, discrepancies between the GB6 and GB16 were assumed to be attributed to the "empty annulus" theory, defined as the effective diameter given by $(D_o\text{-}kd_p)$ where an increase in particle size led to a decrease in effective diameter (Beverloo, Leniger & van de Velde, 1961; Nedderman et al., 1982). It follows the logic that no beads can pass through an orifice when its centre is separated by less than half its diameter ($d_p/2$) from the orifice border (Garcimartín et al., 2009). Conceptually, this was illustrated as follows:

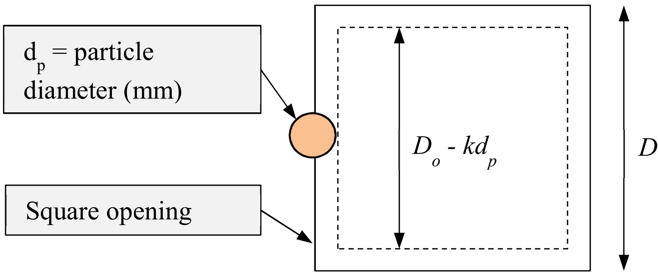

Figure 11-3: Illustrating changes in opening area due to particle diameter

Prior the commencement of the main tests, the bed height was investigated, providing an insight into the effects of lateral earth pressure and its influence on the measured quantity. In Chapter 8.3 it was verified that for a 60mm diameter orifice, bed heights greater than 45mm reproduced similar outputs. As a result, a bed height of 45mm was kept constant throughout all experimental tests. Although, the bed may not have fully covered the orifice it was assumed that due to the area ratio between the opening and nozzle face, a bulging effect would occur. Thus, raising the bed height in front of the nozzle interface and covering the opening during translational movement.

This was further supported by the rate at which the nozzle moved in comparison to the rate which the particles entered through the orifice. Consequently, it is worth mentioning that in the case of MSS tests, changes in bed height had a more pronounced influence on the outputs compared to its MMS counterpart. Its effect was ascertained to be negligible, since MSS tests were performed mainly as a comparative tool for MMS results and less as a subject for empirical analysis. Variances were found to be attributable to forms of efficiency and testing conditions.

Results for the MSS tests were summarised below. As calculated in Appendix H (pg 231), flow rates of 3.21*l*/s (Frequency = 24Hz) and 5.00*l*/s (Frequency = 31.5Hz) for GB6 and GB16 were chosen. The selection was based on the settling velocity and potential crowding of particles.

Table 11-3: Average GB mass collected for MSS configuration

Translational velocity (m/s)	Average Mass Collected (kg)							
	6mm beads, GB6				16mm beads, GB16			
	$D_o = 30$	$D_o = 40$	$D_o = 50$	$D_o = 60$	$D_o = 30$	$D_o = 40$	$D_o = 50$	$D_o = 60$
0.104	8.611	9.661	9.192	8.995	2.899	2.899	9.372	9.451
0.156	6.270	6.918	7.165	6.568	3.434	6.659	6.871	6.949
0.208	4.885	5.855	5.692	5.507	2.853	3.690	5.470	5.776
0.260	4.076	5.208	5.467	5.269	2.312	3.617	5.073	5.187

Table 11-4: Average GB collection rate for MSS configuration

Translational velocity (m/s)	Collection Rate (kg/s)							
	6mm beads, GB6				16mm beads, GB16			
	$D_o = 30$	$D_o = 40$	$D_o = 50$	$D_o = 60$	$D_o = 30$	$D_o = 40$	$D_o = 50$	$D_o = 60$
0.104	0.779	0.874	0.831	0.813	0.262	0.730	0.848	0.855
0.156	0.851	0.938	0.972	0.891	0.466	0.903	0.932	0.943
0.208	0.883	1.059	1.029	0.996	0.516	0.667	0.989	1.045
0.260	0.921	1.178	1.236	1.191	0.523	0.818	1.147	0.293

As summarised in Appendix I, the GB6 particles had an uncertainty that varied from 0.029kg to 0.489kg, and GB16 between 0.040kg and 2.735kg. Greater variances were associated with GB16 due to jamming effects speculated to be caused by the low ratio (R) between the orifice diameter and particle diameter. This was best shown in the visual variability of the results in Figure 11-4b.

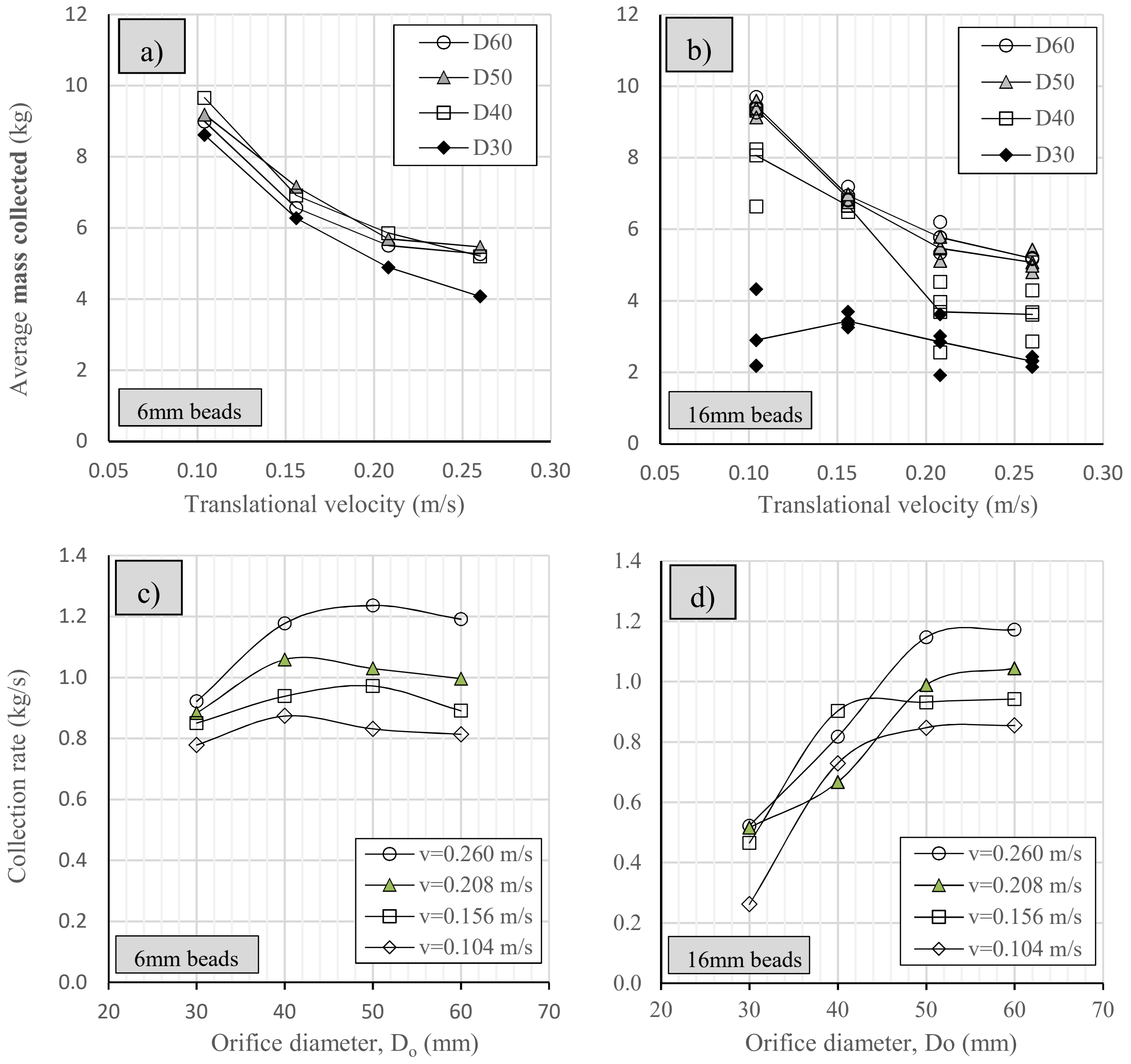

Figure 11-4: Average mass collected versus translational velocity for a) GB6 and b) GB16; and collection rate versus orifice diameter for c) GB6 and d) GB16

Ignoring outliers, the amount of material collected per velocity was concluded to be similar for both bead sizes. However, the accuracy and relations interpreted should be assumed to be a coincidence as the suction velocity for the two setups were non-identical. At this stage, it is worth revisiting the variability amongst the GB16 readings. The highlighted areas in Figure 11-5 indicate the band of uncertainty associated with each orifice size. Areas were found to be more critical for $D_o = 30$ and 40mm.

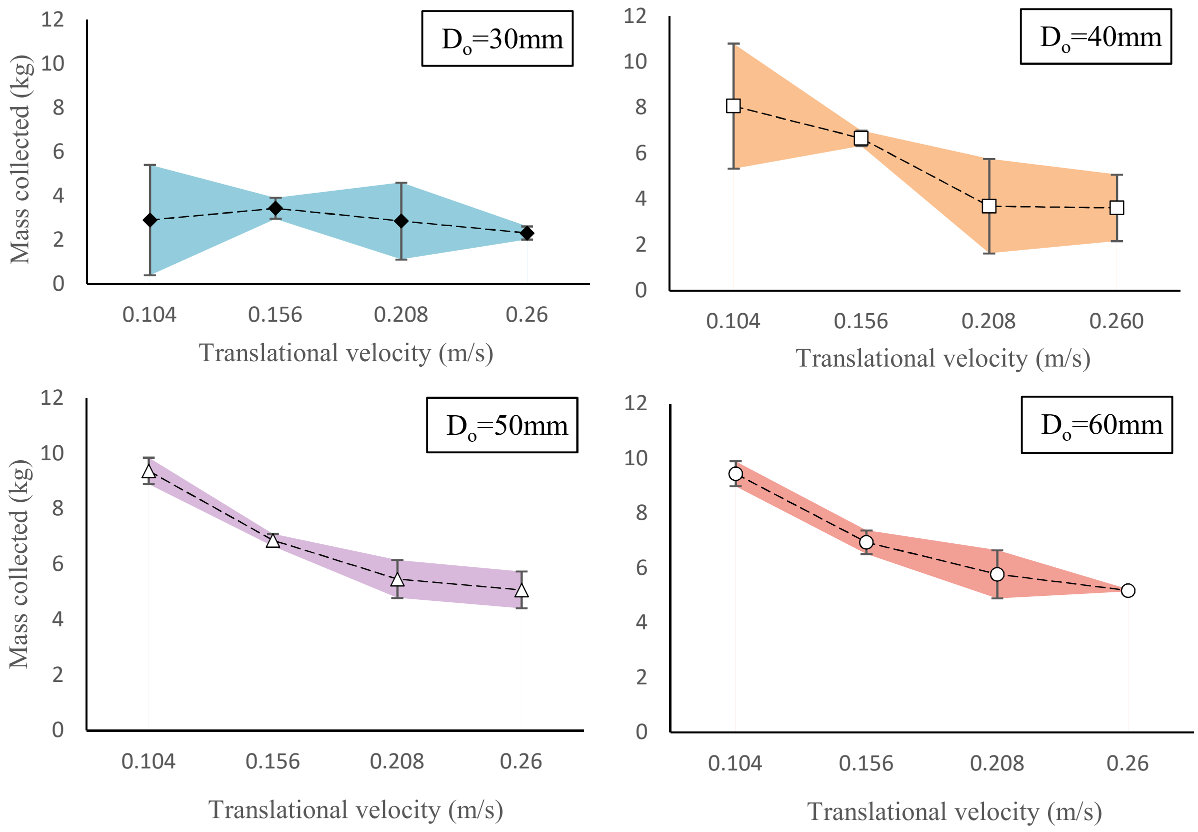

Figure 11-5: Area of variability associated with each orifice size for GB16

Considering the poor representation of results for GB16, caution should be given when utilising them for comparative or design purposes. The introduction of suction had significant effect on the output. For both MMS and MSS, the outputs increased by more than 300% (Based on default parameters for D_o = 50mm and GB6). By increasing the suction velocity, much higher percentages could have been attained.

11.2.2 Recovery Efficiency

The ratio between the volume entrained and volume covered, was an effective indication of the efficiency of the nozzle. The factors that influenced the amount of material collected included the size of the orifice, the translational velocity and the size of the particles. In conjunction with Figure 11-6, the channel and effective recovery ratios for each setup was calculated.

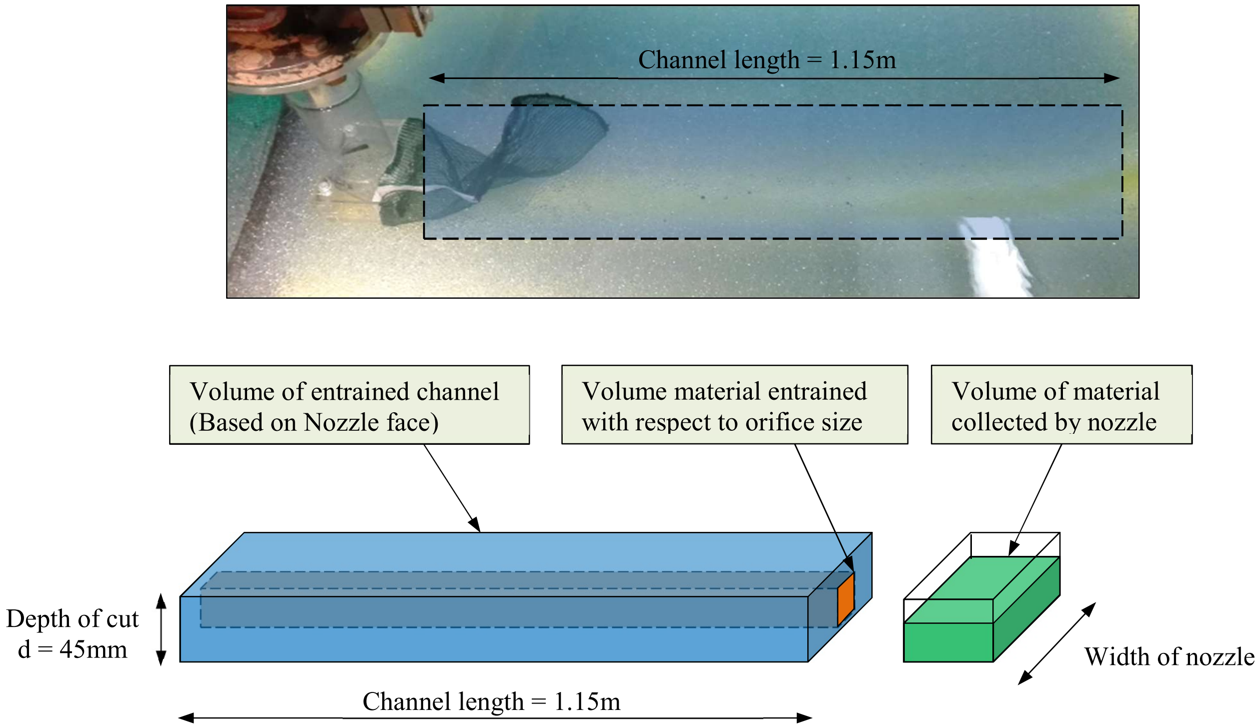

Figure 11-6: a) Elevated view of recovery channel b) front view of entrained nozzle

The effective recovery, using Equation (11-2), indicates the amount of material recovered in relation to the size of the orifice, whereas the normal recovery (Equation (11-1)) refers to the amount collected in relation to the size of the channel covered.

$$\text{Channel Recovery} = \frac{\text{Volume of mass collected (Green volume)}}{\text{Channel volume (Blue volume)}} \tag{11-1}$$

$$\text{Effective Recovery} = \frac{\text{Volume of mass collected (Green volume)}}{\text{Orifice volume (Orange volume)}} \tag{11-2}$$

Mechanically, complete recovery (= 1) was near impossible as it required the orifice to extract materials beyond its prescribed channel. However, under a secondary influence such as suction, complete recovery could be achieved. If the flow rate and corresponding nozzle speed reached a state of dynamic equilibrium (constant mixture flow through orifice) the influence of suction was capable of pulling in material beyond the region covered. Results of recovery were displayed in the plots below. The difference in scale (y-axis) of the two plots demonstrated the importance of including suction for optimal recovery efficiency.

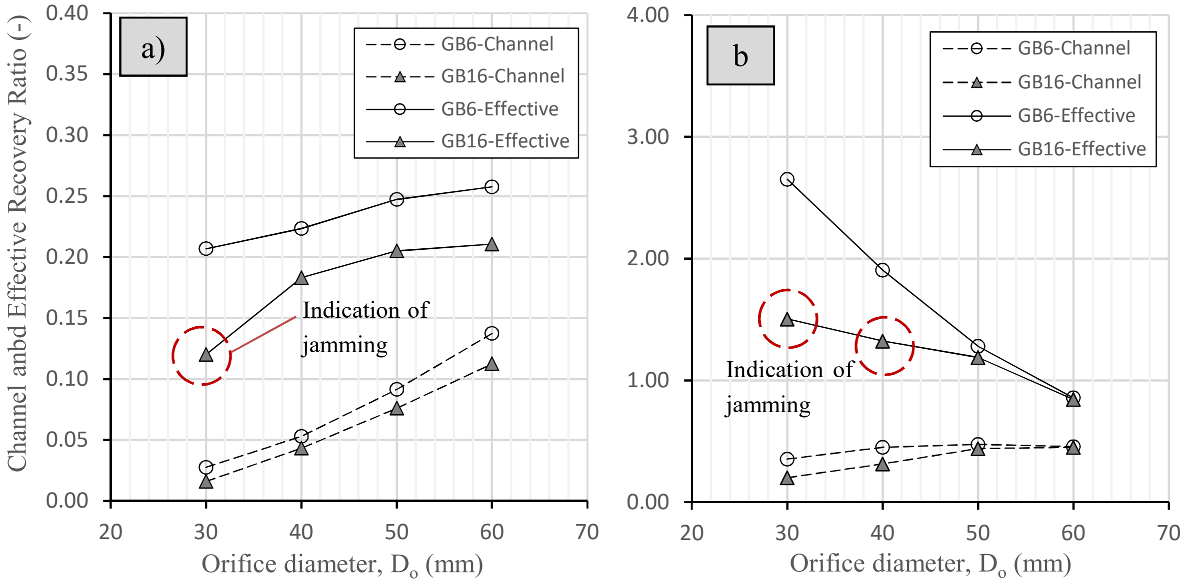

Figure 11-7: a) MMS recovery ratio b) MSS recovery ratio

The difference between GB6 and GB16 was directly related to the mass outputs earlier covered, featuring the introduction of the "empty annulus" effect. Amongst the two graphs, it was evident MSS could recover several times more material than the MMS. Quantitatively, the effective recovery results for the two systems (MMS and MSS) were given in Table 11-5 and Table 11-6, further emphasising the difference in magnitude between the two systems.

Table 11-5: Effective recovery ratio for MMS configuration

Translational velocity (m/s)	Effective Recovery Ratio							
	6mm beads, GB6				16mm beads, GB16			
	$D_o = 30$	$D_o = 40$	$D_o = 50$	$D_o = 60$	$D_o = 30$	$D_o = 40$	$D_o = 50$	$D_o = 60$
0.104	0.206	0.222	0.247	0.257	0.133	0.187	0.202	0.211
0.156	0.206	0.223	0.246	0.258	0.130	0.185	0.206	0.211
0.208	0.207	0.223	0.246	0.256	0.102	0.174	0.208	0.208
0.260	0.208	0.226	0.250	0.258	0.115	0.186	0.204	0.214

Table 11-6: Effective recovery ratio for MSS configuration

Translational velocity (m/s)	Effective Recovery Ratio							
	6mm beads, GB6				16mm beads, GB16			
	$D_o = 30$	$D_o = 40$	$D_o = 50$	$D_o = 60$	1.886	2.952	2.195	1.537
0.104	5.603	3.536	2.153	1.463	2.234	2.437	1.609	1.130
0.156	4.079	2.532	1.678	1.068	1.856	1.350	1.281	0.939
0.208	3.178	2.143	1.333	0.896	1.504	1.324	1.188	0.844
0.260	2.652	1.906	1.281	0.857	1.886	2.952	2.195	1.537

Regarding the channel recovery in the MSS, where the dotted curve started to plateau for larger orifice sizes, values would decrease as changes in orifice size directly affected the magnitude of the fluid velocity through the inlet. The inlet velocities pertaining to each orifice size and corresponding bead size, were summarised as follows (Recall, flow rate for GB6 = 3.21 l/s and GB16 = 5.00 l/s):

Table 11-7: Inlet fluid velocity (m/s)

Orifice diameter, D_o (mm)	**Bead size**	
	6mm (GB6)	**16mm (GB16)**
30	3.57 m/s	5.56 m/s
40	2.01 m/s	3.13 m/s
50	1.29 m/s	2.00 m/s
60	0.89 m/s	1.39 m/s

Therefore, the low effective recovery experienced by the 50mm and 60mm diameter orifices were found to be caused by the decrease in suction velocity. In the MSS, an added parameter of interest within the entire setup, was the mass, C_m, and volumetric, C_v, concentrations of the materials transported through the suction pipe. The average concentrations were calculated for each orifice size under an unchanged translational velocity (v = 0.26m/s). This was accompanied by the appropriate suction velocity. Figure 11-8 illustrates these concentrations along with the relevant expressions used.

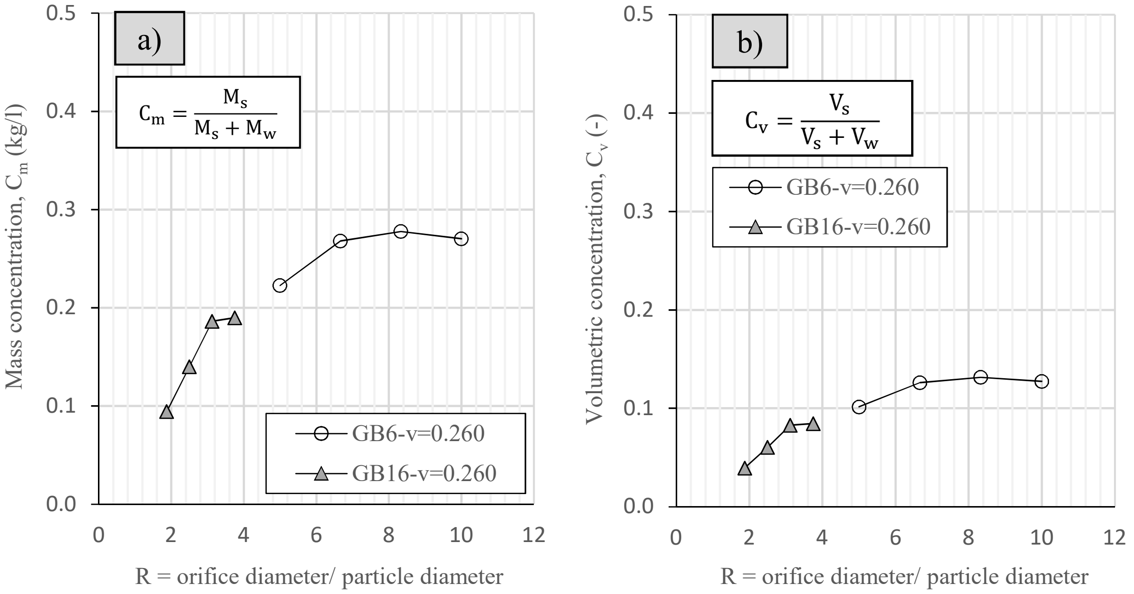

Figure 11-8: a) Mass concentration b) Volumetric concentration

Table 11-9Table 11-8 and Table 11-9 summarise the extracted values from the plots above, giving a more quantitative comparison. No linear relations were deduced amongst the values. However, what was consistent was the notable decrease in magnitude of concentrations for larger orifice sizes (decreasing gradient).

Table 11-8: Mass concentration of beads for MSS

Translational Velocity (m/s)	**Mass concentration, C_m (kg/l)**							
	6mm beads, GB6				**16mm beads, GB16**			
	$D_o = 30$	$D_o = 40$	$D_o = 50$	$D_o = 60$	$D_o = 30$	$D_o = 40$	$D_o = 50$	$D_o = 60$
0.104	0.195	0.214	0.206	0.202	0.050	0.127	0.145	0.146
0.156	0.209	0.226	0.232	0.217	0.085	0.153	0.157	0.159
0.208	0.216	0.248	0.243	0.237	0.093	0.117	0.165	0.173
0.260	0.223	0.268	0.278	0.270	0.095	0.140	0.187	0.190

Table 11-9: Volumetric concentration of beads for MSS

Translational Velocity (m/s)	**Volumetric concentration, C_v (-)**							
	6mm beads, GB6				**16mm beads, GB16**			
	$D_o = 30$	$D_o = 40$	$D_o = 50$	$D_o = 60$	$D_o = 30$	$D_o = 40$	$D_o = 50$	$D_o = 60$
0.104	0.087	0.097	0.092	0.091	0.020	0.054	0.063	0.063
0.156	0.094	0.103	0.106	0.098	0.035	0.066	0.068	0.069
0.208	0.098	0.115	0.112	0.109	0.039	0.050	0.072	0.076
0.260	0.101	0.126	0.132	0.127	0.040	0.060	0.083	0.085

In relation to Figure 11-9 and a 50mm diameter orifice, a comparable relationship between two different particle sizes was recorded. However, unlike changes in R (= D_o/d_p), an increase in velocity, increased the concentration ratios which was expected. A higher translational velocity, translated to the nozzle infiltrating a bed with a higher packing ratio (dense flow) as suction effects had less of an influence.

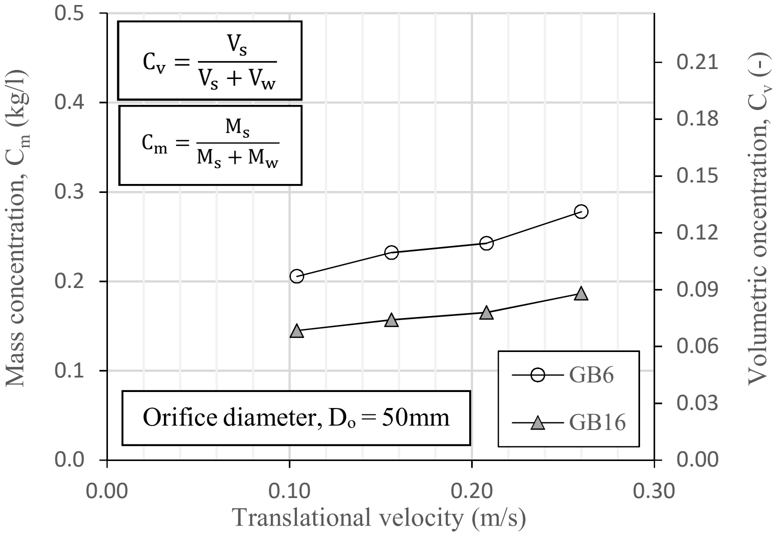

Figure 11-9: Concentration ratios versus translational velocity

This higher packing ratio was best portrayed by the volume of mass collected per selected velocity (Section 11.2.1). The extended duration for low velocities gives way for particles to be hydraulically transported instead of being entrained through inertia, thus reducing the particle concentration near the orifice. Hence, suction plays a more prominent role for low translational velocities as opposed to high.

11.2.3 Overall Flow and Hydraulic Transport through System

With respect to continuity and steady state flow conditions, the flow of fluid through the nozzle inlet was determined to be equal to the flow through the suction pipe. A standard flow rate per particle bead size was used throughout testing. This allowed for the reduction in potential errors instigated by flow rate variability. For the MSS tests, the flow rates used were 3.2 and 5*l*/s for GB6 and GB16 respectively, based on the bead's settling velocities. In practice, achieving the modified output of the Rocky data was unlikely, as the effects of suction had a certain area of influence for particles within the vicinity of the opening. However, of added value, was the effect of incorporating suction and identifying its impact on the measured mass output.

It is worth clarifying that the subject of flow can be referred to different stages or regimes of flow. Naturally, one would describe flow as the movement of water in a confined or unconfined space. In contrast, granular flow entails the movement of particles either mechanically or with the help of a carrying medium, frequently referred to as hydraulic transport (Janna, 2010). To distinguish the body forces at work amongst the different granular flow scenarios, the Reynolds number pertaining to each particle phase was analysed. The phases in this case were based on the criteria described in Chapter 3.4.1, where drag, buoyancy, lift and weight forces were present. In the experimental setup, the regions of interest were assigned as follows (A, B & C):

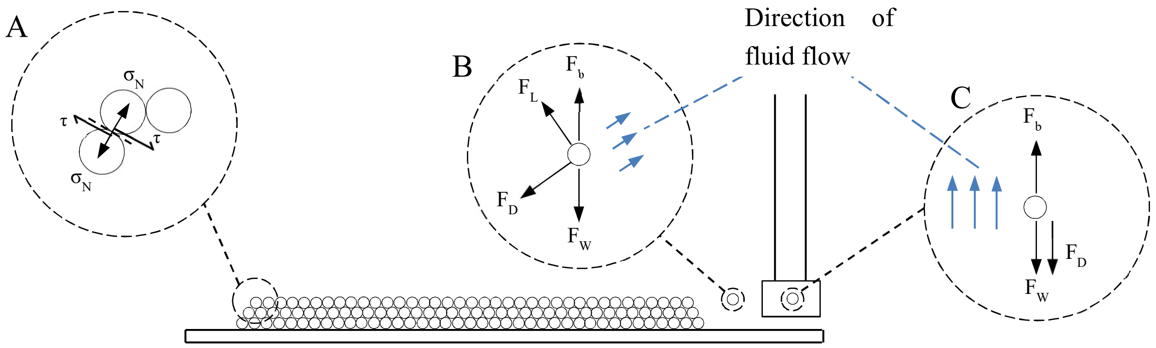

Figure 11-10: Body of forces in MSS for particles under different flow states

These regions were found to be the most critical for the overall flow analysis of the system. Note that regions B and C refer to the phases in the MSS not the MMS. The body of forces on the alternative system were not discussed as the motion of beads through an orifice was related to the contact forces interplayed between particles or physical boundaries. The principles of inertia were more prominent in the MMS, illustrating the resistance of a physical object to changes in its state of motion (Knight, 2008). In contrast, for the MSS the body forces in each region were explained as follows:

11.2.3.1 Region A

In this region, the particles were static in motion and not subjected to any fluid flow, said to be in the fixed bed phase. They were held together by shear forces and the stabilisation of the bottom layer of beads with the footwall. It can also be said that the buoyancy force, F_b, and the weight of the particle, F_W, were in equilibrium. The strength of the particle assembly is dictated by its shear strength, defined as the internal resistance per unit area that the assembly mass can offer to resist failure (Das, 2000). The shear strength is based on Mohr-Coulomb's failure criteria expressed as:

$$\tau = c + \sigma_N \tan \emptyset \tag{11-3}$$

Where,

c = Cohesion in kPa
τ = Shear stress on the failure plane in kPa
σ_N = Normal stress on the failure plane in kPa
Ø = Angle of internal friction in °

For this setup and the granular nature of the materials, the cohesion, *c*, was equal to zero. Additionally, the friction angle was assumed to be fairly low (Ø ≈ 25-30°), thus suggesting the shear strength to be relatively minimal for spherical particles (Soria-Hoyo, Valverde & Castellanos, 2008; Cavarretta, Coop & O'Sullivan, 2010; Lee et al., 2013).

11.2.3.2 Region B

Said to be in the fluidisation stage, the particle near the orifice experienced various reactions to the suction force induced by the displacement pump. The particles in this region were assumed to be subjected to turbulent flow. Considering Table 11-10 and Table 11-11, GB6 and the relevant flow rate velocity, the Reynolds number for each orifice size was calculated.

Table 11-10: Region B-Reynolds number parameters

Parameter	Unit	Orifice Diameter, D_o (mm)			
		30	40	50	60
ρ_w	kg/m³	1000			
μ	N.s/m²	1.002E-03			
v	m/s	3.570	2.008	1.285	0.893

Therefore, using the parameters above and the following formula:

$$\mathrm{Re} = \frac{\rho v L}{\mu}$$

The Reynolds number per orifice was calculated to be:

Table 11-11: Reynolds number of fluid through orifice

Orifice diameter, D_o (mm)	Reynolds number, Re
30	106893
40	80170
50	64136
60	53446

The values, Re, were significantly greater than 5000, indicating that the fluid flow was well within the turbulent range.

11.2.3.3 Region C

A particle in the two-phase flow region was subjected to pure fluid forces, where the particle and fluid were transported at two different velocities (Coulson et al., 1999). As an intermediate indication from Region B, it was assumed that flow would be of the turbulent range. This was further verified, following a similar process as above. The Reynolds number per particle was found to be:

Table 11-12: Reynolds number of fluid through pipe

Particle, d_p (mm)	Reynolds number, Re
6	51038
16	79414

The initial suction rate proposed was dependent on the particle size. The flow needed to be great enough to lift the particles through the pipe and efficient enough such that a build-up of particles, both in or outside the nozzle, would not occur. Flow rates of 3.21*l*/s and 5.00*l*/s were used for the GB6 and GB16 particles respectively (Based on the settling velocity-Appendix H).

11.2.4 Analysis of Interface Parameters

For MMS experiments, the process of entrainment was related to the behaviour of sample coring, where bulging and bearing capacity played a significant role in soil recovery. The testing demonstrated such behaviours when the collection rate was less than the rate of materials covered. For example, if the entrainment and covering rate of the nozzle per meter were to be 1.2kg/m and 1.5kg/m respectively, a build-up of beads would occur, forming a bulge in front of the nozzle (Figure 11-11).

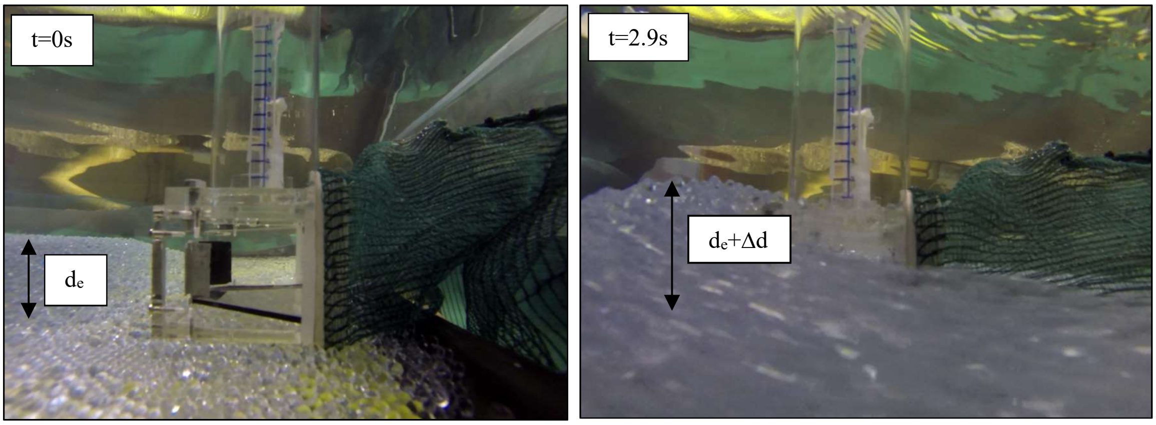

Figure 11-11: Development of bulge height from t = 0s to t = 2.9s
Source: Qiu (2017)

The images obtained from the Go-Pro, provided a good sense of the behaviour of the materials, but what was lacking was the detailed interaction of the beads and how they interacted with one another. Rocky was able to provide a platform for this analysis as shown from the taken screenshots below.

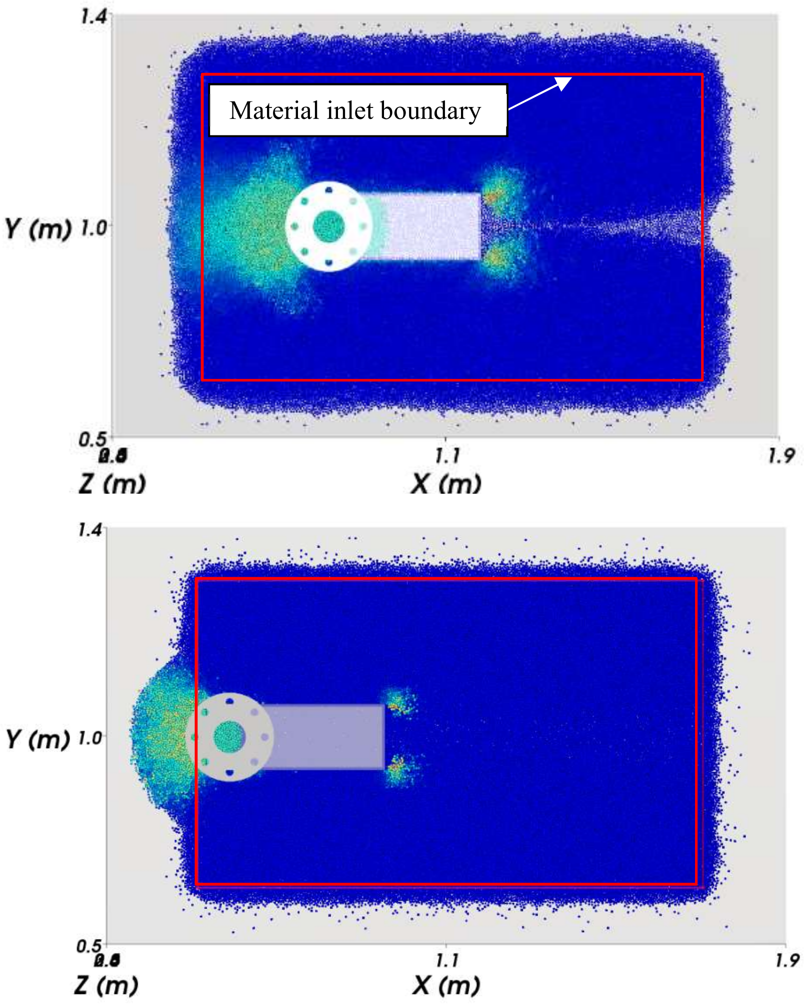

t = 3.2s
Bulge formation near nozzle face. Highlighted particles, subjected to translational velocity.

t = 4.4s
Bulge formation towards end of simulation

Figure 11-12: Elevated view of bulge formations as a function of translational velocity

Note that due to the materials' potential for sliding and rate of collection, the particles displaced away from the orifice in a bulbous manner. The coloured particles in the simulation were subjected to a translational velocity. Experimentally, the increase in velocity of particles through an orifice yielded greater outputs with respect to time. Although, in the contextual frame of recovery, this was not found to be the case. Deduced from the MMS, the translational velocity of the nozzle had a negligible influence on the recovery of the materials per metre. In some regard, the conclusions made by Aguirre et al. (2010) were validated but not fully applicable. This suggested that the velocity adjustment of the particles was irrelevant when analysing the collection of particles under MMS entrainment. This however, was different when suction was involved, as its effects extended beyond the orifice interface, as discussed previously.

The bulge formation lead to variations in the lateral earth pressure over time. Implementing a video analysis process, a maximum bulge height approximately 20mm above the top of the nozzle was measured (Figure 11-13a: Orifice diameter = 30mm). Through calculations, a maximum passive force of 13.29N was computed using Culman's method (Process covered in Appendix E: pg 179). The method consists of an analytical analysis and was selected due to the variability in bulge height (Figure 11-13b). The reader is referred to Das & Sobhan (2014) for a more detailed explanation of the Culman method.

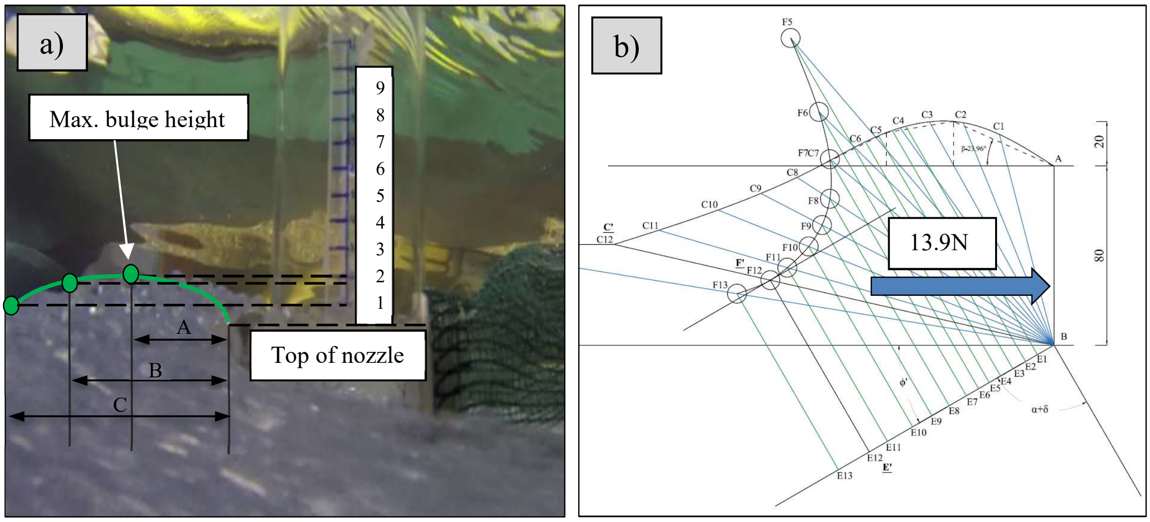

Figure 11-13: a) Bulge height approximation at t = 2.9s for D_o = 50mm b) Culman's graphical analysis

In theory, one would assume the normal force determined in Rocky to be less than the force calculated. This was attributed to the consideration of openings in Rocky and not in the calculations, where the presence of an opening would reduce the size of the area exposed to the particles, thus decreasing the force. Consequently, this was found not to be the case. A normal force of 16.65N was registered for an orifice size of 30mm, 24% greater than the calculated value. However, the variance was thought to be from the assumptions made regarding the angle of internal friction in the Culman calculations and the frictional parameters used in Rocky.

In Appendix C (pg 166), the deviations caused by minor adjustments in friction were presented. This stands to confirm that the relevant frictional properties can be adjusted to achieve normal forces in close approximation with one another. Additionally, theories such as Culman's method, assumes an infinitely long bed where side effects caused by bulging were not considered (Craig & Knappett, 2012).

The calculated force on the face was found to be close to the peak value of the normal force obtained using Rocky. However, this was not an accurate interpretation, since at t ≈ 3.2s, the nozzle was near the edge of the granular bed, bringing in boundary effects. This dispersed the particles forming the bulge, which led to a decrease in force applied as proven from t = 3.2~4.4s (Figure 11-14).

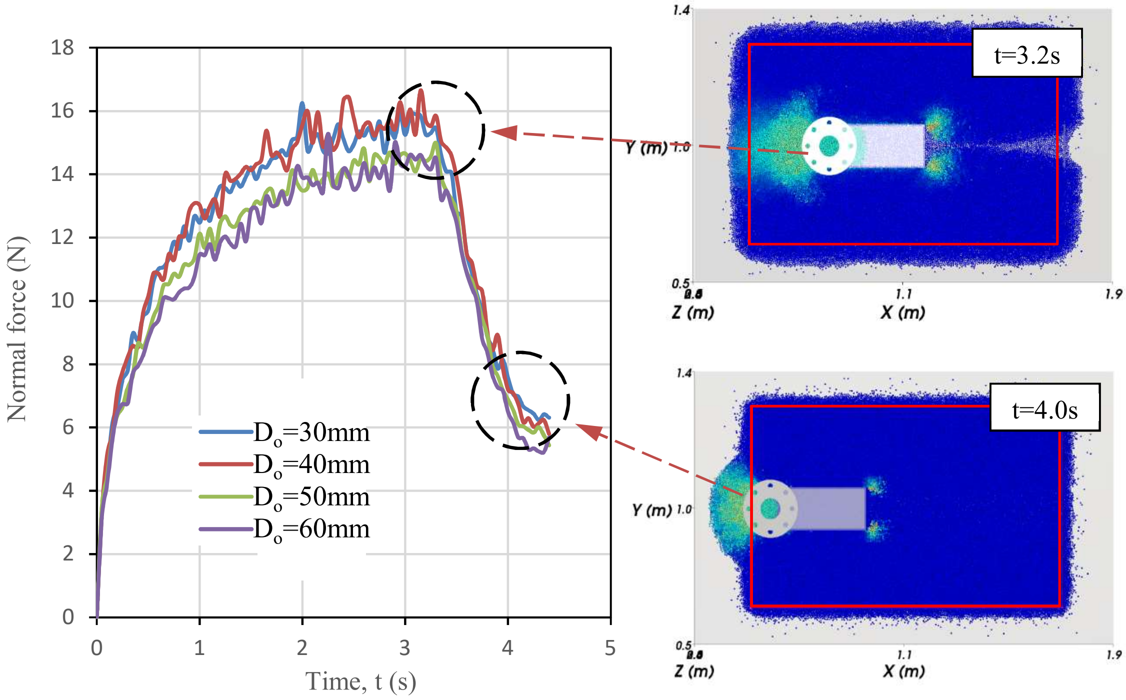

Figure 11-14: Normal forces exerted onto nozzle face

The normal force determined from Rocky was used to identify any behavioural changes with regards to the particles collected. Looking at the mass collected versus the sum of the normal force, and areas experiencing the greatest force, provided sufficient insight into the behaviour of materials near the interface (Figure 11-15).

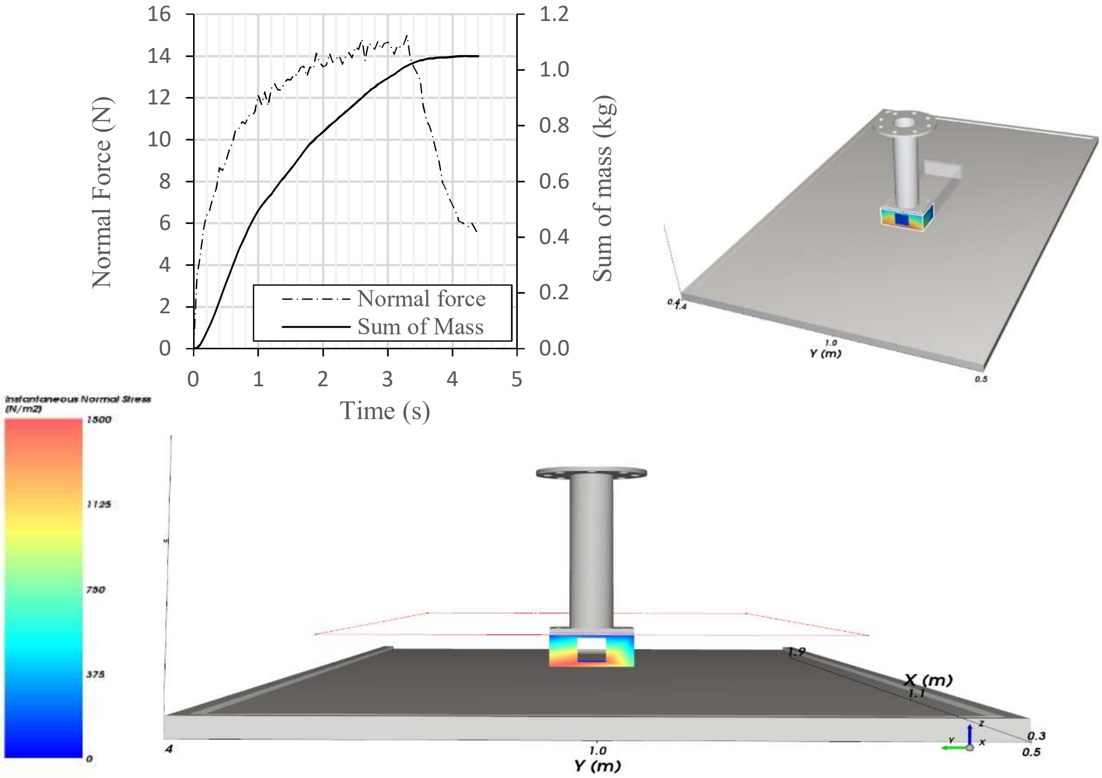

Figure 11-15: Measured normal force on the face of nozzle through Rocky

The drop in magnitude at t = 3.2s indicated that the maximum normal force may not have been reached due to boundary effects. The sum of mass collected started to plateau at around the same time the force started to drop (t = 3.2s), indicating that the boundary effects influenced the final mass output. A larger granular bed in both numerical and physical systems would be needed to minimise such effects. Although not feasible experimentally, the numerical side of it was investigated by running a simulation with a bed length L = 2.0m >1.15m. The graphical interpretation of the modified bed was displayed below, showing a constant growth in normal force due to limited boundary effects.

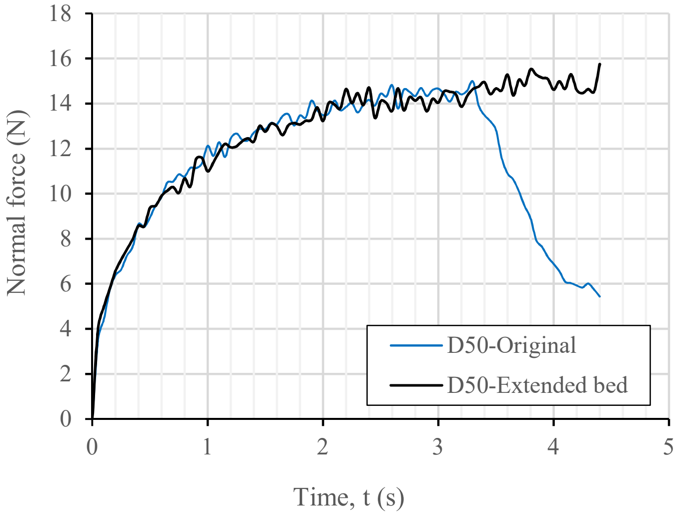

Figure 11-16: Normal force on nozzle with extended bed

11.3 Assessment of Results against Theory

The setting of the experiment is one that is not often covered in literature. As a result, the undertaken study was driven by its complexity and the multiple governing laws at play. Many problems exist, where dominating parameters are isolated and rationalised. The assessment dealt with methods of predicting flow using a theoretical approach and substantiating key components that potentially had an influence on the measured readings.

11.3.1 Predictability of Collection Rate through Constitutive Laws (MMS)

In studies by Aguirre et al. (2010) & De-Song et al. (2003), it was brought to attention that the gravitational component in the Beverloo flow law could be replaced by the diameter dependent velocity vector (Equation (4-10)) as discovered by Janssen (1895). As such, the experiments involved the use of a conveyor belt, which in turn modified the original Beverloo theorem to cater for the constant velocity applied to all particles in 2D, explained through the expression:

$$\mathrm{W}_{2\mathrm{D}} = \rho \mathrm{v} \mathrm{d}_p (\frac{\mathrm{D}_o}{\mathrm{d}_p} - \mathrm{k})$$

From a 3D perspective, an identical approach was taken to that of Aguirre et al. (2010) & De-Song et al. (2003). The Janssen equation was likewise substituted into the Beverloo equation, but for the 3D case.

$$\mathrm{W} = \mathrm{C}\rho_\mathrm{b}\sqrt{\mathrm{g}}\left(\mathrm{D}_o - \mathrm{kd}_p\right)^{\frac{5}{2}}$$

Agreeing with Janssen's approach (i.e. ignoring the effects of retained height when $H > 2D_o$) and considering the empty annulus effect, the discharge velocity, given as $v = [g(D_o - kd_p)]^{1/2}$, was substituted in the equation above, giving the following:

$$\mathrm{W} = \mathrm{C}\rho_\mathrm{b}\mathrm{v}\left(\mathrm{D}_o - \mathrm{kd}_p\right)^2 \tag{11-4}$$

In principle, prior to the modification, the constant gravitational acceleration jointly facilitated the discharge of particles. By replacing this variable, an equivalent velocity stream of particles was required, to satisfy the adjusted equation. However, in the case of the completed experiments, a constant velocity was rarely achievable as the movement of the nozzle through the stationary seabed not only induced a build-up of particles in front of the face but a residual build-up within.

To account for different sized particles of identical index properties, Equation (11-4) was further modified. This allowed the determination for a single set of fitting parameters (C and k) per type of material tested. For example, if steel beads were used instead of glass, it would have its own set of fitting parameters, different to those determined for glass beads. The ratio R ($= D_o/d_p$) was substituted into the equation, formulating the modified expression:

$$W = C\rho_b v d_p^2 (R - k)^2 \tag{11-5}$$

To achieve a constant velocity through an orifice, as described by the modified Beverloo equation, the assumed mass output values determined with Rocky were used (Chapter 10). The values were based on an orifice diameter of D_o = 50mm, and a translational velocity of v = 0.26m/s (default parameters). Since the Beverloo law was empirically based, the constants, C and k were determined through a linear regression analysis. (Refer to Appendix E for full regression analysis: pg 184)

The regression analysis was based on the method implemented by Zatloukal & Šklubalová (2012). A linear relationship between R and $W^{0.5}$ was expected, therefore Equation (11-5) was altered in the form of a linear function (y = mx + c) such that:

$$R = C^{-0.5}\left(\frac{W}{\rho_b v d_p^2}\right)^{0.5} + k \tag{11-6}$$

Here, the y-intercept, c, was equal to the shape coefficient k and the gradient, m, was equal to $C^{-0.5}$. The x-axis values were obtained from the translational speed of the nozzle (v = 0.26m/s), the bulk density of the particles ($\rho_{b,\ GB6\&GB16}$ = 1485kg/m^3) and the calibrated results achieved through Rocky (W).

It was expected that for a given material the coefficients for GB6 and GB16 would be the same. From the plot below, this indeed was the case. The plot illustrates the linear regression analysis performed on the results under dynamic equilibrium (constant flow rate through orifice).

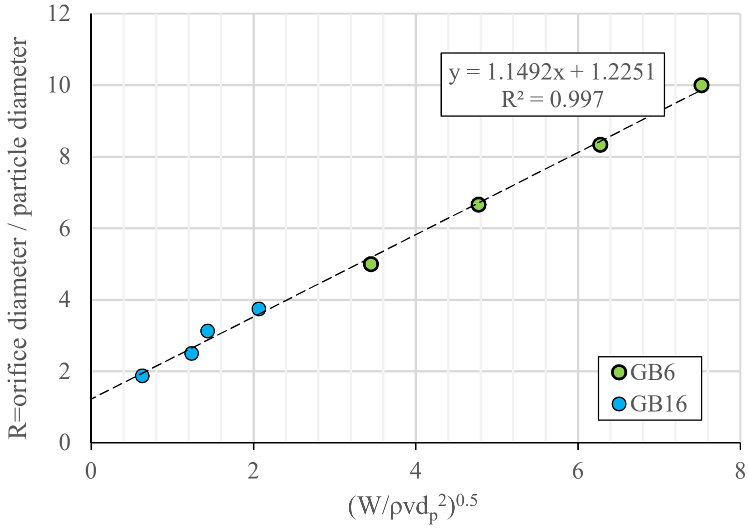

Figure 11-17: Regression Analysis by Zatloukal et al. (2012)

The fitting parameters *C* and *k*, for the spherical glass beads, were summarised in Table 11-13.

Table 11-13: Beverloo law coefficients

Coefficient	Symbol	Zatloukal (2012): $(W/\rho v d_p^2)^{0.5}$
		GB6 and GB16
Discharge coefficient	C	0.757
Shape factor	k	1.225

Typical values for *C* ranged between 0.5-0.8, therefore the values measured were found to be in agreement with literature (Mankoc et al., 2007; Sheldon & Durian, 2010). Values for *k* were generally taken to be between 1 and 3; and 1.5 for spherical particles (Beverloo, Leniger & van de Velde, 1961). Since the shape parameter was found to be in this range, it was concluded that Equation (11-5) fitted optimally with the experimental results.

The shape parameter, *k*, although useful in characterising granular flow, is not clearly defined in literature. Researchers have incorporated $k > 1.0$ to account for the possible existence of the "empty annulus" effect in the outlet for all *R* (Beverloo, Leniger & van de Velde, 1961; Nedderman et al., 1982). Although not fully evident in the coefficient analysis, differences between GB6 and GB16 were observed in the primary outputs discussed in Section 11.2. The final mass flow rates of the glass beads along with the correlating coefficients, formed the following expression:

$$\text{Zatloukal: } W = 0.757\rho_b v\left(D_o - 1.225d_p\right)^2$$

The final plot of the discharge rate, *W* versus *R* (= D_o/d_p) was given in Figure 11-18. The measured Rocky values (Table 11-14) were also plotted onto the graph to assess how well the modified expression characterised their behaviour.

Table 11-14: Measured results calibrated with Rocky

Orifice diameter, D_o (mm)	Mass flow rate, W (kg/s)	
	6mm beads, GB6	**16mm beads, GB16**
30	0.165 (R = 5)	0.039 (R = 1.88)
40	0.316 (R = 6.67)	0.151 (R = 2.50)
50	0.547 (R = 8.33)	0.203 (R = 3.13)
60	0.786 (R = 10)	0.421 (R = 3.75)

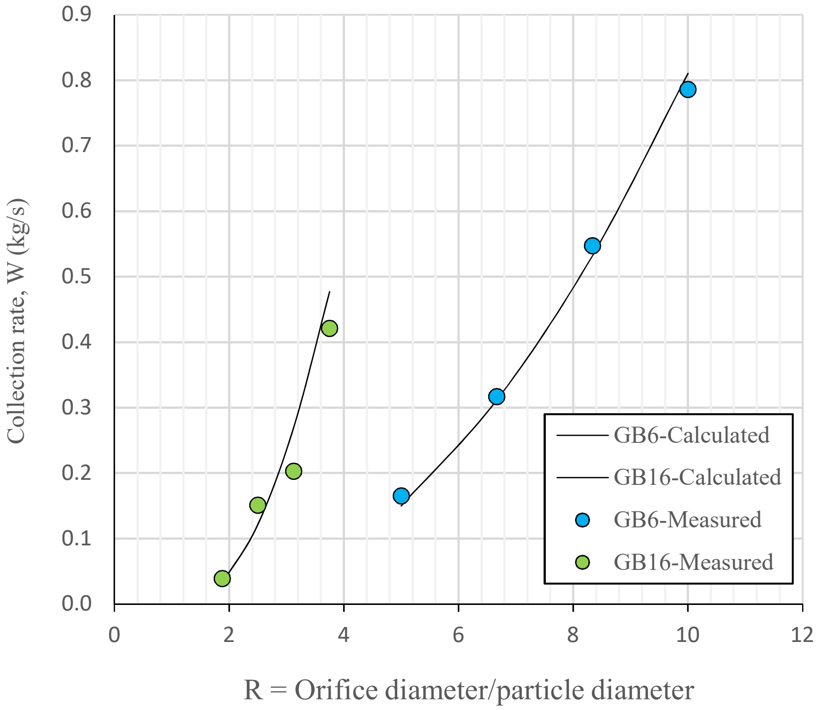

Figure 11-18: Plot of measured values and modified Beverloo Law

The plot verified the suitability of the modified equation in the MMS experiment. However, it was noted that the equation did not fit as well for the larger GB16 particles subjected to irregular flow where R < 3.75. To ensure the robustness of these modifications, a wider range of orifice diameters or $R = D_o/d_p$, had to be examined. Despite the limitation, to further progress with the analysis, the accuracy (%) of the Beverloo expression was tabulated (Table 11-15). The accuracy of a measurement was defined as the mean relative difference between the experimentally measured discharge rate and the rate determined using the modified Beverloo flow equation.

Table 11-15: Summary of the Beverloo flow equation

Particle	Orifice diameter (mm)	R	$W_{calculated}$ (kg/s)	$W_{measured}$ (kg/s)	Accuracy deviation (%)
GB16	30	1.88	0.032	0.039	18.317
	40	2.50	0.122	0.151	19.439
	50	3.13	0.270	0.203	24.968
	60	3.75	0.477	0.421	11.764
GB6	30	5.00	0.150	0.165	9.050
	40	6.67	0.312	0.316	1.503
	50	8.33	0.532	0.547	2.800
	60	10.00	0.810	0.786	3.059

Lower the value of the deviation calculated, the greater the precision of the measurement. Therefore, looking at the accuracies computed for GB16, the high values indicated a poor predication of the collection rate, W (kg/s) relative to the accuracy of the GB6. In analysing the results, agreement between the measured and calculated values were found to be sufficient when accuracies were less than 5%. In contrast, for accuracies > 5%, significant flow failures (e.g. clogging, jamming, pulsating flow) were expected to be the cause. The differences between the measured and calculated values were further interpreted below:

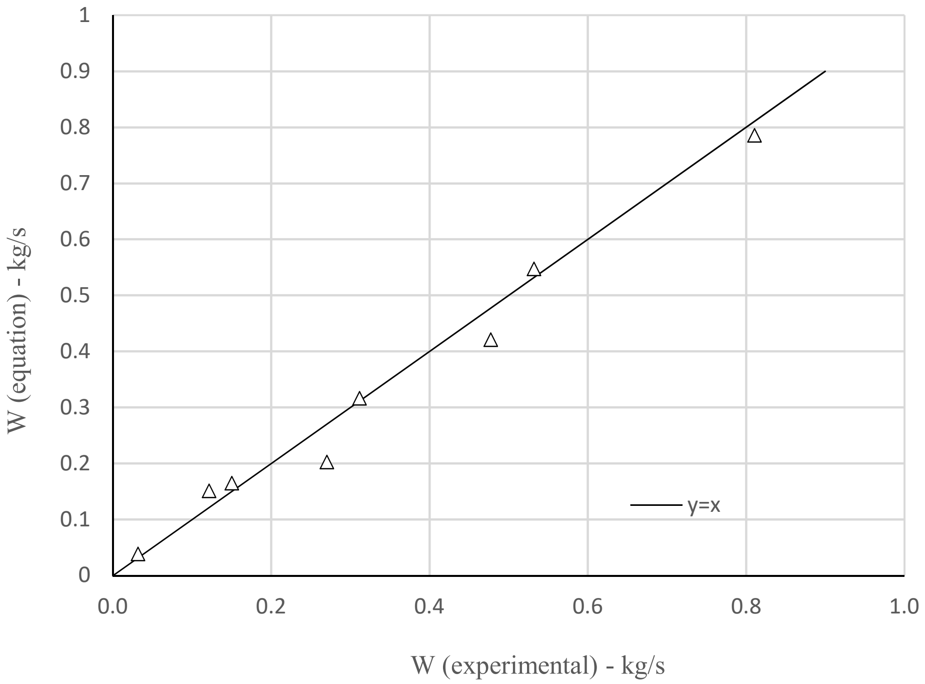

Figure 11-19: Calculated mass flow rate versus measured values for GB6 and GB16

The graphical representation indicates a reasonable correlation between the measured and calculated values (y = x indicates 100% correlation).

11.3.2 Predictability of Collection Rate (MSS)

The hydraulic transport of granular particulates differed greatly in comparison with the MMS counterpart. Through dimensional analysis, the Beverloo flow equation used in the MMS possessed many aspects of critical relevance to the MSS (e.g. orifice diameter and particle velocity). However, introducing suction brought in other parameters that must be considered. This included the type of flow regime induced and the forces induced onto a single particle (Shook, Roco & Brenner, 1991). To understand flow from first principles, it was worth investigating the commonly used equation:

$$Q = \rho_b v_p A \tag{11-7}$$

Here, v_p refers to the velocity of the particles, ρ_b bulk density and A, the area of the orifice. Mass fluid flow is either dominated by viscous forces or inertial forces, depending on the velocity of the mixture. As such, the drag coefficients assigned to particles vary accordingly. Knowing this fact, it is evident that the velocity and concentration of the particles play an important part in dictating the magnitude of flow. Concentration was referred to here in the presence of the bulk density variable introduced in the equation. The variable can be simplified into the following:

$$\rho_b = C_v \rho \tag{11-8}$$

Where, ρ = Particle density in kg/m^3

Therefore,

$$Q = C_v \rho v_p A \tag{11-9}$$

The volumetric concentration, C_v details the total volume occupied by the solid particles, indicating the amount of voids present in the mixture. For a stationary fluidised bed, commonly used terms to define such empty spaces include the porosity (n) or packing ratio (1-n) of the bed. In all the MSS tests, the volumetric concentration for each setup was measured allowing the calculation of a particle's travel velocity with respect to orifice size (Table 11-16).

Table 11-16: Particle velocity in MSS

Translational Velocity (m/s)	Particle velocity, v_p (m/s)							
	6mm beads, GB6				16mm beads, GB16			
	$D_o = 30$	$D_o = 40$	$D_o = 50$	$D_o = 60$	$D_o = 30$	$D_o = 40$	$D_o = 50$	$D_o = 60$
0.104	3.911	2.223	1.416	0.982	5.670	3.304	2.133	1.482
0.156	3.942	2.239	1.438	0.990	5.759	3.347	2.147	1.492
0.208	3.957	2.269	1.447	1.001	5.781	3.289	2.156	1.503
0.260	3.973	2.298	1.480	1.023	5.784	3.326	2.181	1.517

The calculated value can be verified under the simple assumption that the particle velocity matches the fluid velocity. A flow rate of Q = 3.21 *l*/s in an 80mm diameter suction pipe translated to a fluid velocity of, v_f = 1.285 m/s through a 50mm diameter orifice. The inlet velocity plus the translational velocity of 0.26 m/s gave a final speed of 1.545 m/s. Therefore, the values calculated in Table 11-16, were all found to be less than their final fluid speed counterparts. Validating the adequacy of the particle velocities calculated.

Predicting fluid driven flow was difficult because the particles were not subjected to a constant acceleration such that $v \propto (gD_o)^{1/2}$. For a two-phase flow system, where the fluid and coarse particles move at different velocities, the particles tended to accelerate up to the fluid velocity ,v_f (Lafond ,2014).

The volume and mass concentration of particles increased towards the bottom edge of the orifice (Coulson et al., 1999). Calculating the granular flow required the determination of the velocity and concentration properties of the mixture. Commonly employed methods for determining these properties included the use of an electromagnetic flowmeter or applying the gamma-ray absorption method.

11.3.3 Jamming and Clogging Effects

From Table 4-2, the limitations put forward by past researchers were investigated and compared to the outputs achieved in this study. The limitations came in the form of jamming or discontinuity effects and were a function of the ratio (R) between the orifice diameter and particle size. A wide range of *R* values were used throughout testing, providing a platform large enough to investigate the limiting effects covered in literature, most notably the jamming of particles at the orifice. Practically the behaviour was observed through the attached monitoring device and notable changes in iterative mass recordings. A more efficient method of identifying the fluctuations was through the magnitude of the uncertainties associated with each setup (Detailed in Appendix I). Deviations recorded in the MMS results were found to be negligible (See Chapter 11.2.1), thus were not worth re-evaluating. However, it raised an important issue on the clogging criteria. In relation to the larger variances experienced in the MSS configuration (Table 11-17), why is it that for the same *R*, less or no jamming effects were observed in the MMS? Since the only notable differences between the systems had to do with the inlet velocity, *v*, it was suspected that the occurrence of jamming was related to both *R* and *v*.

Table 11-17: Mass collection uncertainties for each setup in MSS

Translational velocity (m/s)	**Uncertainty (kg)-95% Confidence Interval**							
	6mm beads, GB6				**16mm beads, GB16**			
	$D_o = 30$	$D_o = 40$	$D_o = 50$	$D_o = 60$	$D_o = 30$	$D_o = 40$	$D_o = 50$	$D_o = 60$
0.104	0.127	0.217	0.489	0.372	2.505	2.735	0.479	0.457
0.156	0.281	0.029	0.475	0.280	0.475	0.338	0.228	0.432
0.208	0.114	0.155	0.269	0.323	1.746	2.065	0.686	0.880
0.260	0.186	0.299	0.215	0.698	0.298	1.454	0.664	0.040

Considering the MSS, the values highlighted in blue refer to uncertainties > 0.5kg but < 1.0kg. The more critical uncertainties of magnitude >1kg were highlighted in red. The deviations fell into two categories of either pulsating flow or complete jamming. The first describes the alternating stopping and starting behaviour of flow. The second is where flow has been completely restricted for an extended period of time. According to text, jamming generally takes place for R < 4 (Bao et al., 2003). However, experimentally in the MSS, this was found to occur for R approximately < 3.75 (= 60mm/16mm) and to be more critical as the orifice size decreased. Although different, it proves that there exists a critical region where flow becomes disturbed. Other explanations detailed how flow effects, caused by R, could be eliminated by ensuring the orifice diameter was at least six times greater than the particle diameter (Ahmad & Pilpel, 1969).

A method with greater detail included the use of Rocky and noticing the drastic mass collection fluctuations within the user processing tools. The primary results obtained from the experimental tests (MMS) gave visual indications of jamming but were not detailed enough to draw precise conclusions. The variations were minor compared to the larger deviations in the MSS, where collection rates were significantly greater. Assessing the numerical simulations, the effect of complete jamming could not be achieved (only for MMS). However, what was observed was the pulsating phenomenon illustrated in Figure 11-20 b), a plot of GB16 Rocky results which have low ratios of R. Complete jamming in the MMS was not attained as it was suspected that either the inlet velocity was not great enough or the orifice was not small enough. The plot of GB6 Rocky outputs were also given to highlight the difference the two bead sizes.

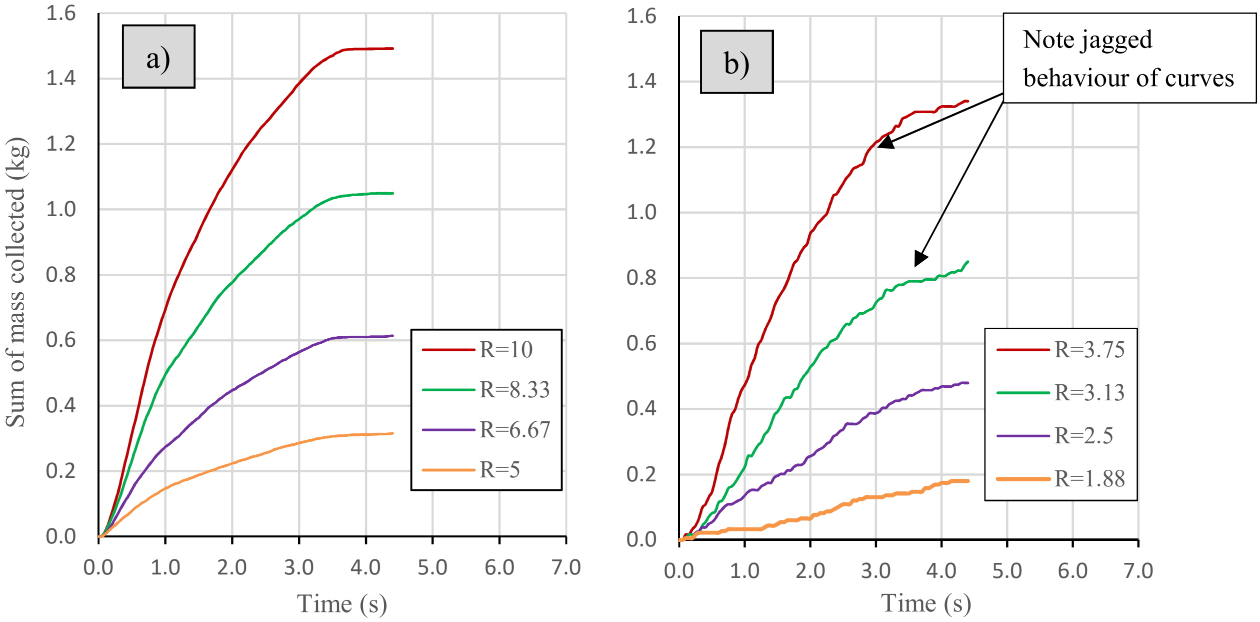

Figure 11-20: Rocky sum of mass outputs for a) 6mm beads and b) 16mm beads

It was shown for a given D_o and d_p there exists a critical R where flow becomes irregular. The formation of the jamming occurrence in the tests were different to the formation of an arch as described in literature (Garcimartín et al., 2009; Guariguata et al., 2012; Lafond et al., 2013). The jamming of suspended particles was related to the hydrodynamics of flowing fluid, including non-uniform fluid velocity profiles or turbulence (Guariguata et al., 2012). It must be reiterated that the exact determination of the jamming boundary was not a set out scope but an added parameter of interest in supporting its existence. Complete jamming was evident in the MSS but less obvious in the MMS. The crowding of particles in front of the nozzle, which led to jamming, was determined to be a function of R and v. This was because in gravity driven flow, particles are subjected to a constant acceleration and high particle concentrations such that jamming is heavily dependent on R (Nedderman et al., 1982; Guariguata et al., 2012). In fluid-driven flow this was different as particles were subjected to a constant velocity and jamming could occur in dilute flow.

11.4Sensitivity Analysis

11.4.1 Effect of Orifice Diameter

The experimental programme required the testing of varying orifice sizes, allowing its influence to be assessed. As expected, from the mass collection results, an increase in orifice size was found to greatly increase the collection rate of GB. Under default parameters in the MMS, increasing the orifice size from 30mm to 60mm increased the collection rate of GB6 from 0.072kg/s to 0.359kg/s and of GB16 from 0.040kg/s to 0.293kg/s. An approximate increase of 80% and 86% were noted respectively. The calibrated results yielded similar increases of 79% and 91%. Readings and statements regarding GB16 should be taken with caution as the values were subjected to jamming and clogging effects (R< 3.75).

It is of interest to note, under a constant velocity (calibrated results), a trend similar to what was reported in literature was achieved (Bao et al., 2003; Aguirre et al., 2010; Alejandra Aguirre, De Schant & Géminard, 2014). This trend is well depicted in the empirical equation, $W = C\rho_b v(D - kd)^2$ used to predict the flow rate (Appendix E). It has been shown in the collected results that there exists a ratio between the orifice size and particle diameter, where flow would pulsate or become non-existent, as previously discussed in Chapter 11.3.3. This was visually evident during the testing of GB16, where ratios (R) between 1.875 and 3.75 were tested. The precise determination of the limiting flow range was not an objective of this study, however to prove that such a limitation does exist for lower values of R was relevant.

The effect of orifice size had a more complex effect within the MSS. The collection rate increased with increasing orifice size under a constant translational velocity but simultaneously decreased due to the lowering of the suction flow with increasing orifice size. Table 11-18 highlights the constant increase in flow rate for the MMS and the variability within the MSS results.

Table 11-18: Effect of orifice diameter with translational velocity, v = 0.26m/s

System Test	Particle diameter, d_p (mm)	Orifice diameter, D_o (mm)	$R = D_o/d_p$	Mass flow rate, W (kg/s)
MMS	GB6	30	5.00	0.072
		40	6.67	0.139
		50	8.33	0.241
		60	10.00	0.359
	GB16	30	1.88	0.040
		40	2.50	0.115
		50	3.13	0.197
		60	3.75	0.293
MSS	GB6	30	5.00	0.921
		40	6.67	1.178
		50	8.33	1.236
		60	10.00	1.191
	GB16	30	1.88	0.523
		40	2.50	0.818
		50	3.13	1.147
		60	3.75	1.173

11.4.2 Effect of Particle Diameter

The effect of changes in particle size were assessed through the mass collection results for GB6 and GB16 in the MMS system. The results indicated that for any given system configuration, the collection rate of the glass beads is highly dependent on the particle size. Under default parameters ($D_o = 50$mm, $v = 0.26$m/s), collection rates of 0.241±0.003 kg/s and 0.197±0.01 kg/s were recorded for GB6 and GB16 respectively (See Table 11-2). The difference in flow rates between the two particle sizes was approximately 18.3%. Apart from particle size, all other parameters and configurations were kept constant in the compared tests.

The observed differences were consistent with the general agreement that an increase in particle size would decrease the granular flow rate (Fowler & Glastonbury, 1959; Mankoc et al., 2007; Medina et al., 2014; Serrano et al., 2015). Most notably, the agreement is reflected in studies on the gravity discharge rate of particles through an orifice whereby an effective discharge diameter defined as $D_o\text{-}kd_p$ was used, introducing the concept of the "empty annulus" (Garcimartín et al., 2009). The shape parameter, k, was usually in the range of 1-3 depending on the particle properties, and can generally be determined experimentally through a regression analysis, covered in Chapter 11.3.

11.4.3 Effect of Velocity

The rate at which the material was entrained was directly proportional to the velocity through the orifice. For MMS, it was noted that the recovery of materials over a given seabed length was consistent for any variations of velocity as mentioned earlier. This brought about the assumption that changes in velocity had a negligible influence in terms of recovery. Thus, further validating that the collection rate was independent of the bulge height formation. Note that bulge height is a function of velocity.

In contrast, in the MSS, the effect of velocity combined with the effect of orifice size was more prominent. The effects of suction extend beyond the region of the orifice. The suction velocity, v_{suc}, and translational velocity of the nozzle, v, were dependent on one another but were operated by different variable speed drives. Inspecting Table 11-19 proved that introducing suction, increased the collection rate several times. The flow rate through each orifice was kept constant. Thus, for a single orifice at different translational velocities, different mass concentrations, C_m, were measured. Similarly, for a single translational velocity and different orifice sizes (i.e. varying suction velocity), the mass concentrations were different.

Table 11-19: Comparison of MMS and MSS

Orifice diameter, D_o (mm)	Average mass collected (kg)		Percentage increase (%)
	MMS	MSS	
30	0.318	4.076	1282
40	0.611	5.208	853
50	1.055	5.467	518
60	1.583	5.269	333

For a given translational velocity, there was a notable peak in the collection rate amongst the range of orifice sizes (Figure 11-21). This emphasised that a suitable orifice size needed to be selected to cater for an optimum collection rate yet be adequate in size for increased recovery efficiency as evident in the MMS.

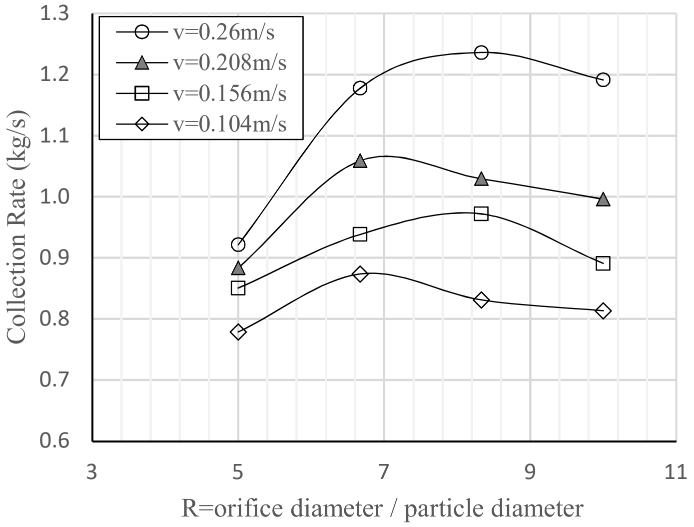

Figure 11-21: MSS - Collection rate versus R = orifice diameter/particle diameter

11.4.4 Overall Sensitivity of Mass Collected and Collection Rate Results

One of the principle objectives was to analyse how changes in orifice diameter, translational velocity, bead size and suction, affected the recovery and collection rate of materials. From all the primary results recorded and the relevant adjustment parameters, the sensitivity of the mass and collection rate outputs were summarised in Table 11-20 and Table 11-21 as follows:

Table 11-20: Overall sensitivity of “mass collected (kg)” outputs

			6mm beads, GB6					**16mm beads, GB16**			
			Translational velocity, v (m/s)					**Translational velocity, v (m/s)**			
			0.104	**0.156**	**0.204**	**0.260**		**0.104**	**0.156**	**0.204**	**0.260**
Without Suction	**Orifice diameter, Do (mm)**	**30**	0.323	0.304	0.323	0.309		0.209	0.192	0.162	0.203
			0.208	0.292	0.318	0.312		0.203	0.218	0.196	0.115
			0.200	0.355	0.312	0.339		0.202	0.189	0.114	0.212
		40	0.601	0.608	0.607	0.650		0.516	0.472	0.453	0.502
			0.625	0.618	0.609	0.606		0.506	0.523	0.462	0.509
			0.595	0.604	0.612	0.594		0.512	0.521	0.511	0.512
		50	1.084	1.058	1.041	1.075		0.900	0.927	0.865	0.825
			1.036	1.043	1.061	1.071		0.836	0.858	0.926	0.894
			1.044	1.046	1.052	1.052		0.851	0.851	0.867	0.899
		60	1.566	1.591	1.591	1.591		1.311	1.306	1.308	1.299
			1.601	1.580	1.541	1.574		1.292	1.283	1.242	1.360
			1.582	1.593	1.595	1.596		1.291	1.311	1.281	1.291
							-				
With Suction	**Orifice diameter, Do (mm)**	**30**	8.591	6.396	4.821	3.975		2.192	3.341	1.922	2.446
			8.681	6.122	4.927	4.155		4.325	3.701	3.017	2.155
			8.561	6.292	4.906	4.097		2.179	3.261	3.620	2.334
		40	9.785	6.934	5.782	5.371		8.240	6.664	4.535	4.298
			9.602	6.907	5.934	5.170		6.640	6.490	2.560	2.869
			9.597	6.913	5.848	5.084		9.320	6.823	3.975	3.684
		50	9.458	7.314	5.541	5.585		9.601	6.865	5.116	4.802
			8.988	6.895	5.744	5.380		9.386	6.761	5.504	4.981
			9.129	7.286	5.790	5.437		9.129	6.986	5.790	5.437
		60	9.184	6.706	5.656	5.659		9.703	7.194	6.207	5.183
			8.818	6.567	5.526	5.008		9.268	6.811	5.781	5.208
			8.983	6.430	5.339	5.139		9.383	6.841	5.339	5.169

Table 11-21: Overall sensitivity of "collection rate (kg/s)" outputs

			6mm beads, GB6				16mm beads, GB16			
			Translational velocity, v (m/s)				Translational velocity, v (m/s)			
			0.104	**0.156**	**0.204**	**0.260**	**0.104**	**0.156**	**0.204**	**0.260**
Without Suction	**Orifice diameter, Do (mm)**	**30**	0.029	0.041	0.058	0.070	0.019	0.026	0.029	0.046
			0.029	0.040	0.058	0.071	0.018	0.030	0.035	0.026
			0.028	0.048	0.056	0.077	0.018	0.026	0.021	0.048
		40	0.054	0.082	0.110	0.147	0.047	0.064	0.082	0.113
			0.057	0.084	0.110	0.137	0.046	0.071	0.084	0.115
			0.054	0.082	0.111	0.134	0.046	0.071	0.092	0.116
		50	0.098	0.144	0.188	0.243	0.081	0.126	0.156	0.187
			0.094	0.141	0.192	0.242	0.076	0.116	0.167	0.202
			0.094	0.142	0.190	0.238	0.077	0.115	0.157	0.203
		60	0.142	0.216	0.288	0.360	0.119	0.177	0.237	0.294
			0.145	0.214	0.279	0.356	0.117	0.174	0.225	0.307
			0.143	0.216	0.288	0.361	0.117	0.178	0.232	0.292
-										
With Suction	**Orifice diameter, Do (mm)**	**30**	0.777	0.868	0.872	0.899	0.198	0.453	0.348	0.553
			0.785	0.830	0.891	0.939	0.391	0.502	0.546	0.487
			0.774	0.854	0.887	0.926	0.197	0.442	0.655	0.528
		40	0.885	0.941	1.046	1.214	0.745	0.904	0.820	0.972
			0.868	0.937	1.073	1.169	0.600	0.880	0.463	0.649
			0.868	0.938	1.058	1.149	0.843	0.926	0.719	0.833
		50	0.855	0.992	1.002	1.263	0.868	0.931	0.925	1.086
			0.813	0.935	1.039	1.216	0.849	0.917	0.996	1.126
			0.826	0.988	1.047	1.229	0.826	0.948	1.047	1.229
		60	0.831	0.931	0.925	0.925	0.877	0.976	1.123	1.172
			0.797	0.917	0.996	0.996	0.838	0.924	1.046	1.177
			0.812	0.948	1.047	1.047	0.849	0.928	0.966	1.169

The colour signatures, where green indicated a high magnitude and red a low magnitude, highlighted the influence of the adjusted parameters. In the system without suction, an optimal mass output and collection rate was achieved using the highest translational velocity and largest orifice size. In retrospect, the system with suction has the highest "mass collected" for the lowest translational velocity (holding the flow rate constant) and maximum "collection rate" for the greatest translational velocity.

In the MSS, it posed the question, what parameter was of greater interest. A high mass output translates to good recovery, whereas a high collection rate translates to more particles collected over time. From an economical constraint where certain production targets must be met for the system to be financially feasible, a company or industry may go for a higher collection rate and a lower recovery.

Hypothetically, the optimal design in terms of translational velocity and orifice size can be determined by weighting the two different sets of outputs (mass collected and collection rate). Consider 6mm beads (GB6) in a system without suction, a translational velocity of v = 0.260m/s and an orifice diameter of D_o = 30mm. The mass collected and collection rate were 0.323kg and 0.029kg/s respectively. Assuming, the interested party or designer opted for a greater collection rate, say 70 % and a lower mass collected (recovery) of around 30%. The weighting of these outputs were as follows:

$$\text{Weighted output} = 30\%\left(\frac{\text{Mass collected (kg)}}{\text{Max output in quadrant}}\right) + 70\%\left(\frac{\text{Collection rate (kg/s)}}{\text{Max output in quadrant}}\right)$$

$$\text{Weighted output} = 30\%\left(\frac{0.323}{1.601\text{kg}}\right) + 70\%\left(\frac{0.029}{0.361\text{kg/s}}\right)$$

$$\text{Weighted output} = 0.0605 + 0.0562$$

$$\text{Weighted output} = 0.117$$

The same process was carried out for each of the combinations available. Doing this, the optimal sensitivity analysis for the two different systems (MMS and MSS) was produced. From Table 11-22, the combinations of variables which gave the best performance of the nozzle were highlighted. This was related to the weighting previously set, which was a trivial parameter based on the targeted specifications of the system.

Additionally, one must also consider the likelihood of irregular flow occurring. Although not as big of a concern in MMS, the MSS was subjected to instances of jamming when the orifice diameter and particle inlet velocity was too high. Therefore, caution should be given when selecting the highest translational velocity (v = 0.260m/s) in the MSS.

Table 11-22: Sensitivity for Optimal Design

			6mm beads, GB6				16mm beads, GB16			
			Translational velocity, v (m/s)				Translational velocity, v (m/s)			
			0.104	**0.156**	**0.204**	**0.26**	**0.104**	**0.156**	**0.204**	**0.26**
Without Suction	**Orifice diameter, Do (mm)**	**30**	0.117	0.137	0.174	0.193	0.089	0.102	0.102	0.149
			0.116	0.132	0.171	0.195	0.087	0.115	0.124	0.085
			0.112	0.160	0.168	0.212	0.086	0.100	0.072	0.156
		40	0.218	0.274	0.327	0.407	0.220	0.250	0.286	0.369
			0.227	0.278	0.3 28	[illegible]	[illegible]	[illegible]	0.292	0.374
			0.216	0.272	0.329	[illegible]	[illegible]	[illegible]	0.323	0.376
		50	0.393	0.477	0.560	[illegible]	0.384	0.491	0.547	0.607
			0.376	0.470	0.571	0.670	0.357	0.454	0.586	0.657
			0.379	0.471	0.566	0.659	0.363	0.451	0.548	0.661
		60	0.568	0.717	0.856	0.996	0.559	0.691	0.827	0.955
			0.581	0.712	0.829	0.985	0.551	0.679	0.785	1.000
			0.574	0.718	0.859	0.999	0.551	0.694	0.810	0.949
							-			
With Suction	**Orifice diameter, Do (mm)**	**30**	0.694	0.677	0.631	0.620	0.181	0.361	[illegible]	0.391
			0.701	0.648	0.645	0.648	[illegible]	[illegible]	[illegible]	0.344
			0.692	0.666	0.642	0.639	[illegible]	[illegible]	[illegible]	0.373
		40	0.791	0.734	0.757	0.838	0.679	0.721	0.607	0.686
			0.776	0.731	0.777	0.806	0.547	0.702	0.343	0.458
			0.775	0.732	0.766	0.793	0.768	0.738	0.532	0.588
		50	0.764	0.774	0.725	0.871	0.791	0.743	0.685	0.767
			0.726	0.730	0.752	0. 839	0.774	0.731	0.737	0.795
			0.738	0.771	0.758	0.848	0.752	0.756	0.775	0.868
		60	0.742	0.722	0.686	0.686	0.800	0.778	0.831	0.828
			0.712	0.710	0.721	0.705	0.764	0.737	0.774	0.832
			0.726	0.722	0.744	0.738	0.773	0.740	0.715	0.825

Without suction (MMS)
Velocity = 0.26 m/s
Orifice diameter = 60mm

With suction (MSS)
Velocity = 0.26 m/s
Orifice diameter = 50/60mm

11.5Analysis of Secondary Tests

Additional tests were undertaken as a direct investigation into the modification of certain physical aspects within the nozzle interface and testing of a varied bed composition. The tests were performed using default parameters where relevant and adjusted according to the type of test carried out (MMS or MSS).

11.5.1 Multiple Orifice Flow

Having completed numerous tests on orifices of different sizes, further inquisitions were made on the effects of multiple orifices on a single plane. Out of the same material, three $D_o = 50$mm cuts were made into a 300mm x 80mm nozzle face, depicted as shown (Detailed drawings in Appendix A):

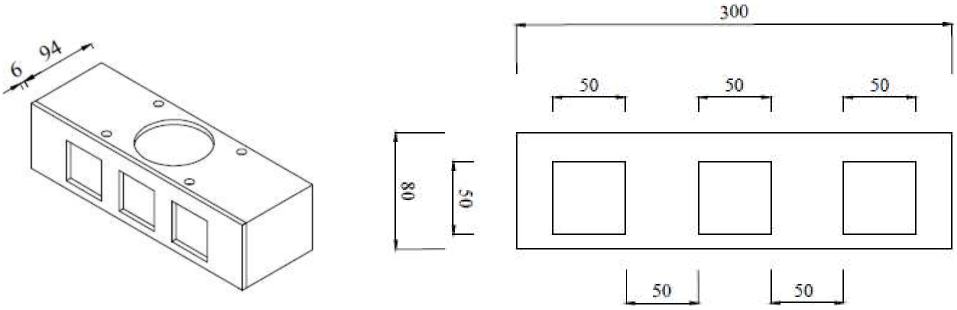

Figure 11-22: Design of multiple orifice nozzle

Adjustments were made to the spacing of the orifices which included 25mm and 50mm gaps between them. Under MMS conditions, the measured outputs were seemingly similar for both spacing proposals. This was found to be the case as the effective recovery was not high enough (>1) to penetrate the materials in the surrounding channel. As a result, it was not necessary to evaluate the MMS orientated tests. On that account, the MSS tests were more relevant whereby the effective recovery was great enough as given in Table 11-23.

Table 11-23: Effective recovery of GB6 in MSS setup

Iteration	Effective Recovery (-)							
	25mm Spacing				50mm Spacing			
	v = 0.104	v = 0.156	v = 0.208	v = 0.260	v = 0.104	v = 0.156	v = 0.208	v = 0.260
1	1.693	1.247	1.110	0.947	1.784	1.368	1.176	0.972
2	1.662	1.242	1.081	0.948	1.752	1.370	1.175	0.996
3	1.688	1.228	1.099	0.953	1.774	1.372	1.161	0.979
Average	1.681	1.239	1.097	0.949	1.770	1.370	1.171	0.982

For 50mm spacing it was observed that a greater recovery ratio was obtained as a direct result of the amount of material entrained. Additionally, the collection rates for the two spacing configurations were quantitatively less than for if the collection rates for a singular 50mm diameter orifice were scaled by a factor of three. This was due to the absence of secondary influences caused by added orifices. The data in the form of collection rate outputs were normalised graphically for a more detailed representation of changes in orifice spacing (Figure 11-23).

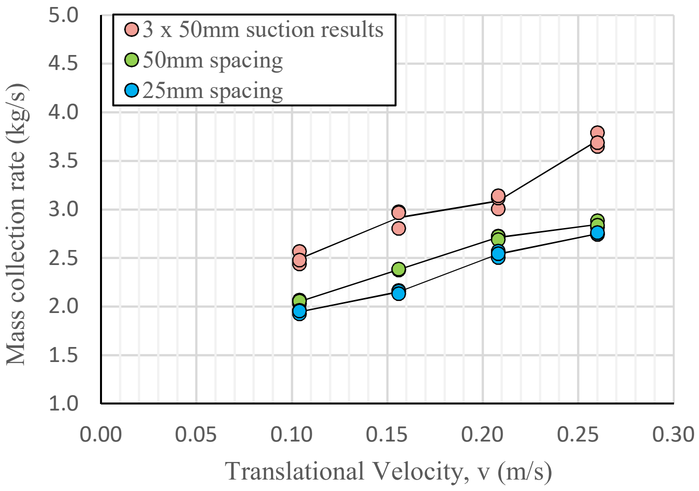

Figure 11-23: Graphical representation of collection rate for multiple orifices

Conceptually the effect was explained using Figure 11-24. The lesser spacing covers a smaller range of materials following the influence of suction beyond the orifice face. Although just a concept, there exists a region in between the orifices where particles are succumbed to less critical suction forces, also known as the dead zone. Therefore, it can be said that an equilibrium or optimum scenario exists whereby the collection rate is great enough to reach an adequate yield yet efficient enough to recover as much material as possible to avoid wastage. Evidently, there is lack of knowledge pertaining to such a system, eluding to the need for computational fluid mechanics to better understand flow behaviours. This was considered to be outside the scope of this study but the overall investigation of multiple orifices was relevant in that there were alternative approaches in improving granular flow.

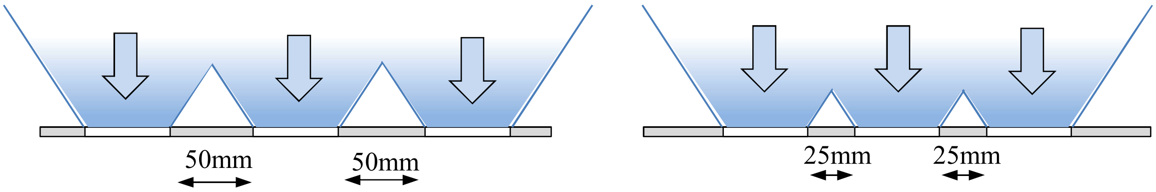

Figure 11-24: Conceptual illustration of flow effects as a function of orifice spacing

The geometry of the new nozzle face (0.3m x 0.08m) was used to verify the increase in effective recovery. The ratio, R, between the area of the orifices and the area of the nozzle was determined to be 0.313 as opposed to 0.208, the ratio for the smaller nozzle (0.15m x 0.08m). Ideally, the aim would be to design for a ratio as high as possible where a greater value correlates strongly to a greater yield. Consequently, this was found to not be the case when suction was implemented. With regards to Figure 11-24, an identical ratio of 0.313 was calculated for both configurations. However, the 50mm spacing gave a greater yield than the 25mm spacing as explained earlier. In an extreme case, a singular orifice with the same area ratio could be used instead of employing multiple orifices. This though to potentially be a method of collecting particles at a more concentrated rate with less wastage. Alternatively, implementing multiple orifices increases the volume of particles recovered.

The discussion raised the question about the conditions under which such systems may be applicable. Suitability was determined to be oriented around the properties of the particles and the operating parameters. For instance, if a flow rate were to be great enough such that for multiple orifices, minimal wastage would occur, it would be more beneficial and economical. On the other hand, in the case of vast quantities of residual materials, a singular orifice may be preferred. This is just one of the many scenarios that exist. Other factors can include targeted particle size or the energy required to lift the solid's concentrations through the suction pipe.

Of great insight was the comparison of recovery ratios between the use of multiple orifice face (0.3m x 0.08m) and the singular orifice face (0.15m x 0.08m). For a greater orifice to nozzle ratio, the normal (channel) recovery of a system would increase. For example, with an area ratio of 0.313, an effective recovery ratio as high as 0.991 was recorded, this was greater than the 0.820 ratio measured for the smaller D_o = 50mm nozzle (MSS conditions). In contrast, the effective recovery was greater for the smaller nozzle as there were no suction interferences caused by additional openings.

11.5.2 50/50 Composition of 6mm and 16mm Glass Beads

In material handling and mining industries, the particles that are dealt are seldom uniform. For interest, a composition of the two different particle sizes was used. With a 50/50 mixture, the prepared bed was tested under default conditions for both MMS and MSS configurations. Note that the frequency (29.5Hz) utilised for GB16 was used, leading to comparisons only applicable between two configurations. The measured collection rates were detailed in Figure 11-25.

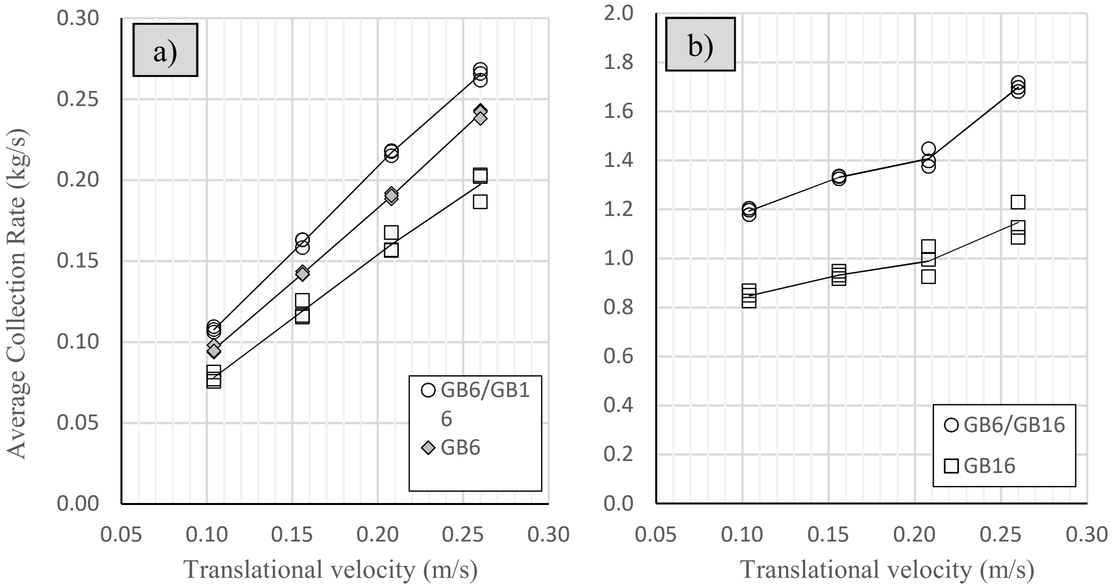

Figure 11-25: Average collection rate for 50/50 composition in a) MMS and b) MSS

Results of the MMS and MSS were expected. When entraining particles without suction, the GB6 occupy void spaces created from the larger GB16, effectively increasing the bulk density of the granular bed from $\rho_b = 1485\text{kg/m}^3$ to 1531kg/m^3 (Detailed in Appendix F). The inclusion of suction affected the collection of particles completely differently. Due to the addition of two unique particle sizes and a flow rate of 5.0*l*/s, the spherical elements were subjected to different velocities. With an already increased bulk density, the GB6 travelled at velocities significantly higher than the GB16, thus, further compounding the total granular flow rate. Approximately 60% of the materials collected in the MSS were GB6, supporting the preceding claim.

On the other hand, in the MMS, the percentage breakdown of particles entrained was found to be 70% GB6 and 30% GB16. This was found to be peculiar as one would assume a 50/50 ratio. Again, this was attributed to the difficulty of larger particles passing through an orifice (i.e. empty annulus), thus essentially generating a bulldozing effect where smaller particles can pass through and the larger ones are left behind. The 60% of GB6 achieved in the MSS was the product of suction, aiding in the passing of GB16 through the orifice.

In Figure 11-25b, behaviour similarities were observed between the mixture and GB16. In assessing the percentage breakdown of particle sizes entrained, the collection rate increased to a maximum value of 1.7kg/s with an orifice diameter D_o = 50mm.

11.6 Scaling Succession of Experiment

Development of theories and relations rely on their acceptance amongst real-life systems. In this scenario where a small scaled-model was used to investigate the behaviour of granular flow, scaling laws (Appendix G) were implemented such that for life-size prototypes or models the features or findings investigated would be applicable. An effective method of verifying the scaling properties was to implement practical adjustments to the geometric and kinematic parameters of the model and setup. A scaling ratio of 2.67 was applied, which was based on the ratio between the two bead diameters (GB6 & GB16). Regarding complete similitude as specified in Appendix G, the following geometries were scaled:

Table 11-24: Scaling verification of experimental setup

Parameter	Scale factor	Initial	Final
Diameter of orifice	$\lambda = 2.67$	60mm	22.5mm
Diameter of particle	$\lambda = 2.67$	16mm	6mm
Channel length	$\lambda = 2.67$	1.15m	0.431m
Velocity	$\lambda^{1/2} = 1.633$	0.26 m/s	0.159 m/s
Bed height	$\lambda = 2.67$	50mm	18.73mm
Mass entrained	$\lambda^3 = 18.963$	1.295 kg	0.0683 kg

To verify the scaling of the experiment, the mass output from the scaling was to correspond with measured results of the scaled experiment. Testing of GB6 under the scaled parameters yielded an output of 0.0680kg (the recorded data can be found in Appendix B). This corresponded with the calculated mass of 0.0683kg, with an accuracy of 99.6%. For a wider range of R, the outputs obtained for GB6 and GB16 were plotted onto a single graph in accordance with the preceding scaling rule.

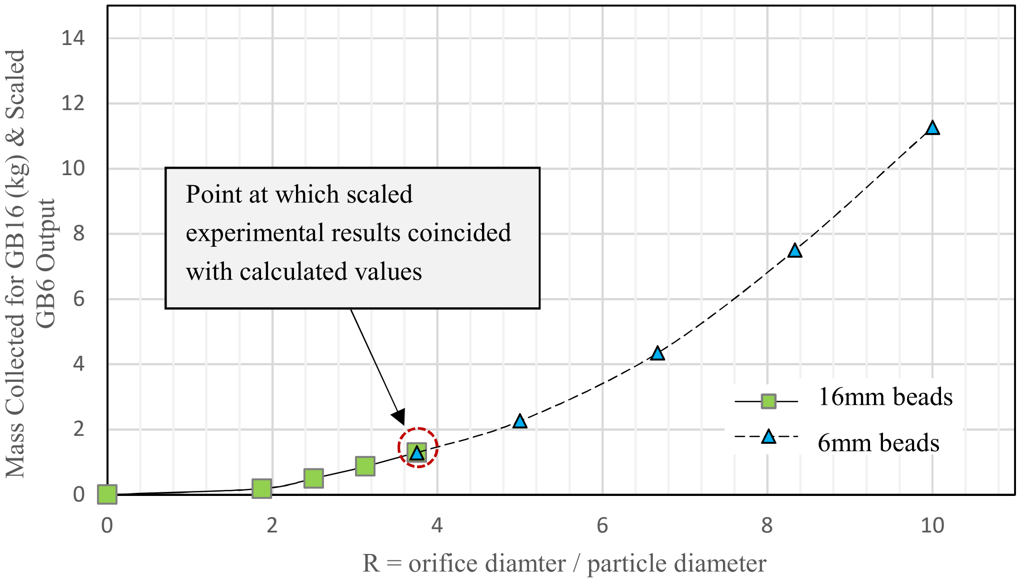

Figure 11-26: Scaling verification of experimental setup between GB6 and GB16

12. Conclusions and Recommendations

12.1 Introduction

The assessments made serve as a guideline for future studies in similar areas. Although categorised as granular flow, the project dealt with multiple engineering aspects that may be applicable in other areas of work. The issue of granular flow through an orifice via mechanical movement or hydraulic transport was a complex task. Therefore, an effective approach to such a problem was to make substantiated assumptions and limit the number of variables analysed per setup. The chapter highlighted the conclusions drawn from the analysis and results, whilst providing recommendations in terms improving the study and future research.

12.2 Optimisation of Granular Flow

The experimental results were used to both calibrate the numerical model and to investigate the interface parameters of the nozzle. Minor variances amongst the results were evident but were accounted for through a normalisation process. However, for larger deviations caused by jamming effects or stagnant flow zones within the nozzle where the ratio, $R = D_o/d_p$ was found to have significant influence, further interpretation was needed. By investigating the behaviour of granular flow per specific R, it was found that there existed a region ($R < 3.75$) where flow would become irregular or cease entirely. The main difference between the MMS and MSS was the influence of suction, capable of increasing the output by over 300%. The two systems, although similar in geometry, were operated under unique conditions and governing parameters.

12.2.1 Mechanical Movement System

Under the assumption of constant flow, the ability of spherical particles to flow over the range of tested orifice inlets, was found to follow the Beverloo law when the shape coefficient, $k = 1.225$ and when the discharge coefficient, $C = 0.757$. Determining the collection rate empirically was found to be an appropriate method under the assumptions made. However, the observed discharge rate was not an intrinsic property of the GB since it was influenced by numerous other factors, including the particle geometry, boundary conditions (bed confinement), experimental method and the equipment used (Nedderman et al., 1982).

The equation relates the collection rate, W, to the diameter of the opening, D_o; particle size, d_p, and bulk density, ρ_b (Mankoc et al., 2007). Under a constant velocity, the collection rate, W, was found to be dependent on the orifice diameter, D_o^2, and not $D_o^{5/2}$ as previously stated, supporting the observation made by Aguirre et al. (2010). Additionally, in terms of satisfying the Beverloo expression dimensionally, where any combination of opening size and particle could be used, the term R was introduced such that $W \propto R^2$. This was defined as the ratio between the orifice diameter and particle diameter.

Combined with the determination of the empirical coefficients, *C* and *k*, it was evident that adjustments had to be made to the cited parameters for increased flow properties. The tests further highlighted the possible existence of the “empty annulus” effect, demonstrating how an increase in particle diameter decreased the particle flow. Overall, the predictability of granular flow with the Beverloo law was not applicable as it required several assumptions to hold true. On the other hand, the law was useful in understanding the relations between the various variables at work.

12.2.2 Mechanical Movement and Suction System

In assessing the hydro-mechanical flow behaviour of either 6mm or 16mm glass beads during entrainment, the change in mass output for various distinct orifice sizes within the visualisation tank was evaluated. Changes in mass outputs were estimated to be as high as 300% for a 50mm diameter orifice and at a translational speed of 0.26m/s. It was apparent that the fluid velocity through the orifice had a significant influence on particle entrainment. The velocity dictated both the concentration and recovery of particles.

Predicting flow required knowledge of the average volumetric concentration of particles entering the opening. The values varied from 0.041 to as high as 0.151. In practice, these values were generally measured instantaneously using devices such as an electromagnetic flowmeter. Other considerations were given to secondary effects related to jamming, where it was found that the orifice had to be > 3.75 times the size of the particle for readings to be valid.

12.2.3 Design Approach

Optimisation of granular flow was related to three aspects. This included a) a high recovery b) a high volumetric concentration and c) a low jamming probability. However, an increase in one variable did not necessarily lead to an increase in the others, instead it had the potential to lower the total output. With this said, there was reason to believe that there existed a region where a combination of these aspects produced the most efficient flow. Based on the results and sensitivity analysis, the optimal recovery efficiency and collection rate for a nozzle system without suction would be one with the greatest translational velocity and largest orifice size. In contrast for the system with suction, an orifice diameter of 50mm at a speed of 0.260m/s would be the optimum when a mass collected of 30% and collection rate of 70% was selected.

12.2.4 Concluding Remarks

The results, theories and techniques used, can be extended into other studies of driven granular flow. The experimental and numerical results successfully showed the level of influence of the parameters investigated. By the end of the study, the reader should have a clear understanding of certain parameters should be adjusted to maximise the performance of a system with regards to particle entrainment through an orifice.

12.3 Further Research

The research represented great strides in the understanding of particle movement through an orifice. The following are the recommendations for future study:

12.3.1 Coupled DEM and Computational Fluid Dynamics

One of the notable limitations within this study was the absence of the numerical simulation for the hydraulic transport of particles. A numerical study of such a phenomenon would provide a comparative platform for both MMS and MSS studies. It is recommended that computational fluid dynamics (CFD) coupled with DEM be applied. The method makes use of applied mathematics and computational software to investigate the behaviour of complex flows.

12.3.2 Improvement of Experimental Setup

One of the main underlying limitations encountered throughout the entire testing process was the potential influence of boundary effects. Although not visually obvious in the experimental tests, the Rocky data demonstrated instances of such effects. Revisiting the graphical outputs, the instant normal force showed a dip in magnitude towards the end of the simulation, suggesting boundary limitations. It is recommended that a larger sample space be used to minimise such effects. Additionally, the spherical glass beads had low friction properties that, when agitated, were easily dispersed. Initial stabilisation of the bottom layer of beads was achieved but during entrainment they were recorded to shear with ease. Therefore, instead of a Plexiglas foot wall, a surface with high frictional properties should be implemented.

12.3.3 Advanced Monitoring Devices

The data measured was extensive but was thought to define only some of the behaviours encountered. More advanced monitoring devices should be installed to have a better understanding of the behaviours and forces present around the interface. For example, the pressure difference across an orifice can be measured using an orifice meter or electromagnetic flowmeter.

12.3.4 Testing a Wider Range of Materials

The use of granular particles with a wider particle size distribution (PSD) is recommended. The wider distribution would make the study more relevant to the current entrainment systems used in practice. Additionally, larger ranges of the ratio between the orifice and particle diameter should be used to validate the Beverloo law under such larger ranges and to verify the occurrence of jamming within fluid-driven flow

References

1) ABB. 2008. Variable-Speed Drive: ABB Technology Guide.
Available: www.abb.com/energyefficiency.

2) Aguirre, M.A., Grande, J.G., Calvo, A., Pugnaloni, L.A. & Géminard, J.C. 2010. Pressure Independence of Granular Flow through an Aperture. Physical Review Letters.

3) Ahmad, M. & Pilpel, N. 1969. Flow of Granular Solids through Horizontal Orifices. Rheologica Acta. 8(4):448–456

4) Al-Khafaji, A.W. & Andersland, O.B. 2007. Geotechnical Engineering and Soil Testing. New York: Oxford University Press.

5) Aguirre, M.A., De Schant, R. & Géminard, J.C. 2014. Granular Flow through an Aperture: Influence of the Packing Fraction. HAL.

6) Anderson, J.L. 2002. Manning's Formula by Any Other Name. In Environmental and Water Resources History. Reston: American Society of Civil Engineers. 44–54.

7) Andreotti, B., Forterre, Y. & Pouliquen, O. 2013. Granular Media: Between Fluid and Solid. New York: Cambridge University Press.

8) Bagnold, R.A. 1954. Experiments on a Gravity-Free Dispersion of Large Solid Spheres in a Newtonian Liquid under Shear. In Proceedings Roy. London. 49–63.

9) Bagnold, R.A. 1956. The Flow of Cohensionless Grains in Liquids. In Proceedings Roy. London. 235–297.

10) Baker, E., Gaill, F., Karageorgis, A. & Lamarche, G. 2016. Offshore Mining Industries. In Assessment of Other Human Activities and the Marine Environment. United Nations, Ed. Cambridge University Press. 363–378.

11) Barbour, S.L. & Krahn, J. 2004. Numerical modeling-prediction or process? Geotechnical News. 22(December):44–52. Available: http://www.geo-slope.com/res/numerical modelling - prediction or process.pdf.

12) De Beers Group. 2016. De Beers Group of Companies.
Available: https://www.debeersgroup.com/en/reports/library.html [2016, April 16].

13) De Beers UK Limited. 2017. De Beers Group of Companies.
Available: http://www.debeersgroup.com/en/explore-de-beers/mining.html [2017, April 09].

14) Beverloo, W.A., Leniger, H.A. & van de Velde, J. 1961. The Flow of Granular Solids through Orifices. Chemical Engineering Science. 15(3–4):260–269.

15) Bloodgood, D.E. & Bell, J.M. 1961. Manning's Coefficient Calculated from Test Data. Water Pollution Control Federation. 33:176–183.

16) Du Boys, P. 1879. Study of the Flow Regime and of the Action Exerted by the Waters on a Bed with Indefinitely Scalable Gravel. Annales des Ponts et Chaussées. 8(49):141–195.

17) Brass, P., Moser, W.O.J. & Pach, J. 2005. Research Problems in Discrete Geometry. New York: Springer.

18) Bray, R.N., Bates, A.D. & Land, J.M. 1979. Dredging : a Handbook for Engineers. London: London: Arnold.

19) British Standards Institution. 2000. Code of Practice for Dredging and Land Reclamation. In (BS 6349-5:1991). United Kingdom: British Standards Institution.

20) Brook, C. 2013. Horizontal Directional Ground Investigation-Reducing Tunneling Risks by Minimising Geological Uncertainty. Tunneling and Underground Construction Society.

21) Brown, R.L. & Richards, J.C. 1959. Profile of Flow of Granules through Apertures. Trans. Inst. Chem. Eng. 38:243–256.

22) Cavarretta, I., Coop, M. & O'Sullivan, C. 2010. The Influence of Particle Characteristics on the Behaviour of Coarse Grained Soils. Géotechnique. 60(6):413–423.

23) Charlier, R.H. 1992. Mining Potential of the Inner Continental Shelf. In Planning the Use of the Earth's Surface. Berlin: Springer-Verlag. 331–370.

24) Chung, J.S. 1991. Deep-Ocean Mining: Technologies for Manganese Nodules and Crusts. International Journal of Offshore and Polar Engineering. 6(4).

25) Clayton, C.R., Siddique, A. & Hopper, R.J. 1998. Effects of Sampler Design on Tube Sampling Disturbance-Numerical and Analytical Investigations. Geotechnique. 48(6):847–867.

26) Coetzee, C.J. 2017. Review: Calibration of the Discrete Element Method. Powder Technology. 310:104–142.

27) Coetzee, C.J. & Els, D.N.J. 2009. Calibration of Discrete Element Parameters and the Modelling of Silo Discharge and Bucket Filling. Computers and Electronics Agriculture. 65(2):198–212.

28) Coulson, J.M., Richardson, J.F., Backhurst, J.R. & Harker, J.H. 1999. Coulson and Richardson's Chemical Engineering. Volume 1: Fluid Flow, Heat Transfer and Mass Transfer. Great Britain: Butterworth-Heinemann.

29) Craig, R.F. & Knappett, J.A. 2012. Craig's Soil Mechanics. V. 8. New York: Spon Press.

30) Cronan, D.S. & David, S. 1999. Handbook of Marine Mineral Deposits. CRC Press.

31) Cui, D., Wu, W., Xiang, W., Doanh, T., Chen, Q., Wang, S., Liu, Q. & Wang, J. 2017. Stick-Slip Behaviours of Dry Glass Beads in Triaxial Compression. Granular Matter. 19(1).

32) Cundall, P.A. & Strack, O.D.I. 1979. A Discrete Numerical Model for Granular Assemblies. Geotechnique. 29(1).

33) Cunningham, B., Tam, J.K.W., Tattersall, J.W. & Seit, R.F.K. 2013. Horizontal Directional Coring (HDC) and Groundwater Inflow Testing for Deep Subsea Tunnels. Hong Kong.

34) Currell, G. & Dowman, A. 2009. Essential Mathematics and Statistics for Science Second Edition. Chippenham, Wiltshire: John Wiley & Sons.

35) Danson, E. 2005. Geotechnical and Geophysical Investigations for Offshore and Nearshore Developments. Netherlands: Technical Committee 1.

36) Das, B.M. 2000. Fundamentals of Geotechnical Engineering. V. 3. United States: Chris Carson.

37) Das, B.M. 2011. Geotechnical Engineering Handbook. J.Ross Publishing.

38) De-Song, B., Xun-Sheng, Z., Guang-Lei, X., Zheng-Quan, P., Xiao-Wei, T. & Kun-Quan, L. 2003. Critical Phenomenon of Granular Flow on a Conveyor Belt. Physical Review E. 67(6).

39) Dey, S. 2014. Fluvial Hydrodynamics: Hydrodynamic and Sediment Transport Phenomena. New York: Springer Berlin Heidelberg.

40) Donohue, T. 2015. Discrete Element Modelling (DEM) Calibration and Classification of Bulk Material (Reprt#8470). New South Wales, Australia.

41) Emori, R.I. & Schuring, D.J. 1977. Scale Models in Engineering: Fundamentals and Applications. 1st ed. Exeter: Pergamon Press.

42) ESSS, GDI & RDI. 2015. Rocky 3 User Manual (V 3.7.0).

43) Di Felice, R. & Scapinello, C. 2010. On the Interaction between a Fixed Bed of Solid Material and the Confining Column Wall: the Janssen approach. Granular Matter. 12(1):49–55.

44) Evonik. 2017. Evonik Industries: Plexiglas GS/Plexiglas XT.

45) Feng, Y.T. & Owen, D.R.J. 2014. Discrete Element Modelling of Large Scale Particle Systems—I: Exact Scaling Laws. Computational Particle Mechanics. 1(2):159–168.

46) Finnemore, E.J. & Franzini, J.B. 2002. Fluid Mechanics with Engineering Applications. Tenth ed. New York: McGraw-Hill.

47) Fischenich, C. 2000. Robert Manning (A Historical Perspective). Vicksburg.

48) Forterre, Y. & Pouliquen, O. 2011. Granular Flows. In Glasses and Grains. Basel: Springer Basel. 77–109.

49) Fowler, R.T. & Glastonbury, J.R. 1959. The Flow of Granular Solids through Orifices. Chemical Engineering Science. 10(3):150–156.

50) Franklin, F.C. & Johanson, L.N. 1955. Flow of Granular Material through a Circular Orifice. Chemical Engineering Science. 4(3):119–129.

51) Furukawa, K., Imai, K. & Kurashige, M. 2000. Simulated Effect of Box Size and Wall on Porosity of Random Packings of Spherical Particles. Acta Mechanica. 140(3–4):219–231.

52) Garcimartín, A., Mankoc, C., Janda, A., Arévalo, R., Pastor, J.M., Zuriguel, I. & Maza, D. 2009. Flow and Jamming of Granular Matter through an Orifice. In Traffic and Granular Flow '07. Berlin, Heidelberg: Springer Berlin Heidelberg. 471–486.

53) Guariguata, A., Pascall, M.A., Gilmer, M.W., Sum, A.K., Sloan, E.D., Koh, C.A. & Wu, D.T. 2012. Jamming of Particles in a Two-Dimensional Fluid-Driven Flow. Physical Review. 86.

54) Gurney, J.J., Levinson, A.A. & Smith, H.S. 1991. Marine Mining of Diamonds off the West Coast of Southern Africa. Gems and Gemology. 27(4):206–219.

55) Harris, D. 2001. Ill- and Well-Posed Models of Granular Flow. Acta Mechanica. 146(3–4):199–225.

56) Hein, J.R., Mizell, K., Koschinsky, A. & Conrad, T.A. 2013. Deep-Ocean Mineral Deposits as a Source of critical Metals for High- and Green-Technology Applications: Comparison with Land-Based Resources. Ore Geology Reviews. 51:1–14.

57) Heller, V. 2011. Scale Effects in Physical Hydraulic Engineering Models. Journal of Hydraulic Research. 49(3):293–306.

58) Hewakandamby, B.N. 2012. A First Course in Fluid Mechanics for Engineers. Ventus.

59) Heydon, D. 2012. Nautilus Minerals: Annual Report 2012. Sydney.

60) Hirshfeld, D. & Rapaport, D.C. 2001. Granular Flow from a Silo: Discrete-Particle Simulations in Three Dimensions. The European Physical Journal E. 4(2):193–199.

61) Hughes, S.A. 1993. Physical Models and Laboratory Techniques in Coastal Engineering. V. 7. (Advanced Series on Ocean Engineering). WORLD SCIENTIFIC. DOI: 10.1142/2154.

62) Hutter, K. & Wang, Y. 2016. Fluid and Thermodynamics-Volume 2: Advanced Fluid Mechanics and Thermodynamic Fundamentals. Switzerland: Springer Berlin Heidelberg.

63) Hvorslev, M.J. 1949. Subsurface Exploration and Sampling of Soils for Civil Engineering Purposes. Vicksberg, Mississippi.

64) Jackson, M. & della Dora, V. 2009. "Dreams so Big Only the Sea Can Hold Them": Man-Made Islands as Anxious Spaces, Cultural Icons, and Travelling Visions. Environment and Planning A. 41(9):2086–2104.

65) Janna, W.S. 2010. Introduction to Fluid Mechanics. 4th ed. Boca Raton: CRC Press.

66) Janssen, H.A. 1895. Tests on Grain Pressure Silos. Zeitschrift des Vereines Deutscher Ingenieur. 39(35):1045.

67) Kasangaki, G.J. 2012. Experimental Study of Hydro-Mechanical Behaviour of Granular Materials. Heriot-Watt University.

68) Ketchum, M.S. 1929. The Design of Walls, Bins and Grain Elevators. New York: McGraw-Hill.

69) Kirby, M. 2017. Sizing of Openings on Suction Nozzle. Cape Town.

70) Klinkmullker, M., Schreurs, G., Rosenau, M. & Kemnitz, H. 2016. Properties of Granular Analogue Model Materials: A Community Wide Survey. Tectonophysics. (684):23–38.

71) Knight, R.D. 2008. Force and Motion. In Physics for Scientists and Engineers: A Strategic Approach. 2nd ed. San Francisco: Pearson Addison-Wesley. 126–145.

72) Kuehnlein, W.L. 2010. Sub-sea Diamond Mining. In Ship and Offshore. 2nd ed. L. Schulz & S. Sadowski, Eds. Schiff & Hafen. 24–25.

73) Lafond, P.G. 2014. Particle Jamming during the Discharge of Fluid-Driven Granular Flow. Colorado School of Mines.

74) Lafond, P.G., Gilmer, M.W., Koh, C.A., Sloan, E.D., Wu, D.T. & Sum, A.K. 2013. Orifice Jamming of Fluid-Driven Granular Flow. Physical Review. 87.

75) Lai Sang, J. 2017. Volumetric Concentration of Materials in Typical Offshore Mining System. De Beers Marine (Pty) Ltd.

76) Lee, J., Yun, T.S., Lee, D. & Lee, J. 2013. Assessment of K0 Correlation to Strength for Granular Materials. Soils and Foundations. 53(4):584–595.

77) Li, B., Chen, Y. & Chen, J. 2016. Modeling of Soil–Claw Interaction using the Discrete Element Method (DEM). Soil and Tillage Research. 158:177–185.

78) Liu, S., Hu, J., Zhang, R., Dai, Y. & Yang, H. 2016. Development of Mining Technology and Equipment for Seafloor Massive Sulfide Deposits. Chinese Journal of Mechanical Engineering. 29(5):863–870.

79) Lommen, S., Schott, D. & Lodewijks, G. 2014. DEM Speedup: Stiffness Effects on Behaviour of Bulk Material. Particuology. 12:107–112.

80) Lunne, T. & Long, M. 2006. Review of Long Seabed Samplers and Criteria for New Sampler Design. Marine Geology. 226(1–2):145–165.

81) Mankoc, C., Janda, A., Arévalo, R., Pastor, J.M., Zuriguel, I., Garcimartín, A. & Maza, D. 2007. The Flow Rate of Granular Materials through an Orifice. Granular Matter. 9(6):407–414.

82) Matousek, V. 1995. Solids Transportation in a Long Pipeline connected with a Dredge. In XIV World Dredging Congress. Amsterdam, Netherlands. 55–73.

83) Medina, A., Cabrera, D., López-Villa, A. & Pliego, M. 2014. Discharge Rates of Dry Granular Material from Bins with Lateral Exit Holes. Powder Technology. 253:270–275.

84) Mills, A.A., Day, S. & Parkes, S. 1996. Mechanics of the Sandglass. European Journal of Physics. 17:97–109.

85) Mitarai, N. & Nakanishi, H. 2012. Granular flow: Dry and wet. The European Physical Journal Special Topics. 204(1):5–17.

86) Nedderman, R.M., Tüzün, U., Savage, S.B. & Houlsby, G.T. 1982. The Flow of Granular Materials—I. Chemical Engineering Science. 37(11):1597–1609.

87) Newton, R.H. & Dunham, G.S. 1945. The TCC Catalytic Cracking Process for Motor Gasoline Production. Transactions of the American Institute of Chemical Engineers. 41(2):215–232.

88) O'Sullivan, C., Bray, J. & Cui, L. 2006. Experimental Validation of Particle-Based Discrete Element Methods. In GeoCongress. 1–18.
Available: http://ascelibrary.org.ezproxy.uct.ac.za/doi/abs/10.1061/40803(187)5 [2016, April 07].

89) Obermayr, M., Dressler, K., Vrettos, C. & Eberhard, P. 2011. Prediction of Draft Forces in Cohesionless Soil with the Discrete Element Method. Journal of Terramechanics. 48(5):347–358.

90) Osterkamp, W.R. & Morton, R.A. 2005. Mining of Coastal Materials. In Encyclopedia of Coastal Science. Dordrecht: Springer Netherlands. 645–647.

91) Pai, S.-I. 1977. Mixture of Fluid and Solid Particles. In Two-Phase Flows. Wiesbaden: Vieweg Teubner Verlag. 116–167.

92) Le Pennec, T., Ammi, M., Messager, J.C., Truffin, B., Bideau, D. & Garnier, J. 1995. Effect of Gravity on Mass Flow Rate in an Hour Glass. Powder Technology. 85:279–281.

93) Perry, R.H. & Green, D.W. 1997. Perry's Chemical Engineers' Handbook. 7th ed. J.O. Maloney, Ed. New York: McGraw-Hill.

94) Preciosa Ornela. 2011. Glass Beads as Grinding Media. Czech Republic.

95) Pringle, G. 2013. Crawling for Diamonds – DeBeers Marine Mining.
Available: https://grantpringle.wordpress.com/2013/03/14/crawling-for-diamonds-debeers-marine-mining/ [2016, April 14].

96) Ramu, M., Prabhu Raja, V. & Thyla, P.R. 2013. Establishment of Structural Similitude for Elastic Models and Validation of Scaling Laws. KSCE Journal of Civil Engineering. 17(1):139–144.

97) Reynolds, O. 1883. An Experimental Investigation of the Circumstances which determine whether the Motion of Water shall be Direct or Sinuous, and of the Law of Resistance in Parallel Channels. Proceedings of the Royal Society of London. 35(224–226).

98) Richardson, K. 2007. A Perspective of Marine Mining within de Beers. Journal of the Southern African Institute of Mining and Metallurgy. 107(6):393–402.

99) Richardson, K. 2014. Statement of Evidence in Chief of Kevin Richardson on behalf of Trans-Tasman Resources Ltd.

100) Roussel, N., Nguyen, T.L.H. & Coussot, P. 2007. General Probabilistic Approach to the Filtration Process. Physical Review Letters. (11).

101) Royal IHC. 2017. Dredge and Marine Mining. Available: https://www.royalihc.com/en/products/mining/dredge-and-marine-mining [2017, June 24].

102) Seccombe, A. 2014. Submarine “crawlers” save diamond industry. Available: http://www.bdlive.co.za/business/mining/2014/06/19/submarine-crawlers-save-diamond-industry.

103) Serrano, D.A., Sanchez-Silva, F., Klapp, M. & Medina, A. 2015. The Hagen-Beverloo law for outflow of granular solids from holes on side walls. Revista Mexicana de Fisica. 61:207–210.

104) Seville, J., Tüzün, U. & Clift, R. 2012. Processing of Particulate Solids. Springer Science & Business Media.
Available: https://books.google.com/books?id=oCnyCAAAQBAJ&pgis=1 [2016, March 05].

105) Shaughnessy, E.J., Katz, I.M. & Schaffer, J.P. 2005. Introduction to Fluid Mechanics. New York: Oxford University Press.

106) Sheldon, H.G. & Durian, D.J. 2010. Granular Discharge and Clogging for Tilted Hoppers. Granular Matter. 12(6):579–585.

107) Shi, Y. & Zhang, Y. 2008. Simulation of Random Packing of Spherical Particles with Different Size Distributions. Applied Physics A. 92(3):621–626.

108) Shook, C.A., Roco, M.C. & Brenner, H. 1991. Slurry Flow : Principles and Practice. Stoneham: Butterworth-Heinemann.

109) Smith, D.G. 1992. Vibracoring: Recent Innovations. Journal of Paleolimnology. 7(2).

110) Sperl, M. 2006. Experiments on Corn Pressure in Silo Cells – translation and comment of Janssen’s paper from 1895. Granular Matter. 8(2):59–65.
Available: http://link.springer.com/10.1007/s10035-005-0224-z.

111) Soria-Hoyo, C., Valverde, J.M. & Castellanos, A. 2008. Effect of Vibration on Flow Properties of Fine Glass Beads. AIChE Journal. 54(4):886–896.

112) Tighe, B.P. & Sperl, M. 2007. Pressure and Motion of Dry Sand: Translation of Hagen’s Paper from 1852. Granular Matter. 9(3–4):141–144.

113) Ting, J.M., Corkum, B.T., Kauffman, C.R. & Greco, C. 1989. Discrete Numerical Model for Soil Mechanics. Journal of Geotechnical Engineering. 115(3):379–398.

114) Tsuji, T., Nakagawa, Y., Matsumoto, N., Kadono, Y., Takayama, T. & Tanaka, T. 2012. 3-D DEM Simulation of Cohesive Soil-Pushing Behavior by Bulldozer Blade. Journal of Terramechanics. 49(1):37–47.

115) TUDelft. 2017. Dredge Pumps and Slurry Transport.
Available: https://ocw.tudelft.nl/courses/dredge-pumps-and-slurry-transport/?view=readings.

116) Verhoef, P.N.W. 1997. Wear of rock cutting tools: Implications for the Site Investigation of Rock Dredging Projects.

117) Vlasblom, W.J. 2003. Introduction to Dredging Equipment. In Designing Dredging Equipment. 1–27.

118) Wegener, S.B. 2015. Application of a Discrete Element Model to the Analysis of Granular Soil Recovery in an Offshore Tubular Vibrocore.

119) Wyatt, C. & Miller, H. 2013. The Use of High Pressure Waterjets to Improve Performance of Rotary Cutter Head Dredges from the Inside Out. 2013 WJTA-IMCA Conference and Expo.

120) Xie, X. & Puri, V.M. 2006. Uniformity of Powder Die Filling using a Feed Shoe: A review. Particle Science Technology. (24):411–426.

121) Yalin, M.S. 1971. Theory of Hydraulic Models. 1st ed. V. 1. E.M. Wilson, Ed. London: The Macmillan Press Ltd.

122) Yaskawa. 2002. E7 Drive User Manual.
Available: http://www.vfds.com/manuals/yaskawa-e7-manual.pdf.

123) Yell, D. & Riddell, J. 1995. ICE Design and Practice Guides-Dredging. London: Thomas Telford Publications.

124) Young, D.F., Munson, B.R., Okiishi, T.H. & Huebsch, Wade, W. 2011. A Brief Introduction to Fluid Mechanics. 5th ed. J. Welter, Ed. Jefferson: Don Fowley.

125) Zatloukal, Z. & Šklubalová, Z. 2012. Effect of Orifice Geometry on Particle Discharge Rate for a Flat-Bottomed, Cylindrical Hopper. Particulate Science and Technology. 30(4):316–328.

APPENDIX A

Detailed Drawings

Main Test

Nozzle Face Components

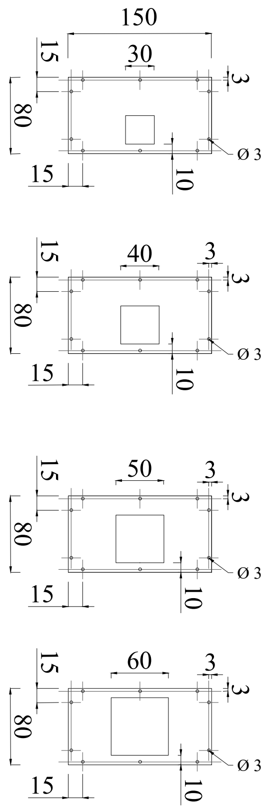

Front View

Nozzle Body Components

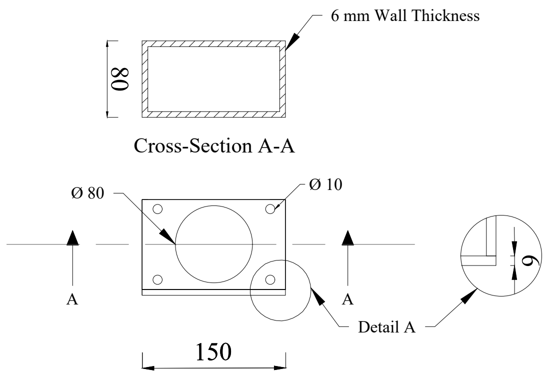

Top View

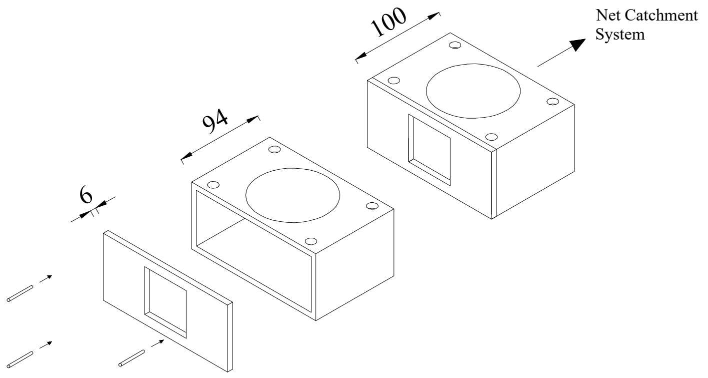

Assembly of Nozzle

Flange Components

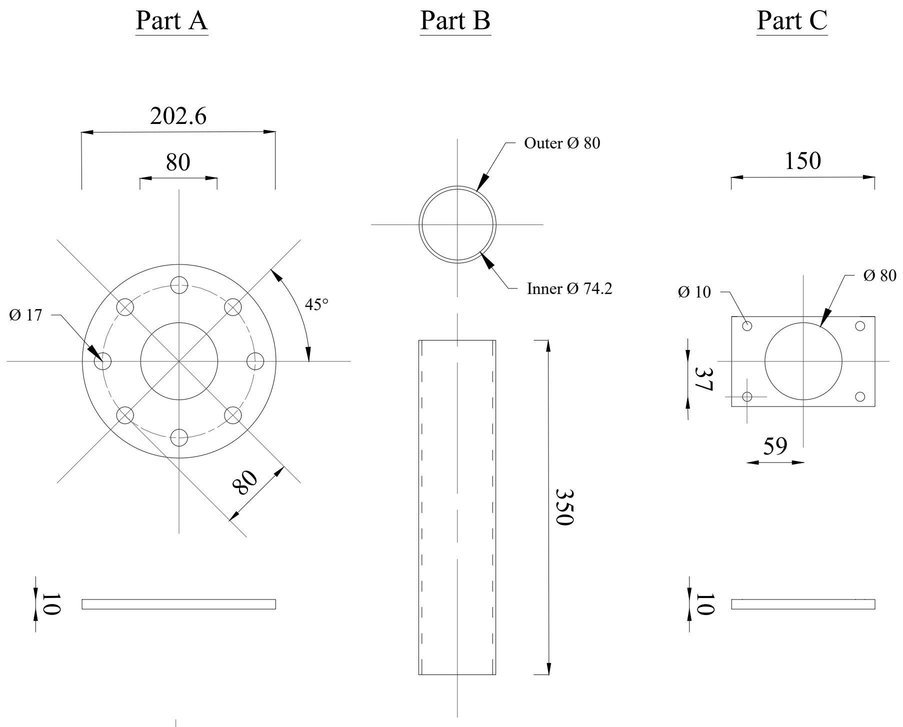

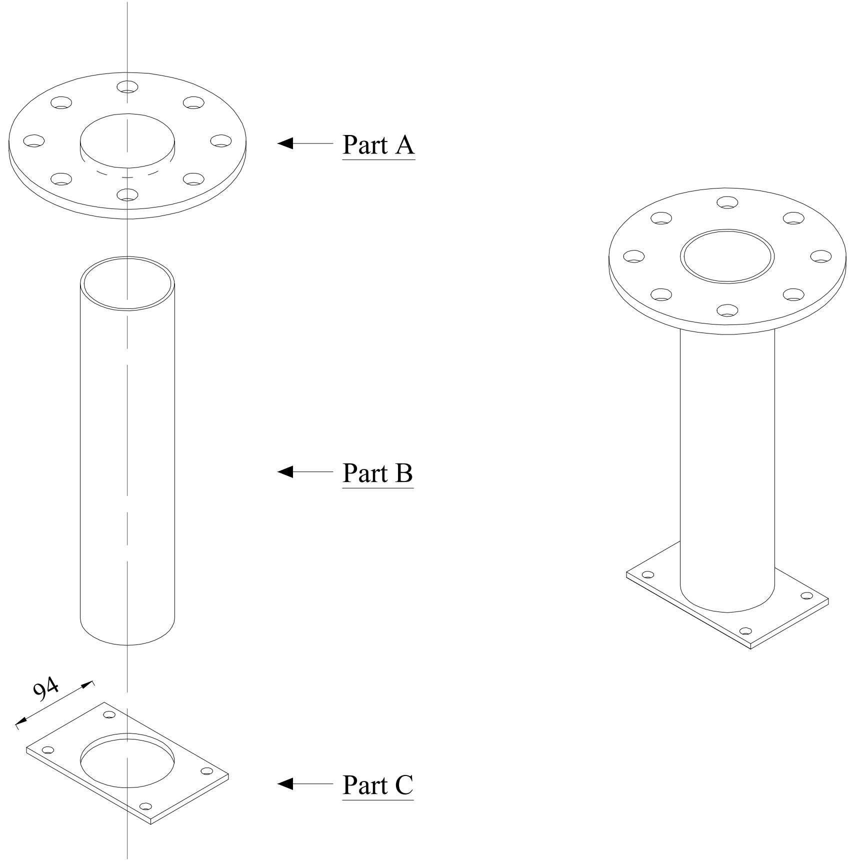

Assembly of Flange

GENERAL NOTES:
1. ALL DIMENSIONS IN MILLIMETERS
2. DIMENSIONS NOT TO SCALE

DEPARTMENTAL DETAILS:

DEPARTMENT OF CIVIL ENGINEERING

UCT
PRIVATE BAG X3
RONDEBOSCH
7701

EMAIL: civ-snape@uct.ac.za
FAX: +27 021 889 7471
TEL: +27 021 850 2584

UNIVERSITY OF CAPE TOWN

PRINCIPAL RESEARCHER/STUDENT SIGNATURE:

SUPERVISOR(S) SIGNATURE

PROJECT/PROJEK:

Granular Flow

DRAWING TITLE:

Nozzle Design

DATE/ DATUUM:	SCALE/ SKAAL:	PAPER SIZE/ PAPIERGROOTE:
15/09/2017	VARIES	A3
DRAWN BY:	ZHENGHUI QIU	

Secondary Test

Multiple Orifice Nozzle

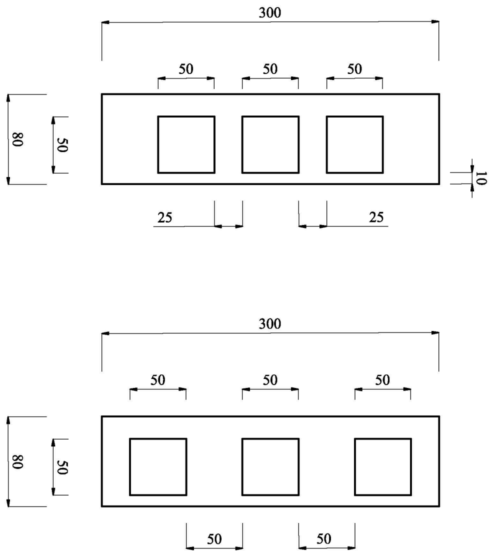

Front View

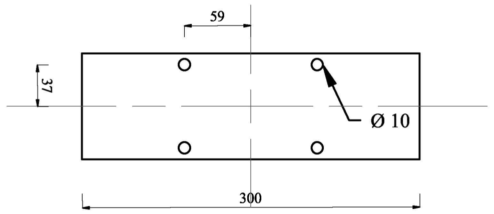

Top View

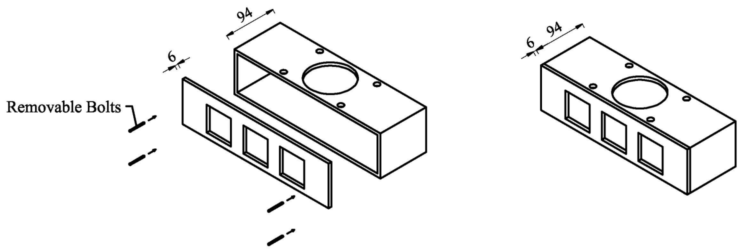

Assembly of Multiple Orifice

Complete Setup

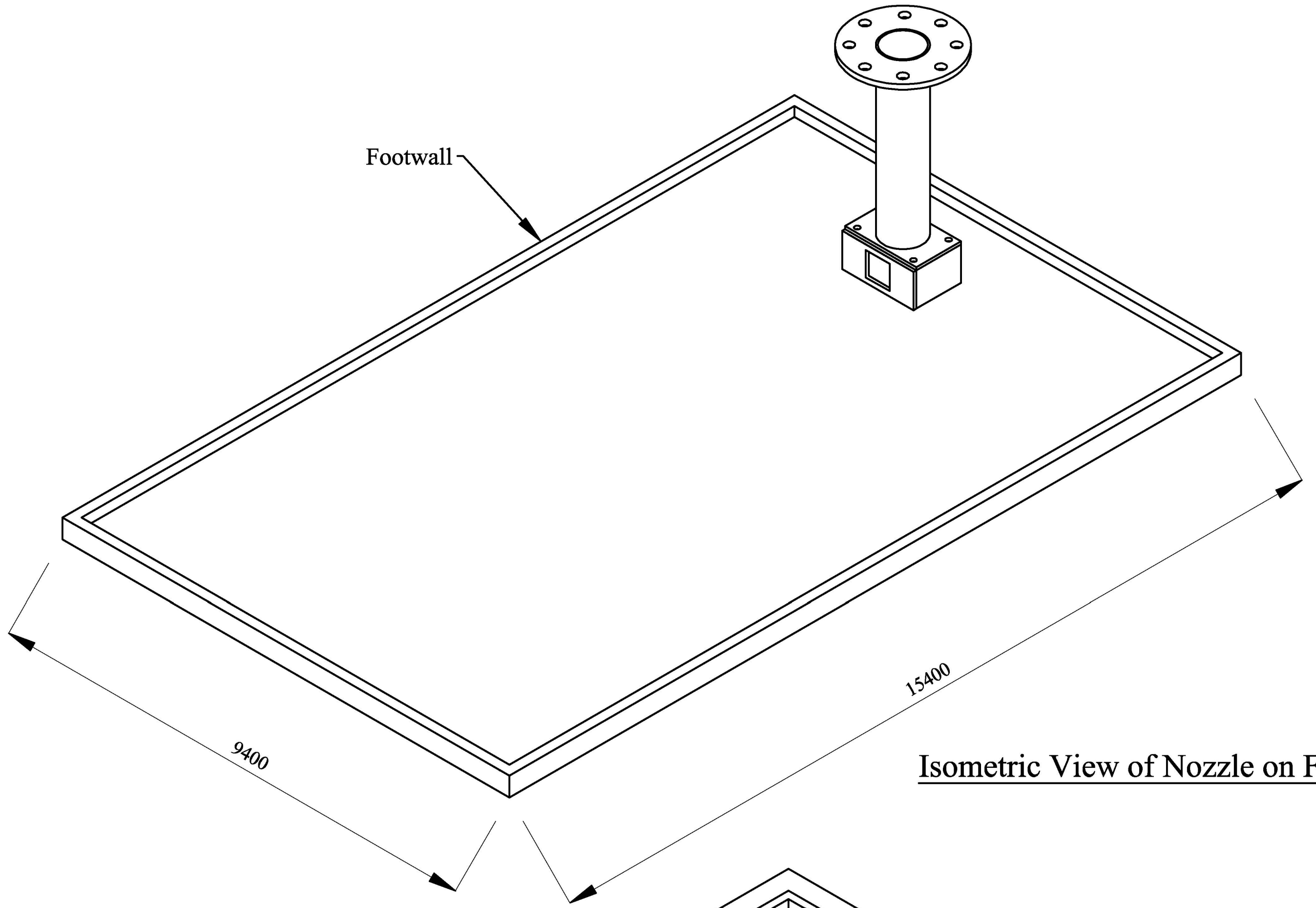

Isometric View of Nozzle on Footwall

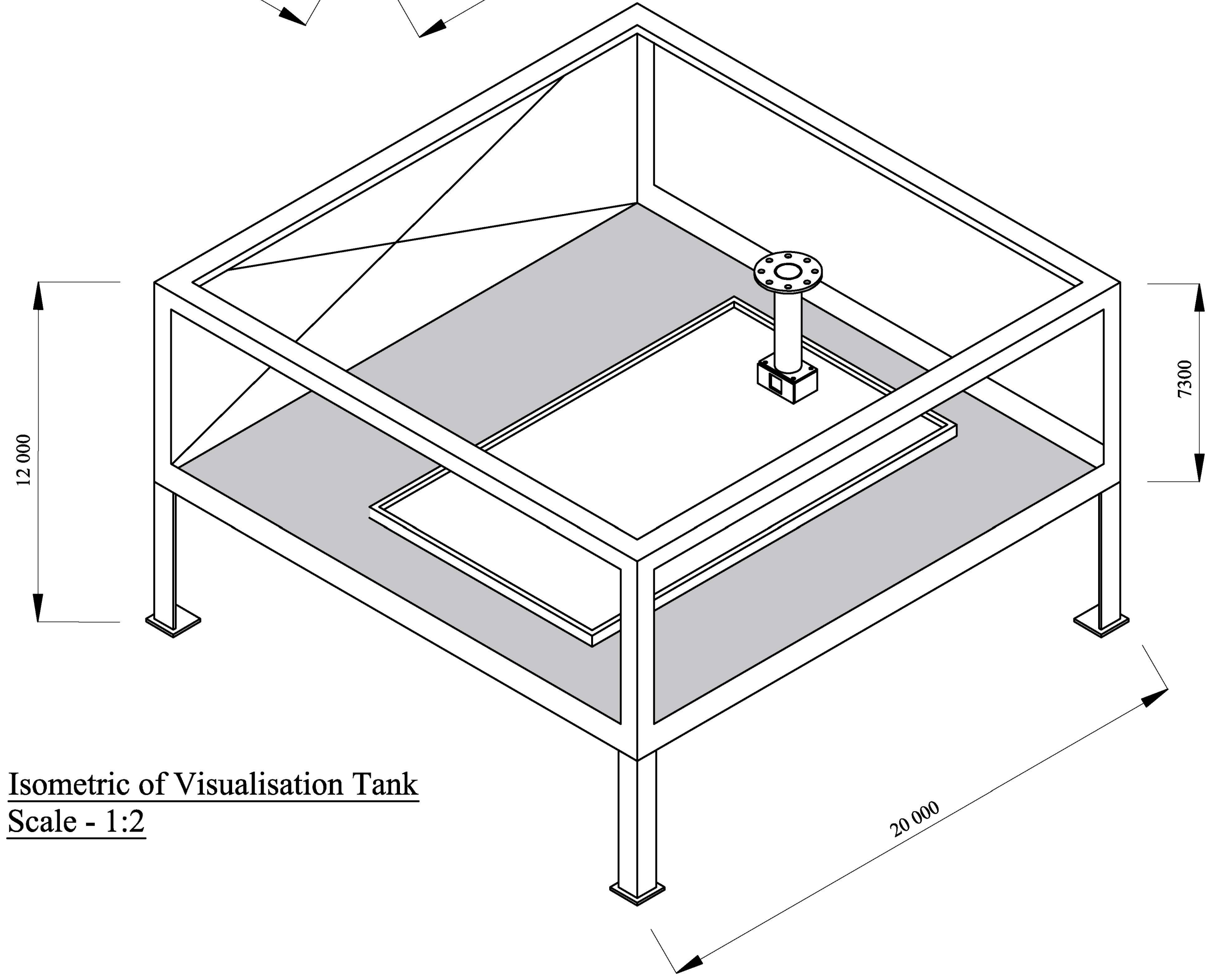

Isometric of Visualisation Tank
Scale - 1:2

GENERAL NOTES:
1. ALL DIMENSIONS IN MILLIMETERS
2. DIMENSIONS NOT TO SCALE

DEPARTMENTAL DETAILS:

DEPARTMENT OF CIVIL ENGINEERING

UCT
PRIVATE BAG X3
RONDEBOSCH
7701

EMAIL: civ-snape@uct.ac.za
FAX: +27 021 889 7471
TEL: +27 021 850 2584

UNIVERSITY OF CAPE TOWN

PRINCIPAL RESEARCHER/STUDENT SIGNATURE:

SUPERVISOR(S) SIGNATURE

PROJECT/PROJEK:

Granular Flow

DRAWING TITLE:

Nozzle Design

DATE/ DATUUM:	SCALE/ SKAAL:	PAPER SIZE/ PAPIERGROOTE:
15/09/2017	VARIES	A3
DRAWN BY:	ZHENGHUI QIU	

APPENDIX B

Raw Lab Data

B 1. Introduction

Below is a summary of the outputs measured for each individual test with their set out parameters and testing conditions.

Lab Testing Results			Test No.	0-36	Page 1 of 10
Prepared by	Zhenghui Qiu		of	327	

Test date	22/05-09/06	Conducted by	Zhenghui Qiu
Test time	9h30	Location	De Beers Marine R&D Testing Facility, Paarden Eiland

Shape of orifice		Square		Circle	
Number of apertures		1		3	
Orifice diameter (mm)		30	40	50	60
Particle diameter (mm)		0.006		0.016	
Additional Notes:					
Translational velocity (m/s)		0.104	0.156	0.208	0.26
Mass of material entrained (kg)	a)	1.084	1.058	1.041	1.075
	b)	1.036	1.043	1.061	1.071
	c)	1.044	1.046	1.052	1.052

Shape of orifice		Square		Circle	
Number of apertures		1		3	
Orifice diameter (mm)		30	40	50	60
Particle diameter (mm)		0.006		0.016	
Additional Notes:					
Translational velocity (m/s)		0.104	0.156	0.208	0.26
Mass of material entrained (kg)	a)	0.601	0.608	0.607	0.650
	b)	0.625	0.618	0.609	0.606
	c)	0.595	0.604	0.612	0.594

Shape of orifice		Square		Circle	
Number of apertures		1		3	
Orifice diameter (mm)		30	40	50	60
Particle diameter (mm)		0.006		0.016	
Additional Notes:					
Translational velocity (m/s)		0.104	0.156	0.208	0.26
Mass of material entrained (kg)	a)	0.323	0.304	0.323	0.309
	b)	0.319	0.292	0.318	0.312
	c)	0.308	0.355	0.312	0.339

Lab Testing Results			Test No.	37-72	Page 2 of 10
Prepared by	Zhenghui Qiu		of	327	

Test date	12/06-16/06	Conducted by	Zhenghui Qiu	
Test time	9h30	Location	De Beers Marine R&D Testing Facility, Paarden Eiland	

Shape of orifice		[✓ Square]		Circle	
Number of apertures		[✓ 1]		3	
Orifice diameter (mm)		30	40	50	[✓ 60]
Particle diameter (mm)		[✓ 0.006]		0.016	
Additional Notes:					
Translational velocity (m/s)		0.104	0.156	0.208	0.26
Mass of material entrained (kg)	a)	1.566	1.591	1.591	1.591
	b)	1.601	1.58	1.541	1.574
	c)	1.582	1.593	1.595	1.596

Shape of orifice		[✓ Square]		Circle	
Number of apertures		[✓ 1]		3	
Orifice diameter (mm)		[✓ 30]	40	50	60
Particle diameter (mm)		0.006		[✓ 0.016]	
Additional Notes:		Note changes in Bead size (GB16)			
Translational velocity (m/s)		0.104	0.156	0.208	0.26
Mass of material entrained (kg)	a)	0.209	0.192	0.162	0.203
	b)	0.203	0.218	0.196	0.115
	c)	0.202	0.189	0.114	0.212

Shape of orifice		[✓ Square]		Circle	
Number of apertures		[✓ 1]		3	
Orifice diameter (mm)		30	[✓ 40]	50	60
Particle diameter (mm)		0.006		[✓ 0.016]	
Additional Notes:					
Translational velocity (m/s)		0.104	0.156	0.208	0.26
Mass of material entrained (kg)	a)	0.516	0.472	0.453	0.502
	b)	0.506	0.523	0.462	0.509
	c)	0.512	0.521	0.511	0.512

Lab Testing Results		Test No.	73-108	Page 3 of 10
Prepared by	Zhenghui Qiu	of	327	

Test date	19/06-23/06	Conducted by	Zhenghui Qiu
Test time	9h30	Location	De Beers Marine R&D Testing Facility, Paarden Eiland

Shape of orifice		[✓ Square]		Circle	
Number of apertures		[✓ 1]		3	
Orifice diameter (mm)		30	40	[✓ 50]	60
Particle diameter (mm)		0.006		[✓ 0.016]	
Additional Notes:					
Translational velocity (m/s)		0.104	0.156	0.208	0.26
Mass of material entrained (kg)	a)	0.900	0.927	0.865	0.825
	b)	0.836	0.858	0.926	0.894
	c)	0.851	0.851	0.867	0.899

Shape of orifice		[✓ Square]		Circle	
Number of apertures		[✓ 1]		3	
Orifice diameter (mm)		30	40	50	[✓ 60]
Particle diameter (mm)		0.006		[✓ 0.016]	
Additional Notes:					
Translational velocity (m/s)		0.104	0.156	0.208	0.26
Mass of material entrained (kg)	a)	1.311	1.306	1.308	1.299
	b)	1.292	1.283	1.272	1.296
	c)	1.291	1.311	1.281	1.291

Shape of orifice		[✓ Square]		Circle	
Number of apertures		[✓ 1]		3	
Orifice diameter (mm)		[✓ 30]	40	50	60
Particle diameter (mm)		[✓ 0.006]		0.016	
Additional Notes:		Suction force implemented. Frequency set at **24.5Hz.**			
Translational velocity (m/s)		0.104	0.156	0.208	0.26
Mass of material entrained (kg)	a)	8.591	6.396	4.821	3.975
	b)	8.681	6.122	4.927	4.155
	c)	8.561	6.292	4.906	4.097

Lab Testing Results			Test No.	109-144	Page 4 of 10
Prepared by	Zhenghui Qiu		of	327	

Test date	26/06-30/06	Conducted by	Zhenghui Qiu
Test time	9h30	Location	De Beers Marine R&D Testing Facility, Paarden Eiland

Shape of orifice		[✓ Square]		Circle	
Number of apertures		[✓ 1]		3	
Orifice diameter (mm)		30	[✓ 40]	50	60
Particle diameter (mm)		[✓ 0.006]		0.016	
<u>Additional Notes:</u>		Suction force implemented. Frequency set at **24.5Hz.**			
Translational velocity (m/s)		0.104	0.156	0.208	0.26
Mass of material entrained (kg)	a)	9.785	6.934	5.782	5.371
	b)	9.602	6.907	5.934	5.17
	c)	9.597	6.913	5.848	5.084

Shape of orifice		[✓ Square]		Circle	
Number of apertures		[✓ 1]		3	
Orifice diameter (mm)		30	40	[✓ 50]	60
Particle diameter (mm)		[✓ 0.006]		0.016	
<u>Additional Notes:</u>		Suction force implemented. Frequency set at **24.5Hz.**			
Translational velocity (m/s)		0.104	0.156	0.208	0.26
Mass of material entrained (kg)	a)	9.458	7.314	5.541	5.585
	b)	8.988	6.895	5.744	5.38
	c)	9.129	7.286	5.790	5.437

Shape of orifice		[✓ Square]		Circle	
Number of apertures		[✓ 1]		3	
Orifice diameter (mm)		30	40	50	[✓ 60]
Particle diameter (mm)		[✓ 0.006]		0.016	
<u>Additional Notes:</u>		Suction force implemented. Frequency set at **24.5Hz.**			
Translational velocity (m/s)		0.104	0.156	0.208	0.26
Mass of material entrained (kg)	a)	9.184	6.706	5.656	5.659
	b)	8.818	6.567	5.526	5.008
	c)	8.983	6.43	5.339	5.139

Lab Testing Results			Test No.	145-180	Page 5 of 10
Prepared by	Zhenghui Qiu		of	327	

Test date	03/07-06/07	Conducted by	Zhenghui Qiu (suction)
Test time	9h30	Location	De Beers Marine R&D Testing Facility, Paarden Eiland

Shape of orifice		Square		Circle	
Number of apertures		1		3	
Orifice diameter (mm)		30	40	50	60
Particle diameter (mm)		0.006		0.016	
<u>Additional Notes:</u>		Suction force implemented. Frequency set at **31.5Hz**			
Translational velocity (m/s)		0.104	0.156	0.208	0.26
Mass of material entrained (kg)	a)	2.192	3.341	1.922	2.446
	b)	4.325	3.701	3.017	2.155
	c)	2.179	3.261	3.62	2.334

Shape of orifice		Square		Circle	
Number of apertures		1		3	
Orifice diameter (mm)		30	40	50	60
Particle diameter (mm)		0.006		0.016	
<u>Additional Notes:</u>		Suction force implemented. Frequency set at **31.5Hz**			
Translational velocity (m/s)		0.104	0.156	0.208	0.26
Mass of material entrained (kg)	a)	8.24	6.664	4.535	4.298
	b)	6.64	6.49	2.56	2.869
	c)	9.32	6.823	3.975	3.684

Shape of orifice		Square		Circle	
Number of apertures		1		3	
Orifice diameter (mm)		30	40	50	60
Particle diameter (mm)		0.006		0.016	
<u>Additional Notes:</u>		Suction force implemented. Frequency set at **31.5Hz**			
Translational velocity (m/s)		0.104	0.156	0.208	0.26
Mass of material entrained (kg)	a)	9.601	6.865	5.116	4.802
	b)	9.386	6.761	5.504	4.981
	c)	9.129	6.986	5.79	5.437

Lab Testing Results			Test No.	181-216	Page 6 of 10
Prepared by	Zhenghui Qiu		of	327	

Test date	17/07-21/07	Conducted by	Zhenghui Qiu
Test time	9h00	Location	De Beers Marine R&D Testing Facility, Paarden Eiland

Shape of orifice		[✓ Square]		Circle	
Number of apertures		[✓ 1]		3	
Orifice diameter (mm)		30	40	50	[✓ 60]
Particle diameter (mm)		0.006		[✓ 0.016]	
Additional Notes:		Suction force implemented. Frequency set at **31.5Hz**			
Translational velocity (m/s)		0.104	0.156	0.208	0.26
Mass of material entrained (kg)	a)	9.703	7.194	6.207	5.183
	b)	9.268	6.811	5.781	5.208
	c)	9.383	6.841	5.339	5.169

Shape of orifice		[✓ Square]		Circle	
Number of apertures		1		[✓ 3]	
Orifice diameter (mm)		30	40	[✓ 50]	60
Particle diameter (mm)		[✓ 0.006]		0.016	
Additional Notes:		**25mm** spacing of multiple orifice			
Translational velocity (m/s)		0.104	0.156	0.208	0.26
Mass of material entrained (kg)	a)	2.821	2.849	2.729	2.9
	b)	2.971	3.054	3.01	3.031
	c)	2.864	2.943	2.987	2.977

Shape of orifice		[✓ Square]		Circle	
Number of apertures		1		[✓ 3]	
Orifice diameter (mm)		30	40	[✓ 50]	60
Particle diameter (mm)		[✓ 0.006]		0.016	
Additional Notes:		**50mm** spacing of multiple orifice			
Translational velocity (m/s)		0.104	0.156	0.208	0.26
Mass of material entrained (kg)	a)	2.839	2.827	2.821	2.821
	b)	2.991	3.015	2.999	2.909
	c)	2.943	3.012	2.998	3.047

Lab Testing Results			Test No.	217-240	Page 7 of 10
Prepared by	Zhenghui Qiu		of	327	

Test date	24/07-28/07	Conducted by	Zhenghui Qiu
Test time	10h30	Location	De Beers Marine R&D Testing Facility, Paarden Eiland

Shape of orifice		Square		Circle	
Number of apertures		1		3	
Orifice diameter (mm)		30	40	50	60
Particle diameter (mm)		0.006		0.016	
Additional Notes:		**50mm** spacing. Suction-Frequency=40Hz			
Translational velocity (m/s)		0.104	0.156	0.208	0.26
Mass of material entrained (kg)	a)	22.85	17.518	15.063	12.452
	b)	22.446	17.545	15.063	12.542
	c)	22.728	17.578	15.063	12.544

Shape of orifice		Square		Circle	
Number of apertures		1		3	
Orifice diameter (mm)		30	40	50	60
Particle diameter (mm)		0.006		0.016	
Additional Notes:		**25mm** spacing. Suction-Frequency=40Hz			
Translational velocity (m/s)		0.104	0.156	0.208	0.26
Mass of material entrained (kg)	a)	21.681	15.973	14.22	12.13
	b)	21.286	15.91	13.85	12.141
	c)	21.616	15.728	14.075	12.21

Shape of orifice		Square		Circle	
Number of apertures		1		3	
Orifice diameter (mm)		30	40	50	60
Particle diameter (mm)		0.006		0.016	
Additional Notes:		No Testing			
Translational velocity (m/s)					
Mass of material entrained (kg)	a)				
	b)				
	c)				

Lab Testing Results			Test No.	241-273	Page 8 of 10
Prepared by	Zhenghui Qiu		of	327	

Test date	31/07-04/08	Conducted by	Zhenghui Qiu
Test time	10h00	Location	De Beers Marine R&D Testing Facility, Paarden Eiland

Shape of orifice		Square		Circle	
Number of apertures		1		3	
Orifice diameter (mm)		30	40	50	60
Particle diameter (mm)		0.006		0.016	
Additional Notes:		Circle orifice tested to verify hydraulic diameter			
Translational velocity (m/s)		0.104	0.156	0.208	0.26
Mass of material entrained (kg)	a)	1.008	1.002	0.997	0.961
	b)	1.008	0.98	1.011	0.998
	c)	0.989	1.009	1.005	1.015

Shape of orifice		Square		Circle	
Number of apertures		1		3	
Orifice diameter (mm)		30	40	50	60
Particle diameter (mm)		0.006		0.016	
Additional Notes:		Circle orifice with suction. Frequency set at **24.5Hz.**			
Translational velocity (m/s)		0.104	0.156	0.208	0.26
Mass of material entrained (kg)	a)	9.346	7.221	4.901	5.435
	b)	8.712	6.965	5.732	5.432
	c)	9.142	7.276	5.715	5.38

Shape of orifice		Square		Circle	
Number of apertures		1		3	
Orifice diameter (mm)		30	40	50	60
Particle diameter (mm)		0.006		0.016	
Additional Notes:		Pressure height independence. Velocity 0.26m/s			
Bed height (mm)		0.025	0.035	0.045	-
Mass of material entrained (kg)	a)	1.097	1.371	1.591	-
	b)	1.091	1.375	1.574	-
	c)	1.088	1.382	1.596	-

Lab Testing Results			Test No.	274-306	Page 9 of 10
Prepared by	Zhenghui Qiu		of	327	

Test date	07/08-11/08	Conducted by	Zhenghui Qiu
Test time	9h30	Location	De Beers Marine R&D Testing Facility, Paarden Eiland

Shape of orifice		Square		Circle	
Number of apertures		1		3	
Orifice diameter (mm)		30	40	50	60
Particle diameter (mm)		0.006		0.016	
<u>Additional Notes:</u>		Pressure height independence. Velocity 0.26m/s			
Bed height (m)		0.055	0.065	0.075	-
Mass of material entrained (kg)	a)	1.601	1.608	1.601	-
	b)	1.605	1.597	1.609	-
	c)	1.621	1.598	1.631	-

Shape of orifice		Square		Circle	
Number of apertures		1		3	
Orifice diameter (mm)		30	40	50	60
Particle diameter (mm)		0.006		0.016	
<u>Additional Notes:</u>		50/50 by volume mix			
Translational velocity (m/s)		0.104	0.156	0.208	0.26
Mass of material entrained (kg)	a)	1.191	1.167	1.189	1.176
	b)	1.173	1.203	1.203	1.187
	c)	1.211	1.202	1.206	1.157

Shape of orifice		Square		Circle	
Number of apertures		1		3	
Orifice diameter (mm)		30	40	50	60
Particle diameter (mm)		0.006		0.016	
<u>Additional Notes:</u>		50/50 by volume mix with suction. Frequency=**31.5Hz**			
Translational velocity (m/s)		0.104	0.156	0.208	0.26
Mass of material entrained (kg)	a)	13.028	10.768	8.000	7.508
	b)	13.322	10.629	7.606	7.595
	c)	13.228	10.856	7.728	7.437

Lab Testing Results			Test No.	307-327	Page 10 of 10
Prepared by	Zhenghui Qiu		of	327	

Test date	26/06-30/06	Conducted by	Zhenghui Qiu
Test time	9h30	Location	De Beers Marine R&D Testing Facility, Paarden Eiland

Shape of orifice		[✓ Square]		Circle	
Number of apertures		[✓ 1]		3	
Orifice diameter (mm)		30	40	[✓ 50]	60
Particle diameter (mm)		[✓ 0.006]		0.016	
Additional Notes:		Scaling verification. Scale factor=3.75(=60mm/16)			
Translational velocity (m/s)		0.104	0.156	0.208	0.26
Mass of material entrained (kg)	a)	0.189	0.175	0.179	0.182
	b)	0.174	0.181	0.183	0.172
	c)	0.178	0.185	0.184	0.182

Shape of orifice		[✓ Square]		Circle	
Number of apertures		[✓ 1]		3	
Orifice diameter (mm)		30	40	50	60
Particle diameter (mm)		[✓ 0.006]		0.016	
Additional Notes:		Scaling verification. Scale factor=3.75(=60mm/16)			
Translational velocity (m/s)		0.104	0.156	0.208	0.26
Mass of material entrained (kg)	a)				0.064
	b)				0.071
	c)				0.069

Shape of orifice		[✓ Square]		Circle	
Number of apertures		[✓ 1]		3	
Orifice diameter (mm)		30	40	[✓ 50]	60
Particle diameter (mm)		[✓ 0.006]		0.016	
Additional Notes:		Additional calibration points for Rocky. L=0.38m & L=0.77m			
Translational velocity (m/s), v=0.26m/s		t=1.5s	t=3.0s		
Mass of material entrained (kg)	a)	0.667	0.912		
	b)	0.609	0.993		
	c)	0.662	0.952		

APPENDIX C

Rocky Configuration

C 1.Introduction

The Appendix describes the contact forces used by Rocky DEM. However, before the review can commence, a brief outline of DEM was introduced. Unlike the Finite Element Method (FEM), DEM is a mesh-free method that does not solve the continuum equations of motion derived by Newton. Hence, not stress-strain constitutive law was needed for the simulated material. Instead, a stress-strain relationship could be obtained as an output through the program. To fully understand the configuration and general algorithm of DEM, the following diagram was created.

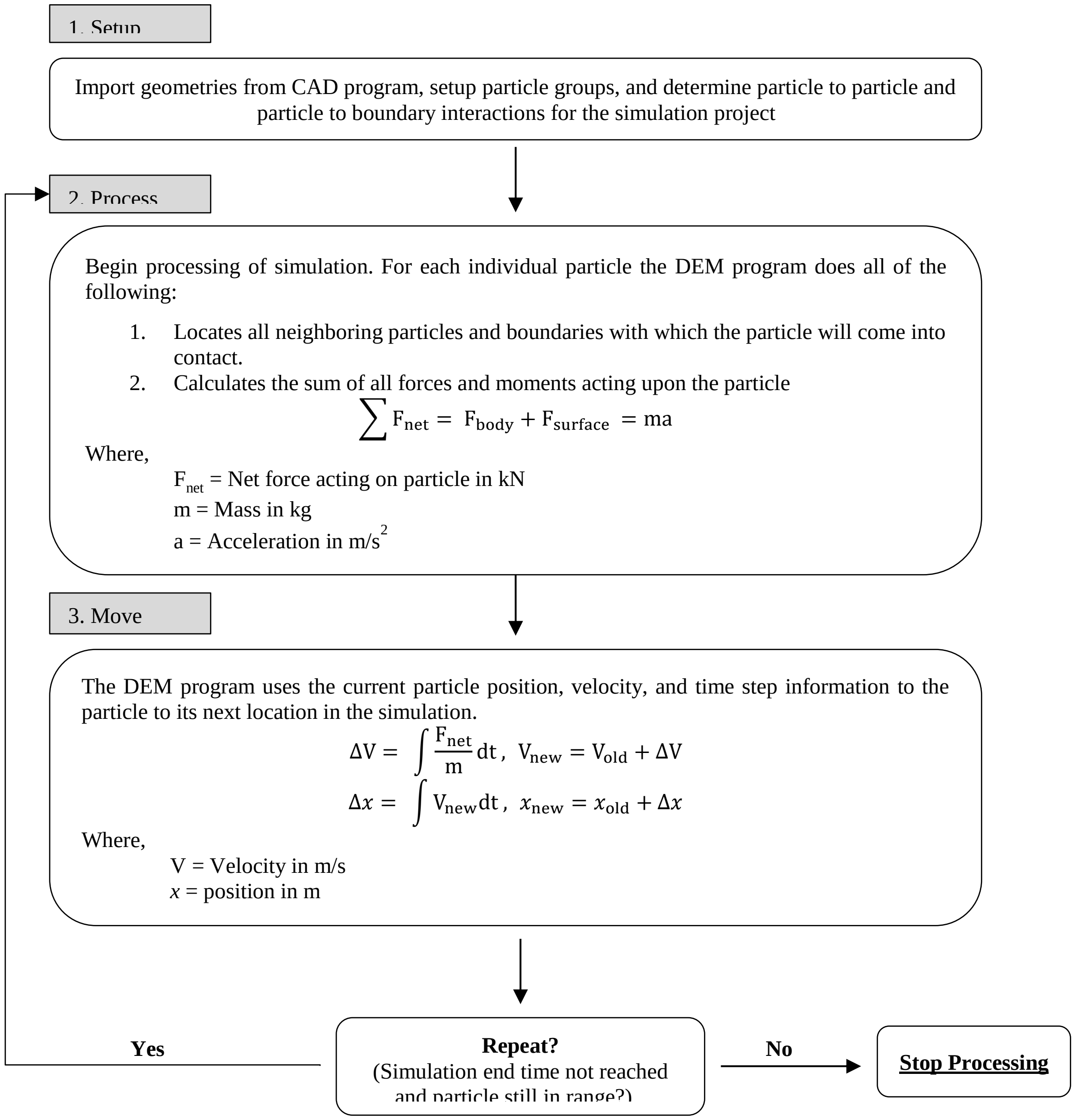

Import geometries from CAD program, setup particle groups, and determine particle to particle and particle to boundary interactions for the simulation project

Begin processing of simulation. For each individual particle the DEM program does all of the following:

1. Locates all neighboring particles and boundaries with which the particle will come into contact.
2. Calculates the sum of all forces and moments acting upon the particle

$$\sum F_{net} = F_{body} + F_{surface} = ma$$

Where,

F_{net} = Net force acting on particle in kN
m = Mass in kg
a = Acceleration in m/s^2

The DEM program uses the current particle position, velocity, and time step information to the particle to its next location in the simulation.

$$\Delta V = \int \frac{F_{net}}{m} dt\,, \; V_{new} = V_{old} + \Delta V$$

$$\Delta x = \int V_{new} dt\,, \; x_{new} = x_{old} + \Delta x$$

Where,

V = Velocity in m/s
x = position in m

(Simulation end time not reached and particle still in range?)

Figure C1: General DEM Algorithm Flowchart

The discrete element method (DEM) is a numerical tool used to predict the behaviour of a large body of solid particles, also known as granular media. The simulation is complex and requires advanced computational software such as Rocky DEM currently used by DBM. The general steps involved with the Rocky software were summarized below.

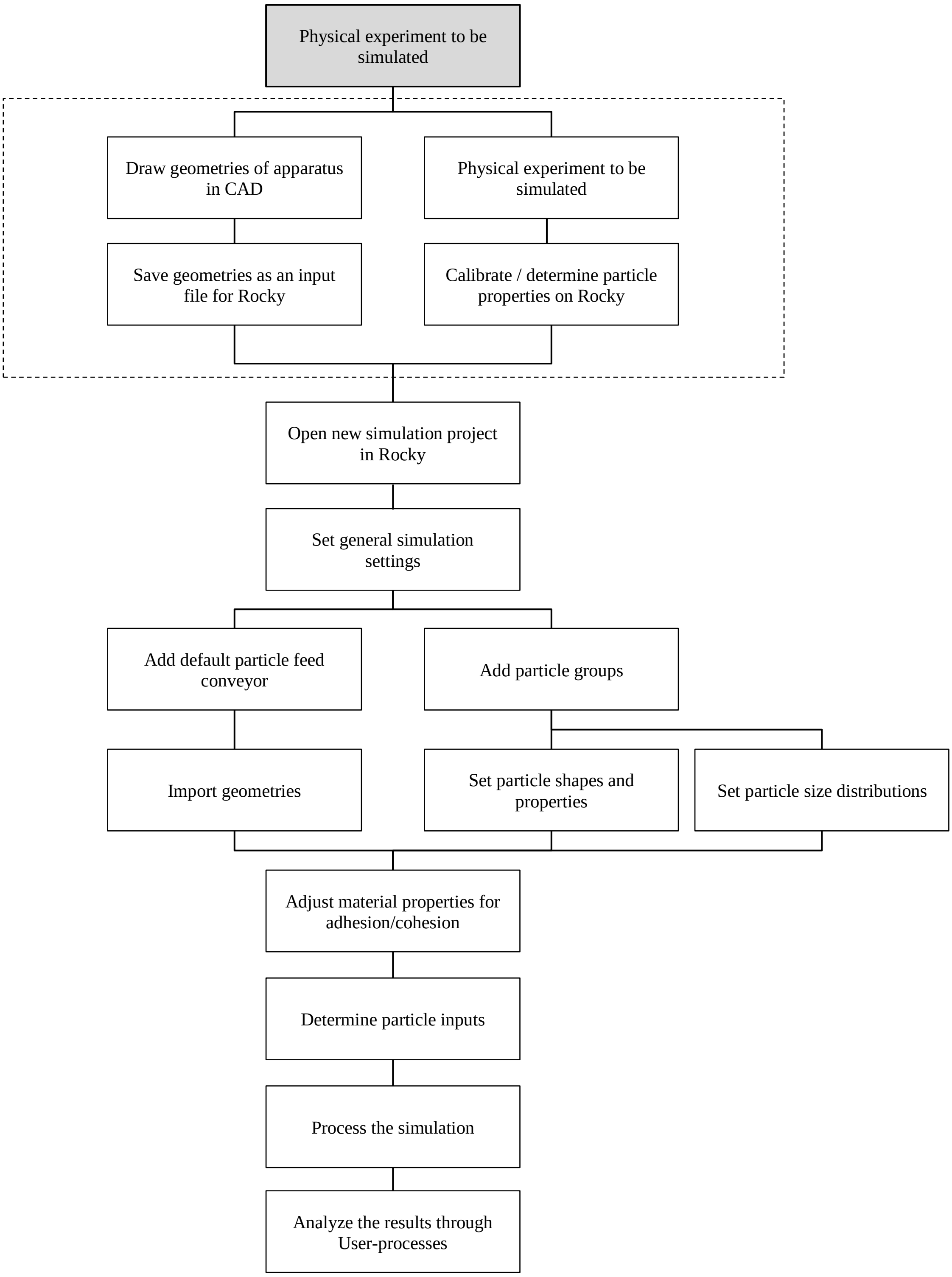

Figure C2: Rocky DEM Simulation Procedure

The contact forces in a Rocky DEM code consists of two parts:

1. Normal to contact plane
2. Tangential to contact plane

For spherical particles such as glass beads, the contact plane is referred to as a perpendicular line to the line that joins the centers of two spheres. For a boundary to particle contact, the line connects the center of a sphere to the nearest point of a triangle (mesh).

The simulation of a large body of particles is most apparent within offshore extraction techniques. An example includes the interaction of granular media with extraction equipment utilised by De Beers Marine (DBM). Other examples can include the flow of sand through an hour glass and the discharge of grains through a hopper. DEM was utilised in this project due to the complexity of granular media and due to limitations incurred through practical testing.

C 2. Rocky Simulation Procedure

This chapter highlights the step by step process carried out to simulate the practical experiments conducted in the DBM lab. The input geometries of the physical components were made to be identical and were sketched using AutoCAD software and saved as an .stl file. The steps taken were as follows:

C 2.1 Import Geometries and Inlet

The geometries imported from AutoCAD 3D included a collection box (in place of a collection net), a flange connection, nozzle cover, square orifice nozzle and a footwall platform.

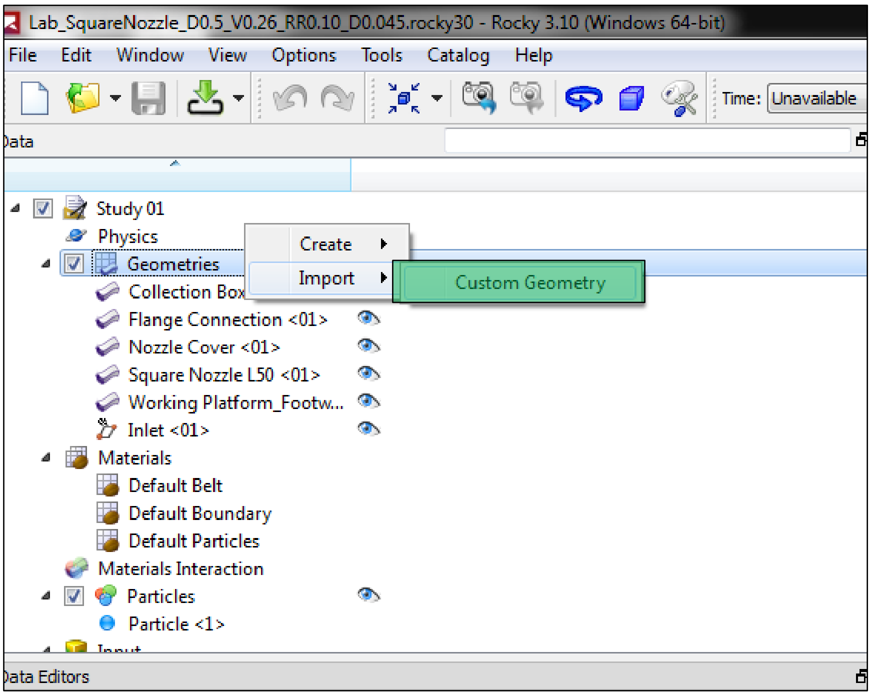

Figure C1: Geometry input

The illustration of the geometries imported into Rocky are shown below:

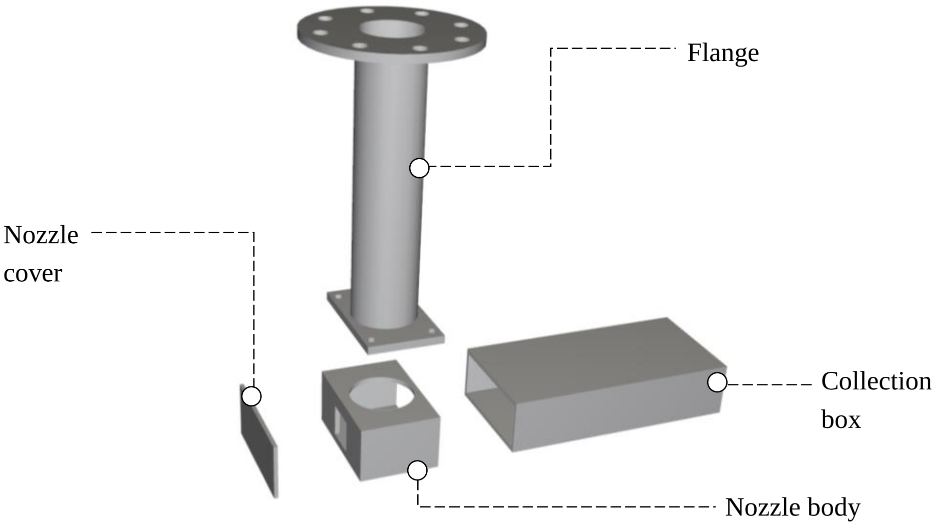

Figure C2: Imported Rocky components

Furthermore, a default inlet used to discharge granular materials was given defined boundaries per the size of the working platform (footwall).

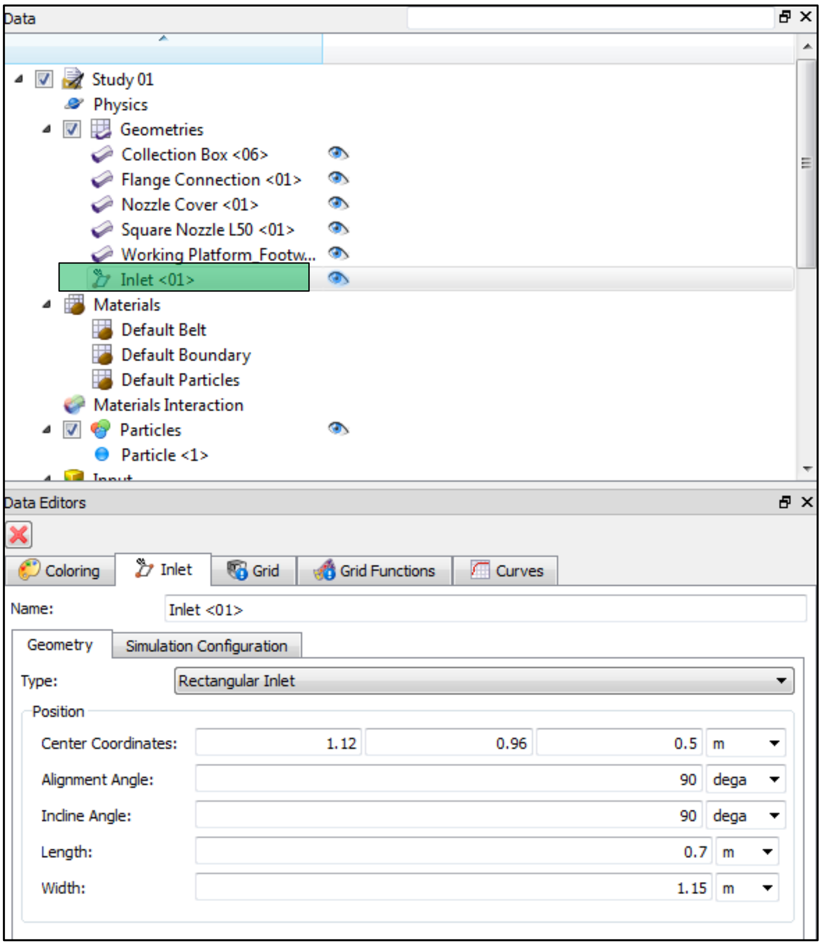
Data

- ☑ Study 01
  - Physics
  - ☑ Geometries
    - Collection Box <06>
    - Flange Connection <01>
    - Nozzle Cover <01>
    - Square Nozzle L50 <01>
    - Working Platform_Footw...
    - Inlet <01>
  - Materials
    - Default Belt
    - Default Boundary
    - Default Particles
  - Materials Interaction
  - ☑ Particles
    - Particle <1>
  - Input

Data Editors

Coloring | Inlet | Grid | Grid Functions | Curves

Name: Inlet <01>

Geometry | Simulation Configuration

Type: Rectangular Inlet

Position

Center Coordinates:	1.12	0.96	0.5	m
Alignment Angle:			90	dega
Incline Angle:			90	dega
Length:			0.7	m
Width:			1.15	m

Figure C3: Inlet properties

C 2.2 Positioning of Components

The components were positioned in Rocky, corresponding to their positions in the physical tests. This was achieved through a 3 axis coordinate system used in both AutoCAD and Rocky. In the case, small adjustments need to be made, an offset input window can be used.

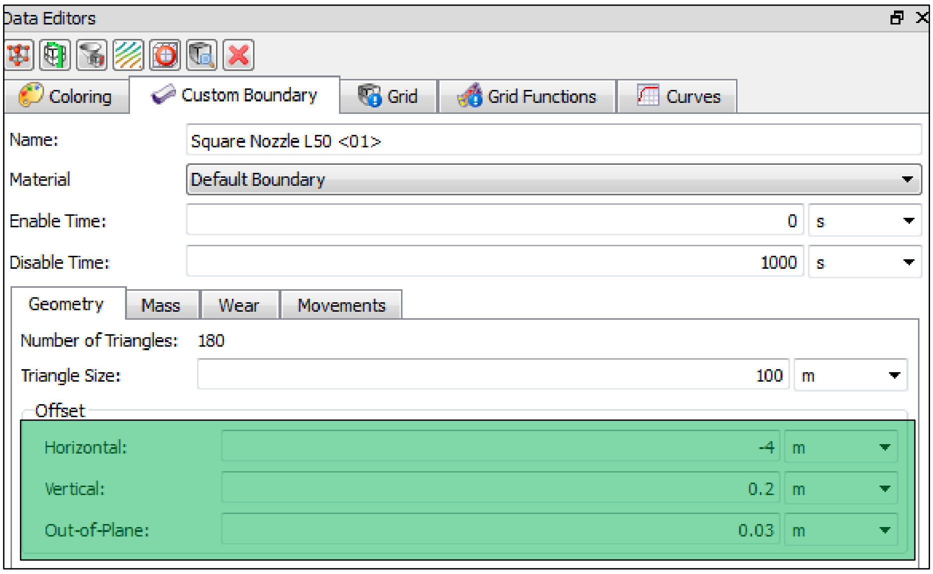

Name: Square Nozzle L50 <01>

Material: Default Boundary

Enable Time: 0 s

Disable Time: 1000 s

Number of Triangles: 180

Triangle Size: 100 m

Offset

Horizontal: -4 m

Vertical: 0.2 m

Out-of-Plane: 0.03 m

Figure C4: Positioning of geometry

C 2.3 Material Properties (Glass beads)

The material properties of glass beads inputted into Rocky were obtained through the certified data specification sheets in Appendix F. A bead density of 1540kg/m^3 was used to account for buoyancy effects (ρ_w = 1000kg/m^3).

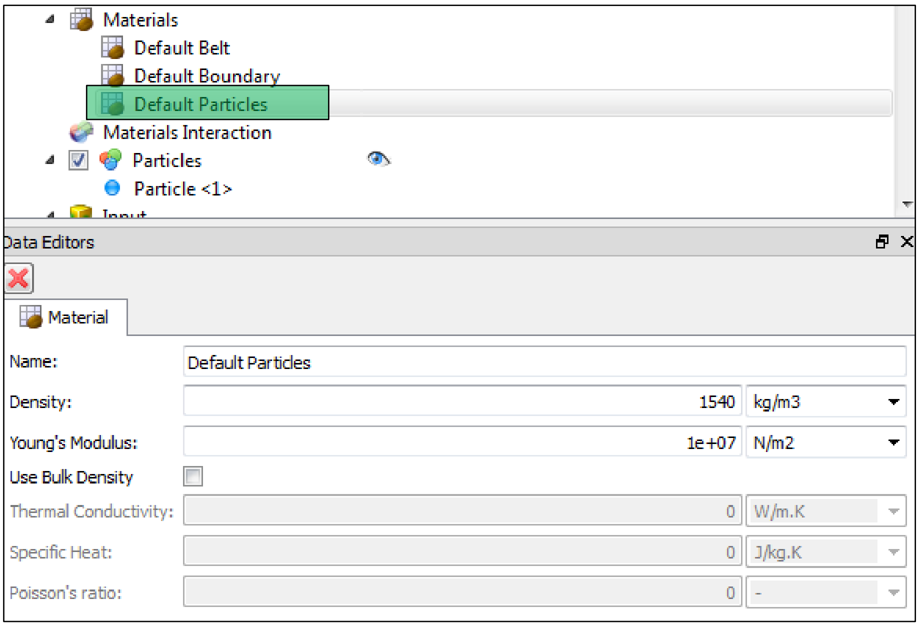

Name: Default Particles

Density: 1540 kg/m3

Young's Modulus: 1e+07 N/m2

Use Bulk Density ☐

Thermal Conductivity: 0 W/m.K

Specific Heat: 0 J/kg.K

Poisson's ratio: 0 -

Figure C5: Particle properties

The materials used in practice were of greater stiffness than the given default value, magnitudes of up to 10 to 100 folds larger. Such values would decrease the size of the time steps thus increasing simulation times by a factor of 10-100. Thus, a compromise was made such that the selected stiffness value was still representative of the sample and did not generate a massive computational expense.

The young's modulus dictates the overlapping of particles as highlighted in Part I, greater the stiffness, less the overlap but smaller the time-step. In contrast, lower the stiffness, greater the overlap and greater its dependence on the spring stiffness of the material (elasticity). It was noted through preliminary simulations and literature, that for low values of young modulus (>10^6 Pa), no significant output changes were apparent. The Young's modulus was set at a default value of 10^7 Pa. (Lommen, Schott & Lodewijks, 2014). (*Full reference can be found in reference list of main report*)

C 2.4 Particle Geometry

The shape of the particles was selected to be spherical with an initial rolling resistance (RR) of 0.1. This value was based on the recommended range provided by the *Rocky User Manual* (2016). Values were slightly altered within this range for calibration purposes.

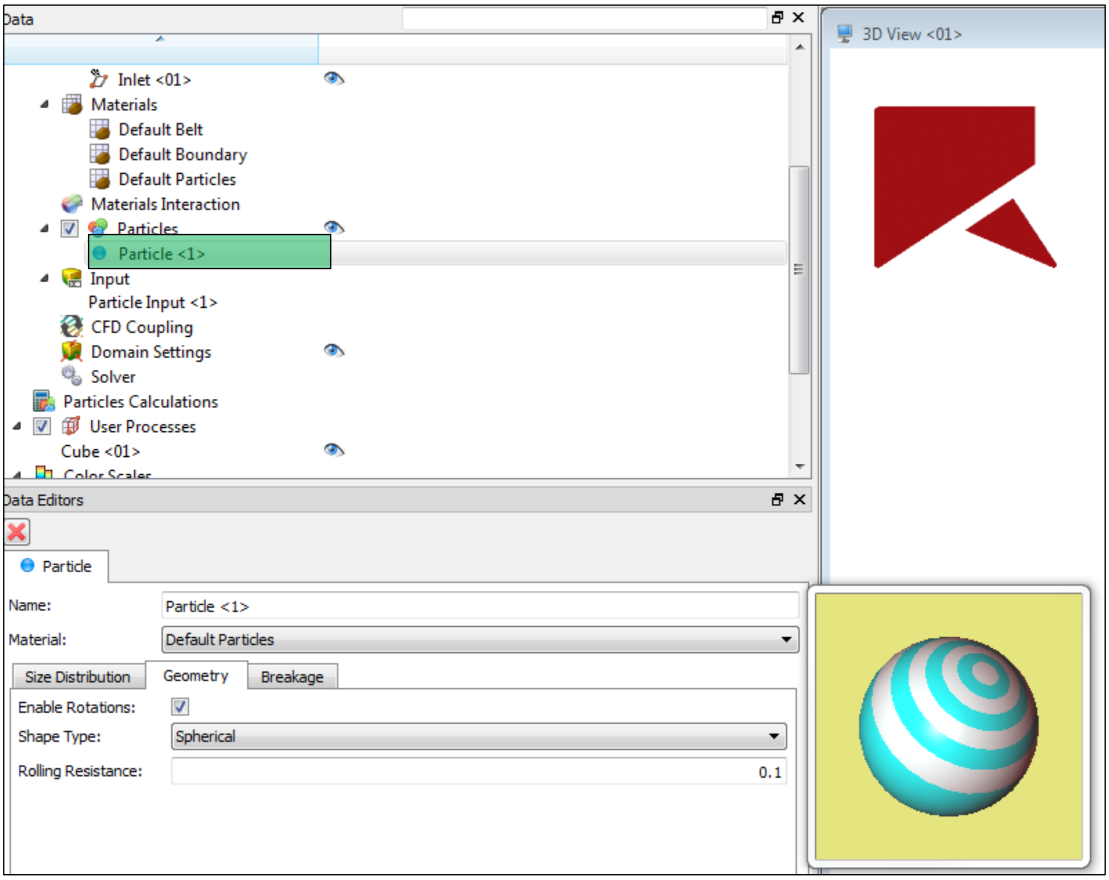

Name: Particle <1>
Material: Default Particles
Enable Rotations: ☑
Shape Type: Spherical
Rolling Resistance: 0.1

Figure C6: Particle properties (continued)

C 2.5 Particle Input

The rate at which the particles entered the simulation was based on the desired bed height. The height was dependent on the density and size of the particles. Assuming a submerged particle density of 1540 kg/m^3 , a dry bulk density of 1485kg/m^3 and a preparation bed height of 50mm, an inlet rate of 18.3 kg/s with a running time of two seconds was needed. The calculations for this was as follows:

1. The granular bed had dimensions of 1.15m x 0.7m x 0.05m, per the experimental tests. Thus, giving a volume of **0.0403m^3** (V).

2. The dry bulk mass of glass beads within the above volume was as follows: (Using a dry bulk density ρ_b of 1485kg/m^3)

$$\text{Mass of dry beads} = \text{V}\times\rho_\text{b}$$
$$\text{Mass of dry beads} = 0.0403\times1485$$
$$\text{Mass of dry beads} = 59.85\text{kg} \approx 60\text{kg}$$

3. To account for buoyancy the following calculations were performed:

Note: Submerged particle density ρ_{sb}, =1540kg/m^3
Dry particle density ρ_d = 2540 kg/m^3
Density of water ρ_w assumed to be 1000 kg/m^3

$$\text{Total submerged mass} = \frac{\text{Mass of dry beads}}{\rho_d}\rho_w$$
$$\text{Total submerged mass} = \frac{60\text{kg}}{2540}(1540)$$
$$\text{Total submerged mass} = 36.6\text{kg}$$

This is the mass to be used in the Rocky simulation, representative of the physical tests, where particles are packed as a bed and submerged in water. A two second running time t_s=2s was selected, thus a discharge rate of 18.3kg/s.

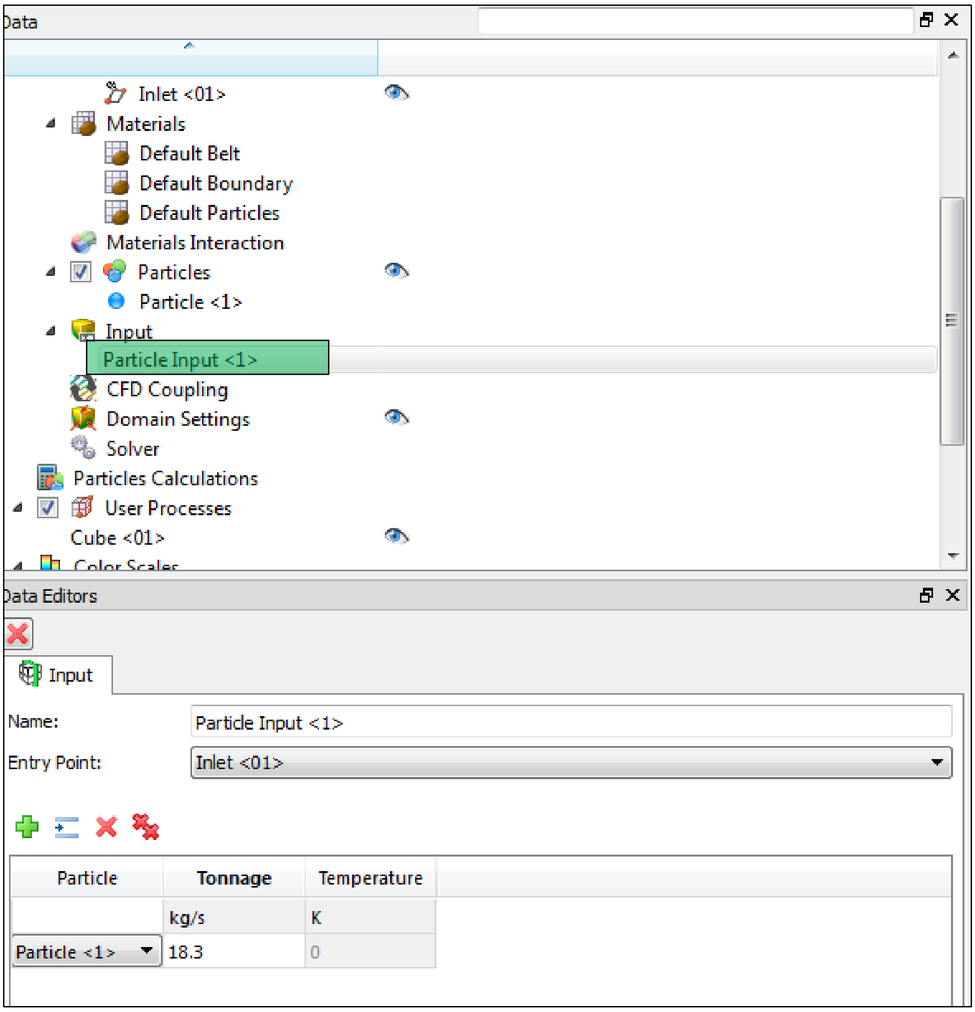

Name: Particle Input <1>

Entry Point: Inlet <01>

Particle	Tonnage	Temperature
	kg/s	K
Particle <1>	18.3	0

Figure C7: Input rate of particles

C 2.6 Translational Movement of Nozzle

The movement of the nozzle commenced at t_s=4s. This provided an adequate adjustment period for the particles after discharge (t_s =2s). The nozzle was given a command to move at a speed between 0.104-0.260 m/s in the y-axis. Thus, simulating the linear movement in the physical tests. A parameter that was kept constant during testing was the entrainment or channel length (*l*=1.15m). Therefore, to correctly achieve this through Rocky, the simulation end times were dependent on the time it took for the nozzle to cover the channel length. For instance, assuming v=0.260m/s:

$$\text{Total simulation time} = \text{particle discharge time} + \text{adjustment period} + \text{channel covering rate}$$

$$\text{Total simulation time} = 2\text{s} + 2\text{s} + (1.15\text{m}/0.26\text{ms}^{-1})$$

$$\text{Total simulation time} = \mathbf{8.423s}$$

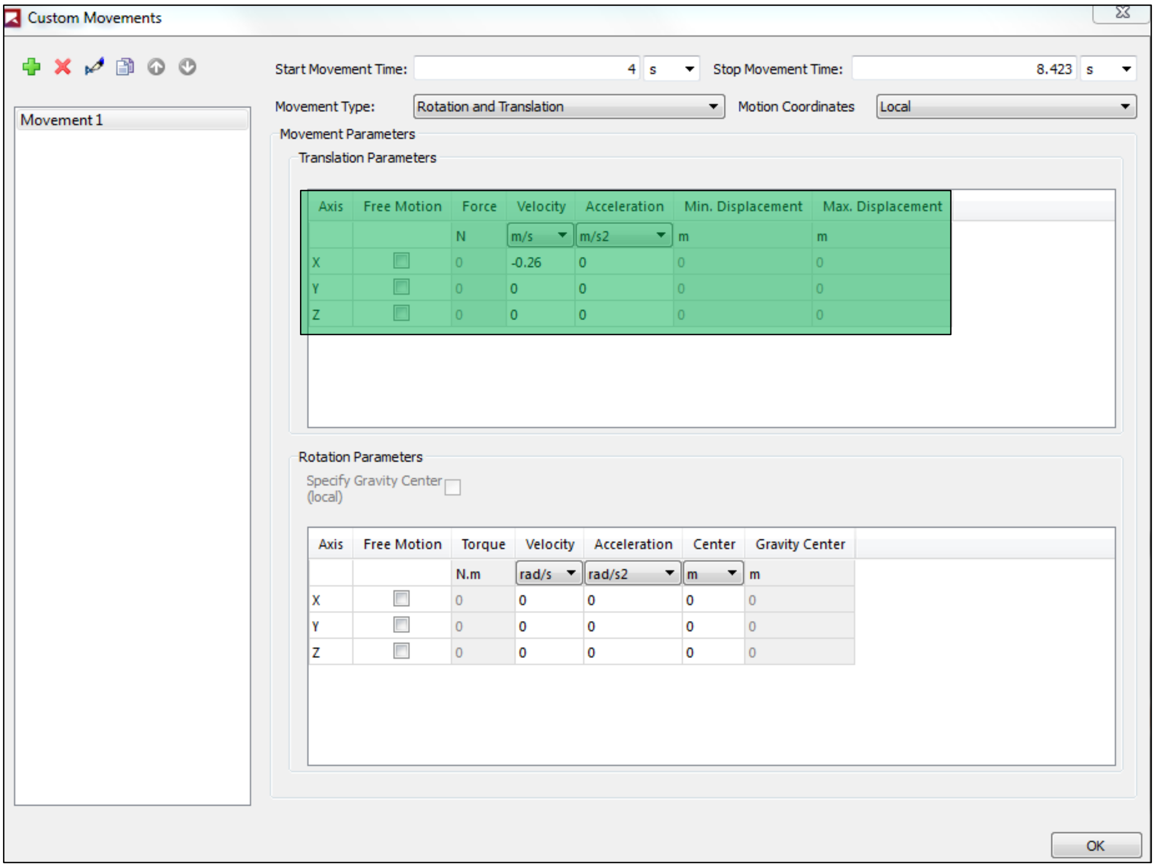

Start Movement Time: 4 s

Stop Movement Time: 8.423 s

Movement Type: Rotation and Translation

Motion Coordinates: Local

Movement Parameters

Translation Parameters

Axis	Free Motion	Force	Velocity	Acceleration	Min. Displacement	Max. Displacement
		N	m/s	m/s2	m	m
X	☐	0	-0.26	0	0	0
Y	☐	0	0	0	0	0
Z	☐	0	0	0	0	0

Rotation Parameters

Specify Gravity Center (local) ☐

Axis	Free Motion	Torque	Velocity	Acceleration	Center	Gravity Center
		N.m	rad/s	rad/s2	m	m
X	☐	0	0	0	0	0
Y	☐	0	0	0	0	0
Z	☐	0	0	0	0	0

Figure C8: Movement of nozzle

C 2.7 User Processes

The main advantage of Rocky was the user-processes made available in the software. This feature allowed for the incremental analysis of particles entering a defined space within the coordinate system. For this study, the defined space also termed as the cube, was made to occupy the space within the nozzle and collection as outlined in blue below.

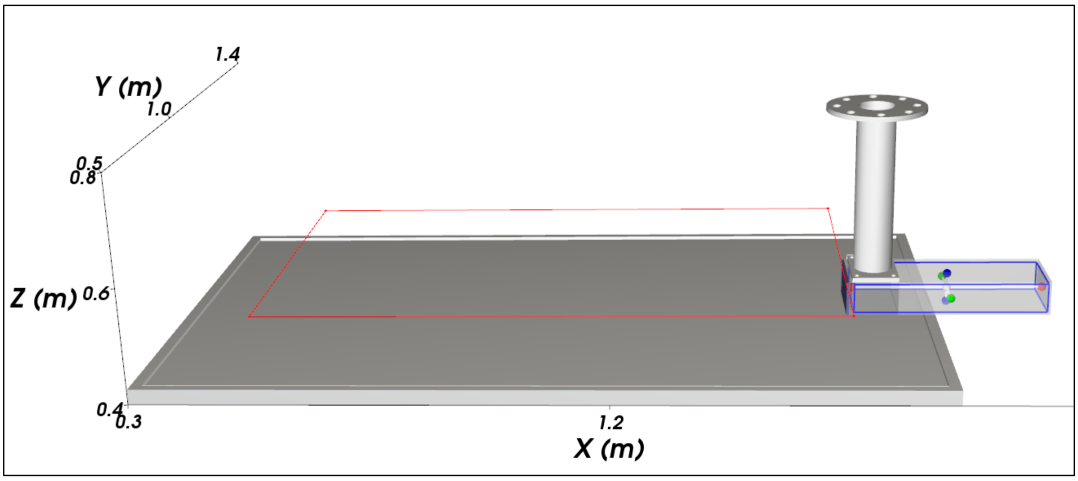

Figure C9: Cube user process and inlet

The main disadvantage with the cube was its inability to move with time. Therefore, in the preliminary analysis the cube was stationary and fixed at its final position which give limited information, similar to the experimental tests. However, the movement of the cube was permitted by running a coded macro-script as follows:

Generated script file.

Name for generated for macro: Cube Time

Commands Description for Macro:

```
'''
import numpy as np
from esss_qt10.qt_traits.process_events import ProcessEvents

#Get project imformation
project = api.GetProject()
#Get study information
study = project.GetStudy()

# Get existing user processes information
user_processes = project.GetUserProcessCollection()
# Get existing user processes names
process_names = user_processes.GetProcessNames()

#user input to choose which process is going to be used on calculations
result = app.AskInput((('Cube Input', [0] + process_names),), 'Configure which process
will be used on calculations', 'Choose the process to be used:')
print result

#check if the process exists
if result:
    process_name = process_names[result[0]]
else:
    raise ValueError('Stop')

#set the cube to be the chosen one
cube = user_processes.GetProcess(process_name)

#getting initial center and size details
center = np.asarray(cube.GetCubeCenter())
size = np.asarray(cube.GetCubeMagnitude())

timeset = study.GetTimeSet()

#### Added these variables for easy modification

cube_velocity = 0.26                          # Velocity of collection box in m/s
cube_origin=np.array([1.01,-0.965754,0.135])        # Original cube center in meters
start_move_time = 7                              # The time that the collection box starts moving
in seconds

time_i=0
mass_i=0

seconds=0
total_mass =0
```

Generated script file Cont.

```
### Center cube before starting loop
cube.SetCubeCenter(cube_origin[0],cube_origin[1], cube_origin[2])

app.GoToFirstTimeStep()
mass_curve = np.zeros(len(timeset), 'd')
mass_flow = np.zeros(len(timeset), 'd')
for dummy_i, timestep in enumerate(timeset):
    actual_time = app.GetCurrentTimeStep()

    time_i=seconds
    seconds = actual_time.second

    if(seconds>=start_move_time): #### Only move the cube once the collection box starts
moving

            ### Apply the velocity to the cube in the Y direction
        cube.SetCubeCenter(cube_origin[0],cube_origin[1]+ (seconds-
start_move_time)*cube_velocity, cube_origin[2])

    ProcessEvents()
    mass_grid_function = cube.GetGridFunction('Particle Mass')
    mass = mass_grid_function.GetArray(time_step=actual_time)
    mass_i=total_mass
    total_mass = sum(mass)
    mass_curve[dummy_i] += total_mass
    if seconds>0:
        mass_flow[dummy_i]=(total_mass-mass_i)/(seconds-time_i)
    app.GoToNextTimeStep()

#print mass_curve
#create a curve containing total mass inside particles for each time
cube.AddCurve('Particle Total Mass at time', timeset, mass_curve, 'kg')
cube.AddCurve('Particle Total Mass Flow Rate at time', timeset, mass_curve, 'kg/s')
```

The script coded above was run in Rocky, thus, allowing the cube to obtain incremental data on the particles entering the orifice with respect to time. The final geometry and coordinates of the cube was as follows:

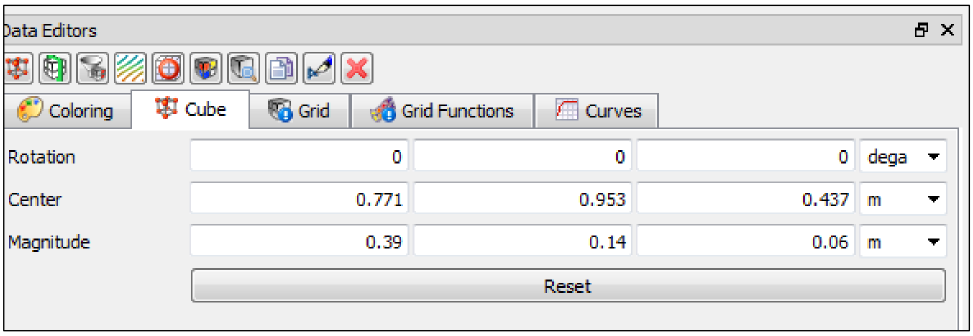

Rotation	0	0	0	dega
Center	0.771	0.953	0.437	m
Magnitude	0.39	0.14	0.06	m

Figure C10: Cube coordinates

At the end of the simulation, a detailed analysis can be made over the recorded data using the tools provided. One of the tools was the graphing function which created a modelled display of the relationship between the sum of the particles entrained through the orifice with respect to time. More accurately, the number of particles that entered the cube user process. The graph of this function was pictured in the Figure below. The interpretation of the results were discussed in the main report.

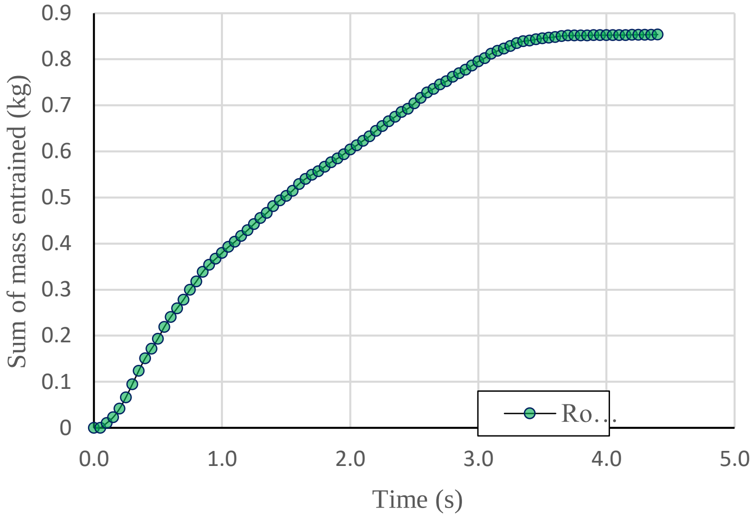

Figure C11: Graphical output from Rocky

C 3.Rocky Friction Adjustment

Below is a graph demonstrating how changes in friction can affect the final values obtained from Rocky.

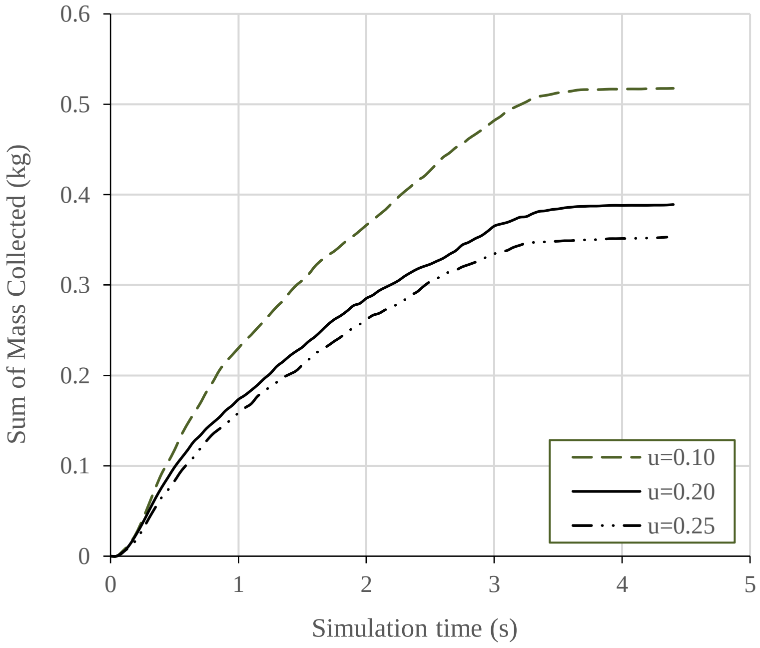

Figure C12: Mass output results recorded for different friction values

APPENDIX D

Output Parameters of Rocky

D 1. Introduction

Appendix D summarises the outputs obtained from the various simulation scenarios conducted in Rocky DEM. The outputs come in the form of total mass readings per time step, which only commenced at t=4s (Initiation time of nozzle movement).

D 2. Output of GB6 & GB16 Diameter Particles

The mass outputs obtained for each simulation took into consideration buoyancy effects such that ρ=1540kg/m3 and not ρ=2540kg/m3. To verify the experimental results with the ones obtained from Rocky, the outputs needed to be modified by multiplying each by 2540 and dividing it by 1540. The results tabulated below were for the default parameters, using v=0.260m/s and bed height of 0.045m.

Table D-1: Rocky mass outputs for GB6 and GB16

Sum of Mass Collected (kg)								
t (s)	GB6				GB16			
	D_o=30	D_o=40	D_o=50	D_o=60	D_o=30	D_o=40	D_o=50	D_o=60
0.00	0.000	0.000	0.000	0.000	0.000	0.000	0.000	0.000
0.05	0.001	0.001	0.002	0.001	0.000	0.000	0.000	0.000
0.10	0.007	0.008	0.014	0.017	0.005	0.005	0.005	0.016
0.15	0.017	0.021	0.035	0.040	0.005	0.005	0.016	0.016
0.20	0.027	0.037	0.059	0.073	0.005	0.005	0.016	0.033
0.25	0.035	0.056	0.083	0.107	0.016	0.022	0.016	0.044
0.30	0.045	0.074	0.110	0.140	0.022	0.027	0.022	0.065
0.35	0.054	0.092	0.139	0.184	0.022	0.038	0.044	0.098
0.40	0.062	0.110	0.171	0.228	0.022	0.038	0.054	0.109
0.45	0.069	0.125	0.203	0.271	0.022	0.049	0.071	0.131
0.50	0.078	0.144	0.233	0.313	0.022	0.054	0.082	0.147
0.55	0.088	0.161	0.266	0.354	0.022	0.065	0.087	0.185
0.60	0.095	0.176	0.296	0.398	0.022	0.082	0.114	0.229
0.65	0.103	0.190	0.326	0.444	0.027	0.093	0.120	0.256
0.70	0.108	0.203	0.356	0.486	0.027	0.104	0.136	0.294
0.75	0.116	0.217	0.380	0.528	0.033	0.109	0.158	0.343
0.80	0.123	0.230	0.405	0.567	0.033	0.109	0.163	0.381
0.85	0.129	0.244	0.432	0.601	0.033	0.114	0.174	0.398
0.90	0.135	0.255	0.454	0.634	0.033	0.120	0.191	0.430
0.95	0.142	0.265	0.475	0.665	0.033	0.125	0.207	0.458
1.00	0.147	0.274	0.495	0.695	0.033	0.136	0.223	0.474
1.05	0.151	0.282	0.513	0.725	0.033	0.147	0.256	0.496
1.10	0.157	0.290	0.527	0.753	0.033	0.153	0.256	0.534
1.15	0.161	0.299	0.543	0.778	0.033	0.153	0.272	0.556
1.20	0.165	0.307	0.554	0.800	0.033	0.153	0.289	0.594
1.25	0.170	0.318	0.571	0.824	0.033	0.163	0.300	0.610
1.30	0.173	0.328	0.586	0.847	0.038	0.169	0.321	0.637
1.35	0.176	0.339	0.602	0.868	0.044	0.174	0.332	0.659

Sum of Mass Collected (kg)								
t (s)	GB6				GB16			
	D_o=30	D_o=40	D_o=50	D_o=60	D_o=30	D_o=40	D_o=50	D_o=60
1.40	0.180	0.347	0.614	0.889	0.044	0.174	0.354	0.681
1.45	0.184	0.356	0.629	0.907	0.044	0.191	0.381	0.714
1.50	0.189	0.364	0.645	0.931	0.049	0.196	0.392	0.735
1.55	0.191	0.375	0.659	0.953	0.054	0.202	0.409	0.752
1.60	0.196	0.384	0.675	0.974	0.054	0.202	0.430	0.768
1.65	0.200	0.394	0.690	0.995	0.060	0.212	0.436	0.790
1.70	0.203	0.402	0.706	1.014	0.060	0.212	0.436	0.817
1.75	0.206	0.409	0.722	1.034	0.060	0.223	0.458	0.844
1.80	0.211	0.419	0.735	1.054	0.060	0.229	0.463	0.855
1.85	0.213	0.426	0.746	1.069	0.065	0.229	0.485	0.877
1.90	0.216	0.434	0.758	1.087	0.065	0.234	0.501	0.893
1.95	0.220	0.441	0.768	1.105	0.065	0.251	0.512	0.904
2.00	0.224	0.448	0.777	1.121	0.065	0.256	0.528	0.937
2.05	0.226	0.452	0.789	1.138	0.076	0.261	0.539	0.948
2.10	0.231	0.460	0.801	1.155	0.076	0.272	0.556	0.964
2.15	0.234	0.465	0.810	1.172	0.082	0.278	0.572	0.975
2.20	0.236	0.470	0.818	1.188	0.082	0.283	0.583	0.986
2.25	0.240	0.477	0.830	1.201	0.087	0.294	0.588	0.997
2.30	0.244	0.484	0.839	1.214	0.087	0.300	0.605	1.024
2.35	0.246	0.490	0.850	1.227	0.093	0.316	0.610	1.051
2.40	0.249	0.496	0.859	1.241	0.098	0.321	0.616	1.057
2.45	0.252	0.501	0.870	1.254	0.104	0.332	0.632	1.073
2.50	0.256	0.508	0.880	1.265	0.109	0.338	0.648	1.089
2.55	0.258	0.514	0.892	1.275	0.109	0.354	0.659	1.106
2.60	0.263	0.519	0.900	1.288	0.109	0.354	0.659	1.117
2.65	0.267	0.525	0.911	1.300	0.120	0.354	0.675	1.133
2.70	0.270	0.531	0.921	1.313	0.120	0.354	0.681	1.139
2.75	0.273	0.538	0.931	1.324	0.125	0.360	0.692	1.144
2.80	0.276	0.541	0.938	1.336	0.125	0.370	0.692	1.149
2.85	0.279	0.548	0.949	1.348	0.131	0.376	0.697	1.177
2.90	0.281	0.554	0.955	1.359	0.131	0.387	0.703	1.193
2.95	0.283	0.558	0.963	1.374	0.131	0.387	0.708	1.204
3.00	0.286	0.564	0.970	1.385	0.131	0.387	0.725	1.215
3.05	0.288	0.569	0.978	1.396	0.131	0.392	0.735	1.220
3.10	0.291	0.573	0.984	1.407	0.131	0.403	0.741	1.231
3.15	0.294	0.579	0.994	1.418	0.136	0.403	0.763	1.237
3.20	0.295	0.584	1.001	1.429	0.136	0.414	0.763	1.242
3.25	0.298	0.588	1.009	1.438	0.136	0.419	0.763	1.247
3.30	0.300	0.591	1.015	1.445	0.142	0.425	0.774	1.264
3.35	0.302	0.595	1.020	1.453	0.142	0.425	0.779	1.264
3.40	0.304	0.600	1.026	1.459	0.142	0.430	0.779	1.286
3.45	0.305	0.603	1.030	1.466	0.142	0.430	0.784	1.291
3.50	0.307	0.606	1.034	1.470	0.142	0.441	0.790	1.296
3.55	0.307	0.607	1.036	1.477	0.147	0.441	0.790	1.302
3.60	0.308	0.609	1.039	1.481	0.147	0.447	0.790	1.307
3.65	0.309	0.609	1.041	1.487	0.147	0.452	0.790	1.307
3.70	0.309	0.609	1.042	1.488	0.147	0.458	0.790	1.307
3.75	0.311	0.610	1.043	1.489	0.158	0.458	0.795	1.307

Sum of Mass Collected (kg)								
t (s)	GB6				GB16			
	D_o=30	D_o=40	D_o=50	D_o=60	D_o=30	D_o=40	D_o=50	D_o=60
3.80	0.311	0.610	1.045	1.490	0.158	0.458	0.795	1.307
3.85	0.311	0.610	1.045	1.491	0.163	0.458	0.795	1.307
3.90	0.311	0.610	1.045	1.490	0.169	0.463	0.795	1.307
3.95	0.312	0.610	1.047	1.490	0.169	0.463	0.806	1.318
4.00	0.312	0.610	1.047	1.491	0.174	0.468	0.806	1.324
4.05	0.312	0.610	1.048	1.491	0.174	0.468	0.806	1.324
4.10	0.313	0.611	1.049	1.491	0.174	0.468	0.812	1.324
4.15	0.313	0.611	1.049	1.491	0.180	0.468	0.817	1.324
4.20	0.313	0.611	1.050	1.491	0.180	0.474	0.817	1.324
4.25	0.313	0.611	1.049	1.491	0.180	0.474	0.823	1.329
4.30	0.314	0.612	1.049	1.492	0.180	0.479	0.823	1.335
4.35	0.314	0.613	1.049	1.492	0.180	0.479	0.839	1.340
4.40	0.316	0.614	1.049	1.492	0.180	0.479	0.850	1.340

The graphical plots of the tabulated data were illustrated as follows.

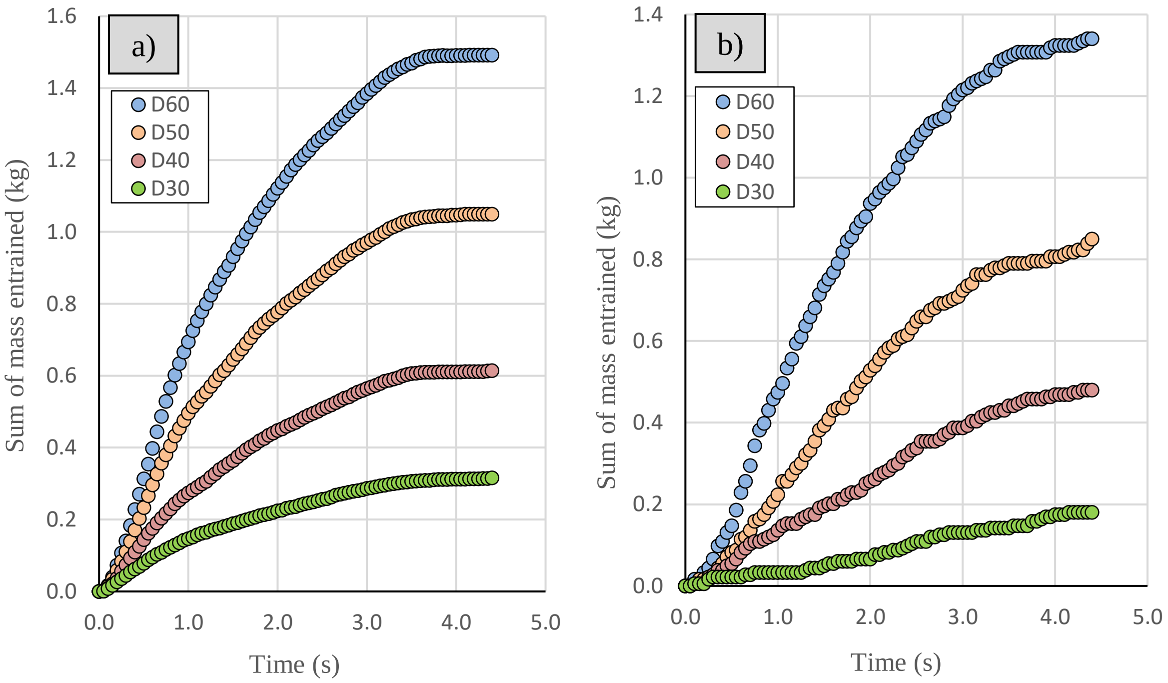

Figure D-1: Graphical simulation of MMS for a) GB6 and b) GB16

In both plots, it was noted that the gradient was consistent from t=0s to t=1s. Therefore, taking the outputs collected from ROCKY up till t=1s, the change in gradient per incremental time step was calculated for each orifice and particle size shown below. The values highlighted in red indicate the start of a consistent negative change in gradient.

Table D-2: Change in Gradient for GB6

t (s)	D_o=30mm			D_o=40mm			D_o=50mm			D_o=60mm		
	Mass (kg)	gradient Δ	% change	Mass (kg)	gradient Δ	% change	Mass (kg)	gradient Δ	% change	Mass (kg)	gradient Δ	% change
0	0	0	0	0	0	0	0	0	0	0	0	0
0.05	0.001	0.023	0.000	0.001	0.017	0.000	0.002	0.046	0.000	0.001	0.029	0.000
0.1	0.007	0.075	69.231	0.008	0.083	79.310	0.014	0.141	67.347	0.017	0.169	83.051
0.15	0.017	0.113	33.899	0.021	0.140	40.411	0.035	0.232	39.256	0.040	0.268	36.786
0.2	0.027	0.134	15.412	0.037	0.184	23.958	0.059	0.293	20.915	0.073	0.365	26.509
0.25	0.035	0.140	4.713	0.056	0.224	17.949	0.083	0.333	12.069	0.107	0.427	14.651
0.3	0.045	0.148	5.548	0.074	0.246	8.949	0.110	0.367	9.138	0.140	0.468	8.712
0.35	0.054	0.155	4.321	0.092	0.263	6.594	0.139	0.397	7.679	0.184	0.524	10.720
0.4	0.062	0.155	0.000	0.110	0.274	3.964	0.171	0.427	6.878	0.228	0.569	7.792
0.45	0.069	0.154	-0.830	0.125	0.278	1.207	0.203	0.451	5.347	0.271	0.602	5.514
0.5	0.078	0.157	1.913	0.144	0.287	3.333	0.233	0.466	3.275	0.313	0.626	3.874
0.55	0.088	0.160	1.863	0.161	0.294	2.135	0.266	0.483	3.557	0.354	0.645	2.837
0.6	0.095	0.158	-1.157	0.176	0.293	-0.342	0.296	0.494	2.125	0.398	0.663	2.803
0.65	0.103	0.158	0.140	0.190	0.293	0.013	0.326	0.502	1.680	0.444	0.683	2.948
0.7	0.108	0.154	-2.537	0.203	0.291	-0.695	0.356	0.509	1.420	0.486	0.695	1.658
0.75	0.116	0.155	0.283	0.217	0.289	-0.473	0.380	0.507	-0.502	0.528	0.704	1.363
0.8	0.123	0.154	-0.685	0.230	0.287	-0.667	0.405	0.506	-0.156	0.567	0.709	0.628
0.85	0.129	0.152	-1.055	0.244	0.287	-0.236	0.432	0.509	0.527	0.601	0.707	-0.209
0.9	0.135	0.150	-1.377	0.255	0.283	-1.227	0.454	0.504	-0.856	0.634	0.704	-0.459
0.95	0.142	0.149	-0.427	0.265	0.279	-1.549	0.475	0.500	-0.833	0.665	0.700	-0.542
1	0.147	0.147	-1.761	0.274	0.274	-1.733	0.495	0.495	-0.989	0.695	0.695	-0.823

Table D-3: Change in Gradient for GB16

t (s)	**D_o=30mm**			**D_o=40mm**			**D_o=50mm**			**D_o=60mm**		
	Mass (kg)	gradient Δ	% change	Mass (kg)	gradient Δ	% change	Mass (kg)	gradient Δ	% change	Mass (kg)	gradient Δ	% change
0	0	0	0	0	0	0	0	0	0	0	0	0
0.05	0	0.000	0.000	0.000	0.000	0.000	0.000	0.000	0.000	0.000	0.000	0.000
0.1	0.005	0.054	100.000	0.005	0.054	100.000	0.005	0.054	100.000	0.016	0.163	100.000
0.15	0.005	0.036	-50.000	0.005	0.036	-50.000	0.016	0.109	50.000	0.016	0.109	-50.000
0.2	0.005	0.027	-33.333	0.005	0.027	-33.333	0.016	0.082	-33.333	0.033	0.163	33.333
0.25	0.016	0.065	58.333	0.022	0.087	68.750	0.016	0.065	-25.000	0.044	0.174	6.250
0.3	0.022	0.073	10.000	0.027	0.091	4.000	0.022	0.073	10.000	0.065	0.218	20.000
0.35	0.022	0.062	-16.667	0.038	0.109	16.666	0.044	0.125	41.667	0.098	0.280	22.222
0.4	0.022	0.054	-14.286	0.038	0.095	-14.286	0.054	0.136	8.571	0.109	0.272	-2.857
0.45	0.022	0.048	-12.500	0.049	0.109	12.500	0.071	0.157	13.462	0.131	0.291	6.250
0.5	0.022	0.044	-11.111	0.054	0.109	0.000	0.082	0.163	3.704	0.147	0.294	1.235
0.55	0.022	0.040	-10.000	0.065	0.119	8.333	0.087	0.158	-3.125	0.185	0.337	12.647
0.6	0.022	0.036	-9.091	0.082	0.136	12.727	0.114	0.191	16.883	0.229	0.381	11.688
0.65	0.027	0.042	13.333	0.093	0.142	4.412	0.120	0.184	-3.409	0.256	0.394	3.192
0.7	0.027	0.039	-7.692	0.104	0.148	3.644	0.136	0.195	5.231	0.294	0.420	6.268
0.75	0.033	0.044	10.714	0.109	0.145	-1.786	0.158	0.211	7.635	0.343	0.458	8.163
0.8	0.033	0.041	-6.667	0.109	0.136	-6.667	0.163	0.204	-3.111	0.381	0.477	4.000
0.85	0.033	0.038	-6.250	0.114	0.135	-1.190	0.174	0.205	0.391	0.398	0.468	-1.884
0.9	0.033	0.036	-5.882	0.120	0.133	-1.069	0.191	0.212	3.193	0.430	0.478	2.159
0.95	0.033	0.034	-5.556	0.125	0.132	-0.966	0.207	0.218	2.778	0.458	0.482	0.728
1	0.033	0.033	-5.263	0.136	0.136	3.158	0.223	0.223	2.440	0.474	0.474	-1.634

Apart from the mass outputs, the normal force exerted onto the nozzle face was also analysed. The magnitude of the force was a function of the retained bulge height with respect to a given time step. The values for each orifice and configuration were summarised as follows:

Table D-4: Normal force on nozzle face for GB6 and GB16 configuration

t (s)	GB6				GB16			
	D_o=30	D_o=40	D_o=50	D_o=60	D_o=30	D_o=40	D_o=50	D_o=60
0	0.009	0.008	0.005	0.010	0.004	0.012	0.014	0.057
0.05	3.347	3.353	3.522	3.200	10.329	12.373	6.567	9.752
0.1	4.530	5.115	4.420	4.206	15.319	20.302	12.477	15.871
0.15	6.093	5.806	5.695	5.616	17.785	29.781	16.570	15.881
0.2	6.674	7.120	6.375	6.453	15.394	23.983	16.441	20.104
0.25	7.509	7.748	6.635	6.742	15.300	22.435	18.031	14.895
0.3	7.807	8.226	7.249	6.763	17.688	19.854	20.691	17.753
0.35	8.967	8.581	7.642	7.711	21.398	29.710	18.510	24.582
0.4	8.752	8.530	8.651	7.946	23.762	23.393	26.603	18.370
0.45	9.508	9.633	8.526	8.280	19.437	28.577	19.532	21.422
0.5	9.695	10.149	8.945	8.820	26.425	28.727	22.623	15.533
0.55	10.613	10.866	9.495	9.205	19.257	24.494	22.682	19.511
0.6	11.006	10.863	9.847	9.401	22.751	23.964	21.666	20.315
0.65	11.072	10.681	10.495	10.089	27.431	29.871	28.886	21.221
0.7	11.338	11.478	10.532	10.080	27.580	32.343	28.748	21.513
0.75	11.868	11.298	10.860	10.049	19.676	30.127	25.664	26.443
0.8	11.657	12.025	10.760	10.270	25.309	35.509	23.494	29.672
0.85	12.358	12.050	11.147	10.389	34.398	28.732	23.585	28.090
0.9	11.908	12.842	11.136	10.428	25.608	30.594	32.758	20.692
0.95	12.674	13.086	11.347	10.763	27.582	28.294	23.317	25.360
1	12.474	13.028	12.123	11.462	35.732	25.157	27.460	31.486
1.05	12.861	12.602	11.677	11.446	31.411	48.640	23.880	25.524
1.1	12.533	12.996	12.283	11.793	31.432	51.097	23.732	27.920
1.15	13.195	13.208	11.629	11.300	40.434	32.730	25.861	28.408
1.2	13.619	12.671	12.444	11.842	33.296	28.765	27.857	29.134
1.25	13.566	14.026	12.670	12.034	35.072	35.382	30.768	25.635
1.3	13.440	13.792	12.394	11.808	32.236	44.517	26.589	30.090
1.35	13.788	13.859	12.364	11.718	24.716	30.012	24.581	31.165
1.4	13.610	14.020	12.707	12.439	34.233	42.847	30.592	28.149
1.45	13.914	14.234	12.880	11.883	36.070	49.006	32.351	26.627
1.5	14.215	14.127	12.863	12.889	34.226	32.532	25.997	35.199
1.55	13.849	14.320	13.141	12.927	27.522	55.143	24.242	35.951
1.6	14.238	14.449	13.079	12.455	29.812	47.263	36.684	30.457
1.65	14.220	15.381	13.447	13.298	33.797	42.224	28.349	24.781
1.7	14.481	14.598	13.525	13.009	36.455	32.361	34.247	27.828
1.75	14.538	14.690	13.028	13.055	43.200	41.901	32.638	27.822
1.8	14.764	14.482	13.471	13.447	32.647	42.508	29.261	30.496

t (s)	**GB6**				**GB16**			
	D_o=30	D_o=40	D_o=50	D_o=60	D_o=30	D_o=40	D_o=50	D_o=60
1.85	14.606	14.123	13.379	13.047	31.099	48.261	35.536	43.403
1.9	15.087	14.789	14.128	13.408	34.217	39.148	31.508	30.229
1.95	15.189	15.023	13.705	14.256	34.449	37.979	27.696	47.338
2	16.246	15.550	13.486	13.898	35.886	41.859	35.173	42.345
2.05	14.747	15.998	13.568	13.899	30.947	42.983	33.664	33.620
2.1	15.051	14.993	14.138	13.656	30.363	30.738	36.820	27.694
2.15	15.262	15.965	13.703	13.735	35.759	48.673	24.168	32.716
2.2	14.751	14.877	13.851	13.434	34.525	37.153	41.852	30.819
2.25	14.659	15.252	14.022	15.283	33.694	31.036	23.545	27.351
2.3	15.128	14.770	13.607	13.671	34.124	35.629	38.304	40.683
2.35	15.582	15.080	13.953	13.567	31.832	33.899	35.492	32.832
2.4	15.107	16.345	14.162	14.180	29.838	40.072	23.427	33.252
2.45	14.728	16.442	13.909	13.991	38.561	43.305	21.796	37.660
2.5	14.947	15.773	14.440	13.514	36.865	43.040	32.455	34.064
2.55	15.350	15.171	14.316	13.711	34.378	52.726	29.417	36.791
2.6	15.220	15.533	14.816	14.360	32.768	43.055	39.145	38.030
2.65	15.474	15.629	13.780	13.818	34.906	41.169	15.295	37.579
2.7	15.107	15.220	14.613	14.217	32.423	47.847	41.387	35.926
2.75	15.668	15.523	14.524	13.877	34.823	42.099	25.506	39.358
2.8	14.680	15.437	14.331	14.257	30.347	40.353	15.185	26.575
2.85	15.470	15.719	14.692	13.485	30.863	40.434	23.470	37.884
2.9	15.161	15.418	14.333	15.004	33.057	47.231	37.357	33.204
2.95	15.957	16.278	14.601	14.338	30.619	33.759	23.303	36.369
3	15.249	15.541	14.659	14.254	37.386	39.998	23.540	31.467
3.05	15.903	16.048	14.431	14.619	33.395	51.177	22.215	36.170
3.1	15.902	15.253	14.087	14.465	34.946	32.168	26.593	29.746
3.15	15.848	16.653	14.517	14.612	32.635	25.831	16.117	28.537
3.2	15.256	15.689	14.410	14.293	26.231	35.831	15.835	31.421
3.25	15.306	15.522	14.567	14.157	31.716	38.546	23.319	28.908
3.3	15.458	15.849	14.984	14.502	31.799	33.222	17.907	27.851
3.35	14.608	15.046	13.918	13.207	26.406	36.858	20.340	28.680
3.4	14.088	14.845	13.487	13.485	28.441	29.973	16.763	26.698
3.45	14.052	14.588	13.217	12.989	28.915	28.980	18.413	21.438
3.5	12.825	13.900	12.825	12.473	26.081	36.273	15.775	23.410
3.55	12.682	12.854	11.581	11.539	22.760	32.896	18.302	31.126
3.6	11.483	11.479	10.904	10.882	29.149	28.789	15.033	27.630
3.65	10.889	11.200	10.628	10.410	29.952	30.611	12.343	21.806
3.7	10.197	10.468	10.087	9.948	29.848	26.957	11.751	19.980

t (s)	GB6				GB16			
	D_o=30	D_o=40	D_o=50	D_o=60	D_o=30	D_o=40	D_o=50	D_o=60
3.75	9.677	10.303	9.433	8.801	23.969	27.061	13.530	19.692
3.8	8.879	8.998	8.903	8.370	20.833	27.461	14.827	26.736
3.85	8.493	8.437	7.936	7.652	26.052	25.307	14.669	27.765
3.9	7.862	8.921	7.632	7.266	22.686	27.740	14.137	22.660
3.95	8.143	7.893	7.190	7.160	25.017	25.610	10.378	19.467
4	7.557	7.196	6.884	6.488	20.085	22.918	21.149	19.447
4.05	7.052	7.087	6.557	6.162	22.548	18.490	10.885	21.014
4.1	6.978	6.740	6.095	5.687	24.621	18.164	22.486	20.568
4.15	6.658	6.163	6.031	5.656	21.132	17.972	17.924	21.533
4.2	6.543	6.293	5.923	5.308	13.945	23.144	18.554	21.644
4.25	6.434	6.018	5.837	5.340	18.699	20.649	12.307	19.633
4.3	6.233	6.133	6.010	5.241	20.340	19.217	17.884	13.865
4.35	6.415	6.232	5.747	5.226	17.843	21.661	23.708	18.477
4.4	6.308	5.796	5.435	5.681	20.128	18.883	22.406	10.936

The graphical interpretation of these results are given below:

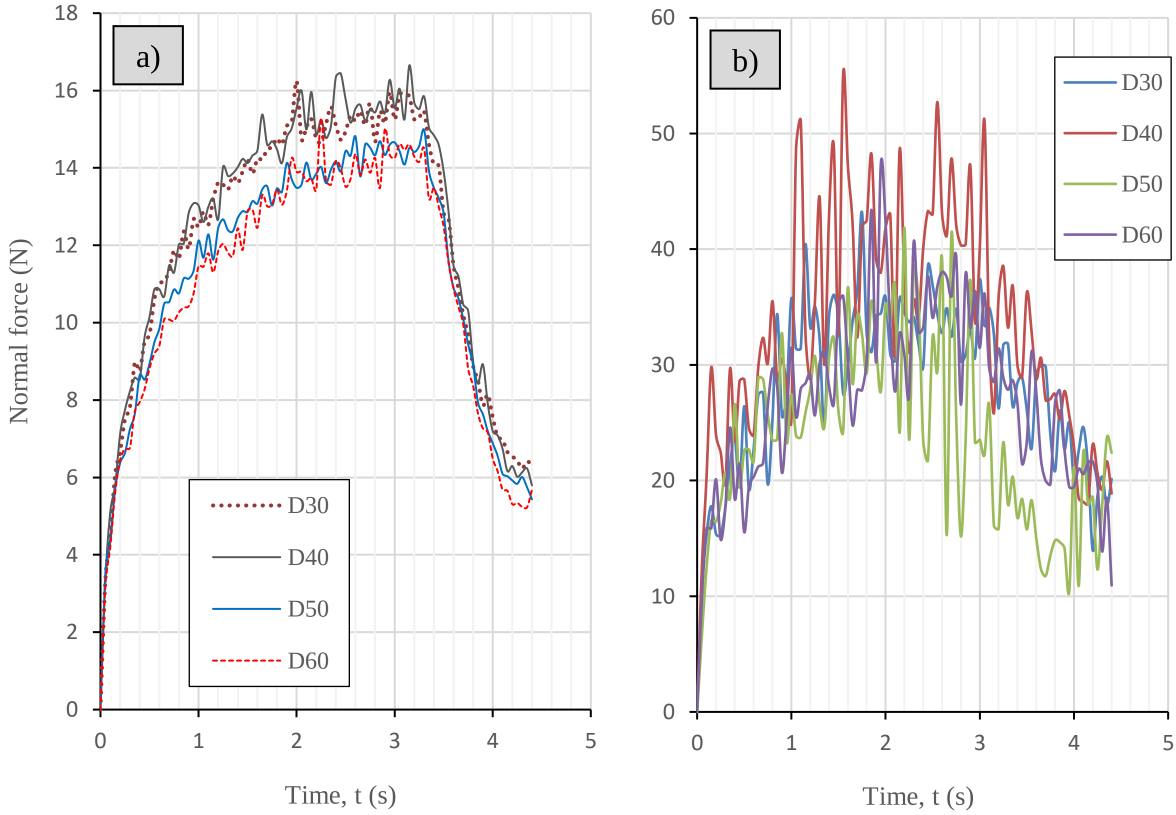

Figure D-2: Graphical simulation of normal force for a) GB6 and b) GB16

APPENDIX E

Detailed Experimental Analysis

E 1. Introduction

The design file was aimed at introducing the reader to the normalized data, detailed procedures and theories associated with the experimental testing. The file includes the process of selecting the various materials and geometries needed to perform the test.

E 2. Lateral Earth Pressure of Prepared Bed

The passive earth pressure of the prepared bed was analysed to understand the amount of pressure exerted onto the nozzle face during collection. The calculated value would be an underestimate of the actual value, due to changes in bed height with respect to time. A bed height H of 45mm was used.

The first step was to determine the passive earth pressure coefficient, given by the following formula:

$$\mathrm{K_p} = \tan^2\left(45^{\circ} + \frac{\emptyset}{2}\right) = \frac{1 + \sin\emptyset}{1 - \sin\emptyset}$$

Where,

$\emptyset$ = Angle of internal friction in °

$\emptyset = 30°$ was used to cater for the initial underestimate. This value was obtained from the outputs achieved by researchers who utilised glass beads in their study (Soria-Hoyo, Valverde & Castellanos, 2008; Lee et al., 2013; Klinkmullker et al., 2016; Cui et al., 2017). Friction angles typically ranged between 25-30°, however 30° was chosen for a more conservative answer. As such, K_p was computed to be equal to 3. The passive earth pressure was then calculated: (Water table level was assumed to be on top of bed surface, thus ignoring surcharge effects)

$$\mathrm{P_p} = \frac{1}{2}K_p H^2 \gamma_{sub} + 2\mathrm{cH}\sqrt{K_p}$$

Where,

γ_{sub}= Submerged unit weight in kN/m^3

H = Height of bed in m

c = Cohesion of soil in kPa

No cohesive forces were present due to size and nature of particles therefore, cohesion c was assumed to be equal to 0kPa. It is also worth highlighting that the calculated values pertain to both 6 and 16mm diameter beads as their material composition was assumed to be identical. Thus, exhibiting similar index properties (eg. γ_b, ρ_{dry}, Ø and void ratio e).

The submerged unit weight γ_b, was calculated to be 8.76kN/m^3. Defined as the saturated bulk unit weight (γ_b = 18.57kN/m^3) minus the unit weight of water (γ_w =9.81 kN/m^3). The bulk unit weight was determined through the use of the following equation and the known porosity (n=0.42).

$$\rho_{sat} = \frac{M_s+M_w}{V} = \rho_s(1-n)+\rho_w(n)$$

$$\rho_{sat} = 2540(1-0.42)+1000(0.42)$$

$$\rho_{sat} = 1893.2\text{kg/m}^3$$

Therefore,

$$\gamma_{sat} = \frac{\rho_{sat}\times g}{1000}$$

$$\gamma_{sat} = \frac{1893.2\times 9.81}{1000}$$

$$\gamma_{sat} = 18.572\text{kN/m}^3$$

The passive force was calculated to be:

$$P_p = \frac{1}{2}3(0.045m)^2(8.76) + 2(0)$$

$$P_p = 0.0266\ kN$$

The pressure distribution illustrating the resultant passive force is as follows:

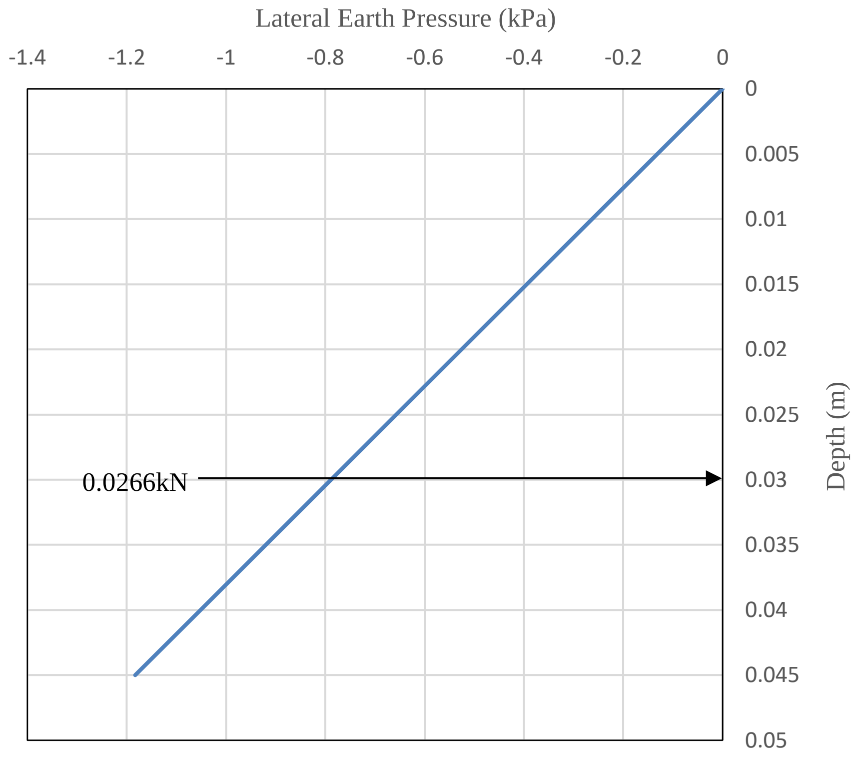

Figure E-1: Pressure distribution of Glass bead bed

However, the force calculated was the immediate force at t=0s, also regarded as the minimum. The critical force occurred when the bulge height in front of the nozzle was at a maximum. Before the formation of the bulge when the materials first accumulated to the top of the nozzle (H=0.08m), the passive force was calculated to be:

$$\mathrm{P_p} = \frac{1}{2} K_p H^2 \gamma_{sub} + 2\mathrm{cH}\sqrt{K_p}$$

$$\mathrm{P_p} = \frac{1}{2} 3(0.08m)^2(8.76) + 2(0)$$

$$\mathrm{P_p} = 0.0841\ kN$$

The critical passive force was found to occur at t=2.9s, according to the maximum bulge height. Due to the height variability of the retained material, Culman's method was found to be the most suitable approach in calculating the resultant passive or normal force on the nozzle face. The shape of the bulge was approximated using the figure below; a screenshot of the maximum bulge height obtained through a video analysis with the help of a scale attached to the side of the suction pipe.

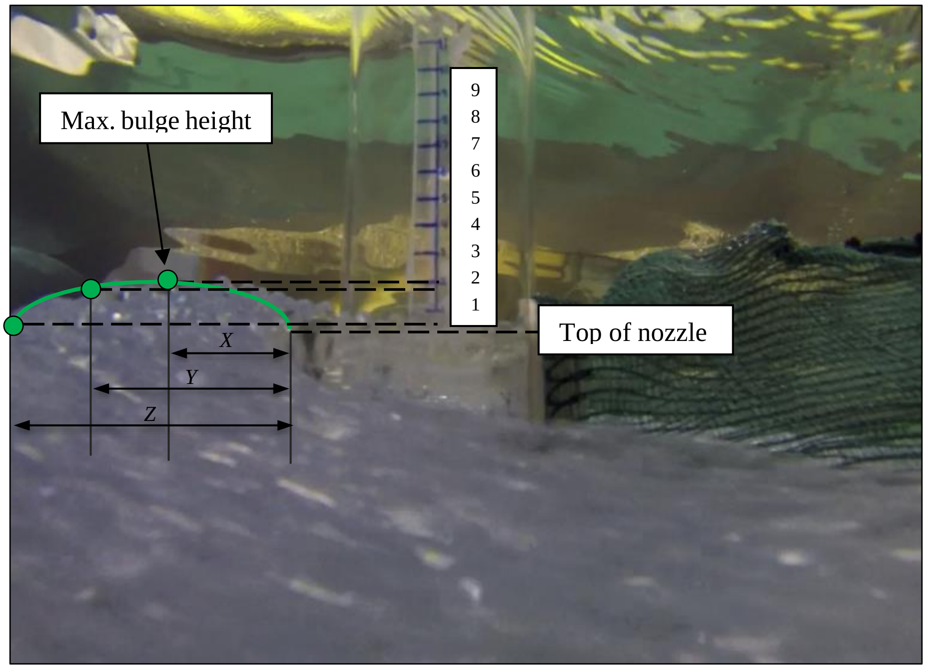

Figure E-2: Bulge height approximation

The max bulge height was found to be 20mm above the top of the nozzle. Using this point at distance X and other points (Y and Z), the bulge surface was plotted. The measurements were summarised as follows:

Table E-1: Constant parameters in Beverloo Law

Point	Distance (mm)	Height (mm)
X	45	20
Y	75	15
Z	105	2

The steps taken in calculating the passive force using Culman's method was as follows:

Step 1: The nozzle face of height (H=8m) was constructed (A-B)

Step 2: A line BE at an angle of Ø=30° was drawn to the horizontal (Repose line)

Step 3: The pressure line BD was drawn at an angle of $\alpha + \delta$. In this case α, the batter angle, was determined to be 90° and δ, the wall friction, was determined to be 0.

Step 4: Trial slip planes from BC1, BC2 to BC13 were drawn. The weights of the wedges ABC1, ABC2 to ABC13 were calculated and plotted to scale as BE1, BE2 to BE13 on the repose line BE.

Step 5: Through E1, E2 to E13, lines were parallel to the pressure line BD, intersecting BC1, BC2 to BC13 at F1, F2 to F13 respectively.

Step 6: A smooth curve was drawn through point F5 to F13. The curve is called the Culman line.

Step 7: A line is drawn parallel to the repose line BE and tangential to the Culman line at such a point where it touches the Culman line, referred to as point F'. Then BF' is joined with a line and extended till a point it intersects the bulge surface line, referred to as C'. BC' is the critical clip plane. Coincidently, BC' was the same BC12.

Step 8: Through F', line F'E' was drawn parallel to the pressure line BD, intersecting the repose line at E'.

Step 9: the weight W of the wedge ABC' was calculated. The resultant passive earth pressure force Pp was given by:

$$\frac{\mathrm{P_p}}{W} = \frac{F'E'}{B'E'}$$

$$\mathrm{P_p} = \mathrm{W}\left(\frac{F'E'}{B'E'}\right)$$

The results were summarised in the table below in conjunction with Figure E-3.

Table E-2: Weight of wedges plotted on line BE

Wedge	Area (m^2)	Weight (kN/m)
ABC1	9.76E-04	8.55E-03
ABC2	1.68E-03	1.47E-02
ABC3	2.42E-03	2.12E-02
ABC4	3.15E-03	2.76E-02
ABC5	3.82E-03	3.35E-02
ABC6	4.45E-03	3.90E-02
ABC7	5.17E-03	4.53E-02
ABC8	6.18E-03	5.42E-02
ABC9	7.20E-03	6.31E-02
ABC10	8.34E-03	7.31E-02
ABC11	9.83E-03	8.61E-02
ABC12	1.09E-02	9.55E-02
ABC13	1.27E-02	1.11E-01

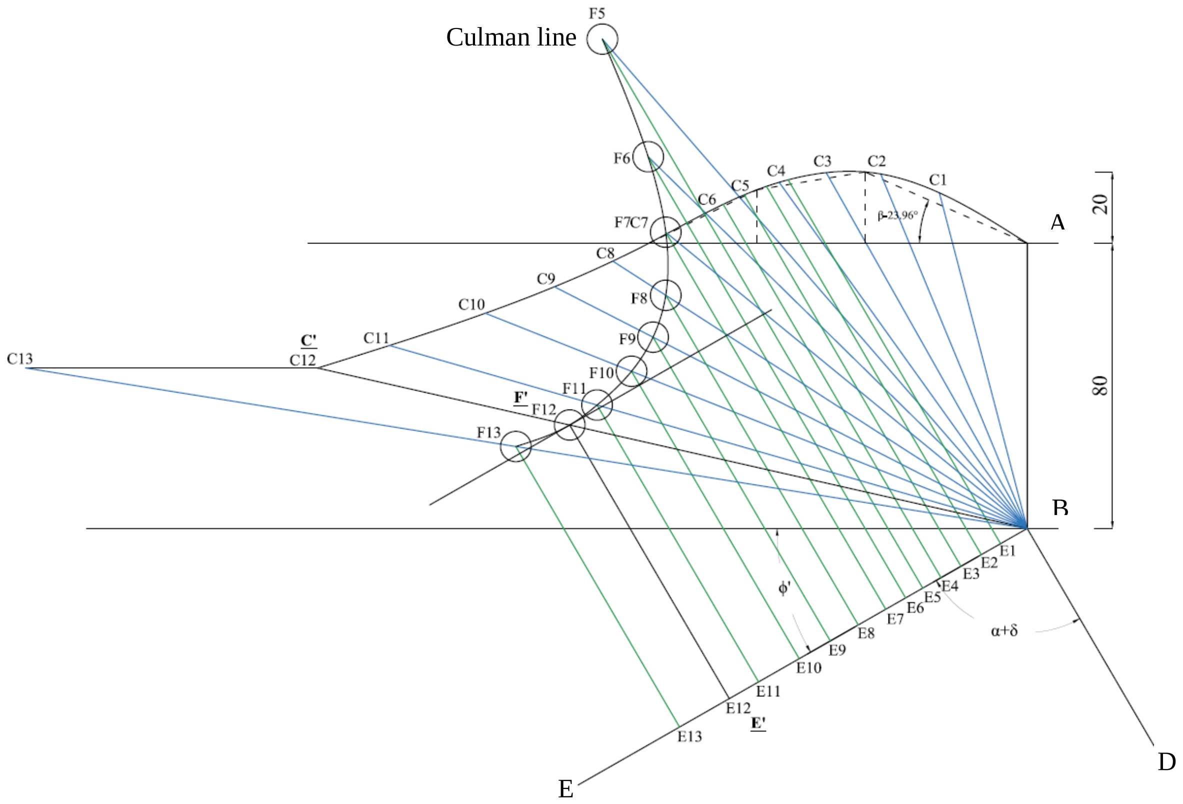

Figure E-3: Analytical analysis of passive force using Culman's method

The weight of the critical wedge ABC':

$$W = \text{Area} \times \rho_{sub}$$

$$W = (1.09 \times 10^{-2}) \times 8.76 kN/m^3$$

$$W = 9.55 \times 10^{-2} kN/m$$

Therefore, with F'E'=8861.42mm and B'E'=9545.26mm:

$$\frac{\text{P}_\text{p}}{W} = \frac{F'E'}{B'E'}$$

$$\text{P}_\text{p} = \text{W}\left(\frac{F'E'}{B'E'}\right)$$

$$\text{P}_\text{p} = 9.545 \times 10^{-3}\left(\frac{8861.42mm}{9545.26mm}\right)$$

$$\text{P}_\text{p} = 0.0886\text{kN}$$

E 3. Key Parameters in the Beverloo Law

Through the review of literature, it was evident that orifice vicinity parameters had a significant influence on the mass flow rate of granular materials through the hopper. Distinctly, these parameters included the discharge coefficient C, the shape coefficient k, and the discharge diameter D.

$$W = C\rho_b\sqrt{g}\left(D - kd_p\right)^{\frac{5}{2}}$$

The prescribed values for the discharge and shape coefficients were determined empirically through numerous physical tests and the diameter of the orifice has a significant effect on the magnitude of the flow. To analyse the impact of the key parameters mentioned, each parameter will be adjusted with the other variables held constant. The following variables were held constant for all three parameter checks:

Table E-3: Constant parameters in Beverloo Law

Parameter	Symbol	Units	Value
Bulk Density	ρ_b	kg/m3	1600
Gravitational acceleration	g	m/s2	9.81
Particle diameter	d	m	-

E 3.1 Effect of Discharge Coefficient

By using the selected values in Table E-1 and selecting the shape coefficient and discharge diameter, k = 1 and D = 0.1 respectively. The effect of the discharge coefficient C is illustrated in the plot of mass flow rate W versus particle diameter d, for different values of C.

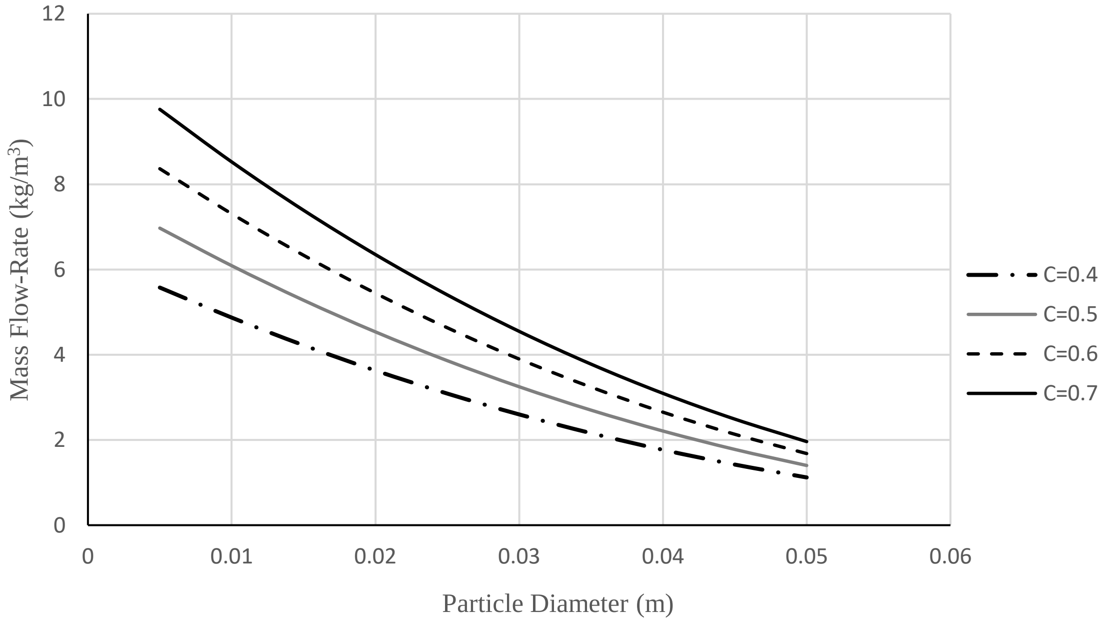

Figure E-4: Effect of discharge coefficient

E 3.2 Effect of Shape Coefficient

Holding the same variables as above to be constant and selecting the discharge coefficient C = 0.6, the effect of the shape coefficient is shown in Figure. As discussed previously, spherical particles generally have a shape coefficient of k = 0.58.

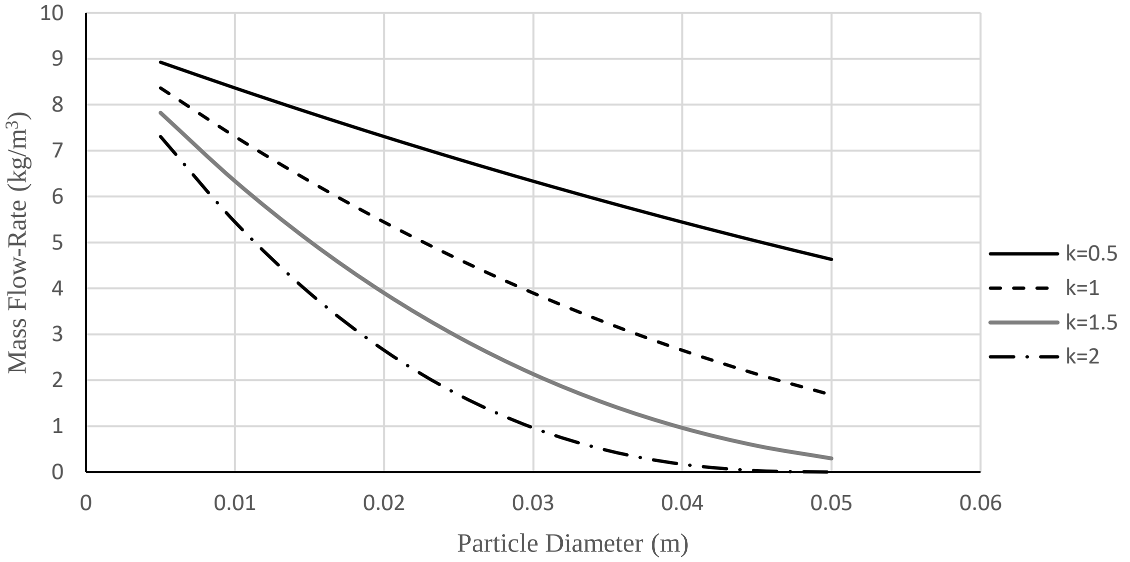

Figure E-5: Effect of shape coefficient

E 3.3 Effect of Discharge Diameter

From Beverloo flow equation, the aperture diameter D has the greatest impact on the discharge rate. Using Figure, note how the discharge rate changes exponentially for different values of D. This relation is influenced by the expression W∝D$^{5/2}$. Therefore, due to the importance of the parameter, it was essential that an effective diameter be calculated, thus the introduction of D – kd.

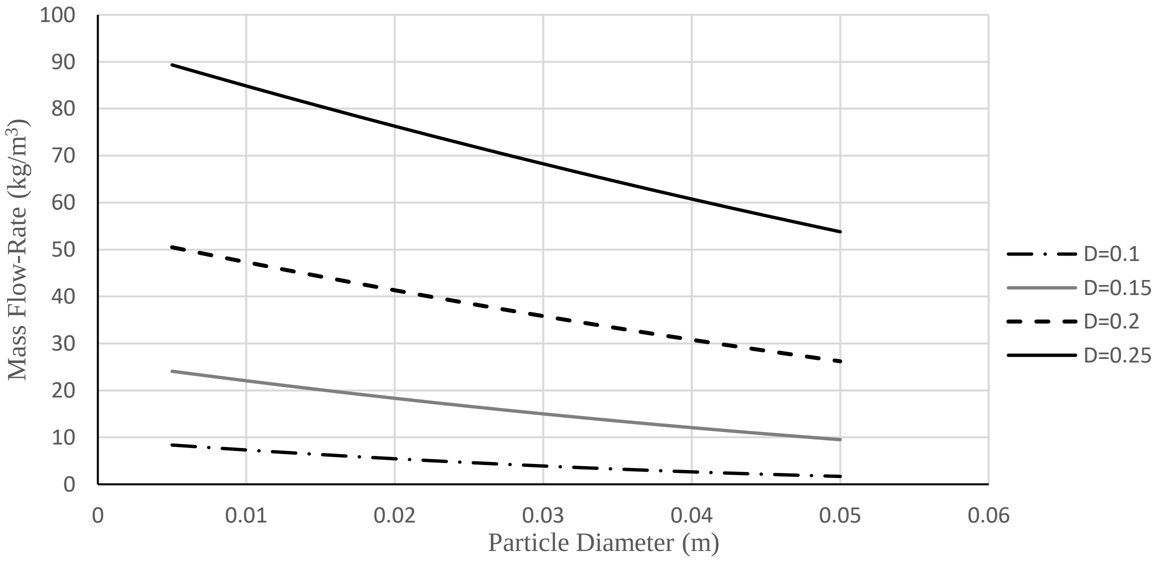

Figure E-6: Effect of discharge diameter

E 4. Determining Beverloo Coefficients: Regression Analysis

After taking into account a constant velocity though an orifice and ignoring the effects of retained pressure height (Janssen, 1895), the proposed equation to evaluate the collection rate of materials is given by the modified empirical equation:

$$\mathrm{W} = \mathrm{C}\rho_{\mathrm{b}}\mathrm{v}\left(\mathrm{D}_{o} - \mathrm{kd}_{p}\right)^{2}$$

The discharge coefficient C and the shape factor k, are free parameters that need to be determined experimentally through a regression analysis. However, to allow the above expression to be modified for a particular material and its associated index properties, the variable, *R*, known as the ratio between the orifice diameter and particle diameter needed to be introduced. The process of substituting $\mathrm{R}=\mathrm{D}_{\mathrm{o}}/\mathrm{d}_{\mathrm{p}}$ was as follows:

$$\mathrm{W} = \mathrm{C}\rho_{\mathrm{b}}\mathrm{v}\left(R\mathrm{d}_{p} - \mathrm{kd}_{p}\right)^{2}$$
$$\mathrm{W} = \mathrm{C}\rho_{\mathrm{b}}\mathrm{v}\left(\mathrm{d}_{p}(R - \mathrm{k})\right)^{2}$$
$$\mathrm{W} = \mathrm{C}\rho_{\mathrm{b}}\mathrm{vd}_{p}{}^{2}(\mathrm{R} - \mathrm{k})^{2}$$

According to literature, a number of methods exist for the determination of coefficients. The one of interest included the method implored by Zatloukal & Šklubalová (2012) due to their mathematical and dimensional approach. A number of other researchers followed similar procedures.

Using Zatloukal et al. (2012), the above newly formed expression was rearranged to make *R* the function of the equation, where:

$$\mathrm{R} = \mathrm{C}^{-0.5}\left(\frac{\mathrm{W}}{\rho_{\mathrm{b}}\mathrm{v}d_{p}^{2}}\right)^{0.5} + \mathrm{k}$$

A linear function, R versus $\left(\frac{W}{\rho_{b}vd_{p}^{2}}\right)^{0.5}$, in the form of ***y=mx+c*** was plotted. Here the y-intercept ***c*** was equal to the shape coefficient *k* and the gradient *m* was equal to $\mathrm{C}^{-0.5}$. The x-axis values were obtained from the translational speed of the nozzle (*v* = 0.26m/s), the bulk density of the particles ($\rho_{\mathrm{b,GB6\&GB16}}$ = 1485kg/m^3) and the calibrated results achieved through Rocky, summarised as follows:

Table E-4: Calibrated Rocky results

D_o (mm)	**W (kg/s)**	
	GB6	**GB16**
30	0.1649	0.0387
40	0.3164	0.1510
50	0.5471	0.2027
60	0.7856	0.4210

*Note: The results for any operation speed (v=0.104m/s-0.26m/s) could have been used for the calibration but the use of 0.26m/s was the more practical approach due to lower simulations times, hence resulting in a more extensive analysis.

The plot of R versus $\left(\frac{W}{\rho_b v d_p^2}\right)^{0.5}$ was as follows:

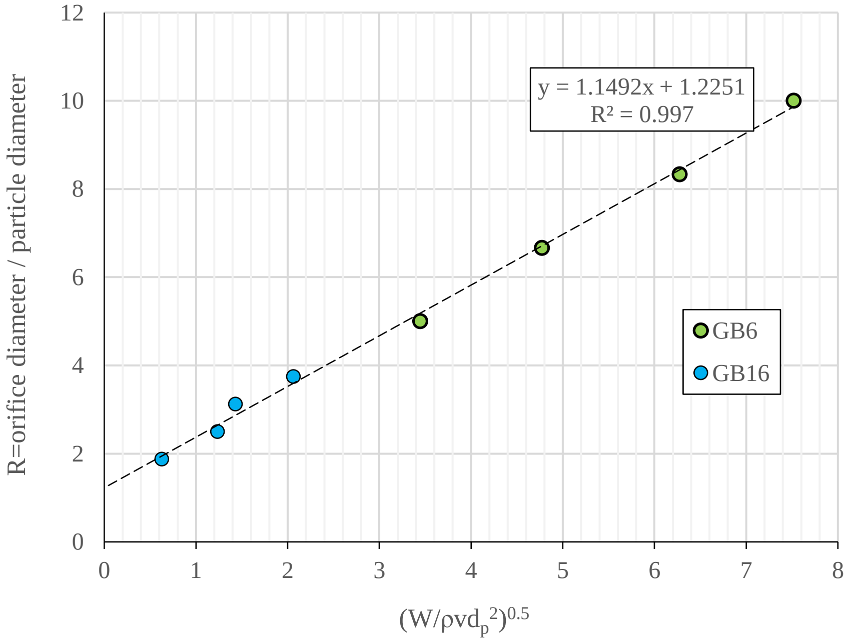

Figure E-7: Regression Analysis by Zatloukal et al. (2012)

By manipulating the gradient and intercept of the linear fit curves, the *C* and *k* values were determined to be:

Table E-5: Coefficients as determined by Zatloukal (2012)

	$(W/\rho_b v d_p^2)^{0.5}$
d_p	**GB6 and GB16**
C	0.757
k	1.225

Using the determined coefficients, the final plot of the collection rate *W* versus ratio *R*, and the assumed output values from Rocky could be configured. The plot of these results were as follows:

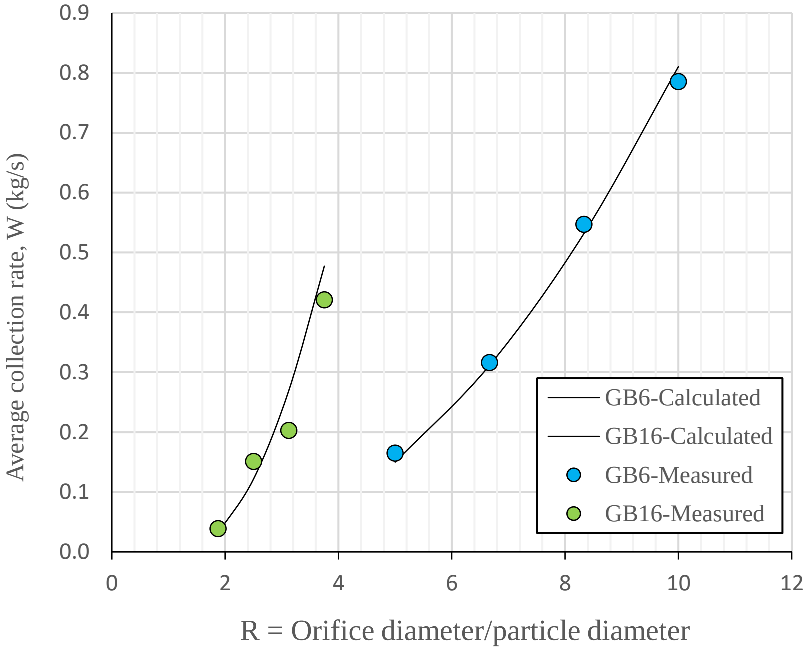

Figure E-9: Plot of measured values and modified Beverloo Law

E 5. Normalization of Collected Data

Using the raw data collected in Appendix B, further calculations were made for interpretation. This included collection rates, amount of effective and normal recovery; and mass and volume concentrations. The methods for calculating these normalised parameters were summarised as follows:

1. Measured entrainment rate, Q:

$$Q = \frac{\text{Mass entrained}}{t}$$

$$Q = \frac{\text{Mass entrained}}{\frac{\text{distance}}{\text{velocity}}}$$

e.g.(MMS,GB6, D_o=30mm, v=0.26m/s, Mass=0.339kg)

$$Q = \frac{0.339\text{kg}}{\frac{1.15\text{m}}{0.26\text{m/s}}}$$

$$Q = \frac{0.339\text{kg}}{4.423s}$$

$$Q = 0.077\text{kg/s}$$

2. Recovery Ratio:

$$\text{Recovery} = \frac{\text{Volume entrained}}{\text{Channel volume}}$$

$$\text{Recovery} = \frac{\frac{Mass\ entrained}{\rho_{bulk}}}{\text{x}\times\text{y}\times\text{z}}$$

e.g.(MMS, GB6, D_o=30mm, v=0.26m/s, Mass=0.339kg)

$$\text{Recovery} = \frac{\frac{0.339}{1485 kg/m^3}}{1.15\text{m}\times0.15\text{m}\times0.045\text{m}}$$

$$\text{Recovery} = 0.0294$$

3. Effective Recovery Ratio:

$$\text{Effective Recovery} = \frac{\text{Recovery ratio}}{\text{Orifice to nozzle face ratio}}$$

$$\text{Effective Recovery} = \frac{\text{Recovery ratio}}{\left(\frac{A_{\text{orifice}}}{A_{\text{face}}}\right)}$$

e.g.(MMS, GB6, D_o=30mm, v=0.26m/s, Mass=0.339kg)

$$\text{Effective Recovery} = \frac{0.0294}{\left(\frac{0.03^2}{0.15\times0.07}\right)}$$

$$\text{Effective Recovery} = 0.343$$

4. Mass Concentration (Used only in MSS):

$$\text{C}_m = \frac{\text{M}_s}{\text{M}_s + \text{M}_w}$$

e.g.(MSS, GB6, D_o=30mm, v=0.26m/s, Q=3.213l/s, Mass=3.975kg)

$$\text{C}_m = \frac{3.975}{3.975 + \text{Qt}}$$

$$\text{C}_m = \frac{3.975}{3.975 + 3.213\left(\frac{1.15\text{m}}{0.26\text{m/s}}\right)}$$

$$\text{C}_m = 0.219$$

5. Volumetric Concentration (Used only in MSS):

$$\mathrm{C}_v = \frac{\mathrm{V}_s}{\mathrm{V}_s + \mathrm{V}_w}$$

e.g.(MSS, GB6, D_o=30mm, v=0.26m/s, Q=3.213l/s, Mass=3.975kg)

$$\mathrm{C}_v = \frac{\frac{M_s}{\rho}}{\frac{M_s}{\rho} + \frac{\mathrm{Qt}}{1000}}$$

$$\mathrm{C}_v = \frac{\frac{3.975}{2540}}{\frac{3.975}{2540} + \frac{3.213(\frac{1.15\mathrm{m}}{0.26\mathrm{m/s}})}{1000}}$$

$$\mathrm{C}_v = 0.099$$

<u>Using the sample calculations, the data was tabulated as follows:</u>

MMS:GB6

D_o=30mm

Test no.	Velocity	Distance	Total mass entrained	Average entrained	Measured entrainment rate	Average entrainment rate	Channel volume	Volume entrained	Recovery channel ratio	Effective recovery ratio
	m/s	m	kg	kg	kg/s	kg/s	m^3	m^3	-	-
1	0.104	1.150	0.323	0.317	0.029	0.029	7.76E-03	2.18E-04	0.028	0.210
2	0.104	1.150	0.319		0.029		7.76E-03	2.15E-04	0.028	0.208
3	0.104	1.150	0.308		0.028		7.76E-03	2.07E-04	0.027	0.200
4	0.156	1.150	0.304	0.317	0.041	0.043	7.76E-03	2.05E-04	0.026	0.198
5	0.156	1.150	0.292		0.040		7.76E-03	1.97E-04	0.025	0.190
6	0.156	1.150	0.355		0.048		7.76E-03	2.39E-04	0.031	0.231
7	0.208	1.150	0.323	0.318	0.058	0.057	7.76E-03	2.18E-04	0.028	0.210
8	0.208	1.150	0.318		0.058		7.76E-03	2.14E-04	0.028	0.207
9	0.208	1.150	0.312		0.056		7.76E-03	2.10E-04	0.027	0.203
10	0.260	1.150	0.309	0.320	0.070	0.072	7.76E-03	2.08E-04	0.027	0.201
11	0.260	1.150	0.312		0.071		7.76E-03	2.10E-04	0.027	0.203
12	0.260	1.150	0.339		0.077		7.76E-03	2.28E-04	0.029	0.221

D_o= 40mm

Test no.	Velocity	Distance	Total mass entrained	Average entrained	Measured entrainment rate	Average entrainment rate	Channel volume	Volume entrained	Recovery channel ratio	Effective recovery ratio
	m/s	m	kg	kg	kg/s	kg/s	m^3	m^3	-	-
1	0.104	1.150	0.601	0.607	0.054	0.055	7.76E-03	4.05E-04	0.052	0.220
2	0.104	1.150	0.625		0.057		7.76E-03	4.21E-04	0.054	0.229
3	0.104	1.150	0.595		0.054		7.76E-03	4.01E-04	0.052	0.218
4	0.156	1.150	0.608	0.610	0.082	0.083	7.76E-03	4.09E-04	0.053	0.223
5	0.156	1.150	0.618		0.084		7.76E-03	4.16E-04	0.054	0.226
6	0.156	1.150	0.604		0.082		7.76E-03	4.07E-04	0.052	0.221
7	0.208	1.150	0.607	0.609	0.110	0.110	7.76E-03	4.09E-04	0.053	0.222
8	0.208	1.150	0.609		0.110		7.76E-03	4.10E-04	0.053	0.223
9	0.208	1.150	0.612		0.111		7.76E-03	4.12E-04	0.053	0.224
10	0.260	1.150	0.65	0.617	0.147	0.139	7.76E-03	4.38E-04	0.056	0.238
11	0.260	1.150	0.606		0.137		7.76E-03	4.08E-04	0.053	0.222
12	0.260	1.150	0.594		0.134		7.76E-03	4.00E-04	0.052	0.217

D_o=50mm

Test no.	Velocity	Distance	Total mass entrained	Average entrained	Measured entrainment rate	Average entrainment rate	Channel volume	Volume entrained	Recovery channel ratio	Effective recovery ratio
	m/s	m	kg	kg	kg/s	kg/s	m^3	m^3	-	-
1	0.104	1.150	1.084	1.055	0.098	0.095	7.76E-03	7.30E-04	0.094	0.254
2	0.104	1.150	1.036		0.094		7.76E-03	6.98E-04	0.090	0.243
3	0.104	1.150	1.044		0.094		7.76E-03	7.03E-04	0.091	0.245
4	0.156	1.150	1.058	1.049	0.144	0.142	7.76E-03	7.12E-04	0.092	0.248
5	0.156	1.150	1.043		0.141		7.76E-03	7.02E-04	0.090	0.244
6	0.156	1.150	1.046		0.142		7.76E-03	7.04E-04	0.091	0.245
7	0.208	1.150	1.041	1.051	0.188	0.190	7.76E-03	7.01E-04	0.090	0.244
8	0.208	1.150	1.061		0.192		7.76E-03	7.14E-04	0.092	0.249
9	0.208	1.150	1.052		0.190		7.76E-03	7.08E-04	0.091	0.246
10	0.260	1.150	1.075	1.066	0.243	0.241	7.76E-03	7.24E-04	0.093	0.252
11	0.260	1.150	1.071		0.242		7.76E-03	7.21E-04	0.093	0.251
12	0.260	1.150	1.052		0.238		7.76E-03	7.08E-04	0.091	0.246

D_o=60mm

Test no.	Velocity	Distance	Total mass entrained	Average entrained	Measured entrainment rate	Average entrainment rate	Channel volume	Volume entrained	Recovery channel ratio	Effective recovery ratio
	m/s	m	kg	kg	kg/s	kg/s	m^3	m^3	-	-
1	0.104	1.150	1.566	1.583	0.142	0.143	7.76E-03	1.05E-03	0.136	0.255
2	0.104	1.150	1.60		0.145		7.76E-03	1.08E-03	0.139	0.260
3	0.104	1.150	1.582		0.143		7.76E-03	1.07E-03	0.137	0.257
4	0.156	1.150	1.591	1.588	0.216	0.215	7.76E-03	1.07E-03	0.138	0.259
5	0.156	1.150	1.58		0.214		7.76E-03	1.06E-03	0.137	0.257
6	0.156	1.150	1.593		0.216		7.76E-03	1.07E-03	0.138	0.259
7	0.208	1.150	1.591	1.576	0.288	0.285	7.76E-03	1.07E-03	0.138	0.259
8	0.208	1.150	1.541		0.279		7.76E-03	1.04E-03	0.134	0.251
9	0.208	1.150	1.595		0.288		7.76E-03	1.07E-03	0.138	0.259
10	0.260	1.150	1.591	1.587	0.360	0.359	7.76E-03	1.07E-03	0.138	0.259
11	0.260	1.150	1.574		0.356		7.76E-03	1.06E-03	0.137	0.256
12	0.260	1.150	1.596		0.361		7.76E-03	1.07E-03	0.138	0.260

MMS:GB16

D_o=30mm

Test no.	Velocity	Distance	Total mass entrained	Average entrained	Measured entrainment rate	Average entrainment rate	Channel volume	Volume entrained	Recovery channel ratio	Effective recovery ratio
	m/s	m	kg	kg	kg/s	kg/s	m^3	m^3	-	-
1	0.104	1.150	0.209	0.205	0.019	0.019	7.76E-03	1.41E-04	0.018	0.136
2	0.104	1.150	0.203		0.018		7.76E-03	1.37E-04	0.018	0.132
3	0.104	1.150	0.202		0.018		7.76E-03	1.36E-04	0.018	0.131
4	0.156	1.150	0.192	0.200	0.026	0.027	7.76E-03	1.29E-04	0.017	0.125
5	0.156	1.150	0.218		0.030		7.76E-03	1.47E-04	0.019	0.142
6	0.156	1.150	0.189		0.026		7.76E-03	1.27E-04	0.016	0.123
7	0.208	1.150	0.162	0.157	0.029	0.028	7.76E-03	1.09E-04	0.014	0.105
8	0.208	1.150	0.196		0.035		7.76E-03	1.32E-04	0.017	0.128
9	0.208	1.150	0.114		0.021		7.76E-03	7.68E-05	0.010	0.074
10	0.260	1.150	0.203	0.177	0.046	0.040	7.76E-03	1.37E-04	0.018	0.132
11	0.260	1.150	0.115		0.026		7.76E-03	7.74E-05	0.010	0.075
12	0.260	1.150	0.212		0.048		7.76E-03	1.43E-04	0.018	0.138

D_o=40mm

Test no.	Velocity	Distance	Total mass entrained	Average entrained	Measured entrainment rate	Average entrainment rate	Channel volume	Volume entrained	Recovery channel ratio	Effective recovery ratio
	m/s	m	kg	kg	kg/s	kg/s	m^3	m^3	-	-
1	0.104	1.150	0.516	0.511	0.047	0.046	7.76E-03	3.47E-04	0.045	0.189
2	0.104	1.150	0.506		0.046		7.76E-03	3.41E-04	0.044	0.185
3	0.104	1.150	0.512		0.046		7.76E-03	3.45E-04	0.044	0.187
4	0.156	1.150	0.472	0.505	0.064	0.069	7.76E-03	3.18E-04	0.041	0.173
5	0.156	1.150	0.523		0.071		7.76E-03	3.52E-04	0.045	0.191
6	0.156	1.150	0.521		0.071		7.76E-03	3.51E-04	0.045	0.191
7	0.208	1.150	0.453	0.475	0.082	0.086	7.76E-03	3.05E-04	0.039	0.166
8	0.208	1.150	0.462		0.084		7.76E-03	3.11E-04	0.040	0.169
9	0.208	1.150	0.511		0.092		7.76E-03	3.44E-04	0.044	0.187
10	0.260	1.150	0.502	0.508	0.113	0.115	7.76E-03	3.38E-04	0.044	0.184
11	0.260	1.150	0.509		0.115		7.76E-03	3.43E-04	0.044	0.186
12	0.260	1.150	0.512		0.116		7.76E-03	3.45E-04	0.044	0.187

D_o=50mm

Test no.	Velocity	Distance	Total mass entrained	Average entrained	Measured entrainment rate	Average entrainment rate	Channel volume	Volume entrained	Recovery channel ratio	Effective recovery ratio
	m/s	m	kg	kg	kg/s	kg/s	m^3	m^3	-	-
1	0.104	1.150	0.900	0.862	0.081	0.078	7.76E-03	6.06E-04	0.078	0.211
2	0.104	1.150	0.836		0.076		7.76E-03	5.63E-04	0.073	0.196
3	0.104	1.150	0.851		0.077		7.76E-03	5.73E-04	0.074	0.199
4	0.156	1.150	0.927	0.879	0.126	0.119	7.76E-03	6.24E-04	0.080	0.217
5	0.156	1.150	0.858		0.116		7.76E-03	5.78E-04	0.074	0.201
6	0.156	1.150	0.851		0.115		7.76E-03	5.73E-04	0.074	0.199
7	0.208	1.150	0.865	0.886	0.156	0.160	7.76E-03	5.82E-04	0.075	0.203
8	0.208	1.150	0.926		0.167		7.76E-03	6.24E-04	0.080	0.217
9	0.208	1.150	0.867		0.157		7.76E-03	5.84E-04	0.075	0.203
10	0.260	1.150	0.825	0.873	0.187	0.197	7.76E-03	5.56E-04	0.072	0.193
11	0.260	1.150	0.894		0.202		7.76E-03	6.02E-04	0.078	0.209
12	0.260	1.150	0.899		0.203		7.76E-03	6.05E-04	0.078	0.211

D_o=60mm

Test no.	Velocity	Distance	Total mass entrained	Average entrained	Measured entrainment rate	Average entrainment rate	Channel volume	Volume entrained	Recovery channel ratio	Effective recovery ratio
	m/s	m	kg	kg	kg/s	kg/s	m^3	m^3	-	-
1	0.104	1.150	1.311	1.298	0.119	0.117	7.76E-03	8.83E-04	0.114	0.213
2	0.104	1.150	1.292		0.117		7.76E-03	8.70E-04	0.112	0.210
3	0.104	1.150	1.291		0.117		7.76E-03	8.69E-04	0.112	0.210
4	0.156	1.150	1.306	1.300	0.177	0.176	7.76E-03	8.79E-04	0.113	0.212
5	0.156	1.150	1.283		0.174		7.76E-03	8.64E-04	0.111	0.209
6	0.156	1.150	1.311		0.178		7.76E-03	8.83E-04	0.114	0.213
7	0.208	1.150	1.308	1.287	0.237	0.233	7.76E-03	8.81E-04	0.113	0.213
8	0.208	1.150	1.272		0.230		7.76E-03	8.57E-04	0.110	0.207
9	0.208	1.150	1.281		0.232		7.76E-03	8.63E-04	0.111	0.208
10	0.260	1.150	1.299	1.295	0.294	0.293	7.76E-03	8.75E-04	0.113	0.211
11	0.260	1.150	1.296		0.293		7.76E-03	8.73E-04	0.112	0.211
12	0.260	1.150	1.291		0.292		7.76E-03	8.69E-04	0.112	0.210

MSS:GB6

D$_o$=30mm

Test no.	Velocity	Total mass entrained	Average entrained	Measured entrainment rate	Average entrainment rate	Volume entrained	Recovery channel ratio	Average recovery	Effective recovery ratio	Mass concentration	Average concentration	Volumetric concentration	Average concentration
	m/s	kg	kg	kg/s	kg/s	m^3	-	-	-	kg/l	kg/l	-	-
1	0.104	8.591	8.611	0.777	0.779	5.79E-03	0.745	0.747	5.590	0.195	0.195	0.087	0.087
2	0.104	8.681		0.785		5.85E-03	0.753		5.648	0.196		0.088	
3	0.104	8.561		0.774		5.76E-03	0.743		5.375	0.194		0.087	
4	0.156	6.396	6.270	0.868	0.851	4.31E-03	0.555	0.544	2.371	0.213	0.209	0.096	0.094
5	0.156	6.122		0.830		4.12E-03	0.531		3.983	0.205		0.092	
6	0.156	6.292		0.854		4.24E-03	0.546		4.224	0.210		0.095	
7	0.208	4.821	4.885	0.872	0.883	3.25E-03	0.418	0.424	1.785	0.213	0.216	0.097	0.098
8	0.208	4.927		0.891		3.32E-03	0.427		3.206	0.217		0.098	
9	0.208	4.906		0.887		3.30E-03	0.426		3.192	0.216		0.098	
10	0.260	3.975	4.076	0.899	0.921	2.68E-03	0.345	0.354	1.285	0.219	0.223	0.099	0.101
11	0.260	4.155		0.939		2.80E-03	0.360		1.785	0.226		0.103	
12	0.260	4.097		0.926		2.76E-03	0.355		2.666	0.224		0.102	

D$_o$=40mm

Test no.	Velocity	Total mass entrained	Average entrained	Measured entrainment rate	Average entrainment rate	Volume entrained	Recovery channel ratio	Average recovery	Effective recovery ratio	Mass concentration	Average concentration	Volumetric concentration	Average concentration
	m/s	kg	kg	kg/s	kg/s	m^3	-	-	-	kg/l	kg/l	-	-
1	0.104	9.785	9.661	0.885	0.874	6.59E-03	0.849	0.838	3.581	0.216	0.214	0.098	0.097
2	0.104	9.602		0.868		6.47E-03	0.833		3.514	0.213		0.096	
3	0.104	9.597		0.868		6.46E-03	0.833		3.512	0.213		0.096	
4	0.156	6.934	6.918	0.941	0.938	4.67E-03	0.602	0.600	2.538	0.226	0.226	0.103	0.103
5	0.156	6.907		0.937		4.65E-03	0.599		2.528	0.226		0.103	
6	0.156	6.913		0.938		4.66E-03	0.600		2.530	0.226		0.103	
7	0.208	5.782	5.855	1.046	1.059	3.89E-03	0.502	0.508	2.116	0.246	0.248	0.114	0.115
8	0.208	5.934		1.073		4.00E-03	0.515		2.172	0.250		0.116	
9	0.208	5.848		1.058		3.94E-03	0.507		2.140	0.248		0.115	
10	0.260	5.371	5.208	1.214	1.178	3.62E-03	0.466	0.452	1.966	0.274	0.268	0.130	0.126
11	0.260	5.170		1.169		3.48E-03	0.449		1.892	0.267		0.125	
12	0.260	5.084		1.149		3.42E-03	0.441		1.861	0.263		0.123	

D_o=50mm

Test no.	Velocity	Total mass entrained	Average entrained	Measured entrainment rate	Average entrainment rate	Volume entrained	Recovery channel ratio	Average recovery	Effective recovery ratio	Mass concentration	Average concentration	Volumetric concentration	Average concentration
	m/s	kg	kg	kg/s	kg/s	m^3	-	-	-	kg/l	kg/l	-	-
1	0.104	9.458	9.192	0.855	0.831	6.37E-03	0.820	0.797	2.215	0.210	0.206	0.095	0.092
2	0.104	8.988		0.813		6.05E-03	0.780		2.105	0.202		0.091	
3	0.104	9.129		0.826		6.15E-03	0.792		2.138	0.204		0.092	
4	0.156	7.314	7.165	0.992	0.972	4.93E-03	0.634	0.622	1.713	0.236	0.232	0.108	0.106
5	0.156	6.895		0.935		4.64E-03	0.598		1.615	0.225		0.103	
6	0.156	7.286		0.988		4.91E-03	0.632		1.707	0.235		0.108	
7	0.208	5.541	5.692	1.002	1.029	3.73E-03	0.481	0.494	1.298	0.238	0.243	0.109	0.112
8	0.208	5.744		1.039		3.87E-03	0.498		1.345	0.244		0.113	
9	0.208	5.790		1.047		3.90E-03	0.502		1.356	0.246		0.114	
10	0.260	5.585	5.467	1.263	1.236	3.76E-03	0.485	0.474	1.308	0.282	0.278	0.134	0.132
11	0.260	5.380		1.216		3.62E-03	0.467		1.260	0.275		0.130	
12	0.260	5.437		1.229		3.66E-03	0.472		1.273	0.277		0.131	

D_o=60mm

Test no.	Velocity	Total mass entrained	Average entrained	Measured entrainment rate	Average entrainment rate	Volume entrained	Recovery channel ratio	Average recovery	Effective recovery ratio	Mass concentration	Average concentration	Volumetric concentration	Average concentration
	m/s	kg	kg	kg/s	kg/s	m^3	-	-	-	kg/l	kg/l	-	-
1	0.104	9.184	8.995	0.831	0.813	6.18E-03	0.797	0.780	1.494	0.205	0.202	0.092	0.091
2	0.104	8.818		0.797		5.94E-03	0.765		1.434	0.199		0.089	
3	0.104	8.983		0.812		6.05E-03	0.779		1.461	0.202		0.091	
4	0.156	6.706	6.568	0.910	0.891	4.52E-03	0.582	0.570	1.091	0.221	0.217	0.100	0.098
5	0.156	6.567		0.891		4.42E-03	0.570		1.068	0.217		0.098	
6	0.156	6.430		0.872		4.33E-03	0.558		1.046	0.214		0.097	
7	0.208	5.656	5.507	1.023	0.996	3.81E-03	0.491	0.478	0.920	0.241	0.237	0.111	0.109
8	0.208	5.526		0.999		3.72E-03	0.479		0.899	0.237		0.109	
9	0.208	5.339		0.966		3.60E-03	0.463		0.868	0.231		0.106	
10	0.260	5.659	5.269	1.279	1.191	3.81E-03	0.491	0.457	0.920	0.285	0.270	0.136	0.127
11	0.260	5.008		1.132		3.37E-03	0.434		0.815	0.261		0.122	
12	0.260	5.139		1.162		3.46E-03	0.446		0.836	0.266		0.125	

MSS:GB16

D_o=30mm

Test no.	Velocity	Total mass entrained	Average entrained	Measured entrainment rate	Average entrainment rate	Volume entrained	Recovery channel ratio	Average recovery	Effective recovery ratio	Mass concentration	Average concentration	Volumetric concentration	Average concentration
	m/s	kg	kg	kg/s	kg/s	m^3	-	-	-	kg/l	kg/l	-	-
1	0.104	2.192	2.899	0.198	0.262	1.48E-03	0.190	0.251	1.426	0.038	0.050	0.015	0.020
2	0.104	4.325		0.391		2.91E-03	0.375		2.814	0.073		0.030	
3	0.104	2.179		0.197		1.47E-03	0.189		1.418	0.038		0.015	
4	0.156	3.341	3.434	0.453	0.466	2.25E-03	0.290	0.298	2.174	0.083	0.085	0.034	0.035
5	0.156	3.701		0.502		2.49E-03	0.321		2.408	0.091		0.038	
6	0.156	3.261		0.442		2.20E-03	0.283		2.122	0.081		0.034	
7	0.208	1.922	2.853	0.348	0.516	1.29E-03	0.167	0.247	1.251	0.065	0.093	0.027	0.039
8	0.208	3.017		0.546		2.03E-03	0.262		1.963	0.098		0.041	
9	0.208	3.620		0.655		2.44E-03	0.314		2.355	0.116		0.049	
10	0.260	2.446	2.312	0.553	0.523	1.65E-03	0.212	0.201	1.591	0.100	0.095	0.042	0.040
11	0.260	2.155		0.487		1.45E-03	0.187		1.402	0.089		0.037	
12	0.260	2.334		0.528		1.57E-03	0.202		1.519	0.095		0.040	

D_o=40mm

Test no.	Velocity	Total mass entrained	Average entrained	Measured entrainment rate	Average entrainment rate	Volume entrained	Recovery channel ratio	Average recovery	Effective recovery ratio	Mass concentration	Average concentration	Volumetric concentration	Average concentration
	m/s	kg	kg	kg/s	kg/s	m^3	-	-	-	kg/l	kg/l	-	-
1	0.104	8.240	8.067	0.745	0.730	5.55E-03	0.715	0.700	3.016	0.130	0.127	0.055	0.054
2	0.104	6.640		0.600		4.47E-03	0.576		2.430	0.107		0.045	
3	0.104	9.320		0.843		6.28E-03	0.809		3.411	0.144		0.062	
4	0.156	6.664	6.659	0.904	0.903	4.49E-03	0.578	0.578	2.439	0.153	0.153	0.066	0.066
5	0.156	6.490		0.880		4.37E-03	0.563		2.375	0.150		0.065	
6	0.156	6.823		0.926		4.59E-03	0.592		2.497	0.156		0.068	
7	0.208	4.535	3.690	0.820	0.667	3.05E-03	0.393	0.320	1.660	0.141	0.117	0.061	0.050
8	0.208	2.560		0.463		1.72E-03	0.222		0.937	0.085		0.035	
9	0.208	3.975		0.719		2.68E-03	0.345		1.455	0.126		0.054	
10	0.260	4.298	3.617	0.972	0.818	2.89E-03	0.373	0.314	1.573	0.163	0.140	0.071	0.060
11	0.260	2.869		0.649		1.93E-03	0.249		1.050	0.115		0.049	
12	0.260	3.684		0.833		2.48E-03	0.320		1.348	0.143		0.062	

D_o=50mm

Test no.	Velocity	Total mass entrained	Average entrained	Measured entrainment rate	Average entrainment rate	Volume entrained	Recovery channel ratio	Average recovery	Effective recovery ratio	Mass concentration	Average concentration	Volumetric concentration	Average concentration
	m/s	kg	kg	kg/s	kg/s	m^3	-	-	-	kg/l	kg/l	-	-
1	0.104	9.601	9.372	0.868	0.848	6.47E-03	0.833	0.813	2.249	0.148	0.145	0.064	0.063
2	0.104	9.386		0.849		6.32E-03	0.814		2.198	0.145		0.063	
3	0.104	9.129		0.826		6.15E-03	0.792		2.138	0.142		0.061	
4	0.156	6.865	6.871	0.931	0.932	4.62E-03	0.596	0.596	1.608	0.157	0.157	0.068	0.068
5	0.156	6.761		0.917		4.55E-03	0.587		1.584	0.155		0.067	
6	0.156	6.986		0.948		4.70E-03	0.606		1.636	0.159		0.069	
7	0.208	5.116	5.470	0.925	0.989	3.45E-03	0.444	0.475	1.198	0.156	0.165	0.068	0.072
8	0.208	5.504		0.996		3.71E-03	0.477		1.289	0.166		0.073	
9	0.208	5.790		1.047		3.90E-03	0.502		1.356	0.173		0.076	
10	0.260	4.802	5.073	1.086	1.147	3.23E-03	0.417	0.440	1.125	0.178	0.187	0.079	0.083
11	0.260	4.981		1.126		3.35E-03	0.432		1.167	0.184		0.081	
12	0.260	5.437		1.229		3.66E-03	0.472		1.273	0.197		0.088	

D_o=60mm

Test no.	Velocity	Total mass entrained	Average entrained	Measured entrainment rate	Average entrainment rate	Volume entrained	Recovery channel ratio	Average recovery	Effective recovery ratio	Mass concentration	Average concentration	Volumetric concentration	Average concentration
	m/s	kg	kg	kg/s	kg/s	m^3	-	-	-	kg/l	kg/l	-	-
1	0.104	9.703	9.451	0.877	0.855	6.53E-03	0.842	0.820	1.578	0.149	0.146	0.065	0.063
2	0.104	9.268		0.838		6.24E-03	0.804		1.508	0.144		0.062	
3	0.104	9.383		0.849		6.32E-03	0.814		1.526	0.145		0.063	
4	0.156	7.194	6.949	0.976	0.943	4.84E-03	0.624	0.603	1.170	0.163	0.159	0.071	0.069
5	0.156	6.811		0.924		4.59E-03	0.591		1.108	0.156		0.068	
6	0.156	6.841		0.928		4.61E-03	0.593		1.113	0.157		0.068	
7	0.208	6.207	5.776	1.123	1.045	4.18E-03	0.538	0.501	1.010	0.183	0.173	0.081	0.076
8	0.208	5.781		1.046		3.89E-03	0.502		0.940	0.173		0.076	
9	0.208	5.339		0.966		3.60E-03	0.463		0.868	0.162		0.071	
10	0.260	5.183	5.187	1.172	1.173	3.49E-03	0.450	0.450	0.843	0.190	0.190	0.084	0.085
11	0.260	5.208		1.177		3.51E-03	0.452		0.847	0.191		0.085	
12	0.260	5.169		1.169		3.48E-03	0.448		0.841	0.189		0.084	

Additional Tests:

Change in bed height: Default parameters @ D_o=60mm

Depth	Velocity	Distance	Total mass entrained	Average entrained	Measured entrainment rate	Average entrainment rate	Channel volume	Volume entrained	Recovery channel ratio	Effective recovery ratio
m	m/s	m	kg	kg	kg/s	kg/s	m^3	m^3	-	-
0.03	0.260	1.150	1.097	1.092	0.248	0.247	7.76E-03	7.39E-04	0.095	0.178
	0.260	1.150	1.091		0.247		7.76E-03	7.35E-04	0.095	0.177
	0.260	1.150	1.088		0.246		7.76E-03	7.33E-04	0.094	0.177
0.04	0.260	1.150	1.371	1.376	0.310	0.311	7.76E-03	9.23E-04	0.119	0.223
	0.260	1.150	1.375		0.311		7.76E-03	9.26E-04	0.119	0.224
	0.260	1.150	1.382		0.312		7.76E-03	9.31E-04	0.120	0.225
0.05	0.260	1.150	1.591	1.587	0.360	0.359	7.76E-03	1.07E-03	0.138	0.259
	0.260	1.150	1.574		0.356		7.76E-03	1.06E-03	0.137	0.256
	0.260	1.150	1.596		0.361		7.76E-03	1.07E-03	0.138	0.260
0.06	0.260	1.150	1.601	1.609	0.362	0.364	7.76E-03	1.08E-03	0.139	0.260
	0.260	1.150	1.605		0.363		7.76E-03	1.08E-03	0.139	0.261
	0.260	1.150	1.621		0.366		7.76E-03	1.09E-03	0.141	0.264
0.07	0.260	1.150	1.608	1.601	0.364	0.362	7.76E-03	1.08E-03	0.139	0.262
	0.260	1.150	1.597		0.361		7.76E-03	1.08E-03	0.139	0.260
	0.260	1.150	1.598		0.361		7.76E-03	1.08E-03	0.139	0.260
0.08	0.260	1.150	1.601	1.614	0.362	0.365	7.76E-03	1.08E-03	0.139	0.260
	0.260	1.150	1.609		0.364		7.76E-03	1.08E-03	0.140	0.262
	0.260	1.150	1.631		0.369		7.76E-03	1.10E-03	0.141	0.265

Multiple Orifice Flow:

MMS: 25mm spacing

Test no.	Velocity	Distance	Total mass entrained	Average Entrained	Measure entrainment rate	Average entrainment rate	Channel volume	Volume entrained	Recovery channel ratio	Effective recovery ratio
	m/s	m	kg	kg	kg/s	kg/s	m^3	m^3	-	-
1	0.104	1.150	2.821	2.885	0.255	0.261	1.55E-02	1.90E-03	0.122	0.220
2	0.104	1.150	2.971		0.269		1.55E-02	2.00E-03	0.129	0.232
3	0.104	1.150	2.864		0.259		1.55E-02	1.93E-03	0.124	0.224
4	0.156	1.150	2.849	2.949	0.386	0.400	1.55E-02	1.92E-03	0.124	0.222
5	0.156	1.150	3.054		0.414		1.55E-02	2.06E-03	0.132	0.238
6	0.156	1.150	2.943		0.399		1.55E-02	1.98E-03	0.128	0.230
7	0.208	1.150	2.729	2.909	0.494	0.526	1.55E-02	1.84E-03	0.118	0.213
8	0.208	1.150	3.010		0.544		1.55E-02	2.03E-03	0.131	0.235
9	0.208	1.150	2.987		0.540		1.55E-02	2.01E-03	0.130	0.233
10	0.260	1.150	2.900	2.969	0.656	0.671	1.55E-02	1.95E-03	0.126	0.226
11	0.260	1.150	3.031		0.685		1.55E-02	2.04E-03	0.131	0.237
12	0.260	1.150	2.977		0.673		1.55E-02	2.00E-03	0.129	0.232

MMS: 50mm spacing

Test no.	Velocity	Distance	Total mass entrained	Average Entrained	Measure entrainment rate	Average entrainment rate	Channel volume	Volume entrained	Recovery channel ratio	Effective recovery ratio
	m/s	m	kg	kg	kg/s	kg/s	m^3	m^3	-	-
1	0.104	1.150	2.839	2.924	0.257	0.264	1.55E-02	1.91E-03	0.123	0.222
2	0.104	1.150	2.991		0.270		1.55E-02	2.01E-03	0.130	0.234
3	0.104	1.150	2.943		0.266		1.55E-02	1.98E-03	0.128	0.230
4	0.156	1.150	2.827	2.951	0.383	0.400	1.55E-02	1.90E-03	0.123	0.221
5	0.156	1.150	3.015		0.409		1.55E-02	2.03E-03	0.131	0.235
6	0.156	1.150	3.012		0.409		1.55E-02	2.03E-03	0.131	0.235
7	0.208	1.150	2.821	2.939	0.510	0.532	1.55E-02	1.90E-03	0.122	0.220
8	0.208	1.150	2.999		0.542		1.55E-02	2.02E-03	0.130	0.234
9	0.208	1.150	2.998		0.542		1.55E-02	2.02E-03	0.130	0.234
10	0.260	1.150	2.821	2.926	0.638	0.661	1.55E-02	1.90E-03	0.122	0.220
11	0.260	1.150	2.909		0.658		1.55E-02	1.96E-03	0.126	0.227
12	0.260	1.150	3.047		0.689		1.55E-02	2.05E-03	0.132	0.238

MSS: 25mm spacing

Test no.	Velocity	Distance	Total mass entrained	Average entrained	Measure entrainment rate	Average entrainment rate	Volume entrained	Recovery channel ratio	Effective recovery ratio	Mass concentration	Average concentration	Volumetric concentration	Average concentration
	m/s	m	kg	kg	kg/s	kg/s	m3	-	-	kg/l	kg/l	-	kg/l
1	0.104	1.150	21.681	21.528	1.961	1.947	1.46E-02	0.940	1.693	0.279	0.277	0.188	0.187
2	0.104	1.150	21.286		1.925		1.43E-02	0.923	1.662	0.274		0.185	
3	0.104	1.150	21.616		1.955		1.46E-02	0.938	1.688	0.278		0.187	
4	0.156	1.150	15.973	15.870	2.167	2.153	1.08E-02	0.693	1.247	0.308	0.306	0.208	0.206
5	0.156	1.150	15.910		2.158		1.07E-02	0.690	1.242	0.307		0.207	
6	0.156	1.150	15.728		2.134		1.06E-02	0.682	1.228	0.304		0.205	
7	0.208	1.150	14.220	14.048	2.572	2.541	9.58E-03	0.617	1.110	0.366	0.362	0.247	0.244
8	0.208	1.150	13.850		2.505		9.33E-03	0.601	1.081	0.357		0.240	
9	0.208	1.150	14.075		2.546		9.48E-03	0.611	1.099	0.362		0.244	
10	0.260	1.150	12.130	12.160	2.742	2.749	8.17E-03	0.526	0.947	0.390	0.391	0.263	0.264
11	0.260	1.150	12.141		2.745		8.18E-03	0.527	0.948	0.391		0.263	
12	0.260	1.150	12.210		2.761		8.22E-03	0.530	0.953	0.393		0.265	

MSS: 50mm spacing

Test no.	Velocity	Distance	Total mass entrained	Average entrained	Measure entrainment rate	Average entrainment rate	Volume entrained	Recovery channel ratio	Effective recovery ratio	Mass concentration	Average concentration	Volumetric concentration	Average concentration
	m/s	m	kg	kg	kg/s	kg/s	m^3	-	-	kg/l	kg/l	-	kg/l
1	0.104	1.150	22.850	22.675	2.066	2.051	1.54E-02	0.991	1.784	0.294	0.292	0.198	0.197
2	0.104	1.150	22.446		2.030		1.51E-02	0.974	1.752	0.289		0.195	
3	0.104	1.150	22.728		2.055		1.53E-02	0.986	1.774	0.293		0.197	
4	0.156	1.150	17.518	17.547	2.376	2.380	1.18E-02	0.760	1.368	0.338	0.339	0.228	0.228
5	0.156	1.150	17.545		2.380		1.18E-02	0.761	1.370	0.339		0.228	
6	0.156	1.150	17.578		2.384		1.18E-02	0.762	1.372	0.339		0.229	
7	0.208	1.150	15.063	15.063	2.724	2.724	1.01E-02	0.653	1.176	0.388	0.388	0.261	0.261
8	0.208	1.150	15.063		2.724		1.01E-02	0.653	1.175	0.388		0.261	
9	0.208	1.150	15.063		2.724		1.01E-02	0.653	1.161	0.388		0.261	
12	0.260	1.150	12.452	12.513	2.815	2.829	8.39E-03	0.540	0.972	0.401	0.403	0.270	0.271
13	0.260	1.150	12.542		2.836		8.45E-03	0.544	0.996	0.404		0.272	
14	0.260	1.150	12.544		2.836		8.45E-03	0.544	0.979	0.404		0.272	

50/50 GB Composition:

MMS

Test no.	Velocity	Distance	Total mass entrained	Average entrained	Measure entrainment rate	Average entrainment rate	Channel volume	Volume entrained	Recovery channel ratio	Effective recovery ratio	Proportionality (kg)	
	m/s	m	kg	kg	kg/s	kg/s	m^3	m^3	-	-	GB6	GB16
1	0.104	1.150	1.191	1.192	0.108	0.108	7.76E-03	8.02E-04	0.103	0.279	0.854	0.337
2	0.104	1.150	1.173		0.106		7.76E-03	7.90E-04	0.102	0.275	0.861	0.312
3	0.104	1.150	1.211		0.110		7.76E-03	8.15E-04	0.105	0.284	0.901	0.31
4	0.156	1.150	1.167	1.191	0.158	0.162	7.76E-03	7.86E-04	0.101	0.273	0.856	0.311
5	0.156	1.150	1.203		0.163		7.76E-03	8.10E-04	0.104	0.282	0.874	0.329
6	0.156	1.150	1.202		0.163		7.76E-03	8.09E-04	0.104	0.282	0.880	0.322
7	0.208	1.150	1.189	1.199	0.215	0.217	7.76E-03	8.01E-04	0.103	0.278	0.857	0.332
8	0.208	1.150	1.203		0.218		7.76E-03	8.10E-04	0.104	0.282	0.876	0.327
9	0.208	1.150	1.206		0.218		7.76E-03	8.12E-04	0.105	0.282	0.885	0.321
10	0.260	1.150	1.176	1.173	0.266	0.265	7.76E-03	7.92E-04	0.102	0.275	0.855	0.321
11	0.260	1.150	1.187		0.268		7.76E-03	7.99E-04	0.103	0.278	0.852	0.335
12	0.260	1.150	1.157		0.262		7.76E-03	7.79E-04	0.100	0.271	0.847	0.31

MSS

Test no.	Velocity	Total mass entrained	Average entrained	Measure entrainment rate	Average entrainment rate	Volume entrained	Recovery channel ratio	Effective recovery ratio	Mass concentration	Average concentration	Volumetric concentration	Average concentration	Proportionality (kg)	
	m/s	kg	kg	kg/s	kg/s	m^3	-	-	kg/l	kg/l	-	-	GB6	GB16
1	0.104	13.028	13.193	1.178	1.193	8.77E-03	1.130	3.052	0.268	0.271	0.126	0.128	8.167	4.861
2	0.104	13.322		1.205		8.97E-03	1.156	3.120	0.273		0.129		8.590	4.732
3	0.104	13.228		1.196		8.91E-03	1.148	3.098	0.271		0.128		8.377	4.851
4	0.156	9.768	9.818	1.325	1.332	6.58E-03	0.847	2.288	0.292	0.293	0.140	0.140	5.426	4.342
5	0.156	9.829		1.333		6.62E-03	0.853	2.302	0.293		0.140		5.508	4.321
6	0.156	9.856		1.337		6.64E-03	0.855	2.309	0.294		0.141		5.555	4.301
7	0.208	8.000	7.778	1.447	1.407	5.39E-03	0.694	1.874	0.310	0.304	0.151	0.147	5.161	2.839
8	0.208	7.606		1.376		5.12E-03	0.660	1.782	0.300		0.144		4.619	2.987
9	0.208	7.728		1.398		5.20E-03	0.670	1.810	0.303		0.146		4.839	2.889
12	0.260	7.508	7.513	1.697	1.699	5.06E-03	0.651	1.759	0.346	0.346	0.172	0.172	4.681	2.827
13	0.260	7.595		1.717		5.11E-03	0.659	1.779	0.348		0.174		4.741	2.854
14	0.260	7.437		1.681		5.01E-03	0.645	1.742	0.344		0.171		4.638	2.799

APPENDIX F

Material Properties and Data Sheets

F 1. Introduction

6mm and 16mm spherical glass beads were selected as the testing material of choice and were certified by Preciosa Ornela (2011). However, it was worth measuring and verifying some of these key parameters, as the numerical simulations were heavily dependent on them. The properties of the Plexiglas used in the physical tests were also given in a certified data sheet by Evonik (2017).

F 2. Laboratory Testing

The specific gravity G_s and bulk density ρ_b were determined according to the British Standards (BS1377-2:1991).

F 2.1. Specific Gravity

The specific gravity was determined using the pyknometer method. The specific gravity was calculated using Equation **Error! Reference source not found.**, in accordance with the testing methods described in BS 1377: Part 2: 1990.

$$G_s = \frac{(\text{Mass 2} - \text{Mass1})}{(\text{Mass4} - \text{Mass1}) - (\text{Mass3} - \text{Mass2})}$$

Where,

Mass 1 = Mass of density bottle in g
Mass 2 = Mass of bottle and dry soil in g
Mass 3 = Mass of bottle, soil and water in g
Mass 4 = Mass of bottle full of water only in g

For the two different particle size, two different sized pyknometers were used (large and small). The measured index properties were detailed

Table H-1: Specific gravity measurements for GB6 and GB16

		Test ID (Pyknometer No.)					
		GB6			**GB16**		
Measurements	**Unit**	1	25	52	A	B	C
Mass of dry soil	g	15.562	15.75	15.736	1004.91	1001.42	963.576
Mass of flask (Mass 1)	g	34.996	35.048	34.362	324.7	450.8	534.7
Mass of flask + dry soil (Mass 2)	g	50.558	50.798	50.098	1329.61	1452.22	1498.28
Mass of flask filled with soil and water (Mass 3)	g	96.863	94.503	93.737	2410.21	2407.48	2382.38
Mass of flask filled with water (Mass 4)	g	87.433	84.884	84.144	1797.6	1797.6	1797.6
Particle density, ρ_s	Mg/m^3	2.538	2.569	2.562	2.562	2.558	2.544
Average particle density, ρ_s or Specific gravity, G_s	Mg/m^3	**2.556**			**2.554**		

F 2.2. Bulk Density

The bulk density was dependent on the packing ratio of the beads. The test consisted of filling up a cylindrical container of known volume and mass with the beads. This was then followed by measuring the mass of the beads within the given volume. The calculations were as follows:

$$\rho_b = \frac{(\text{Mass } 2 - \text{Mass}1)}{V}$$

Where,

Mass 1 = Mass of cylindrical container in kg
Mass 2 = Mass of container with beads in kg
V = Volume of container in m^3

The bulk densities for the different particle sizes were summarised as follows (The 50/50 composition used for comparative purposes):

Table H-1: Bulk density measurements for GB6, GB16 and 50/50

Measurements	**Unit**	**GB6**	**GB16**	**50/50**
Diameter of container	m	0.12	0.12	0.12
Height of container	m	0.5	0.5	0.5
Volume of container (V)	m^3	0.00565	0.00565	0.00565
Mass of container without beads (Mass 1)	kg	0.865	0.865	0.865
Mass with beads (Mass 2)	kg	9.258	9.289	9.523
Dry bulk density	kg/m^3	**1484.20**	**1489.69**	**1531.07**

It was noted that the properties (G_s and ρ_b) for both beads were similar to the verified properties by Preciosa Ornela (2011) in the material data sheet. Therefore, for consistency, the parameters in the sheets were used throughout the study (ρ_b=1485kg/m3 and G_s=2.54).

Source: Preciosa Ornela (2011)

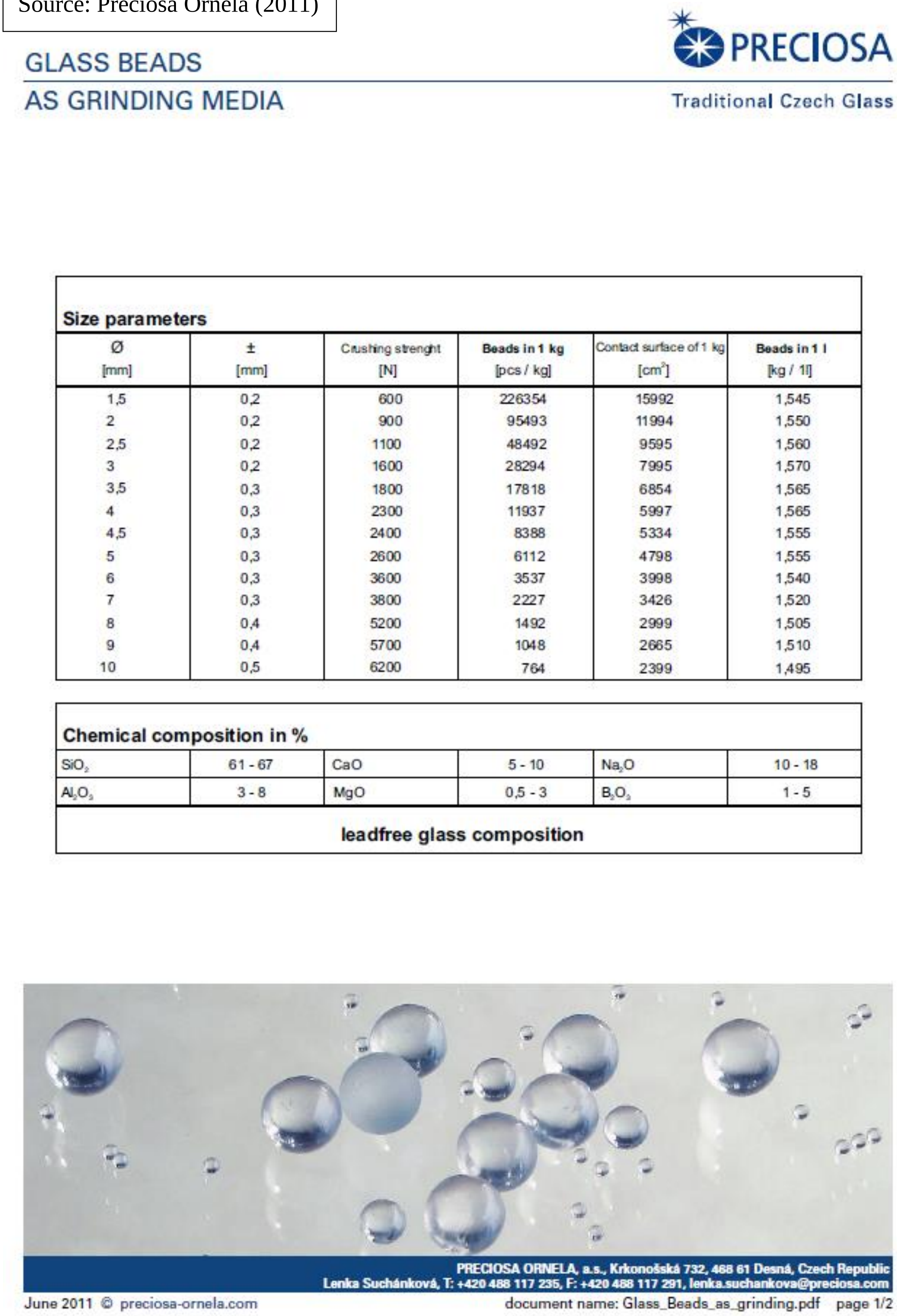

GLASS BEADS
AS GRINDING MEDIA

PRECIOSA
Traditional Czech Glass

Size parameters

Ø [mm]	± [mm]	Crushing strenght [N]	**Beads in 1 kg** [pcs / kg]	Contact surface of 1 kg [cm^2]	**Beads in 1 l** [kg / 1l]
1,5	0,2	600	226354	15992	1,545
2	0,2	900	95493	11994	1,550
2,5	0,2	1100	48492	9595	1,560
3	0,2	1600	28294	7995	1,570
3,5	0,3	1800	17818	6854	1,565
4	0,3	2300	11937	5997	1,565
4,5	0,3	2400	8388	5334	1,555
5	0,3	2600	6112	4798	1,555
6	0,3	3600	3537	3998	1,540
7	0,3	3800	2227	3426	1,520
8	0,4	5200	1492	2999	1,505
9	0,4	5700	1048	2665	1,510
10	0,5	6200	764	2399	1,495

Chemical composition in %

SiO_2	61 - 67	CaO	5 - 10	Na_2O	10 - 18
Al_2O_3	3 - 8	MgO	0,5 - 3	B_2O_3	1 - 5

leadfree glass composition

PRECIOSA ORNELA, a.s., Krkonošská 732, 468 61 Desná, Czech Republic
Lenka Suchánková, T: +420 488 117 235, F: +420 488 117 291, lenka.suchankova@preciosa.com

June 2011 © preciosa-ornela.com

document name: Glass_Beads_as_grinding.pdf page 1/2

Source: Preciosa Ornela (2011)

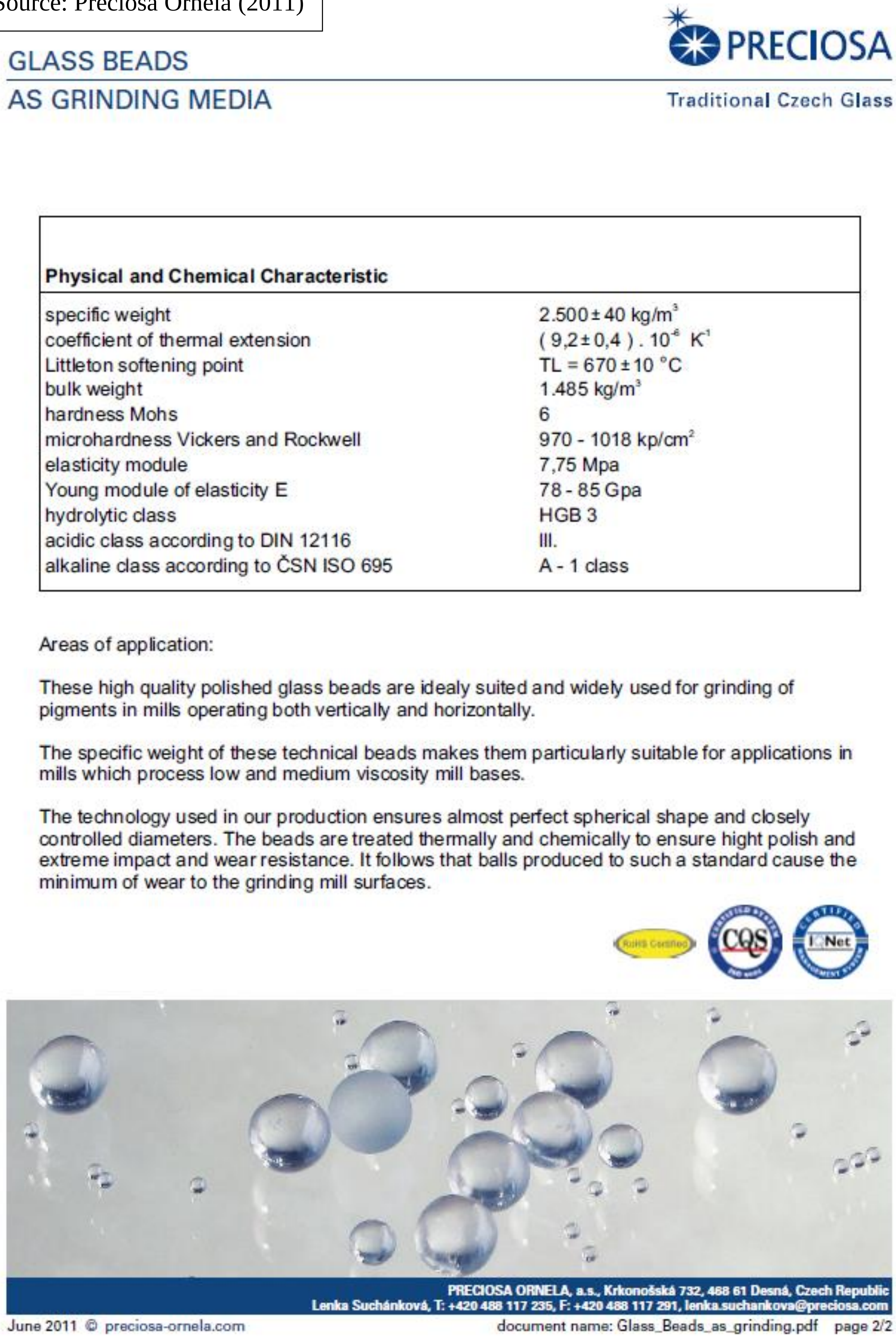

PRECIOSA

Traditional Czech Glass

GLASS BEADS AS GRINDING MEDIA

Physical and Chemical Characteristic	
specific weight	2.500 ± 40 kg/m^3
coefficient of thermal extension	(9,2 ± 0,4) . 10^{-6} K^{-1}
Littleton softening point	TL = 670 ± 10 °C
bulk weight	1.485 kg/m^3
hardness Mohs	6
microhardness Vickers and Rockwell	970 - 1018 kp/cm^2
elasticity module	7,75 Mpa
Young module of elasticity E	78 - 85 Gpa
hydrolytic class	HGB 3
acidic class according to DIN 12116	III.
alkaline class according to ČSN ISO 695	A - 1 class

Areas of application:

These high quality polished glass beads are idealy suited and widely used for grinding of pigments in mills operating both vertically and horizontally.

The specific weight of these technical beads makes them particularly suitable for applications in mills which process low and medium viscosity mill bases.

The technology used in our production ensures almost perfect spherical shape and closely controlled diameters. The beads are treated thermally and chemically to ensure hight polish and extreme impact and wear resistance. It follows that balls produced to such a standard cause the minimum of wear to the grinding mill surfaces.

PRECIOSA ORNELA, a.s., Krkonošská 732, 468 61 Desná, Czech Republic
Lenka Suchánková, T: +420 488 117 235, F: +420 488 117 291, lenka.suchankova@preciosa.com

June 2011 © preciosa-ornela.com document name: Glass_Beads_as_grinding.pdf page 2/2

Source: Evonik (2017)

EVONIK
INDUSTRIES

PLEXIGLAS® GS/PLEXIGLAS® XT

Product Description

PLEXIGLAS®
the original from Röhm

Evonik. Power to create.

Source: Evonik (2017)

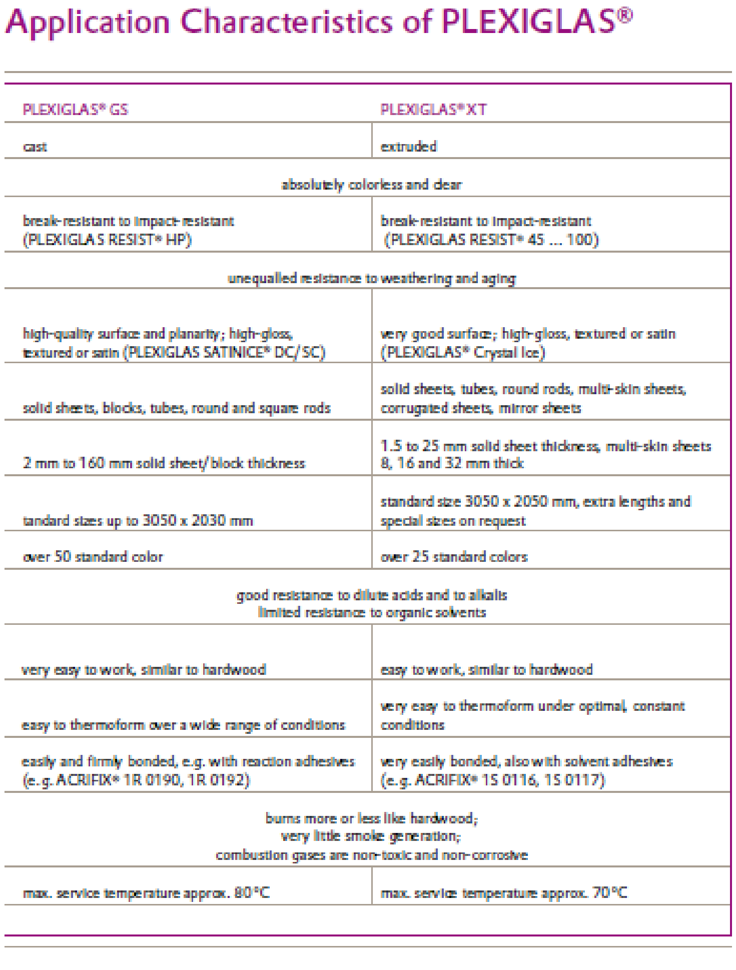

Application Characteristics of PLEXIGLAS®

PLEXIGLAS® GS	PLEXIGLAS® XT
cast	extruded
absolutely colorless and clear	
break-resistant to impact-resistant (PLEXIGLAS RESIST® HP)	break-resistant to impact-resistant (PLEXIGLAS RESIST® 45 ... 100)
unequalled resistance to weathering and aging	
high-quality surface and planarity; high-gloss, textured or satin (PLEXIGLAS SATINICE® DC/SC)	very good surface; high-gloss, textured or satin (PLEXIGLAS® Crystal Ice)
solid sheets, blocks, tubes, round and square rods	solid sheets, tubes, round rods, multi-skin sheets, corrugated sheets, mirror sheets
2 mm to 160 mm solid sheet/block thickness	1.5 to 25 mm solid sheet thickness, multi-skin sheets 8, 16 and 32 mm thick
tandard sizes up to 3050 x 2030 mm	standard size 3050 x 2050 mm, extra lengths and special sizes on request
over 50 standard color	over 25 standard colors
good resistance to dilute acids and to alkalis limited resistance to organic solvents	
very easy to work, similar to hardwood	easy to work, similar to hardwood
easy to thermoform over a wide range of conditions	very easy to thermoform under optimal, constant conditions
easily and firmly bonded, e.g. with reaction adhesives (e.g. ACRIFIX® 1R 0190, 1R 0192)	very easily bonded, also with solvent adhesives (e.g. ACRIFIX® 1S 0116, 1S 0117)
burns more or less like hardwood; very little smoke generation; combustion gases are non-toxic and non-corrosive	
max. service temperature approx. 80 °C	max. service temperature approx. 70 °C

4

Source: Evonik (2017)

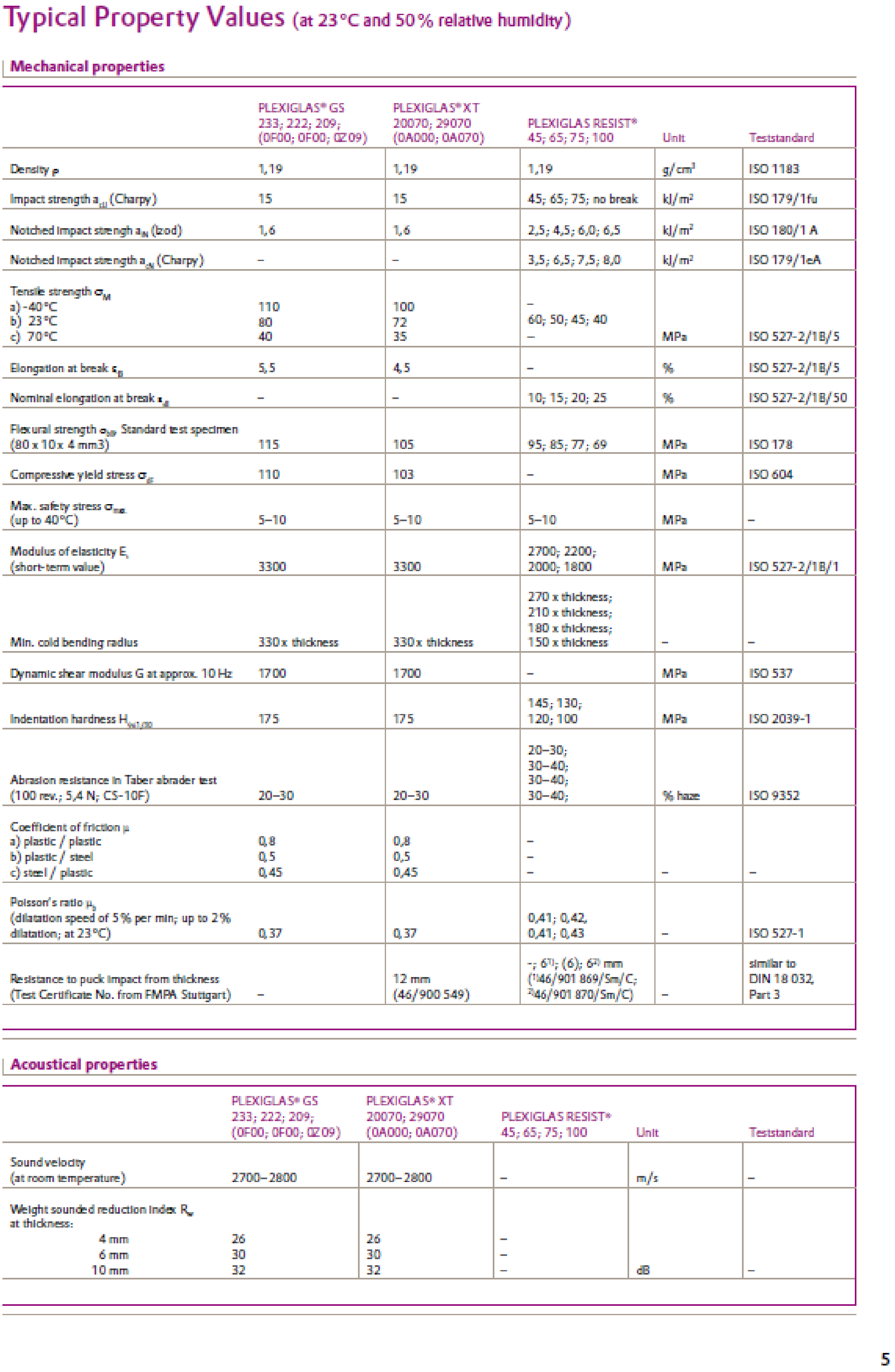

Typical Property Values (at 23 °C and 50 % relative humidity)

Mechanical properties

	PLEXIGLAS® GS 233; 222; 209; (0F00; 0F00; 0Z09)	PLEXIGLAS® XT 20070; 29070 (0A000; 0A070)	PLEXIGLAS RESIST® 45; 65; 75; 100	Unit	Teststandard
Density ρ	1,19	1,19	1,19	g/cm³	ISO 1183
Impact strength a_{cU} (Charpy)	15	15	45; 65; 75; no break	kJ/m²	ISO 179/1fu
Notched impact strengh a_{iN} (Izod)	1,6	1,6	2,5; 4,5; 6,0; 6,5	kJ/m²	ISO 180/1 A
Notched impact strength a_{cN} (Charpy)	–	–	3,5; 6,5; 7,5; 8,0	kJ/m²	ISO 179/1eA
Tensile strength σ_M a) -40 °C b) 23 °C c) 70 °C	 110 80 40	 100 72 35	 – 60; 50; 45; 40 –	MPa	ISO 527-2/1B/5
Elongation at break ε_B	5,5	4,5	–	%	ISO 527-2/1B/5
Nominal elongation at break ε_{tB}	–	–	10; 15; 20; 25	%	ISO 527-2/1B/50
Flexural strength σ_{bB}, Standard test specimen (80 x 10 x 4 mm3)	115	105	95; 85; 77; 69	MPa	ISO 178
Compressive yield stress σ_{dF}	110	103	–	MPa	ISO 604
Max. safety stress σ_{max} (up to 40 °C)	5–10	5–10	5–10	MPa	–
Modulus of elasticity E_t (short-term value)	3300	3300	2700; 2200; 2000; 1800	MPa	ISO 527-2/1B/1
Min. cold bending radius	330 x thickness	330 x thickness	270 x thickness; 210 x thickness; 180 x thickness; 150 x thickness	–	–
Dynamic shear modulus G at approx. 10 Hz	1700	1700	–	MPa	ISO 537
Indentation hardness $H_{961/30}$	175	175	145; 130; 120; 100	MPa	ISO 2039-1
Abrasion resistance in Taber abrader test (100 rev.; 5,4 N; CS-10F)	20–30	20–30	20–30; 30–40; 30–40; 30–40;	% haze	ISO 9352
Coefficient of friction μ a) plastic / plastic b) plastic / steel c) steel / plastic	 0,8 0,5 0,45	 0,8 0,5 0,45	 – – –	–	–
Poisson's ratio μ_b (dilatation speed of 5 % per min; up to 2 % dilatation; at 23 °C)	0,37	0,37	0,41; 0,42, 0,41; 0,43	–	ISO 527-1
Resistance to puck impact from thickness (Test Certificate No. from FMPA Stuttgart)	–	12 mm (46/900 549)	-; 6[1]; (6); 6[2] mm ([1]46/901 869/Sm/C; [2]46/901 870/Sm/C)	–	similar to DIN 18 032, Part 3

Acoustical properties

	PLEXIGLAS® GS 233; 222; 209; (0F00; 0F00; 0Z09)	PLEXIGLAS® XT 20070; 29070 (0A000; 0A070)	PLEXIGLAS RESIST® 45; 65; 75; 100	Unit	Teststandard
Sound velocity (at room temperature)	2700–2800	2700–2800	–	m/s	–
Weight sounded reduction index R_w at thickness: 4 mm 6 mm 10 mm	 26 30 32	 26 30 32	 – – –	dB	–

Source: Evonik (2017)

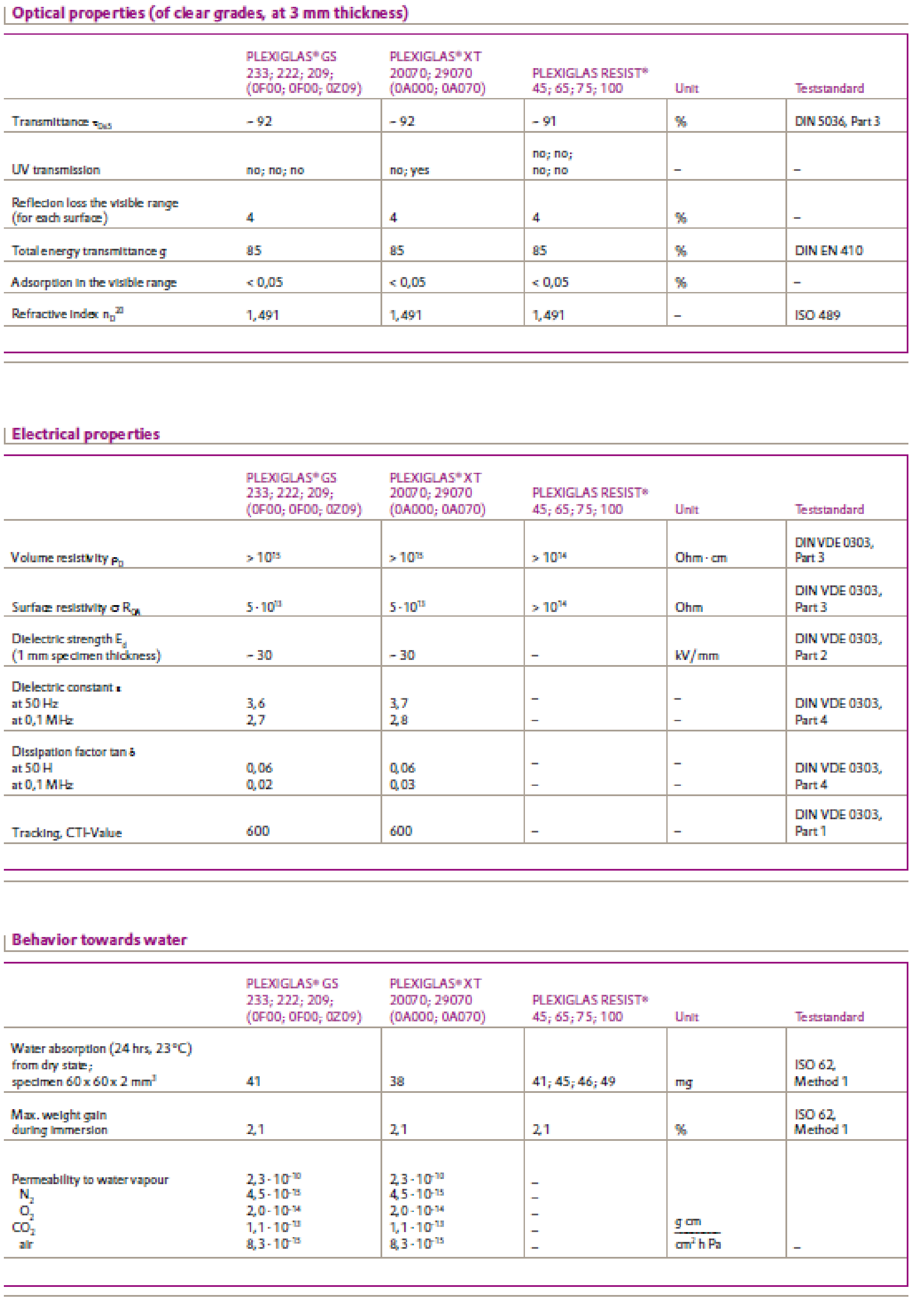

Optical properties (of clear grades, at 3 mm thickness)

	PLEXIGLAS® GS 233; 222; 209; (0F00; 0F00; 0Z09)	PLEXIGLAS® XT 20070; 29070 (0A000; 0A070)	PLEXIGLAS RESIST® 45; 65; 75; 100	Unit	Teststandard
Transmittance τ_{D65}	– 92	– 92	– 91	%	DIN 5036, Part 3
UV transmission	no; no; no	no; yes	no; no; no; no	–	–
Reflecion loss the visible range (for each surface)	4	4	4	%	–
Total energy transmittance g	85	85	85	%	DIN EN 410
Adsorption in the visible range	< 0,05	< 0,05	< 0,05	%	–
Refractive index n_D^{20}	1,491	1,491	1,491	–	ISO 489

Electrical properties

	PLEXIGLAS® GS 233; 222; 209; (0F00; 0F00; 0Z09)	PLEXIGLAS® XT 20070; 29070 (0A000; 0A070)	PLEXIGLAS RESIST® 45; 65; 75; 100	Unit	Teststandard
Volume resistivity ρ_D	$> 10^{15}$	$> 10^{15}$	$> 10^{14}$	Ohm · cm	DIN VDE 0303, Part 3
Surface resistivity σ R_{OA}	$5 \cdot 10^{13}$	$5 \cdot 10^{13}$	$> 10^{14}$	Ohm	DIN VDE 0303, Part 3
Dielectric strength E_d (1 mm specimen thickness)	– 30	– 30	–	kV/mm	DIN VDE 0303, Part 2
Dielectric constant ε					
at 50 Hz	3,6	3,7	–	–	DIN VDE 0303, Part 4
at 0,1 MHz	2,7	2,8	–	–	
Dissipation factor tan δ					
at 50 H	0,06	0,06	–	–	DIN VDE 0303, Part 4
at 0,1 MHz	0,02	0,03	–	–	
Tracking, CTI-Value	600	600	–	–	DIN VDE 0303, Part 1

Behavior towards water

	PLEXIGLAS® GS 233; 222; 209; (0F00; 0F00; 0Z09)	PLEXIGLAS® XT 20070; 29070 (0A000; 0A070)	PLEXIGLAS RESIST® 45; 65; 75; 100	Unit	Teststandard
Water absorption (24 hrs, 23 °C) from dry state; specimen 60 x 60 x 2 mm³	41	38	41; 45; 46; 49	mg	ISO 62, Method 1
Max. weight gain during immersion	2,1	2,1	2,1	%	ISO 62, Method 1
Permeability to water vapour	$2{,}3 \cdot 10^{-10}$	$2{,}3 \cdot 10^{-10}$	–		
N_2	$4{,}5 \cdot 10^{-15}$	$4{,}5 \cdot 10^{-15}$	–		
O_2	$2{,}0 \cdot 10^{-14}$	$2{,}0 \cdot 10^{-14}$	–		
CO_2	$1{,}1 \cdot 10^{-13}$	$1{,}1 \cdot 10^{-13}$	–	$\frac{g\ cm}{cm^2\ h\ Pa}$	
air	$8{,}3 \cdot 10^{-15}$	$8{,}3 \cdot 10^{-15}$	–		–

6

Source: Evonik (2017)

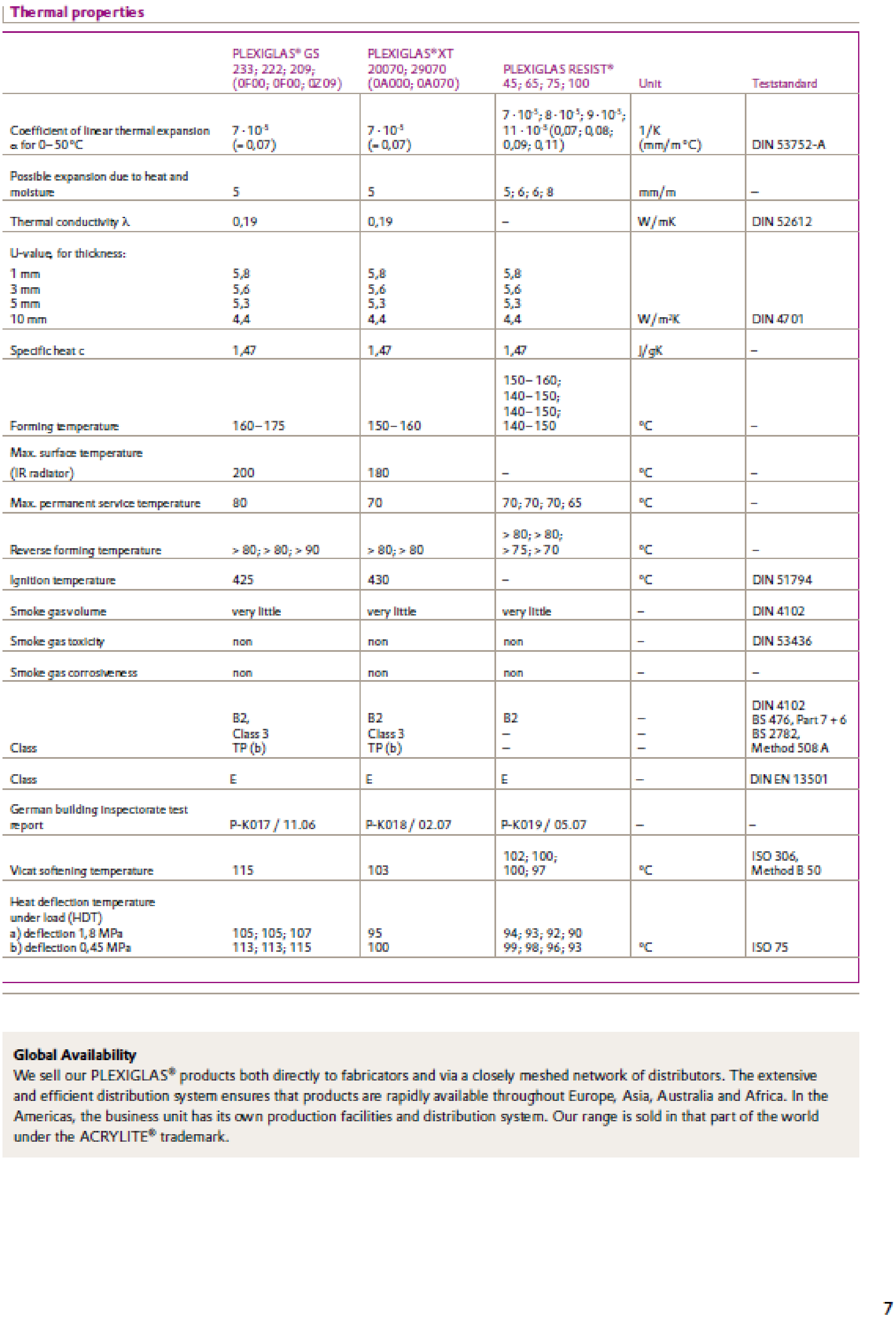

Thermal properties

	PLEXIGLAS® GS 233; 222; 209; (0F00; 0F00; 0Z09)	PLEXIGLAS® XT 20070; 29070 (0A000; 0A070)	PLEXIGLAS RESIST® 45; 65; 75; 100	Unit	Teststandard
Coefficient of linear thermal expansion α for 0–50 °C	$7 \cdot 10^{-5}$ (≈ 0,07)	$7 \cdot 10^{-5}$ (≈ 0,07)	$7 \cdot 10^{-5}$; $8 \cdot 10^{-5}$; $9 \cdot 10^{-5}$; $11 \cdot 10^{-5}$ (0,07; 0,08; 0,09; 0,11)	1/K (mm/m °C)	DIN 53752-A
Possible expansion due to heat and moisture	5	5	5; 6; 6; 8	mm/m	–
Thermal conductivity λ	0,19	0,19	–	W/mK	DIN 52612
U-value, for thickness:					
1 mm	5,8	5,8	5,8		
3 mm	5,6	5,6	5,6		
5 mm	5,3	5,3	5,3		
10 mm	4,4	4,4	4,4	W/m²K	DIN 4701
Specific heat c	1,47	1,47	1,47	J/gK	–
Forming temperature	160–175	150–160	150–160; 140–150; 140–150; 140–150	°C	–
Max. surface temperature (IR radiator)	200	180	–	°C	–
Max. permanent service temperature	80	70	70; 70; 70; 65	°C	–
Reverse forming temperature	> 80; > 80; > 90	> 80; > 80	> 80; > 80; > 75; > 70	°C	–
Ignition temperature	425	430	–	°C	DIN 51794
Smoke gas volume	very little	very little	very little	–	DIN 4102
Smoke gas toxicity	non	non	non	–	DIN 53436
Smoke gas corrosiveness	non	non	non	–	–
Class	B2, Class 3 TP (b)	B2 Class 3 TP (b)	B2 – –	– – –	DIN 4102 BS 476, Part 7 + 6 BS 2782, Method 508 A
Class	E	E	E	–	DIN EN 13501
German building inspectorate test report	P-K017 / 11.06	P-K018 / 02.07	P-K019 / 05.07	–	–
Vicat softening temperature	115	103	102; 100; 100; 97	°C	ISO 306, Method B 50
Heat deflection temperature under load (HDT) a) deflection 1,8 MPa b) deflection 0,45 MPa	 105; 105; 107 113; 113; 115	 95 100	 94; 93; 92; 90 99; 98; 96; 93	°C	ISO 75

Global Availability
We sell our PLEXIGLAS® products both directly to fabricators and via a closely meshed network of distributors. The extensive and efficient distribution system ensures that products are rapidly available throughout Europe, Asia, Australia and Africa. In the Americas, the business unit has its own production facilities and distribution system. Our range is sold in that part of the world under the ACRYLITE® trademark.

APPENDIX G

Scaling Laws

G 1. Introduction

The scaling of physical entities is a fundamental feature in research and design. It is common practice to investigate large scale phenomena, such as granular systems, as scaled down laboratory experiments or numerical models (Pöschel, Salueña & Schwager, 2001). Reason being that full scale models experience a limitation through the capacities of testing facilities and, moreover, scaled down models are less expensive (Ramu, Prabhu Raja & Thyla, 2013). The scaling laws applied in this study were used to provide a setting in which the outputs achieved were relevant to real-life applications, such as mining, dredging and food industries. The laws focused on the modelling of granular materials both numerically and physically, and the scaling of the physical structures to be used in the laboratory experiments. The two approaches were the main areas of interest because of rapid developments in advanced computing and testing facilities. Furthermore, similitude theories were introduced and analysed, highlighting the different forms of similarities.

G 2. Principles of Model Scaling

Model scaling revolves around the principle of maintaining homologous behaviour between the original and scaled system. Common scaling laws dictate that the behaviour between the two systems can be maintained by multiplying the parameters of the original system by a constant scale factor. For instance, considering velocities of different elements on the original system, v_1, v_2, $v_3 \ldots v_n$; and corresponding velocities of the model, v_1', v_2', $v_3' \ldots v_n'$, it follows that the homologous behaviour with respect to velocity to be:

$$\frac{v_1}{v_1'} = \frac{v_2}{v_2'} = \frac{v_3}{v_3'} = \cdots = \frac{v_n}{v_n'} = v^* \tag{0-1}$$

Where,

v^* = Velocity scale factor

In general, the rule applies to five primary quantifiable parameters as suggested by Emori & Schuring (1977), where Equation (0-1) can be modified to suit the interested parameter. There are a number of different approaches to model scaling with Equation (0-1) being the most common. Similitude theories are the basis of scaling laws and become more complex with added governing laws. In the case scale factors of primary quantities are not specified, a constant scale factor, λ, is introduced.

G 2.1 Primary and Secondary Scale Factors

The primary factors are those of length, time, mass, temperature and electric current denoted as l, t, m, θ and i respectively. All other parameters are considered secondary quantities as they can be easily derived from them. Most secondary quantities can be derived from l, t and m. The velocity vector, a secondary parameter, can be expressed as the first derivative of length with respect to time, such that (Emori et al., 1977):

$$\mathrm{v}^* = \frac{\frac{\mathrm{d}l_1}{\mathrm{d}t_1}}{\frac{\mathrm{d}l_1'}{\mathrm{d}t_1'}} = \frac{\frac{\mathrm{d}l_2}{\mathrm{d}t_2}}{\frac{\mathrm{d}l_2'}{\mathrm{d}t_2'}} = \cdots = \frac{\frac{\mathrm{d}l_n}{\mathrm{d}t_n}}{\frac{\mathrm{d}l_n'}{\mathrm{d}t_n'}} \tag{0-2}$$

However, to maintain a homologous behaviour of the original and scaled system, it requires the modification of Equation (0-1) for primary factors such that:

$$l^* = \frac{l_1}{l_1'} = \frac{l_2}{l_2'} = \cdots \mathrm{etc} \quad \mathrm{and}\ t^* = \frac{t_1}{t_1'} = \frac{t_2}{t_2'} = \cdots \mathrm{etc} \tag{0-3}$$

Therefore, by substituting Equation (0-3) into Equation (0-2), the following ratio is determined:

$$\mathrm{v}^* = \frac{l^*}{t^*}\frac{\frac{\mathrm{d}l_1'}{\mathrm{d}t_1'}}{\frac{\mathrm{d}l_1'}{\mathrm{d}t_1'}} = \frac{l^*}{t^*}\frac{\frac{\mathrm{d}l_2'}{\mathrm{d}t_2'}}{\frac{\mathrm{d}l_2'}{\mathrm{d}t_2'}} = \cdots = \frac{l^*}{t^*} \tag{0-4}$$

In the same way, any secondary quantity can be derived from two or more primary ones. Examples of secondary quantities are shown and explained if further detail in Chapter 0.

G 2.2 Representative Quantities and Pi-Numbers

It was earlier discussed that the primary and secondary parameters of a system can be scaled to a model using constant scale factors as evident from Equation (0-1). For instance, it was earlier determined that:

$$\mathrm{v}^* = \frac{l^*}{t^*}$$

The expression can be reformulated as follows:

$$\frac{\mathrm{v}_n}{\mathrm{v}_n'} = \frac{l_n}{l_n'}\frac{t_n'}{t_n} \tag{0-5}$$

Whereby the relation can be further converted into the statement of:

$$\frac{v_n t_n}{l_n} = \frac{v_n' t_n'}{l_n'} \tag{0-6}$$

Noting that the scaled properties of the model are on one side and the original properties on the other, it can be said that the system is in equilibrium under certain conditions. In scale modelling, dimensionless products of this kind, are required to be equal for both scaled model and original, hence the introduction of Pi-numbers (Emori et al., 1977). The use of Pi-numbers is based on the π-theorem derived from Buckingham in 1914 where it utilises the π symbol to represent dimensionless products (Hughes, 1993). The Pi-number, π, indicates the relation described in Equation (0-6) above, where:

$$\pi = \frac{v_n t_n}{l_n} \tag{0-7}$$

Furthermore, the parameters in a pi-number can be substituted by any similar quantity of the application to be modelled. Therefore, the numerical value of the pi-number is dependent on the value of the substituted quantity, if the specific value is maintained for both the scaled model and original system. Through different approaches in conjunction with the pi-number theorem, one is able to identify suitable primary factors to maintain the homologous behaviour between the model and prototype. (Emori et al., 1977)

All relations among primary and secondary factors can be expressed as pi-numbers and are often referred to as common pi-numbers when not associated with any physical laws. Although, pi-numbers derived from governing physical laws are called principal pi-numbers. (Garcimartín et al., 2009)

G 2.3. The Law Approach

The law approach is the method of determining principal pi-numbers derived directly from the governing laws, where the laws governing the original system must prevail in the model (Emori et al., 1977; Hutter & Wang, 2016). Additionally, all model quantities must be scaled in accordance with the primary scale factors. The selection of the correct primary scale factors is best described by the example of a vibrating beam. A vibrating beam is governed by three physicals laws that involves elasticity, inertia and internal friction.

a) Elasticity: Hookes Law

Assuming that Poisson's ratio had negligible influence, the stress and strains were related as follows:

$$\sigma = E\varepsilon \tag{0-8}$$

Where,

σ = Stress in MPa
E = Modulus of elasticity
ε = Strain in mm

b) Force: Newton's Law

The inertial force of any element is government by Newton's law:

$$F = ma \tag{0-9}$$

Where,

F = Force in kN
m = mass in kg
a = Acceleration in m/s^2

c) Internal Friction: Empirical Law

The internal friction is stated to be proportional to the third power of the maximum stress, regardless of the frequency and is expressed as the energy loss per unit volume and per cycle:

$$U = Vc\sigma_m^3 \tag{0-10}$$

Where,

U = Energy dissipation per cycle volume
V = Volume in m^3
c = Material constant
σ_m = Maximum stress in MPa

The pi-numbers are then formed from the three laws mentioned above and are expressed in the following manner:

$$\pi_I = \frac{\sigma}{E\varepsilon} \tag{0-11}$$

$$\pi_{II} = \frac{F}{ma} \tag{0-12}$$

$$\pi_{III} = \frac{U}{Vc\sigma^3} \tag{0-13}$$

The three different pi-numbers are then expressed in terms of primary quantities for ease of application in the model design. The modifications are performed with the assistance of the representative relations between primary and secondary parameters as indicated in the flow diagram.

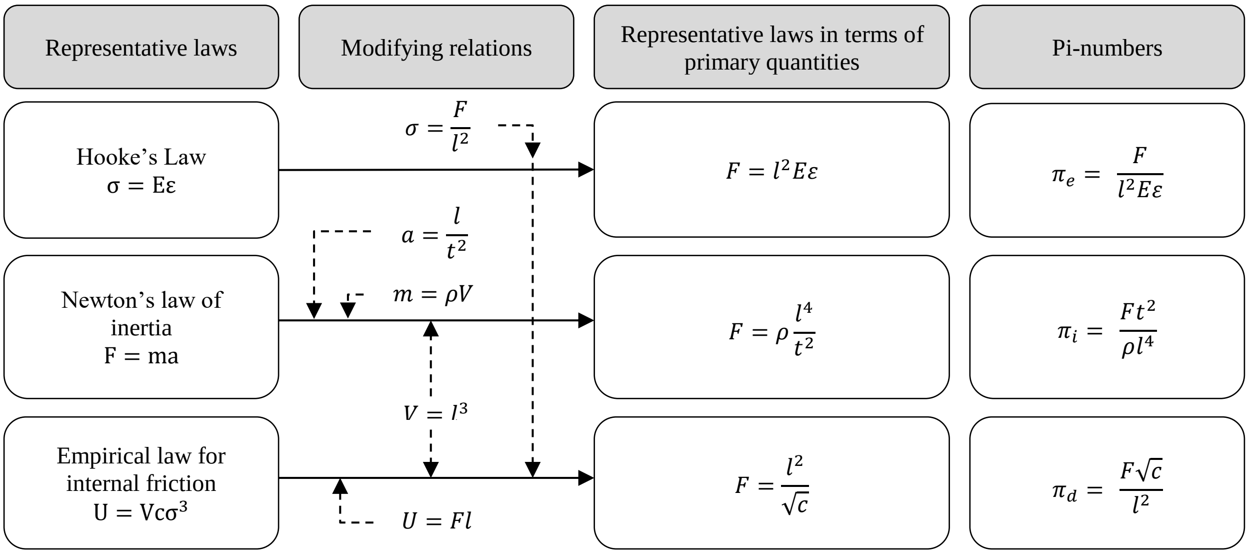

Figure G-1: Derivation of Pi-numbers from Representative Laws
(Adapted from Emori et al., 1977)

Implementation of the three-independent principal pi-numbers will ensure similarity in all modelled quantities of elasticity, inertia and internal friction. In general scaling practice, the principal pi-numbers are modified through the elimination of representative quantities common to all pi-numbers (Emori et al., 1977). A common approach is to select identical materials for both prototype and model, where E=E', c=c' and ρ= ρ'. Thus reducing the first pi-number, π_e, to $F=l^2\varepsilon$ and since geometrical similarity requires equal strains for both model and prototype, the pi-number is further reduced to $F=l^2$. By eliminating the representative force, as indicated in Figure H-1, two pi-numbers can be derived from the three governing laws, as illustrated in the flow diagram below.

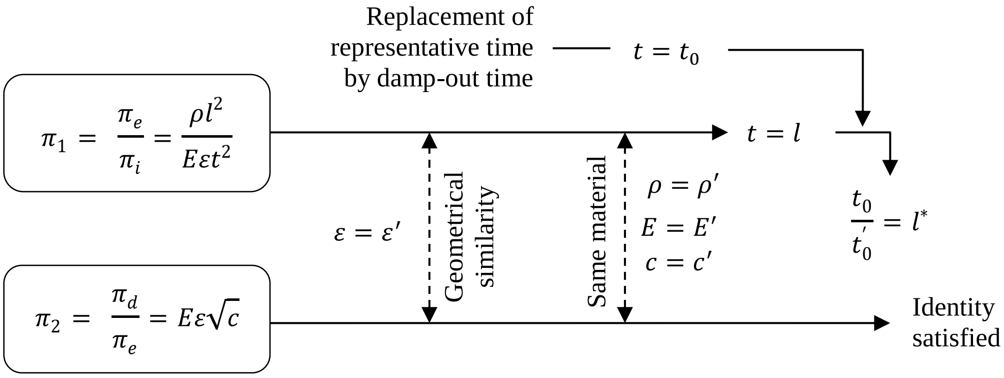

Figure G-2: Modification of Pi-numbers
(Adapted from Emori et al., 1977)

The example is based on the analysis of a vibrating beam, therefore the representative time is replaced by a damp-out time. It can be seen that the original system's damp-out time can be predicted by multiplying the model's measured damp-out time by the length scale factor, $t_o=t_o' l^*$.

The first step is to identify the basic mechanism to be modelled and the governing laws associated with it. The laws must be clearly identified to design the model, however, if the laws are not evident, intuition will play a role in hypothesising the governing laws. Whether or not the hypothesis is correct, the results of the scaled model will be validated by the original system through a numerical analysis.

The governing laws are then expressed as representative quantities given by the five primary factors earlier discussed in Chapter 0. For each of the governing laws, principal pi-numbers can be deduced. These pi-numbers are then combined with other pi-numbers through multiplication and division to obtain more simplified pi-numbers as evident in the previous example. Once obtained, the principal pi-numbers are applied to the original system in order to obtain a scaled model that will provide a relatively accurate indication of the performance of the prototype.

G 2.4. Dimensional Analysis

Dimensional analysis is a useful tool based on the Buckingham π-theorem used to obtain principal pi-numbers. Hughes (1993) explains the tool as a rational method of converting physical variables into dimensionless products. The conversion assists in reducing the number of variables which is particularly useful in determining the number of variables to be considered and the amount encountered during experiments (Hutter & Rajagopal, 1994). Briefly put, dimensional analysis involves these steps:

1. Identify the main independent variables involved in the process;
2. Determine which variable should be the dependent variable;
3. Determine how many independent dimensionless products can be formed from the variables, like the Law Approach detailed in Chapter 0;
4. Reduce the number of system variables equal to that of independent dimensionless products.

With reference to the Buckingham π-theorem and representative quantities, a number of dimensionless products can be formed in relation to the context of the project. The physics behind the majority of hydrodynamic problems can be described by velocity (v), length (l), mass density (ρ), dynamic viscosity (μ), and gravity (g) variables (Yalin, 1971; Hughes, 1993; Heller, 2011). Arranging the five variables into a matrix of primary quantities yields:

	v	l	ρ	μ	g
l	1	1	-3	-1	1
t	-1	0	0	-1	-2
m	0	0	1	1	0

The numerical inputs in the matrix represent the exponents of the primary quantities used to formulate the secondary parameters. From the matrix, it is evident that the number of dimensionless products in the complete set is equal to 5-3=2 since there are five variables and only three basic dimensions. Each of the products in the matrix is described by the expression,

$$\pi = v^{k_1} l^{k_2} \rho^{k_3} \mu^{k_4} g^{k_5} \qquad (0\text{-}14)$$

Where,

π = Notation for a dimensionless product as described in Chapter 0
k_n = Exponents to be determined

The primary quantities for each of the secondary parameters are substituted into Equation (0-14) to yield relationships between dimensions given by:

$$\pi = [lt^{-1}]^{k_1}[l]^{k_2}[ml^{-3}]^{k_3}[ml^{-1}t^{-1}]^{k_4}[lt^{-2}]^{k_5} \qquad (0\text{-}15)$$

Which can be rearranged to give:

$$\pi = [l]^{(k_1+k_2-3k_3-k_4+k_5)}[t]^{(-k_1-k_4-2k_5)}[m]^{(k_3+k_4)} \qquad (0\text{-}16)$$

For Equation (0-3) to become dimensionless, it is necessary for the exponents of respective primary quantities to equal to zero. This produces a set of three independent equations as shown:

$$\begin{aligned} (k_1 + k_2 - 3k_3 - k_4 + k_5) &= 0 \\ (-k_1 - k_4 - 2k_5) &= 0 \\ (k_3 + k_4) &= 0 \end{aligned}$$

Note that the coefficients of the k-values correspond with the inputs in the dimensional matrix above. Therefore the set of equations could have been directly derived from the matrix without any intermediate steps. Any solution that satisfies the equations will provide values for the exponents that can be substituted back into Equation (0-16) to produce a viable dimensionless product. However, since there are three equations with five unknowns; the set is indeterminate, indicating that an infinite number of solutions exist. Hence in this specific case, two of the exponents should be specified, while solving the other three simultaneously.

For example, by selecting $k_1 = 1$ and $k_2 = 1$ the set of equations produces $k_3 = 1$, $k_4 = -1$ and $k_5 = 0$. By substituting the values into Equation (0-3), it results in the dimensionless product:

$$\pi_1 = v^1 l^1 \rho^1 \mu^{-1} g^0 = \frac{\rho v l}{\mu} = \text{Re (Reynolds number)} \tag{0-17}$$

The second dimensionless product is formed by setting $k_1 = 1$ and $k_2 = -1/2$, therefore giving $k_3 = 0$, $k_4 = 0$ and $k_5 = -1/2$. Using these values, it yields:

$$\pi_2 = v^1 l^{-1/2} \rho^0 \mu^0 g^{-1/2} = \frac{v}{\sqrt{gl}} = \text{Fr (Froude number)} \tag{0-18}$$

Thus, it is evident that Reynolds number and Froude number constitute a complete set of dimensionless products which describes the flow scenario where the aforementioned variables were considered significant.(Hughes, 1993)

G 3. Similitude Theories

Similitude is defined as the known relationship between two entities (Dey, 2014). In the context of this research project, the word similitude refers to the relationship between the full scale physical system and a small scale model. In contrast with the basic principles introduced in Chapter 0, similitude theories are used to ensure that physically scaled down models are completely similar to their real world systems without the use of scale effects (Dey, 2014; Hutter et al., 2016). The research project is based on fluvial hydrodynamics which details the complex mechanics of fluid-particle interactions. Therefore a number of relevant aspects must be addressed such as mechanical similarity, scale effects and typical forces and ratios in fluid dynamics. It should be noted that achieving complete similitude between model and prototype where all the force ratios are equal and constant is rarely possible (Emori et al., 1977).

G 3.1. Mechanical Similarity

In order for a physical scaled down model to be completely similar to it real life system, without the use of scale effects, several similarities need to be ensured, namely: (Yalin, 1971; Hughes, 1993; Heller, 2011):

a) Geometric similarity;
b) Kinematic similarity;
c) Dynamic similarity.

a) Geometric Similarity

A number of examples exist where the geometries of a small scaled model are geometrically scaled reproductions of larger items. Such a phenomena indicates that the original item's dimensions were scaled down by a common length factor, λ_l, such that:

$$\lambda_{\mathrm{l}} = \frac{\mathrm{l_p}}{\mathrm{l_m}} = \frac{\mathrm{l}}{\mathrm{l'}} = \mathrm{l}^* \tag{0-1}$$

Where,

l_p = Length of prototype
l_m= Length of model

Therefore the model's lengths, areas and volumes are scaled with λ_l, λ_l^2 and λ_l^3, respectively, in relation to the prototype (Heller, 2011). The geometric scaling may include finer geometric details, for instance, the surface roughness which has an influence on the type of flow.

b) Kinematic Similarity

Movement is defined as the change in distance or length with respect to time. Therefore kinematic similarity refers to the similarity of motion between particles in the prototype and the model. Implying that the velocity ratios for both the model and prototype are the same for all particles at specific time intervals. Indicating that a constant ratio should be noted between time-dependent events in the model and prototype with corresponding time intervals, such that:

$$\lambda_{\mathrm{t}} = \frac{\mathrm{t_p}}{\mathrm{t_m}} = \frac{\mathrm{t}}{\mathrm{t'}} = \mathrm{t}^* \tag{0-2}$$

c) Dynamic Similarity

Systems are referred to as being dynamically similar when all forces acting on the prototype are reproduced at a constant ratio to the model as shown in Equation (0-3). Dynamic similarity ensures that in geometrically similar models time-dependent events occur in a kinematic similar manner.

$$\lambda_{\mathrm{F}} = \frac{\mathrm{F_p}}{\mathrm{F_m}} = \frac{\mathrm{F}}{\mathrm{F'}} = \mathrm{F}^* \tag{0-3}$$

G 3.2. Scale Effects

It was earlier mentioned that achieving complete similitude between model and prototype was rarely possible. In such cases, the deviations in results between the improperly scaled systems are referred to as scale effects. Heller (2011) emphasizes how physical hydraulic tests always involve scale effects when $\lambda \neq 1$. This follows that the force ratios are not identical between the model and the prototype.

The magnitude of the constant scale factor, λ, has direct influence on the scale effects. The greater the ratio, the greater the deviations, thus an increase in expected effects. However, the direct proportion between the two entities does not indicate whether or not the scale effects can be neglected. Their significance depends on the relative importance of the forces involved.

G 3.3 Hydraulic Similitude

Hughes (1993) explains how almost any major problem can be simplified into the interchange of two major forces while the other forces are considered negligible or minor. Based on this assumption, a number of similitude theories for fluid flow have been developed. With reference to Newton's second law, inertial forces (F_i) are always present in flow problems where,

$$F_i = \mathrm{mass} \times \mathrm{acceleration} = \rho l^2 v^2 \tag{0-4}$$

Therefore the inertial forces must be balanced by any other governing force in the flow problem. Typical governing forces found in fluid mechanics include:

Table G-1: Typical forces in fluid flow

Source: Hughes (1993)

Force	Symbol	Description	Expression
Gravitational	F_g	Mass x gravitational acceleration	$\rho l^3 g$
Viscous	F_μ	Shear stress x area	$\mu v l$
Surface tension	F_σ	Unit surface tension x length	σl
Elastic compression	F_e	Young's modulus x area	$E l^2$
Pressure	F_{pr}	Unit Pressure x area	$p l^2$

Where,

g = Gravitational acceleration in m/s^2
μ = Dynamic viscosity
σ = Surface tension in N/mm^2
E = Modulus of elasticity in N/m^2
p = Pressure in kPa

The ratio between the inertial forces to any other governing force provides the relative influence of the considered forces in the flow problem. Thus requiring that the force ratio be maintained at a constant value for both the model and the prototype, hence dynamic similarity. For each of the different force ratios, a similitude theory was derived. The most relevant theories in the research project were identified to be a) Reynolds and b) Froude’s similitude criteria, as mentioned in Chapter 0 of dimensional analysis.

a) Reynolds Criterion

Reynold’s similarity is only applicable when viscous and inertial forces are dominant, with the effect of the remaining forces such as gravity being negligible. The important parameter is the ratio of inertial to viscous forces given by:

$$\frac{\text{inertial force}}{\text{viscous force}} = \frac{\rho l^2 v^2}{\mu v l} = \frac{\rho l v}{\mu} = \mathrm{Re} \qquad (0\text{-}5)$$

The above ratio is known as the Reynolds number (Re), a dimensionless product. The number’s physical interpretation highlights the relative importance of the inertial force on a fluid particle to the viscous force on the particle (Hughes, 1993). Reynolds number was first introduced to distinguish between laminar and turbulent flow as described in Chapter. Similitude between the model and prototype is achieved when Reynolds number is the same for both systems. For example, modifying Equation (0-5) with reference to Equation (0-5) and Equation (0-6), the following relation was derived:

$$\frac{\rho l v}{\mu} = \left(\frac{\rho l v}{\mu}\right)' \qquad (0\text{-}6)$$

$$\left(\frac{v}{v'}\right)\left(\frac{l}{l'}\right)\left(\frac{\rho}{\rho'}\right) = \left(\frac{\mu}{\mu'}\right) \qquad (0\text{-}7)$$

In terms of scale factors, the Reynolds model criteria is:

$$\frac{\lambda_v \lambda_l \lambda_\rho}{\lambda_\mu} = 1 \quad \text{or} \quad \lambda_{\mathrm{Re}} = 1 \qquad (0\text{-}8)$$

b) Froude Criterion

Like Reynolds criteria, the Froude criteria is only applicable when gravity and inertial forces are the most dominant. The remaining forces such as kinematic viscosity are considered negligible or small. The parameter expresses the influence of the forces in a hydraulic flow given by Equation

$$\sqrt{\frac{\text{inertial force}}{\text{gravity force}}} = \sqrt{\frac{\rho l^2 v^2}{\rho l^3 g}} = \frac{v}{\sqrt{gl}} \tag{0-9}$$

The ratio above is known as the Froude Number. The physical interpretation of the number gives the relative significance of the inertial forces in fluid problem to the weight of the particles effected by gravity. Similarly, similitude is achieved between the model and the prototype when the Froude number remains constant for both. Using a similar approach regarding representative quantities and principal pi-numbers, the relation between the governing two forces was derived to be:

$$\frac{v}{\sqrt{gl}} = \left(\frac{v}{\sqrt{gl}}\right)' \tag{0-10}$$

The equation was simplified to:

$$\frac{v}{v'} = \sqrt{\left(\frac{g}{g'}\right)\left(\frac{l}{l'}\right)} \tag{0-11}$$

In terms of scale factors, the Froude criteria was rearranged to give:

$$\frac{\lambda_v}{\sqrt{\lambda_g \lambda_l}} = 1 \quad \text{or} \quad \lambda_{Fr} = 1 \tag{0-12}$$

Assuming that the gravitational acceleration was equal for both systems, λ_g equals unity (λ_g =1), the Froude scaling condition in Equation (0-12) was further simplified to:

$$\lambda_v = \sqrt{\lambda_l} \tag{0-13}$$

Therefore, using the concept of similitude for both Froude and Reynolds, the parameters of interest can be scaled according to the factors summarised in Table H-2. The various parameters were represented in terms of primary quantities mentioned in Chapter 0.

Table G-2: Parameter scale factors used in fluid mechanics

Source: Hughes (1993)

Parameter	Dimension	Froude	Reynolds
Geometric Similarity			
Length	l	λ	λ
Area	l^2	λ^2	λ^2
Volume	l^3	λ^3	λ^3
Rotation	θ	1	1
Kinematic Similarity			
Time	t	$\lambda^{1/2}$	λ^2
Velocity	lt^{-1}	$\lambda^{1/2}$	λ^{-1}
Acceleration	lt^{-2}	1	λ^{-3}
Discharge	l^3t^{-1}	$\lambda^{5/2}$	λ
Dynamic Similarity			
Mass	m	λ^3	λ^3
Force	mlt^{-2}	λ^3	1
Pressure and stress	$ml^{-1}t^{-2}$	λ	λ^{-2}
Energy and work	ml^2t^{-2}	λ^4	λ
Power	ml^2t^{-3}	$\lambda^{7/2}$	λ^{-1}

In general, the Froude criterion is used for modelling flows when inertial forces are balanced by gravitational forces. Examples include most flows that have a free surface. The Reynolds criterion is intended for modelling flows where the viscous forces predominate. Examples include forces on cylinders with low Reynold numbers and laminar boundary layer problems (Hughes, 1993).

G 4. Basic Scaling of Granular Materials

In practice, one of the major concerns governing the scaling of granular materials was the behavioural accuracy of scaled systems compared to the original system. The scaling of a system is effective when the effects that occur in a large system, occur equivalently in the scaled system. To guarantee equivalent dynamic properties between the original and scaled system, the material properties have to be modified in accordance with the scaling factor and the unit of time has to be redefined (Pöschel et al., 2001). The basic principles of scaling identified in Chapter 0 were used in conjunction with similitude theories to determine how granular particles are scaled.

G 4.1 Physical Model

In some cases, the analysis of structural systems with complex boundary and loading conditions can be difficult to simulate on numerical models. Therefore scaled down models are often used to assist engineers in predicting the behaviour of the prototype (Ramu et al., 2013). Referring to a simple granular system, the system may be described as an assembly of spheres of radii R_i, where i = 1,….,n. Using the pairwise force law, the interaction between two spheres, i and j at positions r_i and r_j of radii R_i and R_j respectively can be defined as the following:

$$F_{ij} = \begin{cases} F_{ij}^{n} n_{ij} + F_{ij}^{t} t_{ij} & \text{if} \quad R_i + R_j - \left| r_i + r_j \right| > 0 \\ 0 \end{cases} \tag{0-1}$$

Where,

n = Unit vector in normal direction

t = Unit vector in tangential direction

According to Pöschel et al. (2001), the dynamics of the granular system can be computed by integrating appropriate initial conditions with Equation (0-1) numerically for all i = 1,….,n. Therefore assuming that the dynamics, S, is known for a certain granular system. One can address the potential change in dynamics when dimensions are rescaled by a constant factor λ, i.e. $R'_i \equiv \lambda R_i$, where R'_i is the scaled system. If the system properties are affected, the objective of the scaling laws is to determine a suitable modification of the material properties to assure equivalent dynamics of the systems S and S'.

When scaling large phenomena down to lab-size experiments, the dynamic properties of a material can be significantly different in the scaled system. To guarantee equivalent dynamical properties, the material properties must be modified in a way to assure the scaled system behaves in an identical manner to the original system. Changing the size of the system along with all of its constituents requires the modification of the timescale and material properties in a predefined way. According to Ramu et al. (2013) and Feng & Owen (2014), it was determined that all lengths *x*, associated with the system were scaled by a constant scale factor λ, where:

$$x' = \lambda x \tag{0-2}$$

The characteristic time *t*, of the system, is defined as the time it takes for two particles to travel over the characteristic length just before they collide. The scaling of time is a direct consequence of the spatial scaling described above, provided that the gravity constant remains unchanged for both scaled and unscaled systems. Scaling lengths by a factor λ, implies that the time scale must be scaled by a constant $\lambda^{1/2}$. The factor was calculated from the derivation of Equation (0-3), the equation represented the spatial definition of the characteristic length with the characteristic time of the system.

$$\left(\frac{d^2x}{dt^2}\right)' = \frac{d^2x}{dt^2} \tag{0-3}$$

$$\frac{d^2(\lambda x)}{d(t')^2} = \frac{d^2x}{dt^2}$$

$$t' = \sqrt{\lambda}t$$

The scaling of granular materials relies on certain boundary conditions. The necessary conditions of the scaled system can be obtained through a scaled equation of motion that is exactly equivalent to its unscaled counterpart, ensuring identical trajectories between the systems. In Poschel's (2001) study, the equation of motion for the scaled system during a binary collision or permanent contact focused on two fundamental characteristics of binary collision which included the duration of collision and the coefficient of restitution, e. The latter describes the ratio between the normal relative velocity of the particles before and after the collision. A collision is said to be perfectly elastic when the coefficient of restitution, $e = 1$ and perfectly inelastic when $e = 0$. Both characteristics are dependent on the impact velocity of the viscoelastic spheres. The results in the study indicate that for a constant gravity force, the elastic constant of the material, denoted by Equation (0-4), is scaled by a constant factor λ. This indicates that apart from gravity, all other accelerations must remain unaffected.

$$\frac{Y'}{\emptyset'(1-\nu'^2)} = \lambda\frac{Y}{\emptyset(1-\nu^2)} \tag{0-4}$$

Where,

Y = Young modulus in N/m^2

ν = Poisson ratio

$\emptyset$ = Density in kg/m^3

Following the elastic constant, a dissipative constant, A, exists. Essentially it is defined as the viscous relaxation time of the spheres involved during collision. From the scaled equation of motion in Poschel's (2001) study, it is evident that the dissipative constant in the scaled system must be multiplied by a factor of $\lambda^{1/2}$ such that:

$$A' = \sqrt{\lambda}A \tag{0-5}$$

The scaling scheme used in the scaling of material properties is a useful tool in scaling down real world granular systems. Notably, the original material can be replaced by a substitute material that satisfies the requirements of the constants discussed in this Chapter. However, as mentioned earlier, the scheme is only applicable when both the material properties and the system have been modified.

APPENDIX H

Pump Calibration

H 1. Introduction

One of the key tests involved the suction of particles through an orifice. A variable speed drive (VSD) suction pump was used to carry out these tests. Under ideal conditions, the pump was made to produce continuous flow rates with respect to the selected rotational motor frequency. Initial testing indicated slight deviations from the stipulated parameters given in the report conducted by DBM. Therefore, to validate and calibrate the pump a simple flow rate test was conducted.

H 2. VSD Control Specifications

Before the calibration process, the type of system used must be verified. Suction power is provided by a “Nietche” progressive cavity pump, driven by a model E7 Yasakawa variable speed drive (VSD). At a frequency of 50Hz, the pump provided a suction flow of 10 l/s. The calibration process required a clear understanding of the VSD controls, summarised as follows:

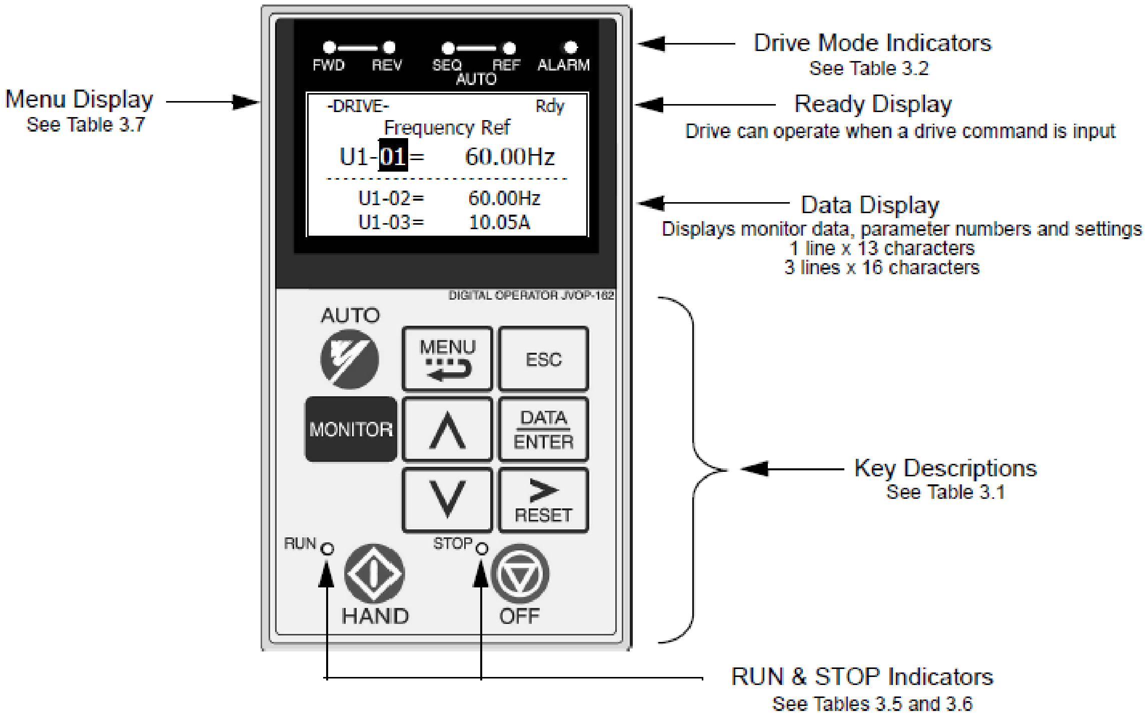

Figure H-1: VSD Controls

Source: (Yaskawa, 2002)

Table H-1: VSD Operator Keys

Source: (Yaskawa, 2002)

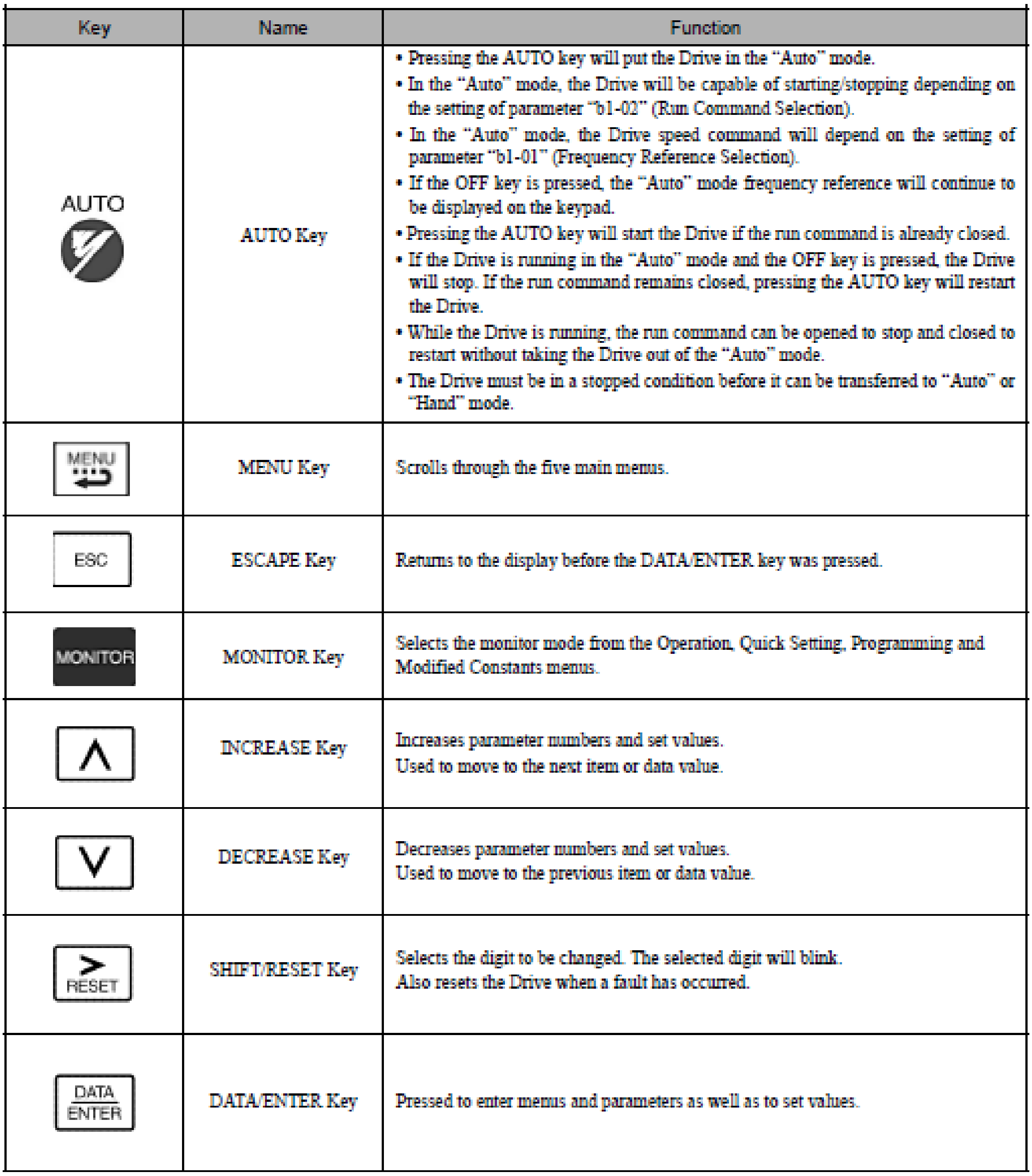

Key	Name	Function
AUTO	AUTO Key	• Pressing the AUTO key will put the Drive in the "Auto" mode. • In the "Auto" mode, the Drive will be capable of starting/stopping depending on the setting of parameter "b1-02" (Run Command Selection). • In the "Auto" mode, the Drive speed command will depend on the setting of parameter "b1-01" (Frequency Reference Selection). • If the OFF key is pressed, the "Auto" mode frequency reference will continue to be displayed on the keypad. • Pressing the AUTO key will start the Drive if the run command is already closed. • If the Drive is running in the "Auto" mode and the OFF key is pressed, the Drive will stop. If the run command remains closed, pressing the AUTO key will restart the Drive. • While the Drive is running, the run command can be opened to stop and closed to restart without taking the Drive out of the "Auto" mode. • The Drive must be in a stopped condition before it can be transferred to "Auto" or "Hand" mode.
MENU	MENU Key	Scrolls through the five main menus.
ESC	ESCAPE Key	Returns to the display before the DATA/ENTER key was pressed.
MONITOR	MONITOR Key	Selects the monitor mode from the Operation, Quick Setting, Programming and Modified Constants menus.
∧	INCREASE Key	Increases parameter numbers and set values. Used to move to the next item or data value.
∨	DECREASE Key	Decreases parameter numbers and set values. Used to move to the previous item or data value.
> RESET	SHIFT/RESET Key	Selects the digit to be changed. The selected digit will blink. Also resets the Drive when a fault has occurred.
DATA ENTER	DATA/ENTER Key	Pressed to enter menus and parameters as well as to set values.

H 3. Pump Calibration

The most effective way of calibrating the pump was by measuring the flow rate output produced at different frequencies. This was done by measuring the output of water directly from the filtration tank using a bucket of known mass and volume. By measuring the approximate time, it took to fill the bucket, the flow rate per selected frequency could be calculated.

Through the process depicted above, the following results were recorded from the test:

- Mass of bucket = 2.56kg
- Mass of bucket and water = 23.35kg

Table H-2: Recorded calibration data

Pump Calibration	Unit	1	2	3	4	5	6	7	8	9	10	11	12
Frequency	Hz	15	15	15	22.5	22.5	22.5	30	30	30	45	45	45
Time	s	19.56	19.57	20.03	7.23	7.55	7.82	4.4	4.33	4.23	2.52	2.53	2.45
Flow rate (measured)	l/s	1.03	1.06	1.04	2.88	2.75	2.66	4.72	4.80	4.91	8.25	8.22	8.48
Average	l/s	**1.05**			**2.76**			**4.81**			**8.32**		

The initial calibration document, indicated that the pump would produce a 10 l/s at a frequency of 45Hz. However, after investigation it was found that this was not the case. When queried, the initial amounts were recorded in 2010. Therefore, due to wear and tear, it was assumed that the flow rate was subjected to pressure constant pressure losses throughout the system. With this assumption, the pump was recalibrated for testing.

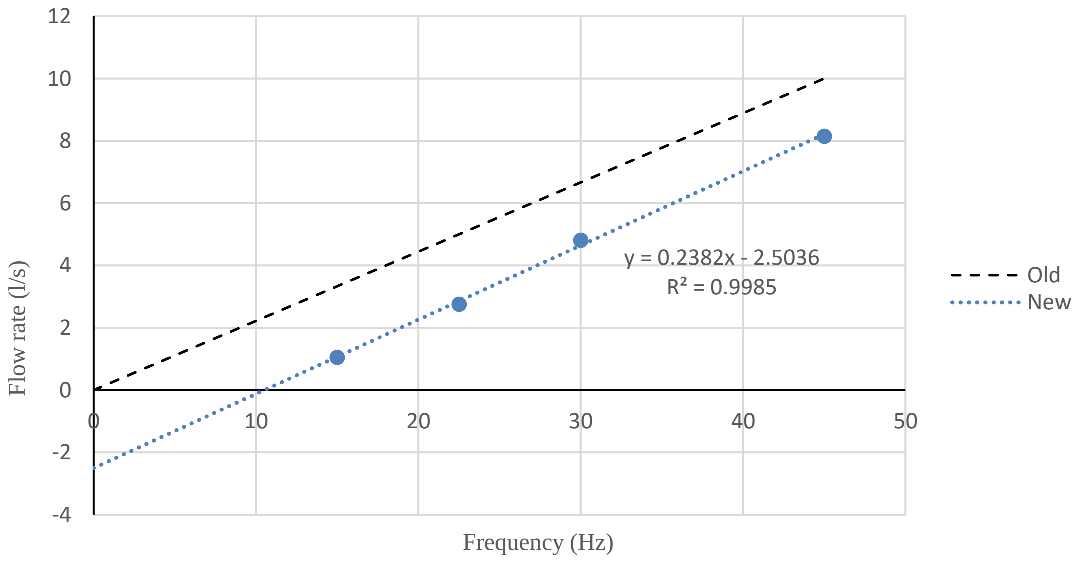

Figure H-2: Calibration curve of pump

From the two calibration curves above, their difference in output is clearly visible. The pump decreased in efficiency due to pressure losses that may have been caused by leakages or wear of equipment. The linear-fit curve expression used to determine the VSD frequency input for the corresponding Flow rate Q, was found to be:

$$(\text{Flow rate, Q})\ y = 0.2382\ (\text{Frequency})x - 2.5036$$

H 4. Optimal Flow Rate Conditions

As the pump carried a certain amount of uncertainty (Appendix I), an optimal flow rate was to be used throughout testing. The flow rate was adjusted according to the testing of materials (GB6 or GB16). The selection of the magnitude of the flow rate in terms of frequency were restricted to the following:

1. Flow must be great enough to carry particles through the vertical suction pipe,
2. The flow rate must work in unison with the mechanical movement of the nozzle to prevent the build-up and clogging of GB within the nozzle.

The approach to these restrictions was to first calculate the settling velocity v_s of a particle within the pipe. This provided the lower limit of the approximate flow rate velocity required. The body forces acting on a single particle suspended in fluid were highlighted below:

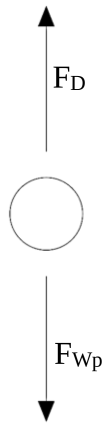

Figure H-3: Body forces on particle

Here F_D refers to the drag force and F_{Wp} refers to the difference between the gravitational and buoyancy forces. With reference to Figure H2, the terminal velocity of a particle in suspension can be determined by balancing the forces over a submerged particle as follows:

$$F_D = F_{W_P}$$

$$\frac{C_D \pi d^2 {v_s}^2 \rho_f}{8} = (\rho_s - \rho_f) g \frac{\pi d^3}{6}$$

$$v_s = \sqrt{\frac{4}{3}\frac{(\rho_s - \rho_f)}{\rho_f}\frac{gd}{C_D}}$$

C_D is defined as the drag coefficient and is a function of the Reynolds number of the particle R_{ep}, defined as:

$$\text{Particle reynold's number } (Re_p) = \frac{\rho v d_p}{\mu} = \frac{v d_p}{\upsilon}$$

Using the graph below, an initial assumption of C_D=1.0 was selected.

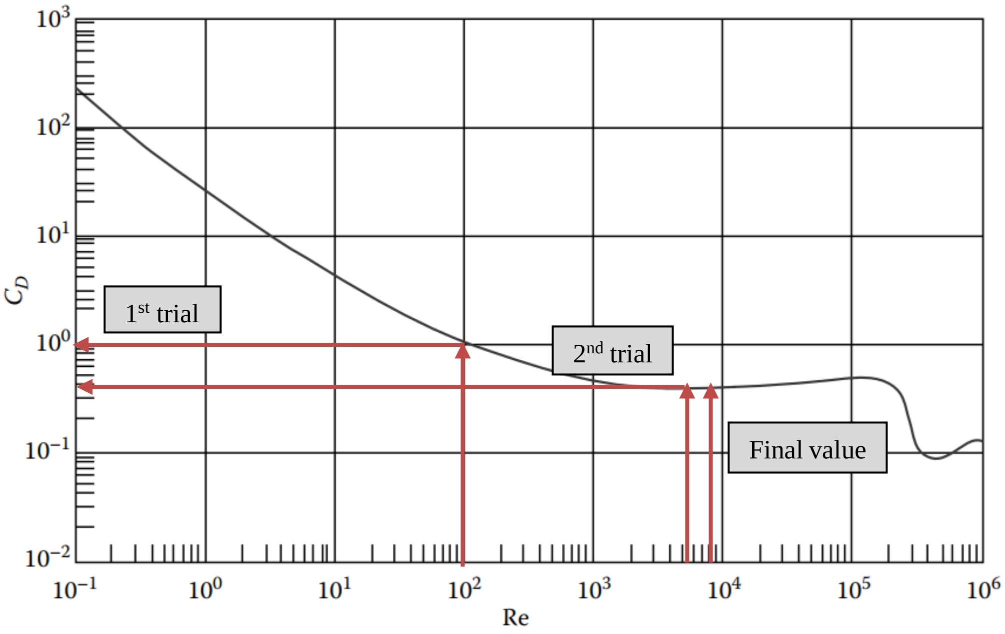

Figure H-4: Coefficient of drag as a function of Reynolds number

Therefore, for GB6 with properties summarised in the table below, the settling velocity was calculated to be:

Table H3: Intrinsic properties of GB6

Parameter	**Symbol**	**Unit**	**Value**
Particle density	ρ_s	kg/m^3	2540
Fluid density	ρ_f	kg/m^3	1000
Drag coefficient	C_D	-	1.0 (1st trial)
Gravity	g	m/s^2	9.81
Particle diameter	d	m	0.006
Dynamic Viscosity	μ	N.s/m^2	1.002x10^{-3}

*Note: Dynamic viscosity μ determined from Finnemore & Franzini (2002) for T=20ºC

$$v_s = \sqrt{\frac{4}{3}\frac{(\rho_s - \rho_f)}{\rho_f}\frac{gd}{C_D}}$$

Using C_D=1.0

$$v_s = \sqrt{\frac{4}{3}\frac{(2540 - 1000)}{1000}\frac{(9.81)(0.006)}{1.0}}$$

$$v_s = 0.348\ m/s$$

And Re_p,

$$Re_p = \frac{\rho v d_p}{\mu}$$

$$Re_p = \frac{(2540)(0.348)(0.006)}{1.002\times10^{-3}}$$

$$Re_p = 5292.93$$

From Figure H3, we find C_D=0.4 which will be the second trial value,

Using C_D=0.4

$$v_s = \sqrt{\frac{4}{3}\frac{(2540 - 1000)}{1000}\frac{(9.81)(0.006)}{0.4}}$$

$$v_s = 0.550\ m/s$$

And Re_p,

$$Re_p = \frac{\rho v d_p}{\mu}$$

$$Re_p = \frac{(2540)(0.550)(0.006)}{1.002\times10^{-3}}$$

$$Re_p = 8360$$

From Figure H3, we find again that Re_p=8360 corresponds with C_D=0.4 which converges to the 2nd trial value. Thus, the settling velocity of GB6 was determined to be:

$$v_s = 0.550\ m/s$$

Since the suction pipe had a diameter of 80mm, the corresponding flow rate required to match the terminal velocity was computed to be:

$$Q = vA$$
$$Q = (0.550)(\pi \frac{0.08^2}{4})$$
$$Q_i = 2.765 \times 10^{-3}\ m^3/s$$

Using the pump calibrations chart, where:

$$Flow\ rate, Q(l/s) = 0.2382 \times (Frequency, Hz) - 2.5036$$
$$2.765 = 0.2382 \times (Frequency, Hz) - 2.5036$$
$$Frequency = 22.12\ Hz$$

This was the minimum frequency value to be used for the VSD input. However, to avoid the potential of clogging within the nozzle, an extra 2Hz was added, giving:

$$Frequency = 24.12 \sim 24Hz$$
$$v_f = 0.639 m/s$$
$$Q_f = 3.213 \times 10^{-3}\ m^3/s$$

The same process was carried for GB16, its values were summarised in the table below:

Table H-4: Input parameters to be used for pump

Parameter	Symbol	Unit	GB6	GB16
Initial velocity	v_i	m/s	0.550	0.898
Initial flow rate	Q_i	l/s	2.765	4.512
Initial Frequency	-	Hz	22.12	29.453
Final Frequency	-	Hz	24.00	31.50
Final velocity	v_f	m/s	0.639	0.995
Final flow rate	Q_f	l/s	3.213	5.000

For the multiple orifice tests a frequency of 40Hz was selected as it was noted through observations that the rate of particles entering the orifices were a lot far greater than the amount that was transported away via the suction pipe. Through trial and error this was the approximate optimum value to prevent the build-up of beads. 40Hz corresponded to a pipe velocity of 1.397m/s and a flow rate of 7.024l/s.

APPENDIX I

Uncertainty Analysis

I 1. Introduction

The experimental nature of the research conducted, brings along with it, several uncertainties associated with the equipment used. Potential errors were found to be in the measuring devices (e.g. rulers, tape measures and mass scale), variable speed drive for the pump motor and measured results. Errors included either random or systematic errors. The former are unpredictable errors brought about things or scenarios that cannot be controlled e.g. noise affecting the readings of a scale. These errors can be reduced by repeating the readings. The latter looks at errors brought about by the measuring equipment or its operator which can be minimised by calibrating the equipment. The uncertainty analysis was carried out according to Currell & Dowman (2009): Chapter 8.2.3.

I 2. Measuring Devices

A sectioned measuring tape was placed alongside the bogey, used as reference mark for the z-coordinated of the nozzle. A sensitive scale was used to measure the mass outputs. Both the tape and scale were subjected to systematic errors.

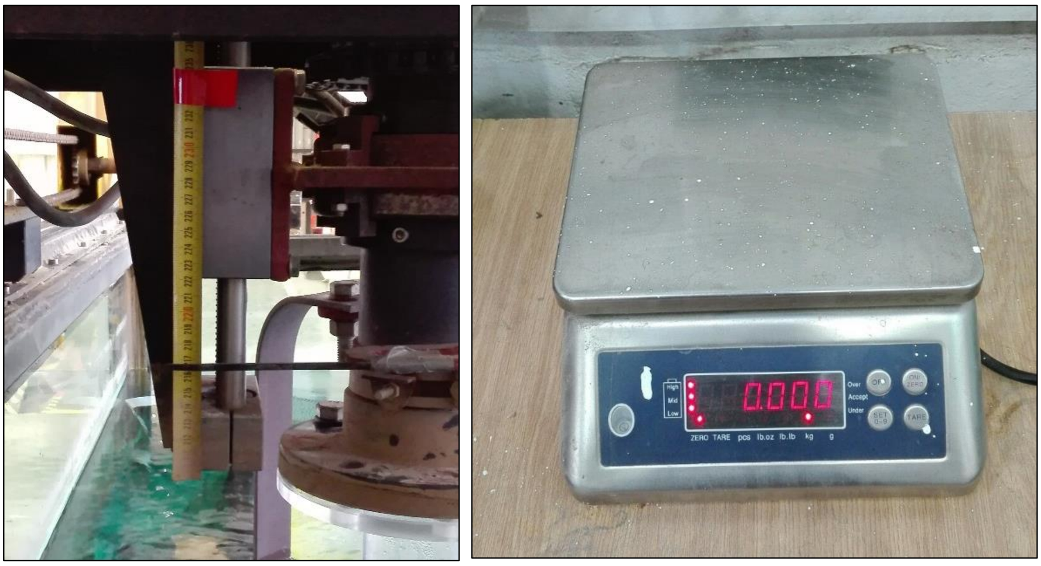

Figure I1: a) Measuring tape attached to bogey system and b) sensitive scale

The positioning was done manually which induced human errors within the measurements. The standard error in these measurements for a 95% confidence interval of replicate measurements, is given by the expression:

$$CI_{95\%} = \bar{x} \pm C_d$$

$$CI_{95\%} = \bar{x} \pm \left(t \times \frac{s}{\sqrt{n}}\right)$$

Where,

$\bar{x}$ = Mean or average value of the measured sample data
n = Sample size
C_d = Confidence deviation
t = t-test value based on degree of freedom and confidence level (See Currell et al.,2009)
s = Standard deviation given by:

$$s = \sqrt{\frac{\sum_1^n (x_i - \bar{x})^2}{n-1}}$$

x_i = Measured data

Furthermore, the standard uncertainty u_x is given by:

$$u_x = \frac{s}{\sqrt{n}}$$

Through this method the standard error associated with the tape measure for a 95% confidence level was calculated as follows:

Table I1: Collected data for measuring tape

Data set	**Measured (cm)**	$(x_i-\bar{x})$	$(x_i-\bar{x})^2$
1	217.1	-0.08	0.0064
2	217.15	-0.13	0.0169
3	216.9	0.12	0.0144
4	217	0.02	0.0004
5	216.7	0.32	0.1024
6	216.85	0.17	0.0289
7	217.2	-0.18	0.0324
8	217	0.02	0.0004
9	217.2	-0.18	0.0324
10	217.1	-0.08	0.0064

$\bar{x}$ = 217.02
s = 0.155
u_x = 0.049
t = 2.262
C_d = 0.111
CI = 217±0.11kg

Therefore, the error in the measuring tape was determined to be:

$$CI_{95\%} = \bar{x} \pm C_d$$

$$CI_{95\%} = 217 \pm 0.11kg$$

The mass scale used in the experiment, was sensitive to three decimal places. For example, a mass output would be given as 2.567kg. Therefore, the precision of the scale was 0.001kg. Although an error, the amount was negligible, considering the amount of material collected.

I 3. Variable Speed Drive Uncertainty

The uncertainty within the produced flow rate was calculated using the calibration curve under a regression analysis. Since the pump was subjected to a constant head loss it was assumed that the flow rate would decrease linearly. This was confirmed by the calibration curve, where a $r^2=0.999$ regression correlation coefficient was achieved.

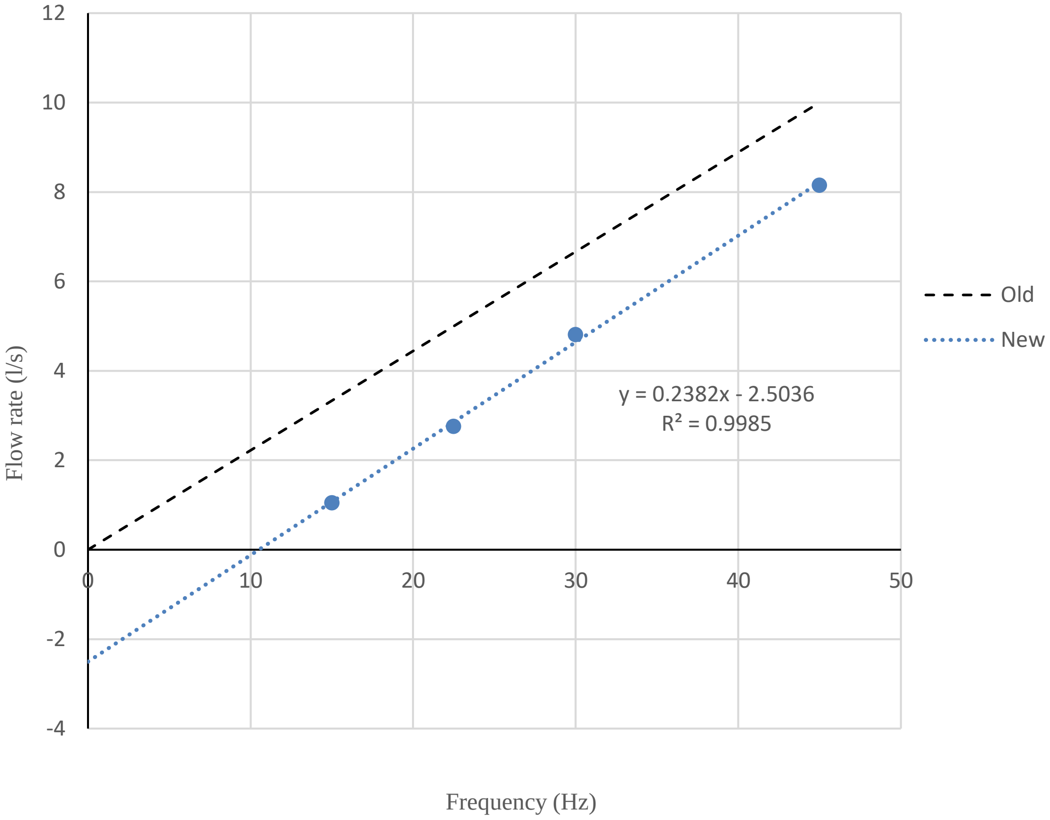

The correlation coefficient *r* as described by Yang (2008), provided a good indication of the relationship between two sets of variables, *x* and *y*. r = 0 indicates that the variables are independent of one another and r=1 indicates an increasing linear relationship, where the increase in the one variable would lead to an increase in the other. $r^2=1$ indicates a perfectly linear relationship between the two variables. For a set of n data points (x_i, y_i), the correlation coefficient r can be calculated using:

$$r = \frac{n\sum_{i=1}^{n} x_i y_i - \sum_{i=1}^{n} x_i \sum_{i=1}^{n} y_i}{\sqrt{\left[n\sum_{i=1}^{n} x_i^2 - \left(\sum_{i=1}^{n} x_i\right)^2\right]\left[n\sum_{i=1}^{n} y_i^2 - \left(\sum_{i=1}^{n} y_i\right)^2\right]}}$$

The same method was carried out for all other linear related graphs carried out throughout this dissertation.

I 4. Uncertainty within Results

The uncertainty within the replicated results were determined according to the method covered for the measuring devices. Then uncertainties pertaining to the MMS tests were as follows:

MMS-GB6:

Test no.	Diameter of orifice (mm)											
	30			40			50			60		
	x_i (kg)	(x_i-x_{avg})	(x_i-x_{avg})^2	x_i (kg)	(x_i-x_{avg})	(x_i-x_{avg})^2	x_i (kg)	(x_i-x_{avg})	(x_i-x_{avg})^2	x_i (kg)	(x_i-x_{avg})	(x_i-x_{avg})^2
1	0.323	-0.005	2.67E-05	0.601	0.010	9.51E-05	1.084	-0.029	8.27E-04	1.566	0.017	3.03E-04
2	0.319	-0.001	1.36E-06	0.625	-0.014	2.03E-04	1.036	0.019	3.71E-04	1.601	-0.018	3.09E-04
3	0.308	0.010	9.67E-05	0.595	0.016	2.48E-04	1.044	0.011	1.27E-04	1.582	0.001	2.01E-06
4	0.304	0.014	1.91E-04	0.608	0.003	7.56E-06	1.058	-0.003	7.56E-06	1.591	-0.008	5.75E-05
5	0.292	0.026	6.67E-04	0.618	-0.007	5.26E-05	1.043	0.012	1.50E-04	1.580	0.003	1.17E-05
6	0.355	-0.037	1.38E-03	0.604	0.007	4.56E-05	1.046	0.009	8.56E-05	1.593	-0.010	9.18E-05
7	0.323	-0.005	2.67E-05	0.607	0.004	1.41E-05	1.041	0.014	2.03E-04	1.591	-0.008	5.75E-05
8	0.318	0.000	2.78E-08	0.609	0.002	3.06E-06	1.061	-0.006	3.31E-05	1.541	0.042	1.80E-03
9	0.312	0.006	3.40E-05	0.612	-0.001	1.56E-06	1.052	0.003	1.06E-05	1.595	-0.012	1.34E-04
10	0.309	0.009	7.80E-05	0.650	-0.039	1.54E-03	1.075	-0.020	3.90E-04	1.591	-0.008	5.75E-05
11	0.312	0.006	3.40E-05	0.606	0.005	2.26E-05	1.071	-0.016	2.48E-04	1.574	0.009	8.87E-05
12	0.339	-0.021	4.48E-04	0.594	0.017	2.81E-04	1.052	0.003	1.06E-05	1.596	-0.013	1.58E-04

$\bar{x}$	=	0.318	=	0.611	=	1.055	=	1.583
s	=	0.016	=	0.014	=	0.014	=	0.016
u_x	=	0.005	=	0.004	=	0.004	=	0.005
t	=	2.201	=	2.201	=	2.201	=	2.201
C_d	=	0.010	=	0.009	=	0.009	=	0.010
CI	=	0.318±0.01kg	=	0.611±0.009kg	=	1.055±0.009kg	=	1.583±0.01kg

MMS-GB16:

Test no.	Diameter of orifice (mm)											
	30			40			50			60		
	x_i (kg)	$(x_i - x_{avg})$	$(x_i - x_{avg})^2$	x_i (kg)	$(x_i - x_{avg})$	$(x_i - x_{avg})^2$	x_i (kg)	$(x_i - x_{avg})$	$(x_i - x_{avg})^2$	x_i (kg)	$(x_i - x_{avg})$	$(x_i - x_{avg})^2$
1	0.209	-0.024	5.96E-04	0.516	-0.016	2.59E-04	0.900	-0.025	6.29E-04	1.311	-0.016	2.53E-04
2	0.203	-0.018	3.39E-04	0.506	-0.006	3.70E-05	0.836	0.039	1.51E-03	1.292	0.003	9.51E-06
3	0.202	-0.017	3.03E-04	0.512	-0.012	1.46E-04	0.851	0.024	5.72E-04	1.291	0.004	1.67E-05
4	0.192	-0.007	5.50E-05	0.472	0.028	7.79E-04	0.927	-0.052	2.71E-03	1.306	-0.011	1.19E-04
5	0.218	-0.033	1.12E-03	0.523	-0.023	5.33E-04	0.858	0.017	2.86E-04	1.283	0.012	1.46E-04
6	0.189	-0.004	1.95E-05	0.521	-0.021	4.45E-04	0.851	0.024	5.72E-04	1.311	-0.016	2.53E-04
7	0.162	0.023	5.10E-04	0.453	0.047	2.20E-03	0.865	0.010	9.83E-05	1.308	-0.013	1.67E-04
8	0.196	-0.011	1.30E-04	0.462	0.038	1.44E-03	0.926	-0.051	2.61E-03	1.272	0.023	5.33E-04
9	0.114	0.071	4.98E-03	0.511	-0.011	1.23E-04	0.867	0.008	6.27E-05	1.281	0.014	1.98E-04
10	0.203	-0.018	3.39E-04	0.502	-0.002	4.34E-06	0.825	0.050	2.49E-03	1.299	-0.004	1.53E-05
11	0.115	0.070	4.84E-03	0.509	-0.009	8.25E-05	0.894	-0.019	3.64E-04	1.296	-0.001	8.40E-07
12	0.212	-0.027	7.52E-04	0.512	-0.012	1.46E-04	0.899	-0.024	5.80E-04	1.291	0.004	1.67E-05

$\bar{x}$	=	0.185	=	0.500	=	0.875	=	1.295
s	=	0.034	=	0.023	=	0.032	=	0.012
u_x	=	0.010	=	0.007	=	0.009	=	0.003
t	=	2.201	=	2.201	=	2.201	=	2.201
C_d	=	0.022	=	0.014	=	0.021	=	0.008
CI	=	0.185±0.022kg	=	0.500±0.014kg	=	0.875±0.021kg	=	1.295±0.008kg

The errors associated with the MSS testing were carried out following the same procedure However, because of the influence the velocity vector on the results, the uncertainty analysis was carried out for every three iterations. Starting with **GB6:**

MSS

D30:

Test no.	Diameter of orifice (mm)											
	0.104			0.156			0.208			0.26		
	x_i (kg)	$(x_i - x_{avg})$	$(x_i - x_{avg})^2$	x_i (kg)	$(x_i - x_{avg})$	$(x_i - x_{avg})^2$	x_i (kg)	$(x_i - x_{avg})$	$(x_i - x_{avg})^2$	x_i (kg)	$(x_i - x_{avg})$	$(x_i - x_{avg})^2$
1	8.591	0.020	4.00E-04	6.396	-0.126	1.59E-02	4.821	0.064	4.05E-03	3.975	0.101	1.01E-02
2	8.681	-0.070	4.90E-03	6.122	0.148	2.19E-02	4.927	-0.042	1.79E-03	4.155	-0.079	6.29E-03
3	8.561	0.050	2.50E-03	6.292	-0.022	4.84E-04	4.906	-0.021	4.55E-04	4.097	-0.021	4.55E-04

$\bar{x}$	=	8.611	=	6.270	=	4.885	=	4.076
s	=	0.051	=	0.113	=	0.046	=	0.075
u_x	=	0.029	=	0.065	=	0.026	=	0.043
t	=	4.303	=	4.303	=	4.303	=	4.303
C_d	=	0.127	=	0.281	=	0.114	=	0.186
CI	=	8.611±0.127kg	=	6.27±0.281kg	=	4.885±0.114kg	=	4.076±0.186kg

D40:

Test no.	Diameter of orifice (mm)											
	0.104			0.156			0.208			0.26		
	x_i (kg)	(x_i-x_{avg})	$(x_i-x_{avg})^2$	x_i (kg)	(x_i-x_{avg})	$(x_i-x_{avg})^2$	x_i (kg)	(x_i-x_{avg})	$(x_i-x_{avg})^2$	x_i (kg)	(x_i-x_{avg})	$(x_i-x_{avg})^2$
1	9.785	-0.124	1.53E-02	6.934	-0.016	2.56E-04	5.782	0.073	5.28E-03	5.371	-0.163	2.65E-02
2	9.602	0.059	3.52E-03	6.907	0.011	1.21E-04	5.934	-0.079	6.29E-03	5.170	0.038	1.47E-03
3	9.597	0.064	4.14E-03	6.913	0.005	2.50E-05	5.848	0.007	4.44E-05	5.084	0.124	1.55E-02

$\bar{x}$	= 9.661	= 6.918	= 5.855	= 5.208
s	= 0.087	= 0.012	= 0.062	= 0.120
u_x	= 0.051	= 0.007	= 0.036	= 0.069
t	= 4.303	= 4.303	= 4.303	= 4.303
C_d	= 0.217	= 0.029	= 0.155	= 0.299
CI	= 9.661±0.217kg	= 6.918±0.029kg	= 5.855±0.155kg	= 5.208±0.299kg

D50:

Test no.	Diameter of orifice (mm)											
	0.104			0.156			0.208			0.26		
	x_i (kg)	(x_i-x_{avg})	$(x_i-x_{avg})^2$	x_i (kg)	(x_i-x_{avg})	$(x_i-x_{avg})^2$	x_i (kg)	(x_i-x_{avg})	$(x_i-x_{avg})^2$	x_i (kg)	(x_i-x_{avg})	$(x_i-x_{avg})^2$
1	9.458	-0.266	7.09E-02	7.314	-0.149	2.22E-02	5.541	0.151	2.27E-02	5.585	-0.118	1.38E-02
2	8.988	0.204	4.15E-02	6.895	0.270	7.29E-02	5.744	-0.052	2.74E-03	5.380	0.087	7.63E-03
3	9.129	0.063	3.93E-03	7.286	-0.121	1.46E-02	5.790	-0.098	9.67E-03	5.437	0.030	9.20E-04

$\bar{x}$	= 9.192	= 7.165	= 5.692	= 5.467
s	= 0.197	= 0.191	= 0.108	= 0.086
u_x	= 0.114	= 0.110	= 0.062	= 0.050
t	= 4.303	= 4.303	= 4.303	= 4.303
C_d	= 0.489	= 0.475	= 0.269	= 0.215
CI	= 9.192±0.489kg	= 7.165±0.475kg	= 5.692±0.269kg	= 5.467±0.215kg

D60:

Test no.	Diameter of orifice (mm)											
	0.104			0.156			0.208			0.26		
	x_i (kg)	(x_i-x_{avg})	$(x_i-x_{avg})^2$	x_i (kg)	(x_i-x_{avg})	$(x_i-x_{avg})^2$	x_i (kg)	(x_i-x_{avg})	$(x_i-x_{avg})^2$	x_i (kg)	(x_i-x_{avg})	$(x_i-x_{avg})^2$
1	9.184	-0.189	3.57E-02	6.706	-0.138	1.91E-02	5.656	-0.149	2.22E-02	5.659	-0.390	1.52E-01
2	8.818	0.177	3.13E-02	6.567	0.001	4.44E-07	5.526	-0.019	3.61E-04	5.008	0.261	6.79E-02
3	8.983	0.012	1.44E-04	6.430	0.138	1.90E-02	5.339	0.168	2.82E-02	5.139	0.130	1.68E-02

$\bar{x}$	= 8.995	= 6.568	= 5.507	= 5.269
s	= 0.150	= 0.113	= 0.130	= 0.281
u_x	= 0.086	= 0.065	= 0.075	= 0.162
t	= 4.303	= 4.303	= 4.303	= 4.303
C_d	= 0.372	= 0.280	= 0.323	= 0.698
CI	= 8.995±0.372kg	= 6.568±0.280kg	= 5.507±0.323kg	= 5.269±0.698kg

The **GB16** uncertainties were also tabulated:

D30:

Test no.	Diameter of orifice (mm)											
	0.104			0.156			0.208			0.26		
	x_i (kg)	(x_i-x_{avg})	$(x_i-x_{avg})^2$	x_i (kg)	(x_i-x_{avg})	$(x_i-x_{avg})^2$	x_i (kg)	(x_i-x_{avg})	$(x_i-x_{avg})^2$	x_i (kg)	(x_i-x_{avg})	$(x_i-x_{avg})^2$
1	2.192	0.707	4.99E-01	3.341	0.093	8.71E-03	1.922	0.931	8.67E-01	2.446	-0.134	1.80E-02
2	4.325	-1.426	2.03E+00	3.701	-0.267	7.11E-02	3.017	-0.164	2.69E-02	2.155	0.157	2.45E-02
3	2.179	0.720	5.18E-01	3.261	0.173	3.00E-02	3.620	-0.767	5.88E-01	2.334	-0.022	4.99E-04

$\bar{x}$	= 2.899	= 3.434	= 2.853	= 2.312
s	= 1.009	= 0.191	= 0.703	= 0.120
u_x	= 0.582	= 0.110	= 0.406	= 0.069
t	= 4.303	= 4.303	= 4.303	= 4.303
C_d	= 2.505	= 0.475	= 1.746	= 0.298
CI	= 2.899±2.505kg	= 3.434±0.475kg	= 2.853±1.746kg	= 2.312±0.298kg

D40:

Test no.	Diameter of orifice (mm)											
	0.104			0.156			0.208			0.26		
	x_i (kg)	(x_i-x_{avg})	$(x_i-x_{avg})^2$	x_i (kg)	(x_i-x_{avg})	$(x_i-x_{avg})^2$	x_i (kg)	(x_i-x_{avg})	$(x_i-x_{avg})^2$	x_i (kg)	(x_i-x_{avg})	$(x_i-x_{avg})^2$
1	8.240	-0.173	3.00E-02	6.664	-0.005	2.50E-05	4.535	-0.845	7.14E-01	4.298	-0.681	4.64E-01
2	6.640	1.427	2.04E+00	6.490	0.169	2.86E-02	2.560	1.130	1.28E+00	2.869	0.748	5.60E-01
3	9.320	-1.253	1.57E+00	6.823	-0.164	2.69E-02	3.975	-0.285	8.12E-02	3.684	-0.067	4.49E-03

$\bar{x}$	= 8.067	= 6.659	= 3.690	= 3.617
s	= 1.101	= 0.136	= 0.831	= 0.585
u_x	= 0.636	= 0.079	= 0.480	= 0.338
t	= 4.303	= 4.303	= 4.303	= 4.303
C_d	= 2.735	= 0.338	= 2.065	= 1.454
CI	= 8.067±2.735kg	= 6.659±0.338kg	= 3.690±2.065kg	= 3.617±1.454kg

D50:

Test no.	Diameter of orifice (mm)											
	0.104			0.156			0.208			0.26		
	x_i (kg)	(x_i-x_{avg})	$(x_i-x_{avg})^2$	x_i (kg)	(x_i-x_{avg})	$(x_i-x_{avg})^2$	x_i (kg)	(x_i-x_{avg})	$(x_i-x_{avg})^2$	x_i (kg)	(x_i-x_{avg})	$(x_i-x_{avg})^2$
1	9.601	-0.229	5.24E-02	6.865	0.006	3.21E-05	5.116	0.354	1.25E-01	4.802	0.271	7.36E-02
2	9.386	-0.014	1.96E-04	6.761	0.110	1.20E-02	5.504	-0.034	1.16E-03	4.981	0.092	8.53E-03
3	9.129	0.243	5.90E-02	6.986	-0.115	1.33E-02	5.790	-0.320	1.02E-01	5.437	-0.364	1.32E-01

$\bar{x}$	= 9.372	= 6.871	= 5.470	= 5.073
s	= 0.193	= 0.092	= 0.276	= 0.267
u_x	= 0.111	= 0.053	= 0.159	= 0.154
t	= 4.303	= 4.303	= 4.303	= 4.303
C_d	= 0.479	= 0.228	= 0.686	= 0.664
CI	= 9.372±0.479kg	= 6.871±0.228kg	= 5.470±0.686kg	= 5.073±0.664kg

D60:

Test no.	Diameter of orifice (mm)											
	0.104			0.156			0.208			0.26		
	x_i (kg)	(x_i-x_{avg})	$(x_i-x_{avg})^2$	x_i (kg)	(x_i-x_{avg})	$(x_i-x_{avg})^2$	x_i (kg)	(x_i-x_{avg})	$(x_i-x_{avg})^2$	x_i (kg)	(x_i-x_{avg})	$(x_i-x_{avg})^2$
1	9.703	-0.252	6.33E-02	7.194	-0.245	6.02E-02	6.207	-0.431	1.86E-01	5.183	0.004	1.34E-05
2	9.268	0.183	3.36E-02	6.811	0.138	1.90E-02	5.781	-0.005	2.84E-05	5.208	-0.021	4.55E-04
3	9.383	0.068	4.67E-03	6.841	0.108	1.16E-02	5.339	0.437	1.91E-01	5.169	0.018	3.12E-04

$\bar{x}$	=	9.451	=	6.949	=	5.776	=	5.187
s	=	0.184	=	0.174	=	0.354	=	0.016
u_x	=	0.106	=	0.100	=	0.205	=	0.009
t	=	4.303	=	4.303	=	4.303	=	4.303
C_d	=	0.457	=	0.432	=	0.880	=	0.040
CI	=	9.451±0.457kg	=	6.949±0.432kg	=	5.776±0.880kg	=	5.187±0.04kg